Internal waves, turbulent mixing and upper ocean heat balances in the southeast Indian Ocean

by

Ajitha Cyriac

Grad. Dip. Marine and Antarctic Science, B.Tech. Aeronautical Engineering

M.Tech. Earth System Science and Technology

Submitted in fulfilment of the requirements

for the degree of Doctor of Philosophy

in

Quantitative Marine Science

(A joint CSIRO and UTAS PhD program)

Institute for Marine and Antarctic Studies (IMAS)

UNIVERSITY OF TASMANIA

June, 2020

Declaration

This thesis contains no material which has been accepted for a degree or diploma by the University or any other institution, except by way of background information and duly acknowledged in the thesis, and to the best of my knowledge and belief no material previously published or written by another person except where due acknowledgement is made in the text of the thesis, nor does the thesis contain any material that infringes copyright.

Signed:

_____

Ajitha Cyriac

Date: June, 2020

_____

"It is our choices that show what we truly are far more than our abilities"

Prof. Albus Dumbledore

"When you want something, all the universe conspires in helping you to achieve it"

Paulo Coelho, Alchemist

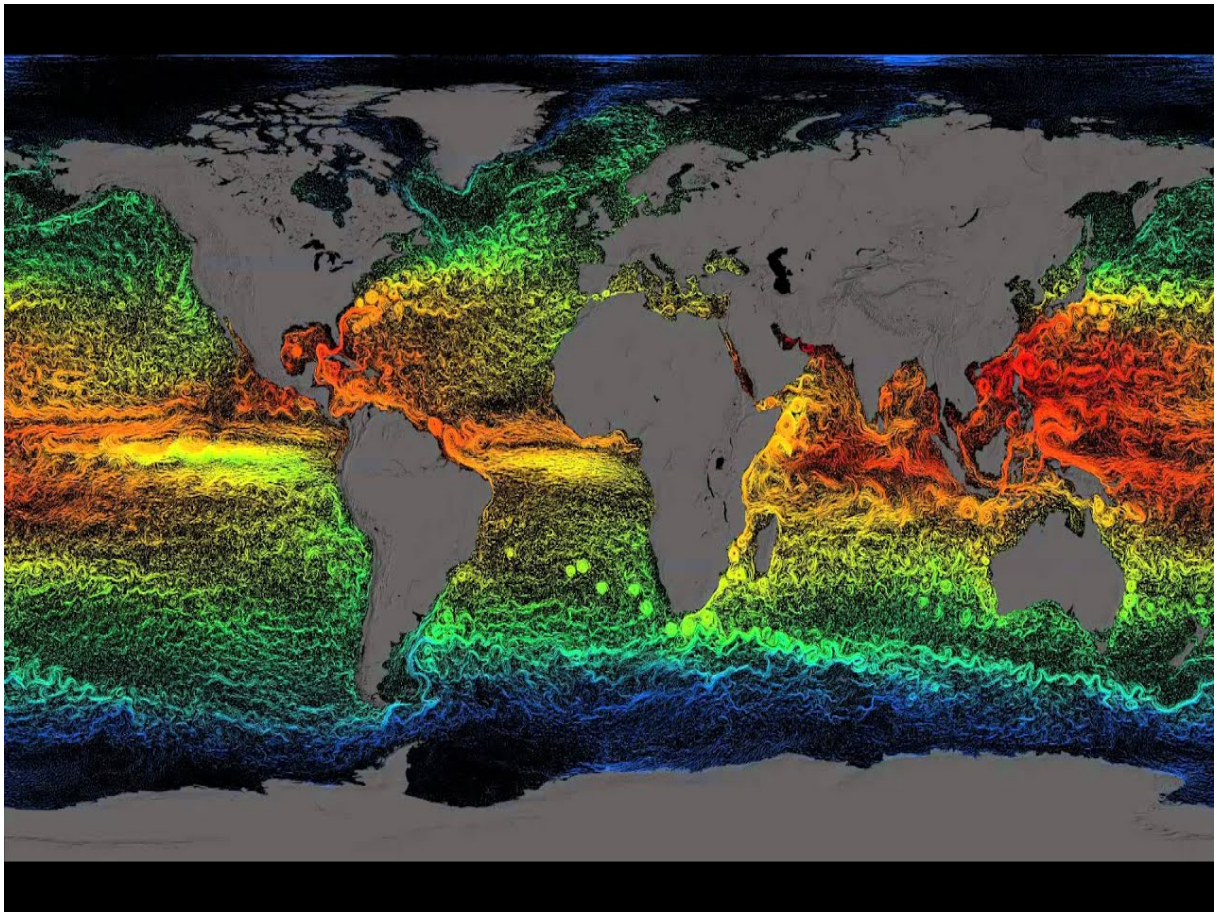

Figure 1: Global sea surface currents from ECCO2 colored by sea surface temperature. Adapted from `https://svs.gsfc.nasa.gov/vis/`.

Statement of Co-authorship

The following people and institutions contributed to the publication of work undertaken as part of this thesis:

Candidate: Ajitha Cyriac, IMAS
Author 1: Dr. Helen Phillips, IMAS
Author 2: Prof. Nathan Bindoff, IMAS
Author 3: Dr. Ming Feng, CSIRO
Author 4: Dr. Michael McPhaden, NOAA

Author details and their roles:

Paper 1, Characteristics of the near-inertial internal waves in the southeast Indian Ocean
Located in Chapter 2

Candidate (84%) performed the analysis, interpreted the results, wrote the manuscript, and acted as corresponding author. Author 1 (10%) and Author 2 (4%) contributed to the original idea and discussion of the results. Author 3 (2%) contributed to several ideas and refinement of the manuscript.

Paper 2, Observations of turbulent mixing in the southeast Indian Ocean
Located in Chapter 3

Candidate (86%) performed the analysis, interpreted the results, wrote the manuscript, and acted as corresponding author. Author 1 (10%) contributed to the original idea and discussion of the results. Author 2 (2%) and author 3 (2%) contributed to several ideas and refinement of the manuscript.

Paper 3, Seasonal evolution of the surface layer heat balance in the eastern subtropical Indian Ocean
Located in Chapter 4

Candidate (80%) performed the analysis, interpreted the results, wrote the manuscript, and acted as corresponding author. Author 1 (8%) and Author 4 (8%) contributed to the original idea and discussion

of the results. Author 2 (2%) and Author 3 (2%) contributed to several ideas and refinement of the manuscript.

We the undersigned agree with the above stated "proportion of work undertaken" for the above published (or submitted) peer-reviewed manuscript contributing to this thesis:

Signed:

_____

Ajitha Cyriac (Candidate)

Signed:

_____

Dr. Helen Phillips

Primary supervisor

Institute for Marine and Antarctic Studies

University of Tasmania

Signed:

_____

Prof. Neil Holbrook

Centre Head, Oceans and Cryosphere

Institute for Marine and Antarctic Studies

University of Tasmania

Authority of Access

The publishers of the paper comprising Chapter 2, 3 and 4 hold the copyright for that content, and access to the material should be sought from the respective journals:

Chapter 4 is an edited version published by ©2019 American Geophysical Union as Cyriac, A., McPhaden, M., Phillips, H., Bindoff, N., and Feng, M. (2019). Seasonal evolution of the surface layer heat balance in the eastern subtropical Indian Ocean. *Journal of Geophysical Research: Oceans*, 124(9), 6459–6477. `https://doi.org/10.1029/2018JC014559`.

Chapter 3 is an edited version under revision in ©2020 American Meteorological Society as Cyriac, A., Phillips, H., Bindoff, N., Mao, H., and Feng, M. (2020). Observations of turbulent mixing in the southeast Indian Ocean. *Journal of Physical Oceanography*.

Appendix A contains the supplementary materials for all of the chapters.

The remaining non-published content of the thesis may be made available for loan and limited copying and communication in accordance with the Copyright Act 1968.

Signed:

_____

Ajitha Cyriac

Date: June, 2020

_____

Acknowledgements

Firstly, I would like to express my sincere gratitude to my supervisory committee. A big thanks to my primary supervisor Helen Phillips for the continuous support throughout my PhD, for her patience, motivation, and immense knowledge. I could not have imagined having a better advisor and mentor for my PhD study. I would like to thank Nathan Bindoff and Ming Feng, for their insightful comments and encouragement throughout my study. Their guidance helped me in all the time of research and writing of this thesis.

I would like to thank Michael McPhaden for the ideas and discussions, that much contributed for the success of this thesis. Thank you for responding quicker to my emails and clarifying my doubts with clear explanations.

Many thanks to Amelie Meyer and Kurt Polzin, who have provided advice, suggestions and shared their knowledge. Their valuable questions and comments improved the quality of the thesis.

I would also like to thank the ARC Centre of Excellence for Climate System Science for the financial support to travel to conferences, summer/winter schools, and amazing workshops. I thank Graduate Research Office for the travel fund which allowed me to visit Kurt Polzin at Woods Hole, USA.

Many thanks to my friends and colleagues at IMAS, ARCCSS, CLEX and everywhere in the world for their friendship and emotional support throughout my PhD. I would like to specially thank my close friends Ramkrushn (Ram), Luwei, Saurabh and Asher who has ensured their technical and emotional support when I was in much need. You made me laugh when I didn't even want to smile.

Finally, I would like to thank my family: my parents and my brothers, for supporting me spiritually throughout writing this thesis and my life in general. Thank you mom and dad for showing faith in me and giving me the liberty to choose what I desired. A big thanks to Joe for giving me the emotional support I needed while I was writing the thesis. Thank you all for believing in me.

Abstract

A unique feature of the circulation in the eastern south Indian Ocean (SIO) is the eastward-flowing, near-surface geostrophic currents, known as the South Indian Countercurrent (SICC) and Eastern Gyral Current (EGC). They act as a source of water for the only poleward-flowing eastern boundary current of the mid-latitude global ocean called the Leeuwin Current (LC). The downwelled waters beneath the LC also supply the intermediate-depth, equatorward-flowing Leeuwin Undercurrent and the anticyclonic subtropical gyre. Instabilities of the Leeuwin Current System generate mesoscale eddies that propagate westward into the SICC jets, which can themselves be unstable. This interaction of the zonal currents and eddy field occurs in a region of strong air-sea exchange and subduction of high-salinity surface waters that contributes to the meridional overturning circulation of the Indian Ocean. Superimposed on the large and mesoscale environment are internal waves which are responsible for most of the turbulent mixing in the stratified ocean through wave breaking. In the interior of the ocean, this turbulent mixing plays an important role in setting the large-scale stratification and consequently, the large-scale circulation where mixing from surface processes cannot provide energy directly.

At present, the global products from in situ and remotely sensed observations provide a good understanding of the large-scale, near-surface circulation and air-sea exchanges. From hydrographic transects, we understand the vertical structure of the zonal currents along three repeat lines, but none close to Australia. Recently, global analyses from the Argo array and a collection of sparse observations provide estimates of vertical mixing in the eastern Indian Ocean, but they differ by an order of magnitude. Moreover, until this study, there were no direct long-term measurements of air-sea fluxes with which to examine the interactions that are central to the upper ocean variability in this region, where the reanalysis products disagree in their magnitudes of the surface fluxes. Thus, a better understanding of the interactions between these different scales of motion and air-sea interface in this region is essential to further our understanding of the Indian Ocean's influence on Australian and regional climate.

This study aims to provide a detailed picture of the geostrophic currents and eddies, air-sea exchange, internal waves and turbulent mixing in the eastern SIO by exploiting high resolution *in situ* observations, reanalysis products, and satellite altimetry. Specific goals of this thesis include: i) characterize the spatial and temporal variability of the near-inertial internal wave field in the SIO and estimate the wave properties and potential sources; ii) quantify the turbulent mixing associated with the breaking of internal waves; iii) investigate potential relationships between the geostrophic circulation, internal waves and mixing in the regional context; and iv) determine the relative roles of atmospheric forcing and ocean processes on the evolution of observed mixed layer temperature.

To achieve these goals, we made use of a collection of *in situ* observations from two hydrographic and microstructure surveys across the strongest SICC jet between 25°S – 32°S, a two-year RAMA flux mooring deployment at 25°S, 100°E, and five Electromagnetic Autonomous Profiling Explorer (EM-APEX) floats which gave 3726 collocated profiles of temperature, salinity and velocity with 8 profiles per day. The floats provided high spatial resolution data with 3 – 4 dbar in the vertical and 3 – 5 km in the horizontal during July – October 2013 up to a depth of 300 m (2160 profiles) and 1200 m (1566 profiles). We also took advantage of additional data from the Argo array, reanalysis products and ocean climatology to provide broader spatial and temporal context for our study. The near-inertial waves are identified by applying a complex demodulation of the high-resolution velocity data provided by the floats. To estimate turbulent mixing, we applied a fine-scale parameterization on the EM-APEX and shipboard data. Using mixed layer heat budget diagnostic models, we analysed the mixed layer heat balance from the mooring data.

We identify many near-inertial internal waves in the EM-APEX records and examine a representative subset of 15 internal waves with near-inertial frequency in the upper 1200 m. The observed near-inertial wave field in the southeast Indian Ocean has a mean vertical wavelength of 89 ± 63 m, a mean horizontal wavelength of 69 ± 85 km, a horizontal group velocity of 3 ± 2 cm s^{-1} and a mean vertical group velocity of 9 ± 7 m day^{-1}. The mean vertical energy flux of the downward propagating beams is more than 40% of the wind work, with the potential to reach the deep ocean. The generation and propagation of the observed near-inertial waves are dependent on the regional dynamics. High energy near-inertial waves, that are consistent with having been generated from a remote region from an earlier wind event and not having generated locally, are observed at a depth of 700 m with kinetic energy of 20 – 30 J m^{-3}, providing energy for the deep ocean mixing. High near-inertial shear variance is observed in the warm core eddies near the surface consistent with trapping of near-inertial waves by the anticyclonic vorticity field. Large near-inertial wave amplitudes associated with patches of high near-inertial shear variance are often observed near the surface following strong wind events suggesting that some waves are generated locally. Most of the observed near-inertial beams are found to be propagating downward and equatorward with a blue-shift of 10 – 15%, suggesting that wind is the main source of energy for the observed beams.

The inferred turbulent mixing in the eastern SIO from EM-APEX floats shows substantial spatial and temporal variability. The mean diapycnal diffusivity for this region is at background levels (O(10^{-6} $m^2 s^{-1}$)) in the upper 250 – 500 m whereas it is elevated between 500 – 1000 m in cyclonic eddies. We find that elevated mixing (O(10^{-3} $m^2 s^{-1}$)) in this region occurs in association with strong wind events, mesoscale eddies and rough bottom topography. Within warm core eddies, near-inertial wave

breaking results in elevated mixing in the upper 400 m. Whereas, higher mixing within cyclonic eddies is associated with downward propagating internal waves with frequencies higher than inertial, possibly due to wave capturing by the strain field of the eddy. From a strain parameterization of CTD data, elevated mixing levels were observed near the sea floor, suggesting a possible role for internal wave generation due to tidal motions or strong geostrophic flows over rough bathymetry. Enhanced mixing is often found where elevated near-inertial wave amplitudes occur, suggesting that the near-inertial waves play an important role in the turbulent mixing distribution of the upper 1000 m. The mixing estimates show that higher diffusivities are found in the Antarctic Intermediate Water (AAIW) layer (O(10^{-3} m^2s^{-1})) and very low diffusivities (O(10^{-6} m^2s^{-1})) are found in the Subantarctic Mode Water (SAMW) layer in this region, suggesting a role for internal wave breaking in the modification of AAIW on its pathway northward. Enhanced mixing in mesoscale eddies is also found to be important for the maintenance of the SICC where its jet-like structure is thought to be associated with potential vorticity gradients generated by the mixing of potential vorticity like a tracer.

We find that on seasonal timescales in the subtropical southeast Indian Ocean, the primary balance in the mixed layer heat budget is between the surface net heat flux, and turbulent entrainment with contribution from horizontal advection at times. Both zonal and meridional advection terms appear to be dominated by the presence of mesoscale eddies and possibly annual and semi-annual Rossby waves propagating from the eastern boundary. During austral summer, all heat flux terms tend to warm the mixed layer, with more contribution from surface net heat flux and meridional advection. During austral winter, horizontal advection warms the mixed layer whereas surface net heat flux and vertical processes cool the mixed layer. Turbulent entrainment is in good agreement with the heat budget residual for most of the year. This analysis is complemented by a 12-year regional ocean heat budget analysis around the mooring using reanalysis products. The seasonal cycle of the heat storage and surface net heating at the mooring location from the long-term analysis is in reasonably good agreement with the 2-year mooring analysis suggesting that this heat budget analysis provides a longer-term context for understanding the processes that drive the surface layer heat budget in this region.

This study shows that the interaction between internal waves and mesoscale eddies is important for the mixing budget and in setting the stratification of the eastern SIO. This thesis improves our understanding of wave-eddy-mean flow interactions and its implications on the large-scale circulation and air-sea exchanges in the eastern SIO. It also prompts us of the importance of the high-resolution ocean and atmosphere observations in understanding multi-scale processes that can have a profound impact on the large-scale circulation and climate system.

Contents

List of Figures

List of Tables

List of Abbreviations

SIO	South Indian Ocean
SICC	South Indian Countercurrent
EGC	Eastern Gyral Current
LC	Leeuwin Current
SEC	South Equatorial Current
LUC	Leeuwin Undercurrent
LCS	Leeuwin Current System
NIW	Near-inertial Wave
IW	Internal Wave
EM-APEX	Electromagnetic Autonomous Profiling Explorer
CTD	Conductivity Temperature Depth
LADCP	Lowered Acoustic Doppler Current Profiler
GPS	Global Positioning System
cpd	cycle per day
SLA	Sea Level Anomaly
CCW	Counterclockwise
CW	Clockwise
PV	Potential Vorticity
MLD	Mixed Layer Depth

AAIW	Antarctic Intermediate Water
SAMW	Subantarctic Mode Water
STUW	Subtropical Underwater
SO	Southern Ocean
KE	Kinetic Energy

Dedicated to my parents . . .

Chapter 1

Introduction

The ocean is a continuously moving fluid with different scales of motion in both space and time (Fig.1.1). Turbulent mixing is at the smallest scales. Internal waves are at scales of ten to hundred meters with a time duration of few minutes to hours. At scales of ten to hundred meters are mesoscale eddies with timescales from weeks to months. The large-scale ocean circulation has a spatial scale the same as that of the ocean basins with a time scale of decades to centuries. Even though the forces relevant to each motion are different, the observed motion in the ocean is a combination of small-scale swirls to large-scale circulation (Ferrari and Wunsch, 2009, Fig. 1.1). The small-scale features such as internal waves interact and coexist with oceanic phenomena of different scales such as large-scale circulation, mesoscale and sub-mesoscale eddies and fronts. The large-scale circulation affects the generation and propagation of internal waves by setting up the stratification that supports the internal wave field. The internal waves feedback to the large-scales when they break by changing the local mixing that in turn affects the evolution of large-scale circulation and eddies. These interactions are important for the long-term variations of the ocean circulation and thereby climate. While the large-scale circulation is well studied, the small-scale processes like turbulent mixing are not well observed and are still uncertain in many regions despite many years of effort. These processes need to be better observed and parameterizations for them included in ocean climate models for better climate prediction.

1.1 Large-scale circulation in the Indian Ocean

The Indian Ocean (IO) is different from other oceans in that it is limited by a northern boundary. This unique feature helps it to drive the monsoon winds, one of the most dynamic interactions between ocean, atmosphere and land (Clemens et al., 1991). The IO has a significant impact on the climate in the form of the Indian Ocean Dipole, feedbacks to the El-Nino Southern Oscillation in the Pacific and other ocean-atmosphere phenomena of varying time scales (Schott et al., 2009). It also influences the socio-economic

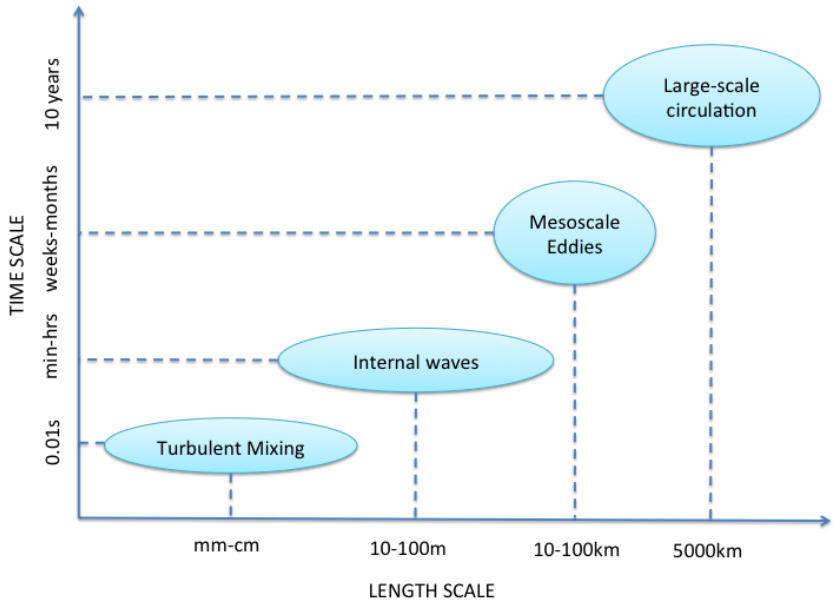

Figure 1.1: Time and length scales of different motions in the ocean, adapted from Talley (2011).

systems of the countries on its rim by influencing rainfall patterns and intensity (supports agriculture), and through fisheries, oil and gas.

1.1.1 Monsoon and surface currents

The differential heating between ocean and land in the IO drives the strong monsoon winds on earth. In the northern hemisphere (boreal) winter, the air above the ocean gets warmer than that over the Asian land mass and drives the winds towards the ocean from the northeast direction (Fig. 1.2b). While in the boreal summer, the pressure cells reverse and winds blow from the ocean towards the continent from the southwest (Fig. 1.2c). The reversal of the monsoon winds cause seasonal reversals in the IO currents (Fig. 1.3).

During the boreal summer monsoon (Fig.1.3a), the westward-flowing South Equatorial Current (SEC) and northward-flowing EACC (East African Coastal Current) feed the Somali Current (SC) that flows northward in this season. During this time, there are three gyres observed in the northwest IO: a recirculation of the SC across the Equator, known as the Southern Gyre; the Great Whirl, which is an anticyclonic circulation near the entrance to the Red Sea; and the Socotra Eddy, which is observed in many summer monsoons northeast of Socotra (Schott et al., 2009). The Southwest monsoon current flows eastward south of India and turns northward east of Sri Lanka, carrying saltier Arabian Sea water into the Bay of Bengal (Jensen, 2003). The South Java Current (SJC), which reverses its direction seasonally, flows northwestward during this time.

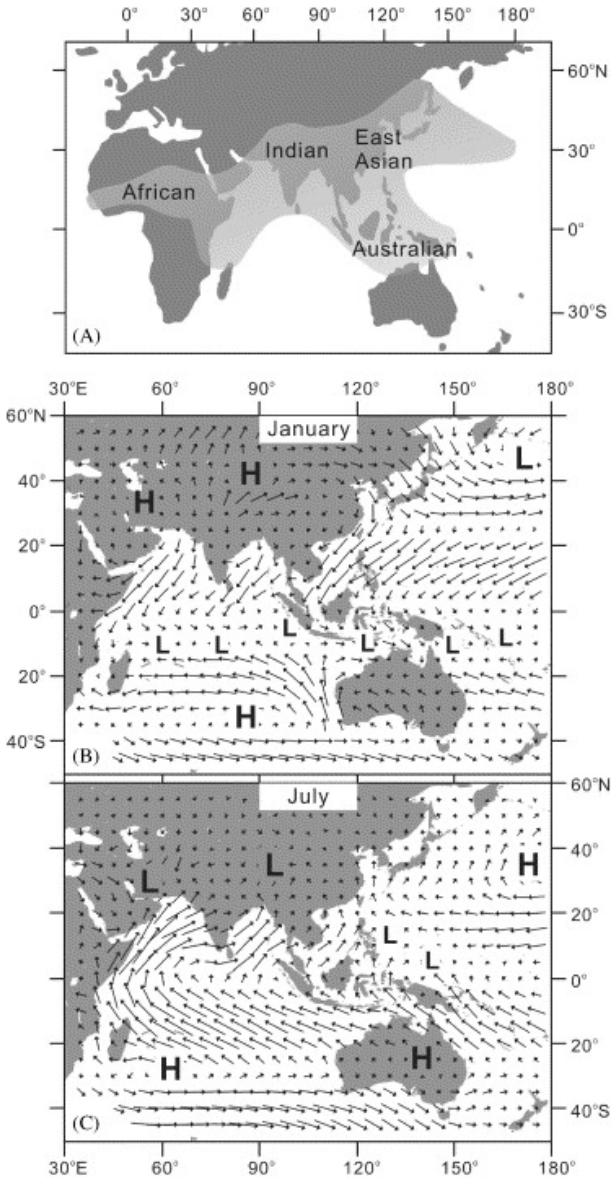

Figure 1.2: Asian Monsoon system: A) distribution of monsoon regions in Asia, Africa and Australia, and wind directions during B) winter (January) C) summer (July) from Wang et al. (2005). The vectors represent the wind direction between high pressure systems (H) and low pressure systems (L).

During the winter monsoon, the SC reverses its direction and flows southward. It meets the northward flowing EACC near 2 – 4°S and supplies water to the eastward flowing SECC, which is masked by the westward Ekman currents during the summer monsoon. During this time, the comparatively fresher water from the Bay of Bengal flows around Sri Lanka to the Arabian Sea (Jensen, 2003; Schott et al., 2009). The SJC flows southeastward during the winter monsoon.

The Indonesian Throughflow (ITF) transports warm and relatively fresh Pacific water to the IO (Birol and Morrow, 2001; Morrow and Birol, 1998), mostly within the upper layers. As the annual mean winds over the equatorial IO are weak and westerly, there is less or no climatological upwelling on the Equator

as there is in other oceans. However, upwelling occurs away from the equator in both hemispheres of the IO, along coastlines where seasonally-varying along-shore winds are upwelling favourable.

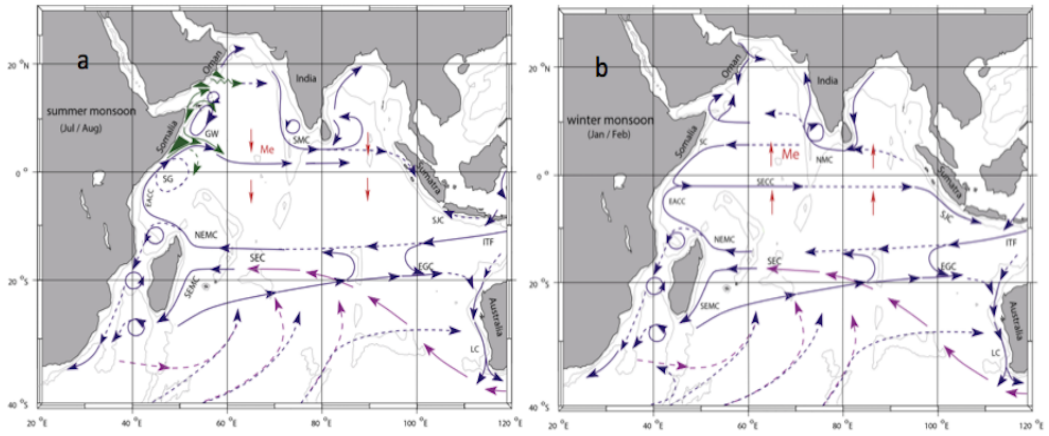

Figure 1.3: Schematic diagram from Schott et al. (2009) of the Indian Ocean currents during (a) Southwest monsoon and (b) Northeast monsoon. The indicated currents are the South Equatorial Current (SEC) and South Equatorial Countercurrent (SECC), Northeast Madagascar Current (NEMC) and Southeast Madagascar Current (SEMC), Southern Gyre (SG) and Great Whirl (GW), Southwest and Northeast Monsoon Currents (SMC and NMC), South Java Current (SJC), Leeuwin Current (LC), East African Coastal Current (EACC), Eastern Gyral Current (EGC) and Indonesian Throughflow (ITF).

1.1.2 Near-surface eastward flows and Leeuwin Current

An important aspect of the circulation in the subtropical south Indian Ocean is the near surface eastward flows. They are broad and shallow and flow in a direction opposite to that predicted by Ekman and Sverdrup theories (Godfrey and Ridgway, 1985). Sverdrup theory predicts a net meridional flow in the south Indian Ocean subtropical gyre, resulting from planetary vorticity changes that balance the wind stress curl. This is accompanied by a westward return flow across the south IO from the centre of the subtropical gyre ($\sim$ 32°S) to the centre of the tropical cyclonic gyre ($\sim$ 10°S). The eastward flows also seem to defy the Ekman theory. The subtropical southeast Indian Ocean is dominated by southwesterly winds, which is expected to result in a westward near-surface flow. Kobashi et al. (2006) and Kobashi and Kubokawa (2012) studied the eastward flows in the North Pacific and called these flows the Subtropical Countercurrent (STCC). They identified three STCCs in the North Pacific and all of them are accompanied by thermal and density fronts at subsurface depths of about 100 – 200 m. These fronts give rise to eastward vertical shears near the surface of the subtropical gyre. There are STCCs in other ocean basins and they may have a similar mechanism to that in the North Pacific (Kobashi et al., 2006; Kobashi and Kubokawa, 2012).

In the subtropical South Indian Ocean (SIO), the eastward flows were recognized as a permanent feature of the IO circulation by the end of the last decade. This geostrophic flow between 25 – 30°S was termed the South Indian Ocean Countercurrent (SICC) by Palastanga et al. (2007), in analogy to the STCC in the Pacific Ocean. Palastanga et al. (2007) and Siedler et al. (2006) identified a secondary subtropical density frontal zone between 20 – 30°S across the basin. They suggested that the SICC could be its associated frontal jet. Using climatological data they identified that the density front is dominated by a meridional salinity gradient that separates the salty waters of the central subtropical SIO from the fresh waters of the ITF. Schott et al. (2009) mentioned these eastward flows as the re-entry of the Aghulas retroflection into the IO that extends to the west coast of Australia whereas Siedler et al. (2006) and Palastanga et al. (2007) suggested that the SICC is nourished by the partial retroflection of the East Madagascar Current (EMC).

With the help of climatological atlases of historical observations and recent shipboard data collected from the southeast Indian Ocean, Menezes et al. (2013) and Menezes et al. (2014) give a clear description of the structure of these eastward flows and the associated density structure. Parts of the eastward flows are concentrated into discrete bands and have been identified as the subtropical South Indian Counter Current (SICC) between 20 – 30°S (Menezes et al., 2014) and the tropical Eastern Gyral Current (EGC) between 14 – 17°S (Menezes et al., 2013) close to Australia. The SICC is much weaker (3 – 6 cm s^{-1}) and shallower (200 – 250 m) as compared to the westward flowing SEC (10 – 15 cm s^{-1}) (Palastanga et al., 2007; Jia et al., 2011b). In earlier studies, not much distinction is made between the EGC and the SICC (Siedler et al., 2006; Palastanga et al., 2007). However, Menezes et al. (2013) has shown that they are two different currents. In the SICC, vertical shear arises from thermal meridional gradients whereas in the EGC, meridional salinity gradients between the salty subtropical water and fresh Indonesian Throughflow water dominate the vertical shear. The SICC consists of three branches namely the northern, central and southern SICC (Fig. 1.4). Among them, the southern branch is the strongest and the northern branch is the weakest. The southern SICC around 26°S is associated with a permanent subsurface thermal front at depths of 100 – 200 m while salinity is of secondary importance (Menezes et al., 2014). This is in contrast to the suggestion of Siedler et al. (2006) and Palastanga et al. (2007).

Both the EGC and SICC are sources of water for the poleward flowing, warm Leeuwin Current (LC) (Divakaran and Brassington, 2011; Domingues et al., 2007; Menezes et al., 2013), flowing along the western coast of Australia. The seasonal cycle of the LC is the same as that of the EGC (Menezes et al., 2013). The LC is stronger during winter and weaker during summer. It is accompanied by a northward-flowing undercurrent, called the Leeuwin Undercurrent (LUC), part of which bends northwestward and westward to flow offshore under the surface eastward flow (Domingues et al., 2007; Godfrey and Ridgway, 1985;

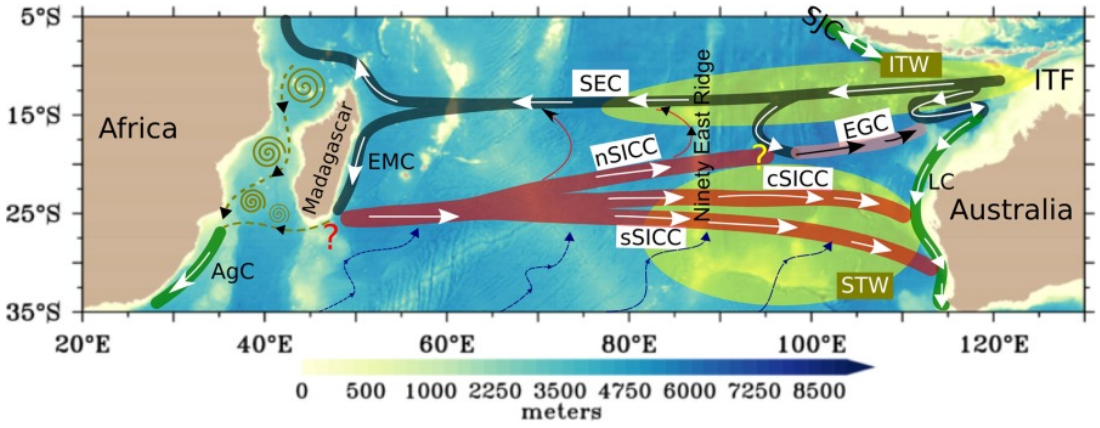

Figure 1.4: Schematic representation of the currents in the SIO from Menezes et al. (2014). The three branches of SICC: northern SICC (nSICC), central SICC (cSICC), and southern SICC (sSICC); South Equatorial Current (SEC); East Madagascar Current (EMC); Eastern Gyral Current (EGC); ITF; Aghulas Current (AgC); Leeuwin Current (LC); South Java Current (SJC). Light green shadings show Indonesian Throughflow Water (ITW) and Subtropical Water (STW) regions.

Furue et al., 2017).

Ocean reanalysis data and climatological data (Divakaran and Brassington, 2011; Palastanga et al., 2007; Schott et al., 2009), reveal that the eastward flows are accompanied by a mid-depth westward flow at about 500 m in agreement with the large scale Sverdrup flow (Siedler et al., 2006, Fig. 1.5). The eastward flow is more dominant and deep as it reaches the western Australian coast whereas the westward flow is dominant in the sub-surface and it is weak and narrow towards the surface (Divakaran and Brassington, 2011).

1.1.3 Leeuwin Current and mesoscale eddies

Mesoscale eddies are ubiquitous in the ocean with length scales of 10 – 100 km and time scales of a few days to months. Some eddies extend from the surface to the ocean bottom whereas others extend only into the thermocline. Eddies are mainly generated near strong currents and can have warm or cold cores with opposite directions of rotation. Anticyclonic eddies rotate anticlockwise in the southern hemisphere and have warm cores with elevated sea surface and deepened density contours at the centre. By contrast, cyclonic eddies rotate clockwise in the southern hemisphere, have cold cores with depressed sea surface and doming isopycnals in the interior.

Eddies are large reservoirs of kinetic energy in the ocean. They can transport heat, momentum and nutrients and they can transfer energy and accelerate the mean currents (Morrow et al., 2004). The zonal mass transport induced by eddies is comparable to that of the large-scale circulation even in regions where the background current is not strong (Zheng et al., 2015). Eddies distribute properties of the mean

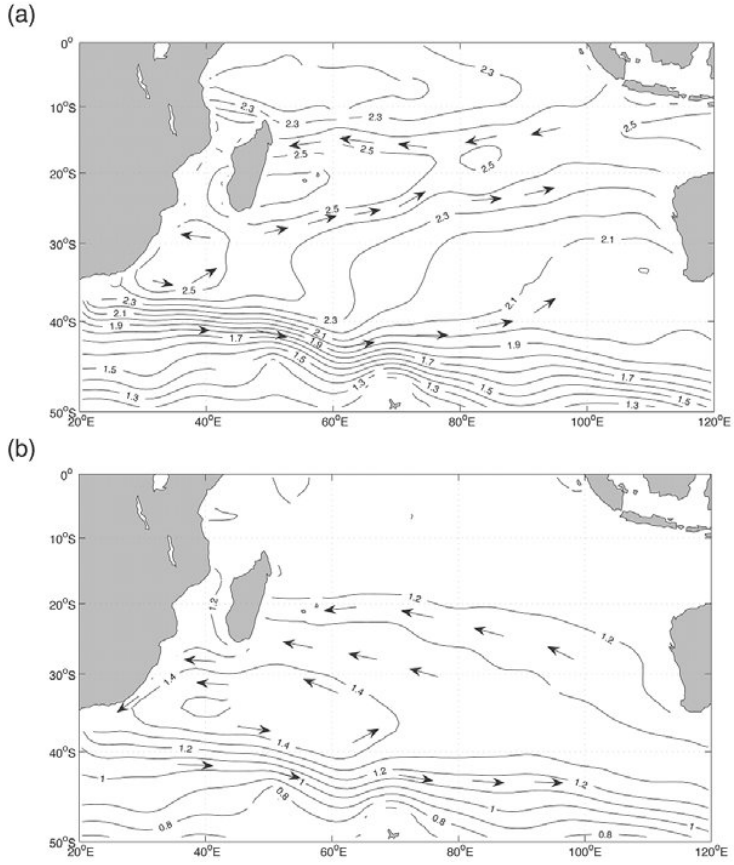

Figure 1.5: Dynamic topography of the SIO relative to 2000 m a) at the surface showing eastward flow b) at 500 m depth showing subsurface westward flow from (Palastanga et al., 2007). Units are in $m^2\ s^{-2}$.

current through their outer ring (Early et al., 2011) by detaching from and sometimes by re-merging with the mean current.

Instability of the large-scale currents is a major source of mesoscale eddies (e.g. Ferrari and Wunsch, 2009; Jia et al., 2011b). Barotropic instability extracts energy from the kinetic energy in the horizontal shear, whereas baroclinic instability feeds on the potential energy available from the tilting of isopycnals. High eddy kinetic energy (EKE) is usually associated with strong mean flows (Fig. 1.6) such as the Antarctic Circumpolar Current and boundary currents (e.g. Wilkin and Morrow, 1994; Jia et al., 2011b). Away from strong currents, eddies can be generated from rapidly fluctuating winds (e.g. Frankignoul and Müller, 1979; Müller and Frankignoul, 1981). Baroclinic eddies are the sinks for a large amount of potential energy generated by winds (Wunsch and Ferrari, 2004) where the energy input ultimately dissipates through small-scale turbulence. However, the corresponding mechanisms and thus the crucial depth dependence are still unclear.

Unlike other eastern basins, the southeast IO is a region of high mesoscale, seasonal and interannual variability (Birol and Morrow, 2001). One of the few zonal bands of high EKE in the world ocean is

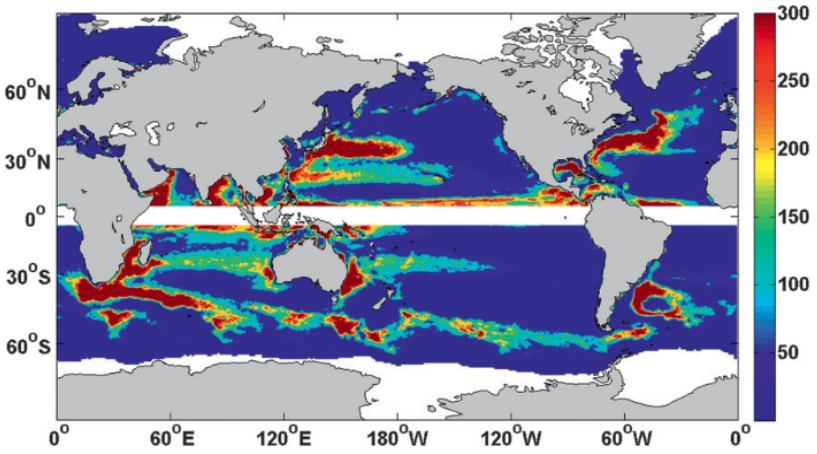

Figure 1.6: EKE ($cm^2\ s^{-2}$) from sea surface anomaly data calculated for the global ocean (Jia et al., 2011b). The band of high EKE at 25°S is clear.

found in the SIO near 25°S (Fig. 1.6). It has been proposed that this band is mainly generated from the baroclinic instability of the SICC and the subsurface westward flows beneath the SICC (Jia et al., 2011b; Qiu et al., 2008). The narrow, poleward flowing LC also plays an important role in the observed eddy variability over this region. Among the midlatitude eastern boundary currents, the LC has the strongest EKE which peaks during austral winter associated with the strengthening of the LC (Feng et al., 2005, 2003). The annual and semi-annual Rossby waves propagating from the eastern boundary also contributes to the mesoscale variability in this region (Morrow and Birol, 1998).

The interaction between LC and LUC results in the formation of pairs of cyclonic and anticyclonic eddies (Rennie et al., 2007). From their model simulations, Rennie et al. (2007) found that the LUC produces cyclonic eddies which are dominant in the subsurface whereas the anticyclonic eddies are strong at the surface. Observations also show a similar vertical structure for the eddies where warm core eddy has strong vertical shear at the surface (Feng et al., 2007). Anticyclonic eddies tend to propagate westward and equatorward, whereas cyclonic eddies tend to propagate westward and poleward in the southeast Indian Ocean (Morrow et al., 2004). Waves and occasional eddies originating from the eastern boundary travel westward and approach the SICC (Siedler et al., 2006) and dissipate (Zhai et al., 2010). Warm core eddies generated from the LC can effectively transport heat and salt anomalies into the subtropical IO with most of the heat content in the eddies occurring in the thermocline and mode water layers (Morrow et al., 2003).

1.2 Air-sea fluxes

Internal wave breaking changes the local mixing in the ocean interior and impacts the evolution of the large-scale circulation. Near the ocean surface, changes in local mixing due to external and subsurface forcing can impact the local mixed layer dynamics by varying the mixed layer depth and stratification which will affect the exchange of heat fluxes between the ocean and atmosphere (e.g. Halkides and Lee, 2011). This is of great importance in the eastern SIO, a region of strong ocean heat loss through the air-sea interface due to the influence of the Indonesian Throughflow. On interannual to decadal scales, the upper ocean heat content of the IO has increased since 1960 with enhanced warming in the SIO (Levitus et al., 2000). The northern boundary of the Indian Ocean along with strong air-sea interaction drives strong seasonal and interannual variability that modifies the temperature of the surface ocean. In the annual mean, the eastern SIO is a region of both heat (Yu et al., 2007; Josey et al., 1999) and freshwater (Zhang and Talley, 1998) loss. The combination of heat loss and strong evaporation results in high salinity surface waters which later subduct into the thermocline. These subducted waters feed the downwelling branches of southern and cross-equatorial cells of the shallow meridional overturning circulation of the IO (Lee, 2004). This heat loss also results in deeper winter mixed layers in the southern SIO compared to other subtropical oceans (Schott and McCreary, 2001). From model studies, the mixed layer depth variability in this region is found to be correlated with the heat and freshwater fluxes on intraseasonal and interannual time scales (Schiller and Oke, 2015).

The heat loss from ocean to atmosphere in the LC is equivalent to that of a western boundary current (Josey et al., 1999). This heat loss is mainly due to evaporative cooling when warm LC surface waters meet the cold air temperatures in the south, and frequent southern ocean wind storms (Feng et al., 2009). This loss of heat extends further westward from the coast into the SICC through the westward movement of LC eddies (Domingues et al., 2007; Feng et al., 2008; Morrow et al., 2003). On interannual timescales, the strength of the LC and the net surface heat loss from the current are higher during La-Nina years and lower during El-Nino years (Feng et al., 2003). The mixed layer heat budget in the eastern SIO is found to be mainly balanced between LC heat advection and air-sea fluxes on both seasonal and interannual timescales in a global eddy-permitting model (Feng et al., 2008).

In recent decades, the SST has been increasing in the LC region (Feng et al. (2008) and references therein) possibly with some contribution from the increased frequency of Ningaloo Nino, characterised by anomalous warm SSTs in the LC region (Feng et al., 2015). Such anomalous warming has a great impact on marine ecosystems off the western coast of Australia (Wernberg et al., 2013; Feng et al., 2013). The recent marine heat wave of 2015/16 off southeast Australia resulted in severe ecological and

economic impacts. It has caused mass bleaching of corals in the Great Barrier Reef (Hughes et al., 2017), shifts in marine species distribution (Last et al., 2011), outbreak of oyster disease (Oliver et al., 2017) and the presence of species that were not observed previously (Last et al., 2011; Oliver et al., 2017).

The annual mean of reanalysis and climatology products in the SIO differ considerably in magnitude (Yu et al., 2007, Fig. 1.7). This difference makes it difficult to understand the implications of the warming tendency of the Indian Ocean in the climate system. A major reason for this difference is the lack of enough observations of air-sea fluxes to validate the flux products (Josey et al., 2013). Surface heat fluxes play an important role in the ocean heat budget and transport (Yu et al., 2007). It is thus important to estimate the heat fluxes accurately for a better understanding of the climate system.

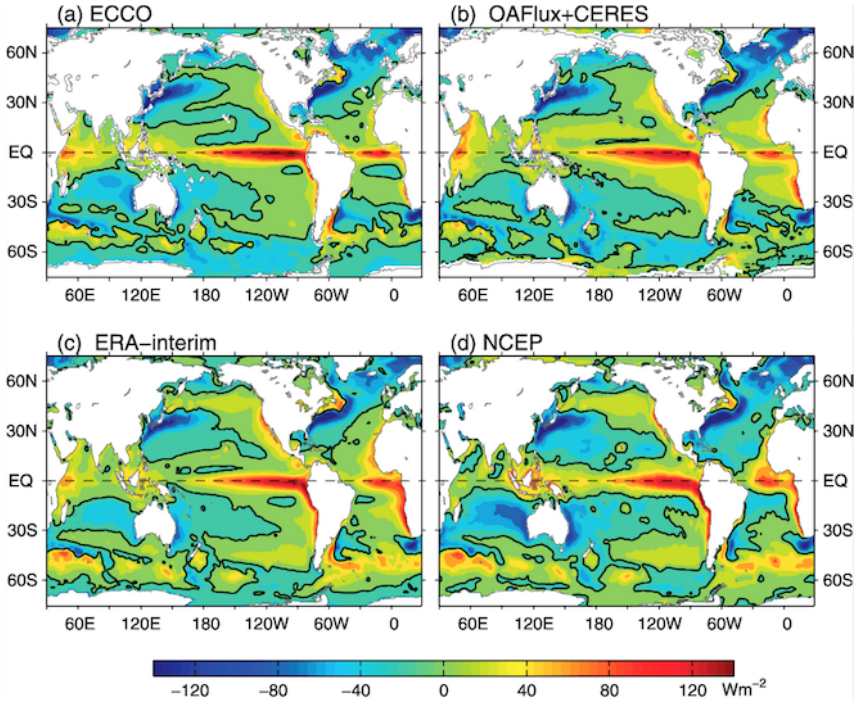

Figure 1.7: Comparison of mean net heat flux from different data products during hiatus period from 2000 – 2010 (Liang and Yu, 2016), when the observed globally-averaged surface temperature time series shows little increase or even a slightly negative trend. Positive values denote that the ocean gains heat.

1.3 Internal waves

Waves generated in the interior of the ocean and atmosphere caused by disturbances at the interface between different density layers are called Internal Waves (IW). IWs are ubiquitous in the ocean with a vertical length scale of 10 – 100 m and time scales from minutes to hours. Their vertical amplitudes are higher than the amplitude of the waves seen at the ocean surface (Fig.1.8) suggesting that the restoring forces within the ocean are smaller than those at the ocean surface. Unlike surface waves whose energy propagates only in the horizontal direction, the energy of IWs can propagate both horizontally

and vertically at once. They are operated on mainly by two restoring forces: 1) buoyancy due to ocean stratification and 2) the Coriolis force. As a result, IWs can occur in the ocean interior at all frequencies between the Coriolis frequency f and buoyancy frequency N (Garrett, 2001). At frequency N, waves propagate horizontally with pure vertical particle motions and at frequency f, particles move horizontally with vertical wave propagation (Garrett, 2001; Talley, 2011, Fig. 1.9).

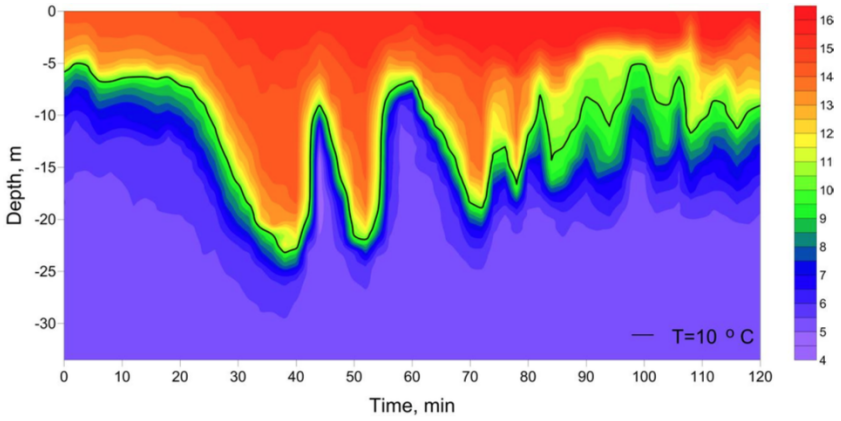

Figure 1.8: A train of IWs observed in temperature during a field experiment in the White Sea. Horizontal axis is time with depth in Y-axis (Kozlov et al., 2014).

The IWs with frequency close to f stand apart from the rest of the spectrum. These bands of IWs, called Near-Inertial waves (NIW), have almost circular particle motions (anti-clockwise in Southern Hemisphere) (Leaman and Sanford, 1975; Garrett, 2001; Talley, 2011). At higher frequencies, most of the energy (Wunsch and Ferrari, 2004) and vertical shear (Alford et al., 2017) of the IW spectrum is in the near-inertial band that is visible as a peak close to f (Ferrari and Wunsch, 2009; Garrett, 2001, Fig.1.10). Their propagation direction is linked to the source near the surface (Alford et al., 2016). The wind-generated NIWs are dominated by downward propagating energy with upward phase velocity (Leaman and Sanford, 1975). Fu (1981) suggested that the inertial waves observed at a particular region could be either locally generated (local wave field) or remotely generated as random IWs and propagated poleward (global wave field). NIWs can be generated either due to wind forcing (Dasaro, 1985) or as a result of the ocean's attempts to attain equilibrium particularly after the passage of a storm and at fronts and eddies (geostrophic adjustment) (Gill, 1984; Silverthorne and Toole, 2009; Alford et al., 2013; Nagai and Hibiya, 2015).

NIWs are different from the low frequency internal tides, generated by the barotropic tides flowing over bathymetry. The vertical component of the barotropic tide over a bottom slope can oscillate the isopycnals at the same tidal frequency as the horizontal component. These isopycnal oscillations result in the generation of waves at tidal frequency, the internal tides. They can transmit energy over long

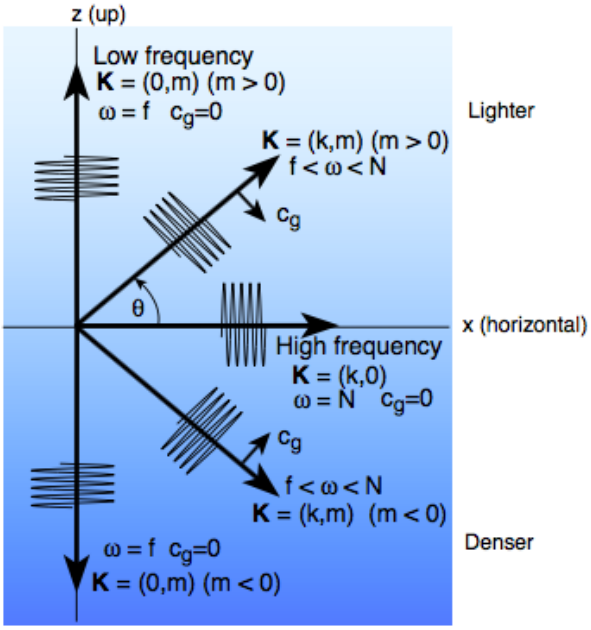

Figure 1.9: Schematic of properties of IW propagation in different directions in a XZ plane. The big arrows show the phase propagation through wave vector (k, m). The group velocity Cg (small arrows) is perpendicular to the wave vector (Talley, 2011).

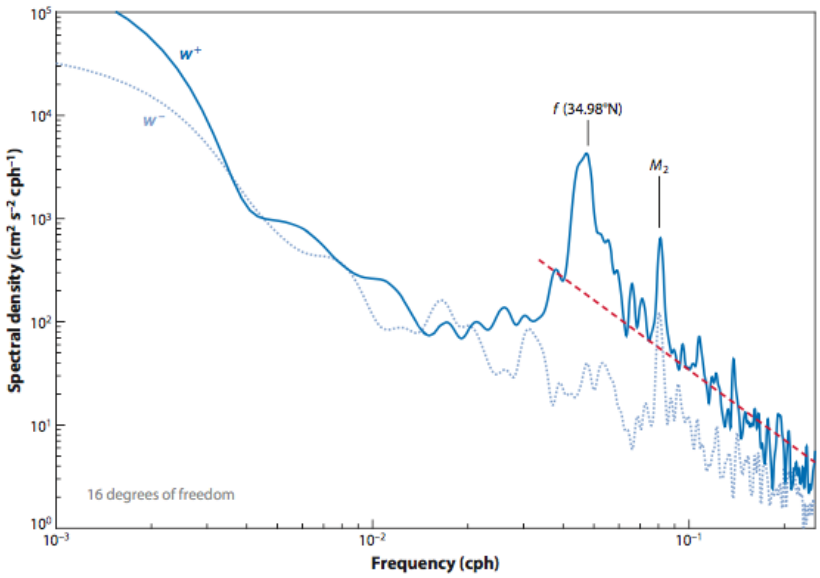

Figure 1.10: Rotary spectrum from the WHOI699 current meter data (152.042°E, 34.980°N). The clockwise component (ω^+, solid blue line) has more energy than the counter-clockwise (ω^-, light blue line) component. The peaks near f and tidal frequency M2 are visible (Alford et al., 2016).

distances from the generation sites (Rudnick et al., 2003) since IWs can transmit energy both in vertical and horizontal directions.

Another category of IWs is the non-linear internal waves, mostly associated with tides flowing over banks or straits (Talley, 2011). They are high frequency, high amplitude waves that occur both in the ocean and the atmosphere. They consist of a single elevation or depression and maintain their form

during propagation and interaction with other non-linear waves. There are different types of non-linear internal waves such as bores, undular bores, solitary waves, and wave trains (Zhang et al., 2015, and references therein).

An important but not well resolved category of internal waves is internal lee waves. They are generated as a result of geostrophic flow over rough topography. These waves play a crucial role in the Southern Ocean circulation where the mean flow interacts with rough bathymetry (Nikurashin and Ferrari, 2010), generating lee waves that drive enhanced mixing near the sea floor.

1.4 Turbulent mixing

Turbulent mixing plays an important role in large-scale oceanic processes such as water mass transformation, the global overturning circulation and stratification. It also contributes to distributing heat, salt, chemicals and organisms throughout the world oceans. However, since mixing is patchy and intermittent, it is difficult to describe mixing from the limited ship-based observations (Whalen et al., 2012). It is important to understand the small-scale mixing and how to parameterize it in numerical models that have grid scales larger than the mixing scales (Garrett, 2003).

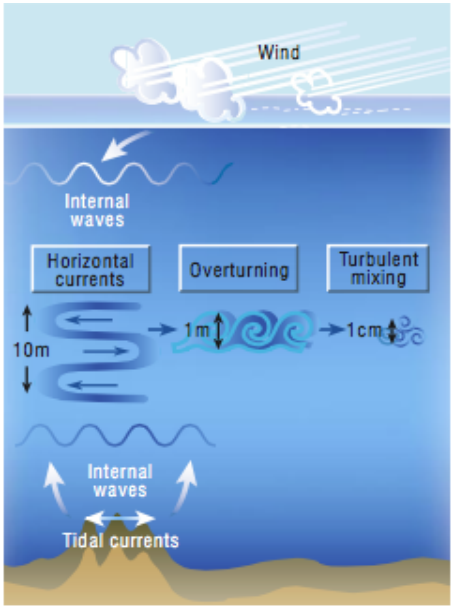

Figure 1.11: Generation of internal waves and the scales of different processes that lead to mixing (Garrett, 2003).

1.4.1 Sources of mixing

A major contribution of mixing in the ocean interior comes from breaking of internal waves (Gregg et al., 2003, Fig.1.11). Internal waves operate at a much smaller scale than mesoscale eddies (100 m wavelength as opposed to 100 km). When the waves break, the resulting turbulence transfers energy to molecular dissipation scales (Levy et al., 2012). Large vertical shear associated with internal waves in the near-inertial band play an important role in driving instabilities leading to irreversible mixing in the ocean interior (Ferrari and Wunsch, 2009). IW breaking occurring away from the topography almost balances the observed open ocean background mixing ($O(10^{-5})$ m^2 s^{-1}) but not the global average ($O(10^{-4})$ m^2 s^{-1}) to maintain the global overturning circulation (Wunsch and Ferrari, 2004). The upper ocean can be mixed readily by surface processes such as convection and wind forcing (Wunsch and Ferrari, 2004). Internal tides and internal lee waves introduced at greater depths are efficient at mixing the deep ocean (Wunsch and Ferrari, 2004). Internal lee waves are an important source of turbulent mixing and a significant energy sink for geostrophic flow in the deep ocean (Nikurashin and Ferrari, 2011).

The interaction between mesoscale eddies and internal waves is potentially crucial for mixing in the ocean (eg. Whalen et al., 2018). Understanding and quantifying this interaction is important in determining the ocean's energy budget (Clement et al., 2016). An important mechanism of this interaction is the trapping and dissipation of NIWs in the cores of warm core eddies (Jaimes and Shay, 2009; Kunze, 1995; Lee and Niiler, 1998). The NIWs trapped in a warm core eddy are not free to propagate out. In the case of a warm core eddy with a negative vorticity core, the NIWs travel from the surface vertically downward and will reach the base of the region of negative vorticity inside the eddy. As the wave approaches the base, its vertical wavelength and group velocity will shrink and its energy will get accumulated. This accumulated energy can be lost to the mean flow, or propagate out as waves, or result in turbulence, dissipation and mixing (Kunze, 1995). On the contrary, in a cold core eddy, the NIWs propagate freely away from the core and near-inertial energy will be present only in the surface layer (Lee and Niiler, 1998). Also, combining satellite altimetry and *in situ* current meter observations, Clement et al. (2016) found that the anticyclonic eddies impinging on the western boundary of the North Atlantic can generate internal waves that drain energy from the mesoscale eddy field. They also observe enhanced internal wave-driven dissipation rates in anticyclonic eddies corresponding to strong near-bottom velocities.

1.4.2 Estimation of mixing

Turbulent diffusion is the process of transporting mass or tracers such as temperature from one location to another by random fluctuations in the flow. For any property C, the net flux Q_c due to turbulent diffusion

can be written as

$$Q_c = -K_c \nabla C \tag{1.1}$$

where ∇C is the gradient of the property and K_c is called the turbulent diffusion coefficient or diffusivity.

The diffusivity or eddy diffusivity for mass across isopycnals (diapycnal diffusivity) K_ρ is a manifestation of turbulent mixing in the ocean. Following Osborn (1980), one can write the eddy diffusivity for density as

$$K_\rho = \Gamma \frac{\varepsilon}{N^2} \tag{1.2}$$

where N is the buoyancy frequency, a convenient measure of stratification, and Γ is the mixing efficiency which is often assumed to be constant (Γ = 0.2). N is generally calculated from vertical profiles of temperature and salinity. The dissipation rate ε is the rate at which turbulent kinetic energy is dissipated into heat by molecular viscosity. There are several methods by which we can estimate ε and thereby K_ρ.

Estimating turbulence requires measurements on the centimeter scale at which the turbulent kinetic energy is dissipated. Thus both direct and indirect methods have been introduced to measure the dissipation rate in the ocean, most of which are based on fine-scale or micro-scale observations. Direct measurements of diapycnal mixing can be obtained by tracking a man-made tracer released into the ocean and by measuring its vertical spread over time (Ledwell et al., 2011). Mixing can also be measured indirectly from perturbations in temperature, conductivity and shear by microstructure measurements (Gregg et al., 2003). However, these measurements require expensive instruments and an experienced team to deploy and recover them. This drawback has limited the microstructure measurements to a few locations in the world ocean, and very little information about mixing variations in time.

Dissipation rate is directly related to the energy and shear of the IW field through wave-wave interactions (Gregg, 1989; Henyey et al., 1986; Polzin et al., 1995). By combining the finescale measurements of velocity (shear) and density (strain) from the IW field with the theoretical models of energy transfer from IWs of large scales to IWs of smaller scales, we can measure the turbulent dissipation rate (Gregg, 1989; Henyey et al., 1986). At smaller scales, the rate of downscale energy transfer into those scales and the energy dissipated from them are similar (Clement et al., 2016). Since it is comparatively easy to get vertical density and velocity measurements, finescale parameterization is widely used to infer the dissipation rate. The main concept behind finescale parameterization is that turbulence at small scales is the result of a downscale energy transfer due to nonlinear wave-wave interactions (Polzin et al., 2014). This method has two main assumptions: 1) Most of the mixing is caused by breaking of IWs 2) The energy cascade due to non-linear interactions of IWs result in energy dissipation (Waterman et al., 2013; Whalen et al., 2015). However, this method does not hold well in regions where turbulence is caused

by processes other than IWs such as at boundaries and near topography where the internal wave field is strongly non-linear (Klymak and Moum, 2007).

1.5 Thesis objectives

The southeast Indian Ocean is a region where the large-scale ocean circulation interacts and coexists with mesoscale eddies and internal waves. The annual mean wind stress of this region is dominated by southeasterly trade winds. Previous studies show that mesoscale eddies can efficiently transfer energy from wind generated NIWs to the ocean interior (e.g. Zhai et al., 2005; Elipot et al., 2010) and result in elevated turbulent mixing (e.g. Whalen et al., 2018). Partly because of the lack of enough observations, the NIW field in this region is not well studied.

By combining direct and indirect measurements of turbulence, Waterhouse et al. (2014) calculated a global average diapycnal diffusivity of $O(10^{-5}\ \mathrm{m^2 s^{-1}})$ above 1000 m depth, and $O(10^{-4}\ \mathrm{m^2 s^{-1}})$ below 1000 m depth with higher values in the abyssal ocean. Their results suggest that the eastern part of IO has comparatively lower diffusivity ($O(10^{-6}\ \mathrm{m^2 s^{-1}})$). However, Whalen et al. (2012) found that the areas of enhanced diffusivities are associated with increased EKE. They reported an average diapycnal diffusivity of the $O(10^{-5}\ \mathrm{m^2 s^{-1}})$ over 250 – 500 m of the upper eastern south Indian Ocean, one order higher than that of Waterhouse et al. (2014). Whalen et al. (2012) used only the strain information available from density profiles of Argo floats which can be compromised by the use of a constant shear-strain ratio while estimating the dissipation rate. The estimates of Waterhouse et al. (2014) used shear-strain parameterization of sparse observations with no microstructure measurements in the south Indian Ocean. We thus need more observations of both shear and strain with high temporal and spatial resolution to resolve the internal wave field and estimate mixing, and also to provide details of the eddy field and background flows in the southeast Indian Ocean.

The south Indian Ocean is a region of high evaporation and air-sea heat loss resulting in high sea surface salinity. However, the disagreement of reanalysis products in this region makes it difficult to understand the role of air-sea fluxes in the watermass variability. Prior to this study there were no direct measurements of air-sea fluxes in this climatically important region. This thesis provides new work that contributes to the validation of surface flux products and provides a better understanding of the air-sea interactions in this region.

In a broad sense, the present study examines the different scales of motion and the interactions between them in the eastern SIO using observational datasets, reanalysis products and satellite altimetry. The primary dataset used for this study is obtained from EM-APEX floats which sampled different scales

from small-scale internal waves and inertial oscillations to large-scale mesoscale eddies and the eastward flows. We also used time series of air-sea flux data collected from the only flux mooring in the entire subtropical Indian Ocean to investigate the role of different processes including the large-scale circulation on the mixed layer heat budget in this climatically important region. Specific objectives include:

- Characterize the spatial and temporal variability of near-inertial waves and estimate their properties in the southeast Indian Ocean.
- Quantify the vertical mixing associated with the breaking of internal waves and characterize its temporal and spatial variability.
- Investigate the possible sources of near-inertial waves and vertical mixing observed in this region.
- Analyse the mixed layer heat budget in this region and determine the relative roles of atmospheric forcing and ocean processes in the observed velocity and watermass changes.

This thesis contains five chapters. Each research chapter from Chapter 2 – 4 is a self-contained research paper. Chapters 2 and 3 are prepared for submission to the Journal of Physical Oceanography. Chapter 4 has been published online in Journal of Geophysical Research: Oceans.

The structure of the thesis is as follows:

Chapter 2 identifies the near-inertial internal waves in the southeast Indian Ocean using EM-APEX float data. Using a complex demodulation, the near-inertial waves are extracted from the data. Strong NIW beams generated at the surface due to wind systems are seen to propagate below the mixed layer and often well below. This has implications on the overturning circulation where the deep reaching NIWs can provide energy for mixing. The near-inertial shear variance in anticyclonic eddies is higher than that in cyclonic eddies suggesting that the waves are trapped inside the core of anticyclones due to their relative vorticity. This study characterises the spatial and temporal structure of the NIWs in the southeast Indian Ocean using high resolution EM-APEX data.

Chapter 3 investigates the spatial and temporal variability of turbulent mixing in the southeast Indian Ocean. The diapycnal mixing is estimated by applying a shear-strain parameterization on the hydrographic and velocity data collected from the EM-APEX floats. The presence of internal waves can be identified as coherent features in the velocity profiles. In anticyclonic eddies, high diffusivity is observed near the surface in agreement with the theory of inertial wave trapping. Elevated diffusivity in cyclonic eddies is associated with internal waves captured by the mesoscale strain field of the eddy. The elevated diffusivity in cyclonic eddies occurs well below the mixed layer and extends across the depth

ranges occupied by Subantarctic Mode Water and Antarctic Intermediate Water. This study provides direct observations of enhanced mixing that contributes to the modification of watermasses that drives the meridional overturning circulation. Anticyclonic eddies are found to strongly impact the near surface mixing, whereas the cyclonic eddies are clearly important for deep ocean mixing and watermass transformation. The effectiveness of the shear-strain parameterization has been evaluated using direct measurements of turbulent mixing in the upper 300 m from a microstructure profiler.

Chapter 4 analyses the mixed layer heat budget in the subtropical Indian Ocean using a 2-year time series collected from the only off-equatorial flux mooring in the south Indian Ocean. The study is complemented by a 12-year analysis of the heat budget using reanalysis, satellite and Argo data in a small region around the mooring. It is shown that on seasonal timescales, the mixed layer heat storage in the eastern south Indian Ocean is mainly balanced by a combination of surface fluxes and turbulent entrainment, with a contribution from horizontal advection at times. The horizontal advection is dominated by mesoscale eddies and annual and semi-annual Rossby waves emanating from the eastern boundary.

Chapter 5 provides a summary and discussion of the whole thesis.

Chapter 2

Characteristics of wind-generated near-inertial waves in the southeast Indian Ocean

Abstract

This study presents the characteristics and spatio-temporal structure of near-inertial waves and their interaction with Leeuwin Current eddies in the eastern South Indian Ocean as observed by Electromagnetic Autonomous Profiling Explorer (EM-APEX) floats. The floats sampled the upper ocean during July – October 2013 with a frequency of 8 profiles per day up to 1200 dbar. Near-inertial waves (NIWs) are found to be dominant in the data from the frequency spectra. By applying a complex demodulation technique, the amplitudes of the NIWs are estimated from the velocity profiles. The NIW energy propagated from the base of the mixed layer downward into the ocean interior, following beam characteristics of linear wave theory. We visually identified a total of 15 near-inertial internal waves from the float data. The identified near-inertial beams have a mean vertical wavelength of 89 $\pm$ 63 m, a mean horizontal wavelength of 69 $\pm$ 85 km, a mean horizontal group velocity of 3 $\pm$ 2 cm s^{-1} and a mean vertical group velocity of 9 $\pm$ 7 m day^{-1}. The mean vertical energy flux of the downward propagating beams is more than 40% of the wind work, with the potential to reach the deep ocean. A strong near-inertial beam with a kinetic energy of 20 – 30 J m^{-3} found propagating below 700 m suggests that the NIWs can contribute to deep ocean mixing. A blue shift of 10 – 15% in the energy spectrum of the NIWs is observed in the upper 1200 m which becomes more pronounced towards the equator. The impacts of mesoscale eddies on the characteristics and propagation of the observed NIWs are also investigated. The elevated near-inertial shear variance in anticyclonic eddies suggests trapping of NIWs. Cyclonic eddies in contrast, were associated with weak near-inertial shear variance near the surface.

2.1 Introduction

a) *Internal waves*

Breaking of internal waves cause most of the mixing in the stratified ocean which influences the generation and evolution of mesoscale eddies and large-scale circulation. Internal waves occur in all frequencies between the inertial frequency (f) and buoyancy frequency (N). The main sources of internal waves in the ocean are wind (Dasaro, 1985), barotropic tides over rough topography (Egbert and Ray, 2000; Rudnick et al., 2003), and interaction of geostrophic flow with bottom topography (Nikurashin and Ferrari, 2010). The near-inertial wave (NIW) band, mostly generated from wind, with frequencies close to f are dominant and energetic in the internal wave spectra (Leaman and Sanford, 1975; Garrett, 2001). Recent studies show more and more evidence of apparent interactions between the large-scale circulation and other oceanic phenomena of different scales such as mesoscale eddies, fronts and internal waves (e.g. Alford et al., 2013; Whalen et al., 2018).

Using Levitus climatology, Munk and Wunsch (1998) estimated that a total of 2.1 TW of energy is required to maintain the global overturning circulation and abyssal stratification in the ocean. They found that 1.2 TW of energy is the contribution from wind to the energy budget of which 0.2 TW is from wind-generated internal waves which radiate into the abyss from the surface. Various studies using mixed layer slab models have tried to quantify the contribution of NIWs to the global energy balance (Alford and Gregg, 2001; Watanabe and Hibiya, 2002; Alford, 2003; Jiang et al., 2005; Chaigneau et al., 2008) and find a range between 0.29 – 0.7 TW of energy input into the global mixed layer. The slab model does not take into account the effect of mesoscale activity on the inertial currents (Chaigneau et al., 2008). Recent observational and model studies (Lee and Niiler, 1998; Kunze, 1985; Zhai et al., 2005; Elipot et al., 2010) have shown that mesoscale eddies play an important role in transferring the near-inertial energy generated at the surface into the ocean interior.

b) *Regional ocean circulation*

The near surface circulation of the eastern south Indian Ocean (SIO) is dominated by broad, geostrophic zonal currents in the upper 200 – 300 m that flow eastward against the prevailing southeasterly trade winds (Fig. 2.1, Schott et al. 2009). The eastward flows originate near the southern tip of Madagascar and concentrate into several jets as they flow towards Australia (Siedler et al., 2006; Palastanga et al., 2007; Menezes et al., 2014). These jets have been identified as branches of the South Indian Countercurrent (SICC) between 20 – 30°S (Menezes et al., 2014) and the Eastern Gyral Current (EGC) between 14 – 17°S (Menezes et al., 2013). The SICC consists of three branches namely the northern, central and southern SICC. Among them, the southern branch is the strongest and the northern branch is the weakest.

On approaching the coast these jets tilt toward the south and merge with the poleward flowing Leeuwin Current (LC). The zonal flows exist due to the presence of a strong meridional density gradient between the warm fresh waters of the South Equatorial Current (SEC) and the cooler, salty subtropical waters to the south (Godfrey and Ridgway, 1985; Godfrey, 1996; Schott and McCreary, 2001). They are strong enough to overwhelm the offshore Ekman transport driven by southeasterly trade winds, and are the major source of water into the LC (Furue et al., 2017).

Below 300 m, the LC is accompanied by the Leeuwin Undercurrent (LUC) which flows equatorward along the continental slope, beneath and just offshore of the LC (Thompson, 1987; Furue et al., 2017). The LUC leaves the Australian coast near 22°S (Furue et al., 2017), bending northwestward and westward to flow beneath the surface eastward flow (Domingues et al., 2007; Godfrey and Ridgway, 1985). The fate of the LUC outflow is not clear. However, it likely merges with the broad westward flows of the anticyclonic subtropical gyre away from the coast (Domingues et al., 2007; Furue et al., 2017).

Superimposed on the seasonal and longer term variability is a rich mesoscale eddy field that is generated at the coast and propagates offshore. The interaction between the LC and LUC results in the formation of cyclonic-anticyclonic eddy pairs (Rennie et al., 2007). The cyclonic eddies generated from the LUC are dominant below the surface whereas the anticyclonic eddies formed from the LC are surface intensified. The LC appears to become unstable near 28°S leading to some of the LC transport being carried offshore by eddies near and south of this latitude (Feng et al., 2005, 2007). The rich mesoscale eddy field offshore of the LC is unusually strong relative to other eastern boundary regions, and contributes to large ocean to atmosphere fluxes of heat (Domingues et al., 2006). Eddy formation in the LC has a clear annual cycle with more eddies formed when the LC transport is strong (Jia et al., 2011b). The LC transport varies annually with a maximum during June – July (Feng et al., 2003). The seasonal variation may be due to the current strengthening as the monsoonal winds ease (Godfrey and Ridgway, 1985; Smith et al., 1991) or seasonal variations in sea level pressure to the north (Ridgway and Godfrey, 2015).

The near-surface eastward flows and Leeuwin Current System (LCS) have received considerable attention in recent times. With the help of observational data and climatological atlases, (Menezes et al., 2013, 2014) give a clear description of the horizontal structure and dominant features of these eastward flows. Theoretical and modelling studies (Furue et al., 2013; Benthuysen et al., 2014) have also discussed the drivers of these flows and how they feed into the LCS. Furue et al. (2017) describe a large-scale downwelling of the near-surface onshore flows at the coast. They find that approximately 4 Sv downwells from LC depths into the LUC in the depth range 200 to 900 m. The downwelling is balanced by an offshore return flow. The watermass transformations required to effect this overturning are not clear,

and the spatial structure of the subsurface westward flows away from the coast has been relatively little studied.

Partly because of the lack of observations, the NIW field in the eastern SIO is not well known. The mixing caused by these waves can impact the large-scale circulation in this region which is found to be sensitive to vertical mixing from regional model studies (Furue et al., 2013; Benthuysen et al., 2014). This paper is the first in a series investigating different scales of variability in the eastern subtropical Indian Ocean and their interactions using observations from an array of Electromagnetic Autonomous Profiling Explorer (EM-APEX) floats with which we can examine both near-inertial processes, and mesoscale and large-scale processes. The EM-APEX in this experiment collected 8 profiles of velocity, temperature and salinity each inertial period ($\approx$ 27 hours) up to 1200 m depth at 30°S. Thus they offer a unique opportunity to examine the internal wave field using both a time series analysis approach as used for mooring data (e.g. Alford et al., 2012) and drifter data (Chaigneau et al., 2008), and also through examination of the vertical propagation of internal waves that is possible with high vertical resolution data (e.g. Meyer et al., 2016).

The paper is organised as follows. In section 2, the characteristics of EM-APEX floats and other auxiliary data are described. Different data analysis techniques applied to the data are discussed in Section 3. Section 4 describes the regional oceanographic conditions during the profiling of the floats. The characteristics of the observed near-inertial beams are analysed in Section 5. Section 6 investigates the factors that influence the generation and propagation of the NIW beams in the upper and deep ocean. The interaction between NIWs and mesoscale eddies are analysed in Section 7 with a discussion and conclusion of the study in Section 8.

2.2 Data

2.2.1 EM-APEX floats

Deployment

The primary data used for this study (temperature, salinity, pressure and horizontal velocity) was recorded by five EM-APEX floats deployed in the eastern SIO between 25°S and 32°S along 105°E, in July 2013 (Fig. 2.1). The deployment was part of Voyage SS2013 V04 of the Australian Marine National Facility *RV Southern Surveyor*. The selected latitude band covers the strongest and deepest part of the eastward flows, the southern branch of the SICC (Menezes et al., 2014). Eddy kinetic energy is also high in this band surrounding 25°S (Jia et al., 2011b).

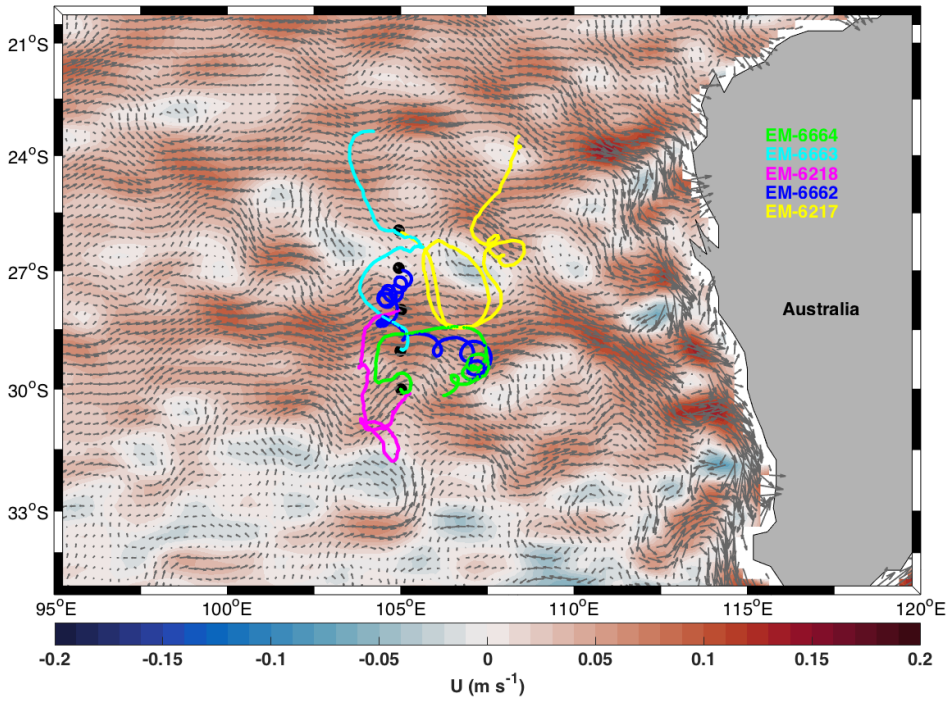

Figure 2.1: Mean surface geostrophic velocity from satellite altimetry during 2005 – 2015 (dark grey arrows). Shading represents the magnitude of the mean zonal current and different coloured lines show the track of each float. The black dot shows the location where each float was deployed along 105°E.

The floats were deployed immediately following a full-depth CTD/lowered ADCP cast, as the ship moved away from the station. The five floats were spaced at intervals of 1.5° latitude along 105°E. In Fig. 2.1 the rich mesoscale environment is revealed in the float tracks, overlaid on a long-term surface geostrophic velocity field that highlights the background eastward flows. The shipboard CTD data were used as high-quality reference profiles to test the calibration of the EM-APEX CTD and velocity in the first few profiles. The data processing report for the shipboard hydrographic data is available at `https://www.cmar.csiro.au/data/trawler`.

EM-APEX background

The EM-APEX float is a combination of absolute velocity profiler (Sanford et al., 1978) and Argo profiler (Roemmich et al., 2004). In addition to the standard Argo components for measuring temperature, salinity and pressure, the EM-APEX includes a compass, accelerometer, five electrodes and external fins to rotate the float as it moves vertically. The electrodes measure the electrical potential difference across the float that is generated by the movement of sea water through the earth's magnetic field. The theory of motional induction then allows the depth varying ocean velocity relative to a depth-independent reference velocity to be calculated (Sanford et al., 1978). The reference velocity is found by estimating the

displacement caused by the measured relative velocities along a path from the surface to the bottom of a down profile and back to the surface. The difference between this integrated displacement and that measured from GPS surface positions is then attributed to the reference velocity (see Phillips and Bindoff, 2014).

Mission

The profiling mission of the floats is a compromise between obtaining the largest possible depth range with a profiling frequency that resolves the inertial cycle, requiring pairs of down-profiles separated by half an inertial period, and similarly for up-profile pairs. The inertial period at 27°S is 26.4 hours. This gave 8 profiles (4 down-up pairs) to 1200 m depth in each inertial period with an average fall/rise rate of 11 cm s^{-1}, allowing the near-inertial and sub-inertial frequencies in the data to be separated accurately. The velocity profiles clearly show the presence of inertial oscillations through mirror imaging of two velocity profiles separated by half an inertial period throughout the water column (Fig. 2.2). Although the five floats were deployed across a 7° latitude range, we chose to set identical missions for each float, anticipating that they would migrate substantially during their lifetime.

Data return

The five EM-APEX returned a total of 3726 profiles of temperature, salinity and velocity. Table 2.1 provides information about the spatial and temporal coverage of each float. EM-6663 covered the greatest meridional distance experiencing an inertial range of 0.8 – 0.97 cpd whereas EM-6217 had the greatest zonal coverage. After the deployment, two of the floats, EM-6217 and EM-6218, exhibited spikes in the velocity data known to be symptomatic of a high-pressure leak in the float hull (John Dunlap, pers. comm.) The maximum pressure was reduced until the spiking disappeared. These two floats continued to profile successfully to 300 m depth for the same period as the three deeper floats, with the added advantage of completing twice the number of profiles per inertial period. The suspected reason for this fault is deterioration in the agar gel protecting the electrodes, as there was about a 12 month period between production and deployment of these two floats. EM-6217 returned 1102 profiles and EM-6218 returned 1058.

Towards the end of the deployment voyage, the profiling mission for the deeper floats was changed to add a drift at 1000 m depth for about 18 hours. The drift was added to extend the life of the float but still allow a rapid burst of profiling over an inertial period between drifts. During the drift the floats measured temperature, salinity and pressure. Velocity measurements are only possible when a float is moving vertically and rotating around its vertical axis.

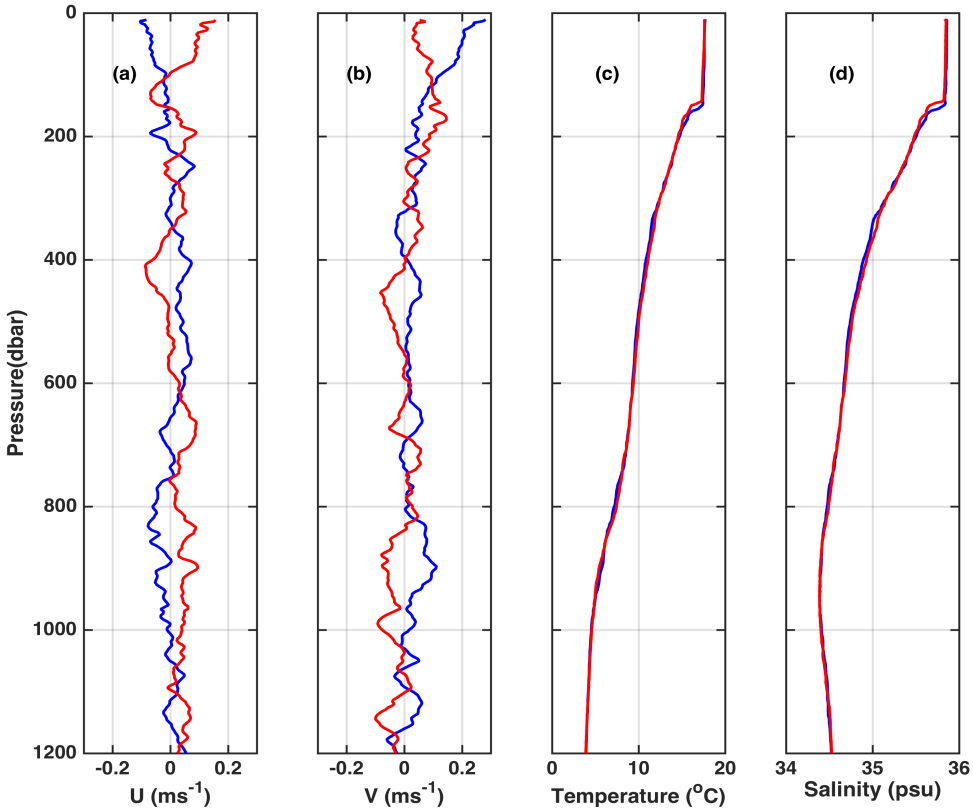

Figure 2.2: Half inertial pair profiles of (a) zonal velocity, (b) meridional velocity, (c) temperature, and (d) salinity from EM-6664. Profile 107 (blue) and profile 111 (red) are separated by 12 hours where the inertial period at the profile locations is one day (29.96°S) .

QC and calibration

Occasionally the GPS position of the profile was wrong considering the position of the float at earlier and later profiles. These wrong positions were removed and the missing locations were linearly interpolated from the profile positions before and after the one in question.

The pressure sensor on the floats may develop a pressure drift with time. The surface pressure for a given profile was subtracted from all pressure values in that profile, effectively resetting the surface pressure to zero. The first pressure in each float record was higher. These values were replaced by the offset value of the adjacent profile.

The EM-APEX temperature, salinity and pressure measurements are obtained from a Sea Bird Electronics SBE-41 CTD, mounted above the electrodes on the upper end cap. Vertical sample spacing was 2 – 3 m. The temperature and salinity profiles were compared with the CSIRO Atlas of Regional Seas 2009 (CARS2009, `www.cmar.csiro.au/cars`) climatology to identify erroneous data and spikes. The climatology was interpolated at each profile location and plotted along with the float measurements and

Float	6664	6663	6218	6662	6217
Deployment date	10 Jul 2013	11 Jul 2013	12 Jul 2013	12 Jul 2013	13 Jul 2013
Date of last profile	25 Oct 2013	23 Oct 2013	02 Oct 2013	12 Oct 2013	05 Oct 2013
Latitude range	28.4 – 30.1°S	23.3 – 29.0°S	28.0 – 31.7°S	26.9 – 29.7°S	23.4 – 28.4°S
Longitude range	104.2 – 107.5°E	103.5 – 105.6°E	103.7 – 105.2°E	104.3 – 107.6°E	104.9 – 108.5°E
Depth (dbar)	1200	1200	300	1200	300
No. of profiles	520	518	1058	528	1102
f range (cpd)	0.95 – 1.0	0.80 – 0.97	0.94 – 1.0	0.90 – 0.99	0.8 – 0.95

Table 2.1: Deployment information and the inertial band covered by each float based on the latitudinal extent of their tracks.

each profile was inspected visually. Occasional spikes were detected and removed. Much of the salinity data from EM-6217 was dominated by extensive spiking and was not used for this study. The cause of the failure may have been related to the high pressure leak described earlier. For all other floats, temperature and salinity measurements are in good agreement with the climatology below 200 m depth where the seasonal and diurnal variability is less. We also checked for drift in the conductivity sensor. No drift was evident in the data based on examination of salinity on potential temperature surfaces at the deepest common level of each float.

The vertical spacing of velocity measurements is approximately 3 – 4 m. For the calibration of relative velocity measured by the floats and estimation of absolute velocity, we followed the procedure in Phillips and Bindoff (2014). The steps involved are:

- calibrate the angle between the electrode axes and the compass orientation.
- Remove all the velocity spikes using a depth dependent cut-off based on a statistical analysis of the RMS error velocity. For velocities above 100 m, we excluded values greater than 2 cm s^{-1}.
- Estimate the absolute velocity from the float-measured relative velocities by adding a depth independent offset, which is equivalent to the depth-averaged absolute velocity from the sea surface to the sea floor (Sanford, 1971). The offset is calculated as the difference between the displacement due to the measured relative velocities along a path from the surface to the bottom of a down profile and back to the surface, and the actual displacement of the float measured by GPS.

We then interpolated the temperature, salinity and velocity measurements onto a uniform pressure grid of 3 dbar before the analysis.

2.2.2 Sea level anomaly, geostrophic velocity, winds and tides

Daily sea level anomaly (SLA) and absolute surface geostrophic velocities are distributed by Archiving, Validation, and Interpretation of Satellite Oceanographic data (AVISO) on a $0.25^\circ \times 0.25^\circ$ spatial grid. The daily SLA data is computed with respect to a 20-year mean reference period (1993 – 2012). The data were obtained from `https://cds.climate.copernicus.eu`. The float tracks are analysed using the SLA maps to identify float profiles associated with mesoscale eddies. SLA is interpolated to the position and time of each float profile to construct along-trajectory records of SLA. Warm core (cold core) eddies are associated with positive (negative) SLA.

Hourly wind stress data is obtained from the National Center for Environmental Prediction (NCEP) Climate Forecast System Version 2. It is a fully coupled model in which the interaction between atmosphere, ocean, land and sea ice is incorporated. The data has a spatial resolution of $0.5^\circ \times 0.5^\circ$ (Kanamitsu et al., 2002).

Tides contribute to mixing in the ocean especially in regions of significant bathymetric features (Egbert and Ray, 2000). A widely used source of tidal data is the TOPEX/Poseidon 7.2 (TPXO7.2) global tidal model that uses the Laplace tidal equations and along track altimeter data from TOPEX/Poseidon satellites to estimate the depth averaged barotropic currents. Here we use TPXO7.2 to estimate the tidal constituents along the EM-APEX float tracks during their profiling time. Between the eight primary (M_2, S_2, N_2, K_2, K_1, O_1, P_1, Q_1), two long period (Mf, Mm) and three non-linear (M_4, MS_4, MN_4) harmonic tidal constituents, we concentrate on the primary components. Since the floats were near the turning latitudes for K_1 (30.001°S) and O_1 (27.614°S) tidal components, the energy at the inertial frequency could also include that of tides (Poulain and Centurioni, 2015).

2.3 Methods

2.3.1 Rotary spectra

Rotary spectra reveal the characteristics of variability at different time scales and decomposes the velocity vector into counterclockwise (CCW) and clockwise (CW) rotating circular components (Elipot and Lumpkin, 2008). We treated the velocity data from each float as a time series and examined the rotary spectrum of velocity on depth surfaces. We first linearly interpolated the time series onto a 30-minute

grid. Then we used a multi-taper spectral analysis with 8 tapers from the JLAB package (Lilly, 2017) to estimate a single rotary spectrum from the time series for each float. Since the diurnal tidal frequency can coincide with the inertial frequency, we removed the tidal contribution by subtracting the depth averaged barotropic tidal velocity from the float-measured absolute velocity corresponding to each location and time of the float, following Elipot et al. (2010). The tidal velocity arising from the eight primary tidal constituents estimated along the float track using the TPXO 7.2 tidal inversion model is quite small (0.01 – 0.02 m s^{-1}) compared to the amplitude of the float-measured velocities (0.33 – 1.4 m s^{-1}).

2.3.2 Complex demodulation

Complex demodulation is the process of extracting a particular frequency component from a velocity or scalar time series to determine the temporal variation at that frequency. A general approach to complex demodulation is to use the least-squares method to fit the desired parameters to sequential segments of the time series data. An advantage of this approach is that the data need not be regular in time. The method separates the velocity components for a particular frequency into CCW and CW rotating circular components (Elipot and Lumpkin, 2008; Gonella, 1972). Depending on the hemisphere, only one of the above rotary components (CW component in the northern hemisphere and CCW component in the southern hemisphere) dominates the inertial currents (Elipot and Lumpkin, 2008; Leaman and Sanford, 1975; Martini et al., 2014; Thomson and Emery, 2014). Thus, we can then analyse a single rotary component rather than two scalar components.

Here we estimate the amplitudes and phases of the internal waves at near-inertial frequency using complex demodulation of the observed velocity components. We first Wentzel-Kramers-Brillouin (WKB) scaled the velocities, following Leaman and Sanford (1975) as $u_{wkb} = u.\sqrt{N(z)/N_0}$. A WKB stretched depth is also calculated as $z_{wkb} = \int_0^z N(z)/N_0 dz$ to account for the wavenumber changes. Here, N_0 is a reference buoyancy frequency of 3 cph. We then applied the complex demodulation on the velocity time series in each depth level at the centre time (t_k) in a window of ± 1 inertial periods ($\approx$ 48 hours, 16 profiles). The amplitude and phase of the inertial component in the velocity data are extracted using back rotation of the velocity vector with respect to a reference time t_0 (July 1, 2013) before the floats were deployed (Dasaro et al., 1995). The measured velocity component can be expressed as

$$U_c = A_c^+ e^{i(f_c(t_j-t_0)+\varepsilon_c^+)} + A_c^- e^{-i(f_c(t_j-t_0)+\varepsilon_c^-)} + \overline{U}_c + \overline{V}_c + a_{uc}(t_j - t_c) + a_{vc}(t_j - t_c) \tag{2.1}$$

where U is the complex velocity $u + iv$ and u (v) is the eastward (northward) velocity component at each

depth level c. (A^+, A^-) are the amplitudes and $(\varepsilon^+, \varepsilon^-)$ are the phases of the CCW and CW rotating inertial components, respectively. The time index in each window, j, varies from 1 to n, where n is the number of data points in the chosen window. The demodulation method is based on the assumption of a 'quasi-steady' state so that the wave properties do not change much over the period of the window (Federiuk and Allen, 1996). The floats are moving in space so we take f_c to be the average of local inertial frequencies in each window. $\overline{U}$, $\overline{V}$ are the mean eastward and northward velocities in each window. The last two terms allow for a low-frequency trend in the background current in each window, and a_u and a_v are the slopes of the trend in the eastward and northward direction. The wave frequency at the location of each profile using this method can be obtained as (Federiuk and Allen, 1996)

$$\omega_c = f_c - \frac{\partial \varepsilon_c^{\pm}}{\partial t} \tag{2.2}$$

and the vertical wave number as

$$m_c = \frac{\partial \varepsilon_c^{\pm}}{\partial z} \tag{2.3}$$

The dispersion relation for the internal wave can be written as

$$\frac{k_h^2}{m^2} = \frac{f^2 - \omega_0^2}{\omega_0^2 - N^2} \tag{2.4}$$

where ω_0 is the intrinsic frequency and k_h is the horizontal wave number ($k_h = \sqrt{k^2 + l^2}$). Here (k, l, m) is the wave vector. In the absence of a mean flow, intrinsic frequency ω_0 equals the wave frequency ω.

From the dispersion relation, k_h can be obtained as

$$k_h = \pm m \sqrt{\frac{f^2 - \omega_0^2}{\omega_0^2 - N^2}} \tag{2.5}$$

The group velocity C_g is given by the gradient of the frequency with respect to the wave number. By implementing the hydrostatic approximation, assuming $\omega_0^2 \ll N^2$, the magnitude of the horizontal group velocity can be obtained as

$$C_{gh} = \sqrt{\left(\frac{kN^2}{\omega_0 m^2}\right)^2 + \left(\frac{lN^2}{\omega_0 m^2}\right)^2} \tag{2.6}$$

where $k = k_h \sin\varepsilon$ and $l = -k_h \cos\varepsilon$ are the horizontal wave vector components.

2.3.3 Relative vorticity, Potential vorticity and Mixed layer depth

The vertical component of the relative vorticity (ζ) can be written as

$$\zeta = \frac{\partial v}{\partial x} - \frac{\partial u}{\partial y} \tag{2.7}$$

where u (v) is the daily surface geostrophic eastward (northward) velocity component obtained from satellite altimetry. The ζ values are then subsampled at the time and location of each float profile to construct the along-trajectory variations. Relative vorticity helps us to identify the mesoscale eddies in the float tracks where southern hemisphere warm (cold) core eddies have positive (negative) ζ values within their perimeter.

The potential vorticity (PV) can be written as $Q = \frac{(f+\zeta)}{\rho}\frac{\partial \rho}{\partial z}$, where f is the planetary vorticity and ζ is the relative vorticity. In regions of weak currents, ζ is negligible and thus the PV can be written as $Q = -(f/\rho)(\partial\rho/\partial z)$. Following Talley (2011) the PV used in this study is $Q = fN^2/g$, where g is the acceleration due to gravity (9.8 m s^{-2}). The buoyancy frequency N is estimated from the float data using $N^2 = -\frac{g}{\rho_0}\frac{\partial \rho_\theta}{\partial z}$, where ρ_θ is the potential density relative to the sea surface calculated from the EM-APEX salinity, temperature and pressure profiles. The vertical gradient is calculated using a pressure window of 9 m.

The mixed layer depth (MLD) is defined as the depth at which the potential density changes by 0.03 kg m^{-3} relative to that at 15 m depth (de Boyer Montegut et al., 2004) for all floats except EM-6217. Since the salinity data from EM-6217 was erroneous, we estimated the MLD using a temperature criterion of 0.2°C threshold (de Boyer Montegut et al., 2004).

2.4 Observed watermass and velocity structure

The float trajectories were strongly influenced by the eddy field with little evidence of advection by the eastward flows (Fig. 2.1). All floats experienced a large change in latitude, and steering by eddies. Several floats exhibited tight loops in their trajectories, suggestive of being caught in mesoscale eddies. In Fig. 2.3, weekly maps of SLA provide an indication of the position of eddies at the time the profiles were collected. There is a clear correspondence between the direction of movement of the floats and the surface geostrophic velocity field inferred from the sea level maps.

The floats provide a detailed picture of the upper ocean watermass and velocity structure along their trajectories. Fig. 2.4 presents the three deep floats (EM-6662, EM-6663 and EM-6664) with the horizontal

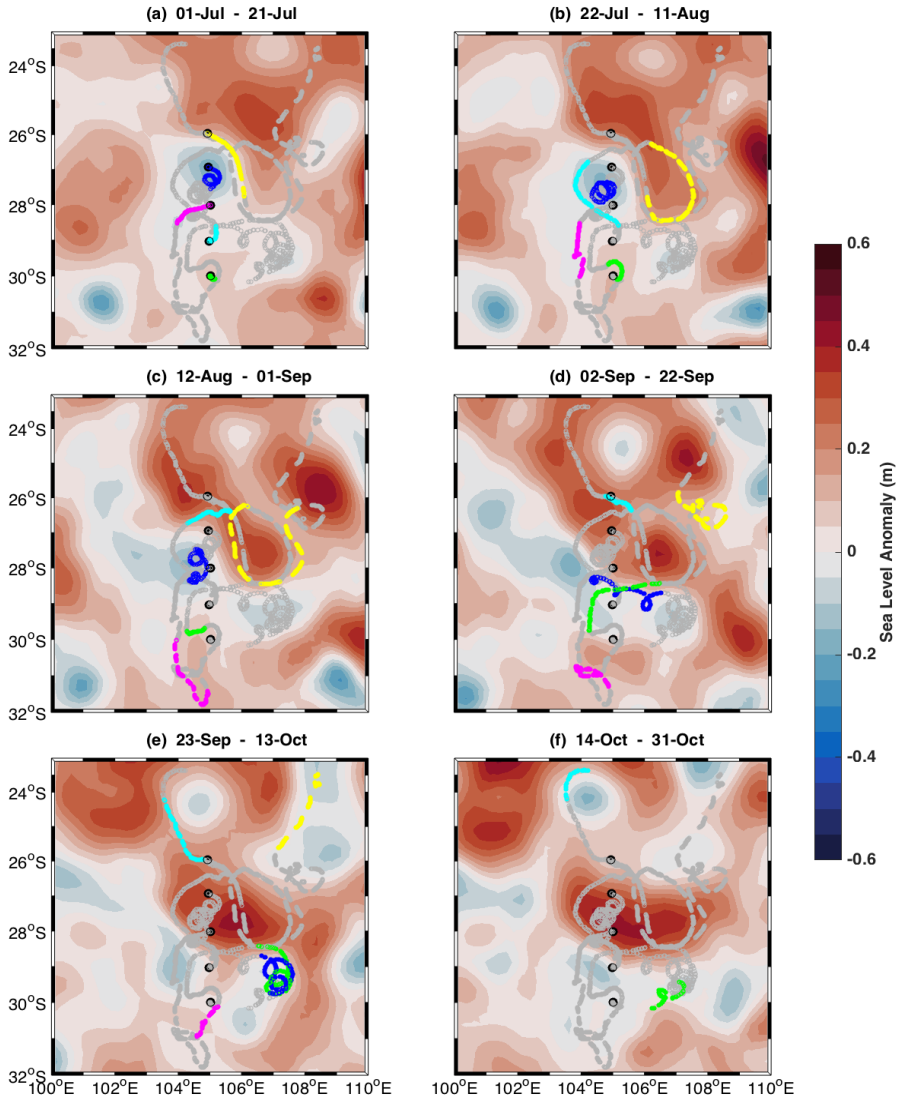

Figure 2.3: Three week average of sea level anomaly from AVISO (colour shading) overlaid with the float tracks (grey lines). The colored dots (same color for each float as in Fig. 2.1) represent the float positions during each week.

axis as cumulative profile number, and a vertical line to separate one trajectory from the next. The motivation for using profile number is that it gives the same visual weight to each profile rather than having one profile take up greater space where the speed of the float and distance travelled are large.

The floats move through a rich eddy field where the height of the isopycnals varies considerably. However, the isopycnal height change is not always a good indicator of the presence of an eddy. For example, a float entering a cold (warm) core eddy will experience a shoaling (deepening) of isopycnals. But once within the eddy, the isopycnal height may rise and fall as the float moves relative to the eddy centre. We thus use the SLA field and ζ to identify when the floats encountered eddies (Fig. 2.4a).

EM-6662 was deployed in a cyclonic eddy and spent its entire life looping in a clockwise direction.

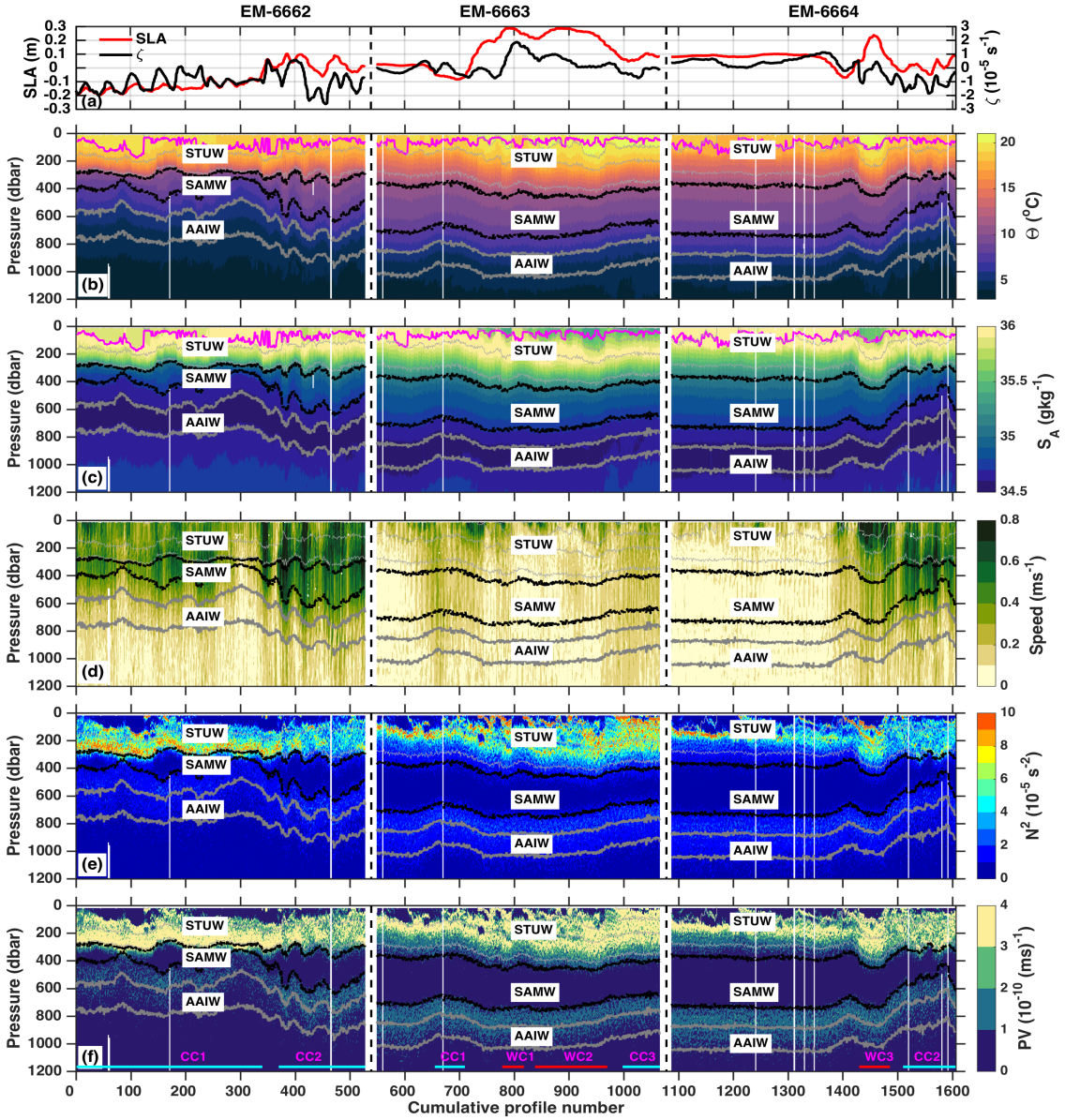

Figure 2.4: Along-stream evolution of a) sea level anomaly (red line) and relative vorticity (black line), b) conservative temperature, c) absolute salinity, d) speed, e) buoyancy frequency, and f) potential vorticity. The light grey lines are isopycnals with an interval of 0.7 kg m^{-3}. The heavy grey contours in all panels show the density range of AAIW (27.1 – 27.3 kg m^{-3}) and heavy black lines show SAMW (26.7 – 26.9 kg m^{-3}). The STUW is the high salinity near-surface water. EM-6662 profiled two cold core eddies (CC1 and CC2). EM-6663 profiled two warm core eddies (WC1 and WC2). EM-6664 profiled another warm core (WC3) and the same cold core eddy in EM-6662 (CC2). The evolution of the mixed layer along the float tracks are marked over temperature and salinity (magenta line).

Animations of SLA show that this float was caught up in two separate cyclonic eddies (CC1 and CC2), with a transition between the two near profile 340. The float took about 4 – 5 days to complete one loop in the eddies. Isopycnal heights vary by up to 200 m depth but there is no clear relationship between isopycnal height change and variations in SLA and vorticity. CC1 is associated with a decrease in SLA and negative ζ along the float track whereas CC2 doesn't show a depression in sea level but has strong

negative vorticity. In CC2, isopycnals are more affected below 200 m in agreement with the model results of Rennie et al. (2007).

EM-6663 was deployed in a location with SLA close to zero. It tracked northward and eastward, orbiting the western side of the cyclonic eddy where EM-6662 was trapped (CC1), and the southern edge of two warm core eddies to the north (WC1 and WC2). It then continued northward and eastward along the western boundary of another cold core eddy (CC3). The presence of CC1 and CC3 are more evident from the uplifting of isopycnals at depth with only weak signatures in SLA and relative vorticity (Fig. 2.4b). The presence of two discrete warm core eddies WC1 and WC2 are identified between cumulative profiles 770 – 980 based on SLA animations and ζ variability as well as isopycnal movement.

EM-6664 was deployed in a region of weak positive SLA with anticyclonic vorticity. It moved westward, northward and then eastward on the southern side of a large warm core eddy (WC3) before becoming caught up in the same cold core eddy that trapped EM-6662 (Fig. 2.3 and 2.4).

Among the two shallow floats EM-6217 and EM-6218, EM-6217 made two large excursions around a warm core eddy and then headed northward as far as 23°S. EM-6218 moved almost due southward to 32°S and then returned to north of 30°S. Its circular excursions were not easily related to individual eddies. These two floats are not included in Fig. 2.4 due to their depth limitation. However, we plot the upper 300 m of these floats together in Fig. A.1.

MLD is drawn as a magenta line in each vertical section (Fig. 2.4b). It varies from 30 – 180 m depth and has no apparent dependence on the position of the float relative to eddies. The maximum current speeds experienced in warm and cold core eddies are up to 0.8 m s^{-1}. Warm core eddies have surface intensified currents, whereas cold core eddies have subsurface velocity maxima around 200 – 400 m. The impact of the eddies on the water column can extend to the limit of the observations (1200 m) both in terms of elevated current speeds and changes in isopycnal height (e.g. EM-6662 profiles 350 – 528). Their impact is substantially less in some of the profiles (e.g. EM-6662 profiles 100 – 200). However, this reduced depth of impact is more likely due to the position of the profile relative to the centre of the eddy, rather than large variability in vertical extent of eddies.

Warm, salty subtropical underwater (STUW) lies at the surface in profiles south of around 26°S. In warm core eddies, the STUW is capped by a warm fresh layer that is possibly LC water that was trapped during the formation of the eddy close to the Australian coast (Morrow et al., 2003; Mao et al., 2018). North of 25°S the STUW is found beneath the warmer fresher waters of the Indonesian - Australian basin, which is supplied by the Indonesian Throughflow.

The SAMW is identified as a PV minimum (less than 1 $\times 10^{-10}$ $(\mathrm{ms})^{-1}$) between potential density contours 26.7 – 26.9 kg m^{-3} in a depth range of 300 – 700 m (not shown). The thickness of the SAMW layer varies considerably from 350 m at the beginning of the EM-6663 and EM-6664 records, and is close to zero in parts of the EM-6662 record. The AAIW salinity minimum of about 34.5 g kg^{-1} has fairly uniform thickness of approximately 200 m in all profiles. The density range is of AAIW is 27.1 – 27.3 kg m^{-3}, which is found between 450 m and 1050 m depth.

2.5 Evidence of near-inertial waves

The isopycnal heights displayed in Fig. 2.4 clearly show high frequency fluctuations with depth ranges of tens of metres and the current speed in Fig. 2.4d shows alternating strong and weak currents every few profiles. In the following we isolate these near-inertial oscillations from the lower frequency variability using complex demodulation. NIWs can be identified as a prominent peak near the inertial frequency (Fig. 2.5). At this frequency, the CCW polarization is dominant in all floats as expected for the southern hemisphere. However, it is not elevated very much over the CW component. Additional peaks at diurnal (O_1, K_1) and semidiurnal (M_2) tidal frequencies are also observed. The floats covered a wide range of inertial frequencies (Table 2.1) since they moved in a 7° latitude window. There is also a peak at $f + M_2$ harmonics. The energy peak at inertial frequencies supports the suggestion from Fig. 2.4 of the presence of near-inertial waves in the data.

Using complex demodulation, we obtained the CCW and CW components of the NIWs along the float tracks. Most of the strong beams are observed near the surface (Fig. 2.6) as is expected for wind-forced near-inertial motion. The CCW component of the amplitudes are dominant compared to the CW component as is expected for the southern hemisphere. After the passage of a storm, wind-generated NIWs are known to propagate both horizontally and vertically from the mixed layer (e.g. Zervakis and Levine, 1995). We observe strong beams that span a range of isopycnals near the surface and also at depth (e.g. EM-6662, 800 m depth). Comparatively weak beams propagate along the isopycnals (e.g. EM-6663, profiles from 550 – 650 at $\sim$ 800m). Here we consider beams with amplitudes larger than 0.1 m s^{-1} in the CCW component, the global average of NIW amplitude (Chaigneau et al., 2008), to be strong beams.

Internal waves can also be identified from coherent features in vertical profiles of horizontal velocity (Meyer et al., 2016). Following Meyer et al. (2016), we identified coherent features in velocity profiles at depths corresponding to the beams of high near-inertial amplitude by plotting anomalies of u and v relative to the vertically smoothed profile. The smoothed profiles were created using a vertical moving

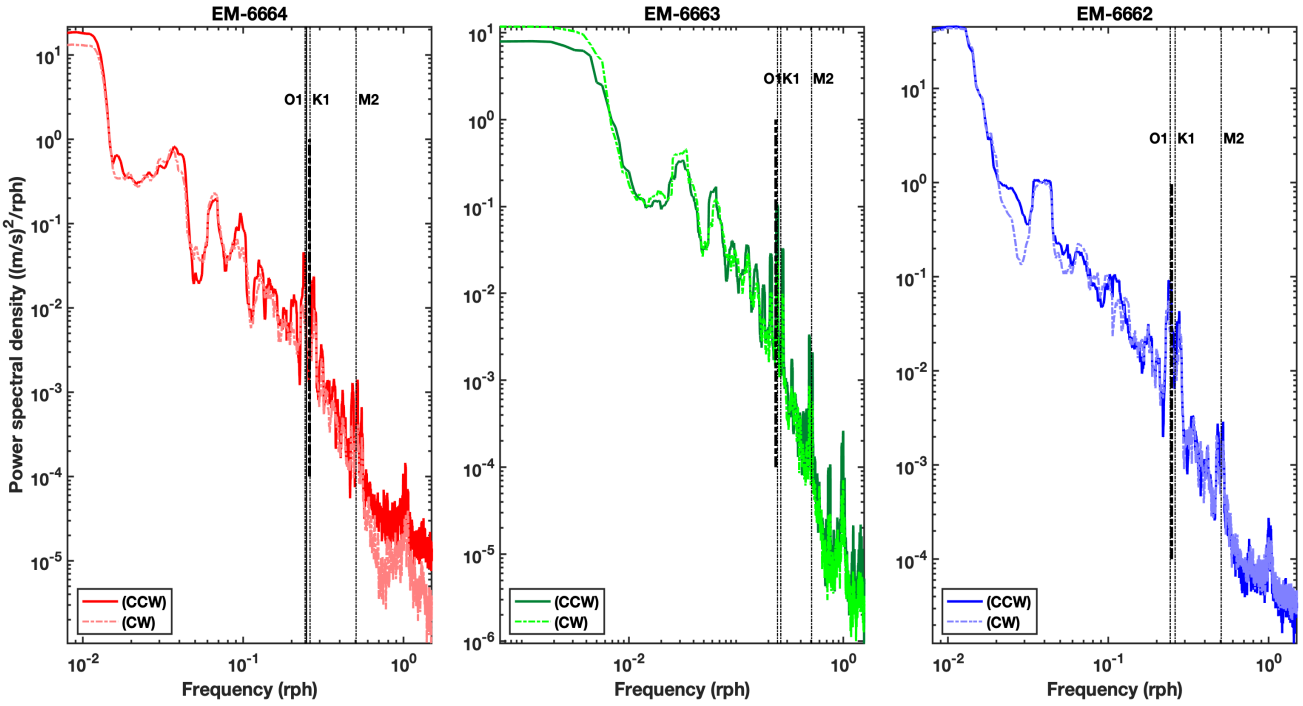

Figure 2.5: Velocity rotary spectra of EM-6664 (red), EM-6663 (green) and EM-6662 (blue) at a depth of 400 m. The heavy lines are the counterclockwise (CCW) components and dashed light lines are the clockwise (CW) components. The average inertial frequency covered by each float is marked by thick vertical dashed lines. Thin dashed black lines show the frequencies of diurnal (K_1 and O_1) and semidiurnal (M_2) tidal components.

average window of 500 m. Figure 2.7 shows an example of such a beam from EM-6662 between 650 and 1100 m depth. Elevated NIW amplitudes from the demodulation is found between profiles 440 to 520. Figure 2.7 zooms in on profiles 472 – 480 to provide a clearer view. The upward phase propagation implies a downward energy propagation suggesting that the beam was likely generated at the sea surface. This beam is discussed more in Section 2.6. We observe similar coherent features in the velocity profiles corresponding to other regions of high NIW amplitude identified through the complex demodulation.

Wave packets

Both downward and upward propagating beams can be identified from the NIW velocities, reconstructed from the amplitude and phase from complex demodulation of the deep floats, where most of them are propagating downward (Fig. 2.8). The group velocities of the beams are similar to those found in the North Pacific Alford et al. (2012). The beams were identified by visual inspection in close up plots of amplitude and corresponding coherent features in velocity profiles (Fig. 2.8). We identified a total of 15 clear NIW beams with a mean amplitude of 10 ± 3 cm s^{-1} from all the floats and document their properties in table 2.2. The properties of the beams from EM-6217 were not estimated since the float's salinity measurements were erroneous. We first estimate the wave frequency and vertical wave

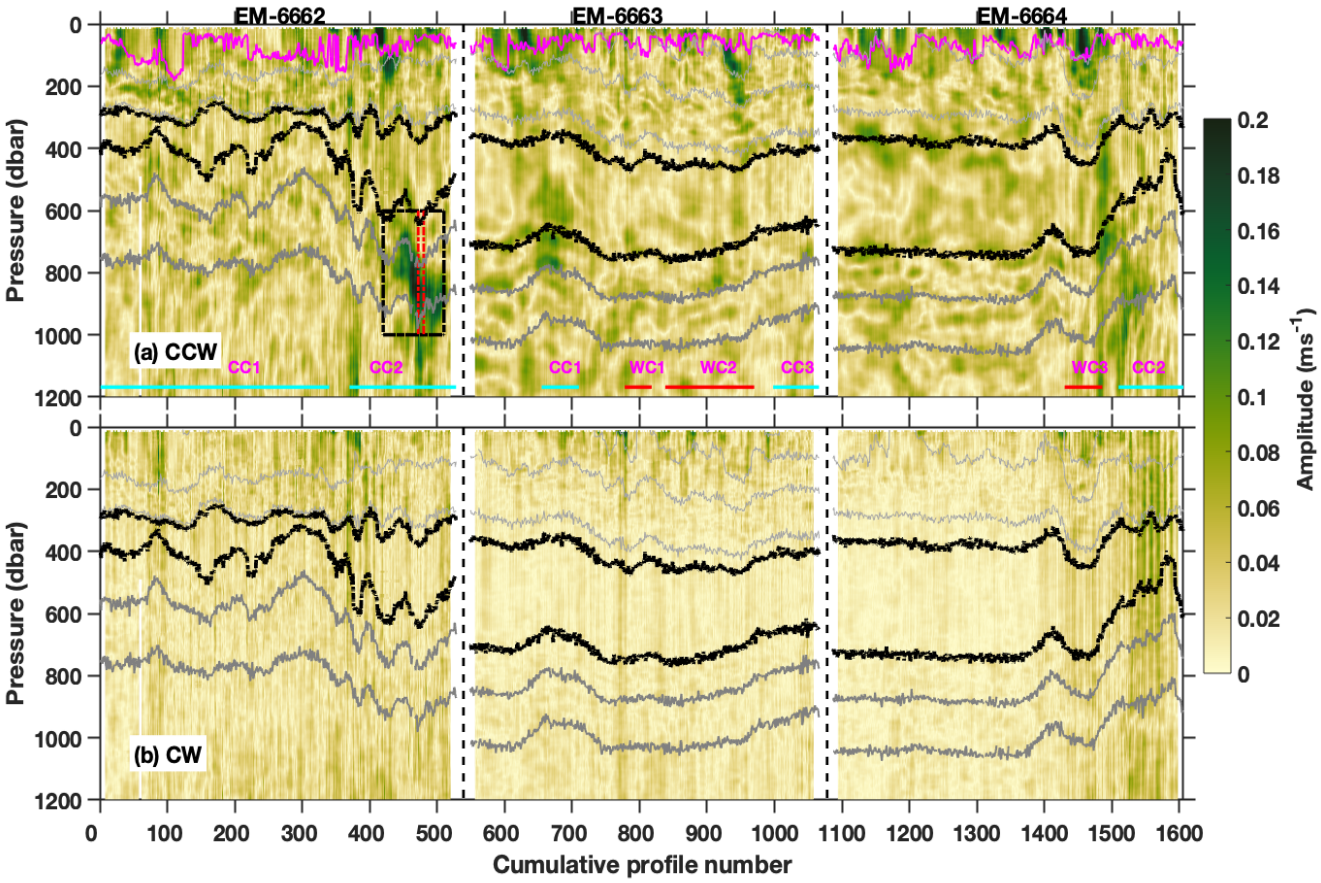

Figure 2.6: Near-inertial amplitudes of a) CCW and b) CW components along the float tracks. The isopycnals and the watermasses are the same as in fig. 2.4. The magenta line represents the mixed layer depth. Dashed box highlights a strong beam of NIW amplitude. The red dashed lines inside the black box represents profiles which are examined in Fig. 2.7.

number in each window using equations 2.2 and 2.3. We consider this frequency as the intrinsic wave frequency, ω_0 since the float follows the mean flow. This is a major difference between drifting and moored observations where one has to infer ω_0. Then we use ω and m in equations 2.5 and 2.6 to estimate the horizontal wave number and group velocity. We then average the profiles corresponding to each beam to get their properties.

The properties are highly sensitive to the ω and m estimates. We also calculated the mean and standard deviation of the properties. The low standard deviation shows that all of the waves have similar ω and m. Most of the beams are observed within the upper 500 m and very few beams are observed below the thermocline. Beam 10 has the largest vertical wavelength of 180.6 m whereas Beam 13 has the smallest vertical wavelength (17.2 m). Similarly, Beam 15 has the largest horizontal wavelength (346.9 km) whereas Beam 14 in the thermocline has the smallest wavelength of 9.4 km. The beams have a mean frequency of $(0.98\pm0.09)f$ with a vertical wavelength of 89 ± 63 m. The mean horizontal wavelength of the beams is 69 ± 85 km and horizontal group velocity of 3 ± 2 cm s $^{-1}$. The beams have a mean vertical

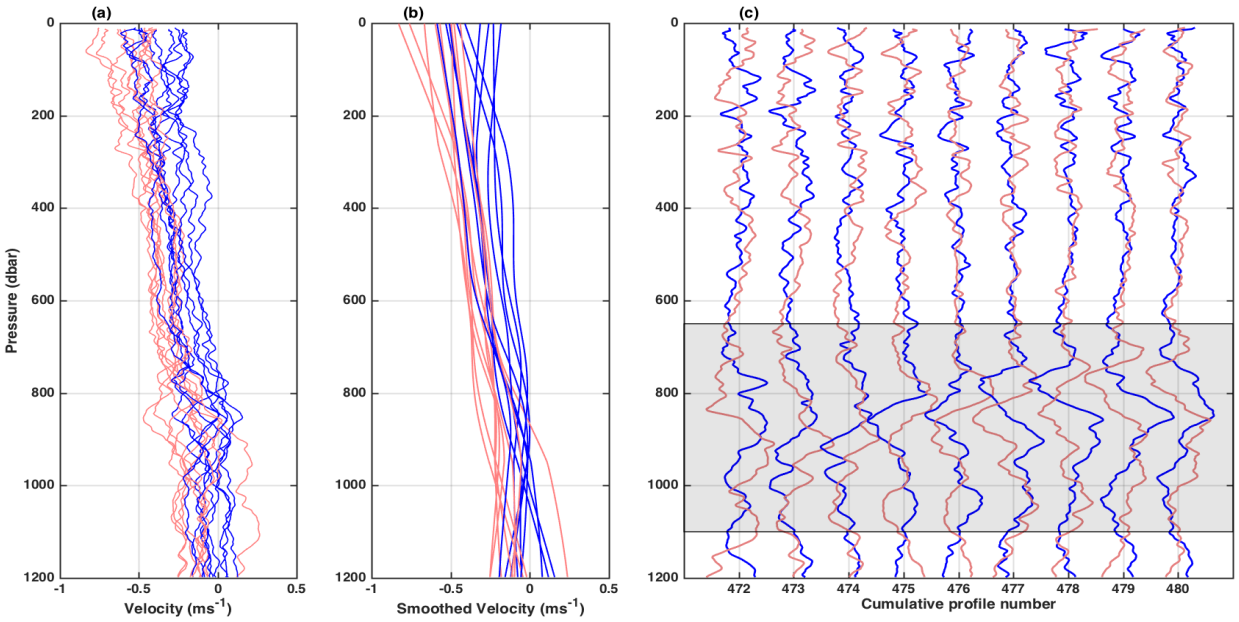

Figure 2.7: a) Zonal (blue) and meridional (red) components of velocity profiles of EM-6662 from profile 472 to 480. b) Corresponding smoothed velocities from a vertical moving average window of 500 m. c) Velocity anomaly obtained by subtracting smoothed velocity profiles from the measured velocity profiles. The grey shading identifies the coherent feature approximately between 650 – 1100 m.

No.	*Float*	*Profile*	*Depth* (m)	*Amplitude* (cms^{-1})	$\omega \times 10^{-5}$ $(rad\ s^{-1})$	ω/f	m (cpm)	λ (m)	$K_h \times 10^{-5}$ $(rad\ m^{-1})$	λ_h (km)	C_{gh} $(cm\ s^{-1})$	C_{gz} $(m\ day^{-1})$
1	6664	35-75	330-400	6.9	7.2	0.99	0.01	80.9	9.72	122.2	0.5	1.7
2	6664	143-165	370-440	5.8	7.6	1.05	0.03	29.2	290	69.8	0.6	1.5
3	6664	235-250	200-245	7.2	6.4	0.88	0.02	52	21	16.4	2.2	5.8
4	6664	395-420	660-750	8.5	7.3	1.02	0.1	220.7	9.24	29	1.8	23.7
5	6664	446-452	800-920	9.2	7.5	1.04	0.01	69.5	22.8	48.6	1.1	9.1
6	6664	200-220	110-150	6.7	7	0.96	0.03	33.2	29.1	31.3	2.5	3
7	6663	378-388	90-160	13.6	7.1	1.1	0.02	51	160	120	5	11.2
8	6663	90-100	100-150	12.6	6.2	0.9	0.009	111.4	6.5	60.8	2.2	16.7
9	6663	110-135	670-730	7.9	8.1	1.1	0.01	83.3	51.7	13.6	1.7	1.2
10	6663	66-80	280-300	9.5	5.7	0.8	0.01	180.6	6.23	22.6	1.9	8.4
11	6662	455-480	750-950	10.6	6.5	0.9	0.01	191.4	27	34.5	2.2	8.2
12	6662	24-32	90-110	12.8	6	0.92	0.02	47.2	13.7	79.9	2.9	13.8
13	6662	114-126	210-250	10.5	8	1.1	0.06	17.2	61.6	35.1	6.1	23
14	6218	80-115	120-146	11.9	7	1.0	0.02	47.8	11.5	9.4	1.2	3.7
15	6218	950-1010	180-216	12.3	7.1	0.95	0.009	112.7	39.9	346.9	5.6	5.3
Mean	-	-	-	10	7	0.98	0.03	89	50	69	3	9
St.Deviation	-	-	-	2.5	0.7	0.09	0.02	63.2	77	85	2	7

Table 2.2: The NIWs and their properties observed from the float data. The float number, amplitude, frequency ω, ω/f, vertical wavenumber m, vertical wavelength λ, horizontal wavenumber K_h, horizontal wavelength λ_h, horizontal group velocity C_{gh}, vertical group velocity C_{gz}, depth and profile numbers in which the waves are observed. The mean and standard deviation of the properties of the beams are at the bottom of the table.

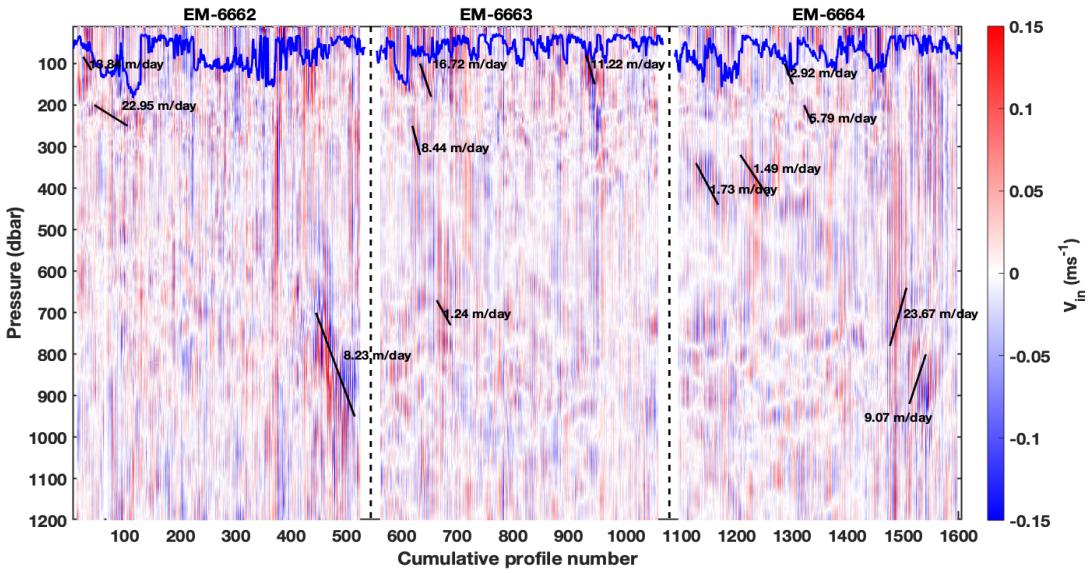

Figure 2.8: The meridional component of the near-inertial currents. The vertical velocity of each beam is indicated with the respective downward or upward slopes.

group velocity of 9 ± 7 m day^{-1}. Meyer et al. (2016) presented the properties of internal waves in the Southern Ocean (SO) identified from coherent features in the velocity field. The wave properties we find in the southeast Indian Ocean are similar to those found in their SO study.

Meridional propagation

The inertial waves observed at a given location can be a combination of locally generated (local wave field) waves as a response to wind forcing and remotely generated waves that have propagated to that location from their generation site (global wave field) (Fu, 1981; Alford, 2003). The NIWs with frequency slightly higher than the local inertial frequency tend to propagate toward the poles and will quickly reach a latitude where the local inertial frequency is equal to the wave frequency. Then the waves propagate back towards low latitudes where the local inertial frequency is lower than the wave frequency. When the waves propagate downward and equatorward, they tend to keep the local inertial frequency of their origin location which will be higher than that at the lower latitudes. This tendency of the waves is called blue shift (Alford, 2003; Simmons and Alford, 2012).

We estimated the blue shift along the float trajectories and with depth. We calculated the velocity rotary spectra over a moving window of width 10 days along the float trajectory and then compared the peak inertial frequency with the mean local inertial frequency of the window, following Simmons and Alford (2012), at different depth levels. The blue shift is evident from the float EM-6663 which covered the most latitudes (Fig. 2.9). The ratio of f_{peak}/f_{local} increases towards the equator and reaches up to 10 –

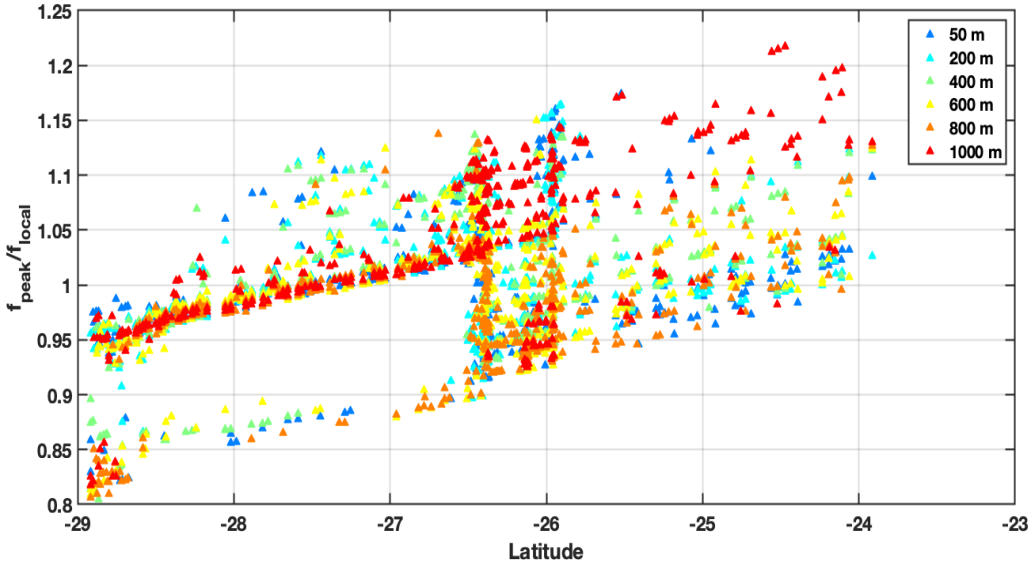

Figure 2.9: Blue shift along the trajectory of EM-6663 with latitude and depth (colors from blue to red) for a moving window of 10 days.

15% of the local inertial frequency. There is also a tendency of the blue shift to increase with depth but not very strongly.

2.6 Influencing factors

2.6.1 Upper ocean

Wind stress imparts energy into the ocean surface resulting in the generation of inertial currents in the mixed layer. These currents excite NIWs at the base of the mixed layer that propagate into the ocean interior (Dasaro, 1985). Strong wind events often generate large inertial current amplitudes in the mixed layer (Fig. 2.10). Moderate wind events also result in comparatively large amplitudes. One of such beam was observed by float EM-6663 between profiles 900 – 1000, immediately below the mixed layer. Even though the wind stress is moderate ($\sim$ 0.1 Nm^{-2}) in the region at the time of these profiles, this beam has a strong amplitude of 0.13 ms^{-1} and higher inertial energy (>15 Jm^{-3}). It has a vertical wavelength of 51 m and a horizontal wavelength of 120 m (Table 2.2, Beam 7).This beam is also visible from the velocity profiles as a coherent feature similar to that in Fig. 2.7. The non-association of strength between wind and inertial amplitudes could be because the wind components and the inertial currents are out of phase and their lateral structures do not match (Alford et al., 2012).

The amount of energy transferred from wind to the mixed layer, or wind work, can be obtained as

$$\Pi = \tau . U_{in} \tag{2.8}$$

where τ is the wind stress and U_{in} is the near-inertial velocity with components (u_{in}, v_{in}) (Silverthorne and Toole, 2009). When the wind stress and the inertial currents are in the same direction (positive wind work), the energy will transfer from the atmosphere into the ocean. The wind work is negative when the wind stress is in the opposite direction to the surface current, which will increase the near-surface shear in both atmospheric and oceanic boundary layers resulting in turbulent dissipation (Dasaro, 1985). We estimated the wind work in the mixed layer using equation 2.8 and compared it with the observed near-inertial KE (Fig. 2.10 b and d) estimated using $KE_{in} = \frac{1}{2}\rho_0 \left(u_{in}^2 + v_{in}^2\right)$, where ρ_0 is the density (Silverthorne and Toole, 2009). The wind work estimated from the float data is similar in magnitude to estimates from mooring data in Dasaro (1985).

The large input from the wind is associated with high inertial kinetic energy (KE_{in}) near the surface. High KE_{in} ($\sim$ 30 J m^{-3}) is associated with stronger inertial currents and energy transfer as expected (Fig. 2.10c and d). These high values are of similar magnitude with those observed in mooring data in the North Pacific (Alford et al., 2012; Plueddemann and Farrar, 2006). Below the mixed layer, energy is weaker ($<$ 10 J m^{-3}) except within strong beams. Higher energy inertial currents (Fig. 2.10c) seem to excite strong NIWs at the mixed layer base which propagate into the ocean interior below cold core (e.g. EM-6662, profiles from 400 – 450) and within warm core (e.g. EM-6663, profiles from 900 – 1000) eddies.

2.6.2 Deep ocean (500 – 1200 m)

Wind

We observe high KE_{in} below 700 m associated with a downward propagating NIW (Fig. 2.7). This is the only deep reaching beam with energy $>$ 20 J m^{-3} which is similar in magnitude to the beams near the surface. It has a vertical wavelength of 191.4 m, horizontal wavelength of about 34.54 km and vertical group velocity of 8.23 m day $^{-1}$ (Table 2.2, Beam 11). Since the beam does not seem to propagate from the surface in the float track (Fig. 2.6), it must have been generated at another place at some early time and propagated downward and equatorward (Zervakis and Levine, 1995; Alford and Gregg, 2001) to its observed position and depth. With a vertical group velocity of $\sim$ 9 m day^{-1}, this beam would take about 77 days to reach 700 m. The float profiled the beam around 28 September. We looked at the surface maps of wind speed over the region about 77 days before the beam was observed (Fig. 2.11). A strong wind system, that evolved over several days with southerly wind speeds larger than 20 m s^{-1}, stayed

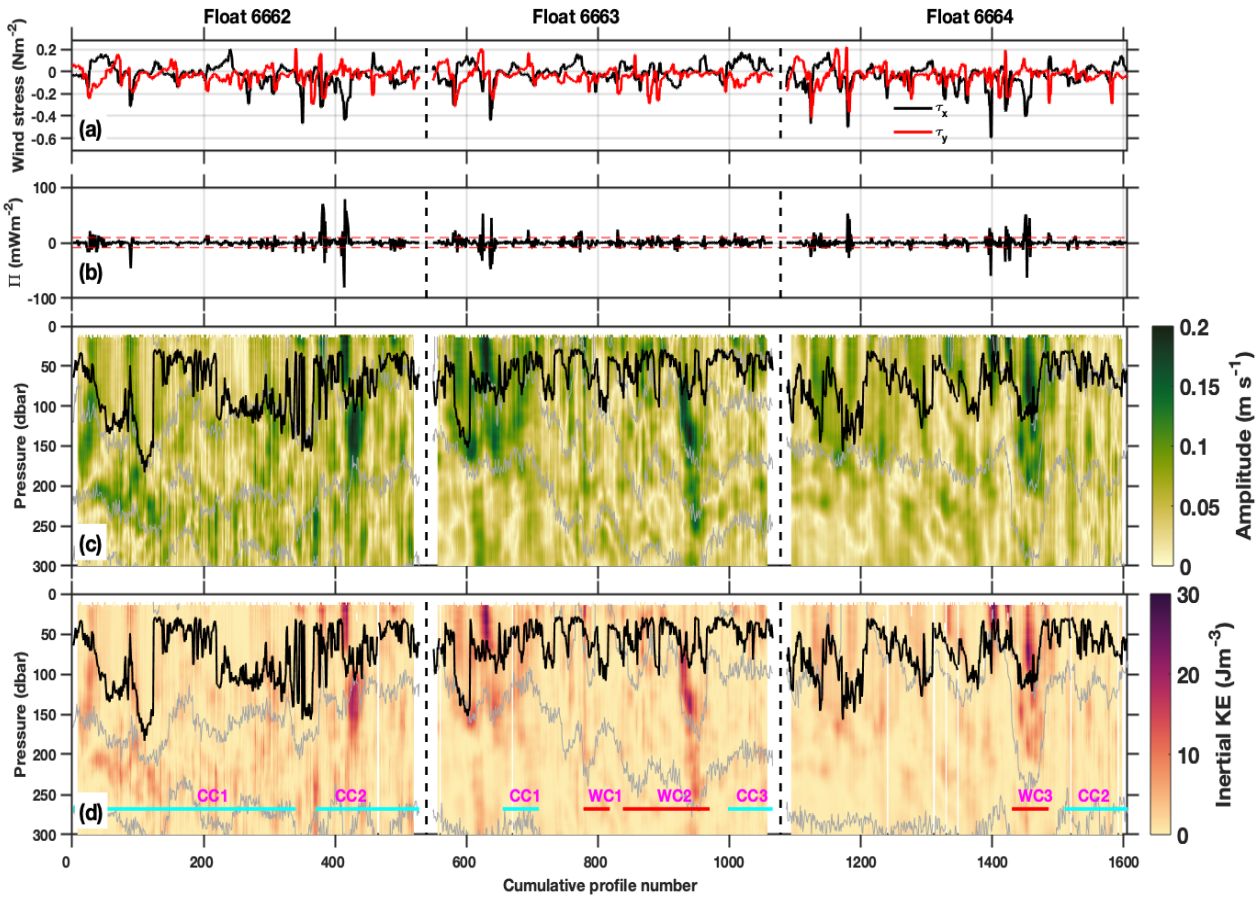

Figure 2.10: a) Wind stress components, b) wind work , c) near-inertial CCW amplitudes and d) near-inertial KE along the float tracks in the upper 300 m. The red dashed lines on panel b) are one standard deviation. In c) and d), heavy black line is the mixed layer depth and grey contours are isopycnals.

over the region and then faded away (12 – 14 July). The observed beam could be generated from this passing cyclonic wind system and propagated towards lower latitudes where the local inertial frequency is lower than that at the wave's origin site and was observed by float EM-6662 (Alford, 2003; Simmons and Alford, 2012).

Following Alford et al. (2012), we also attempted to estimate the vertical energy flux carried by near-inertial motions as $F_z = c_{gz}E$ where KE_{in} is assumed as E. We multiplied the mean vertical group velocity of the downward beams, $c_{gz} = 1.04 \times 10^{-4}$ ms^{-1} (9.05 m day^{-1}) with the mean of their KE_{in}. We then compared it with the wind work associated with the corresponding float profiles in which the beams were observed. The mean energy flux of the beams is about 47.36% of the wind work, which has the potential to reach deep ocean.

If we assume that the vertical flux of the deepest beam transiting 700 m, 3.24×10^{-4} Wm^{-2} is dissipated in the immediate 100 m depth below (AAIW layer, fig. 2.4), it will result in a dissipation rate of $\varepsilon = F_z/(\rho \times 100) = 3.15 \times 10^{-9}$ m^2 s^{-3} where ρ = 1027.13 kg m^{-3}, with an associated diffusivity

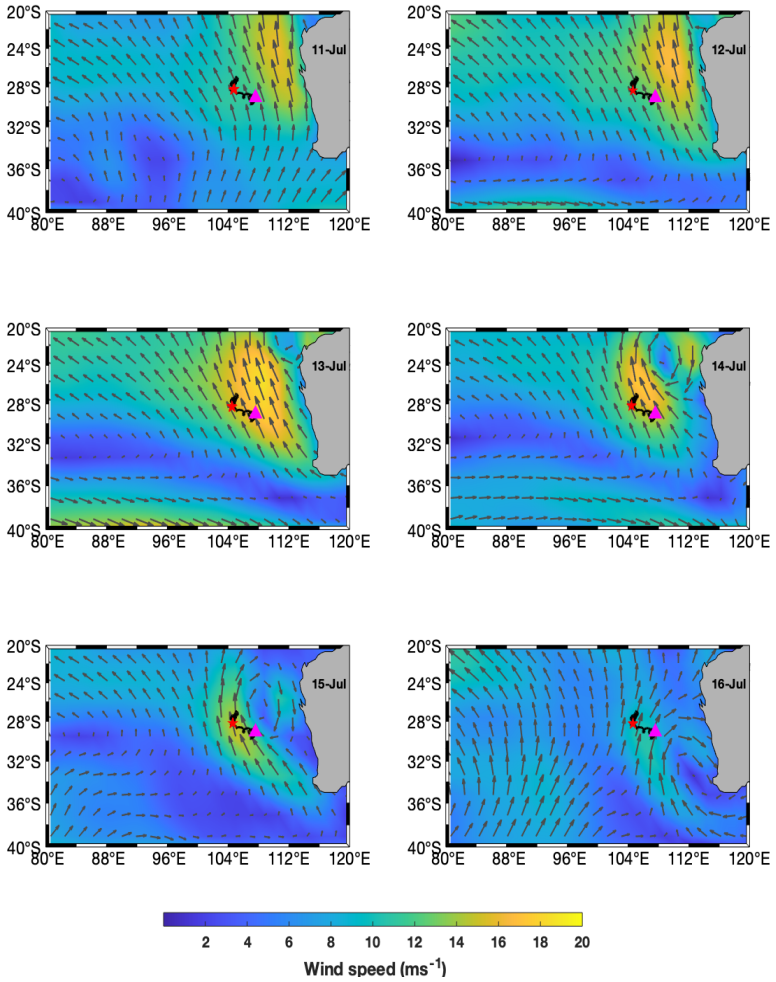

Figure 2.11: Daily maps of surface wind speed (color shading) with the arrows showing direction during the deep reaching beam was generated. The track of the float EM-6662 is also marked (black line). The red dots are the float locations at each day and the pink triangle is where the beam was observed.

of $K_\rho = \Gamma\varepsilon/N^2 = 4.2 \times 10^{-5}$ m^{2}s^{-1}. This is of the same order of magnitudes for dissipation rate and diffusivity respectively) as that estimated through fine-scale parameterization at this depth range for the corresponding profiles (Chapter 3, table 3.3). Further, following Alford et al. (2012), if we assume that the vertical flux of this beam transiting 700 m is evenly distributed up to 1200 m of the water column, it will result in a very moderate dissipation rate of 2.63×10^{-10} m^2 s^{-3} and a diffusivity of 5.6×10^{-6} m^{2}s^{-1}. This suggests that NIWs play an important role in providing energy to the deeper levels in regions where the surface currents are not very strong.

Topographic roughness

NIWs are associated with large near-inertial shear variance (e.g. Elipot et al., 2010). Following Martini et al. (2014), the near-inertial shear variance along the float tracks can be calculated as

$$S_{in}^2 = \left(\frac{\partial u_{in}}{\partial z}\right)^2 + \left(\frac{\partial v_{in}}{\partial z}\right)^2 \tag{2.9}$$

where u_{in} and v_{in} are the zonal and meridional components of NIW velocities respectively and dz is taken as 10 m.

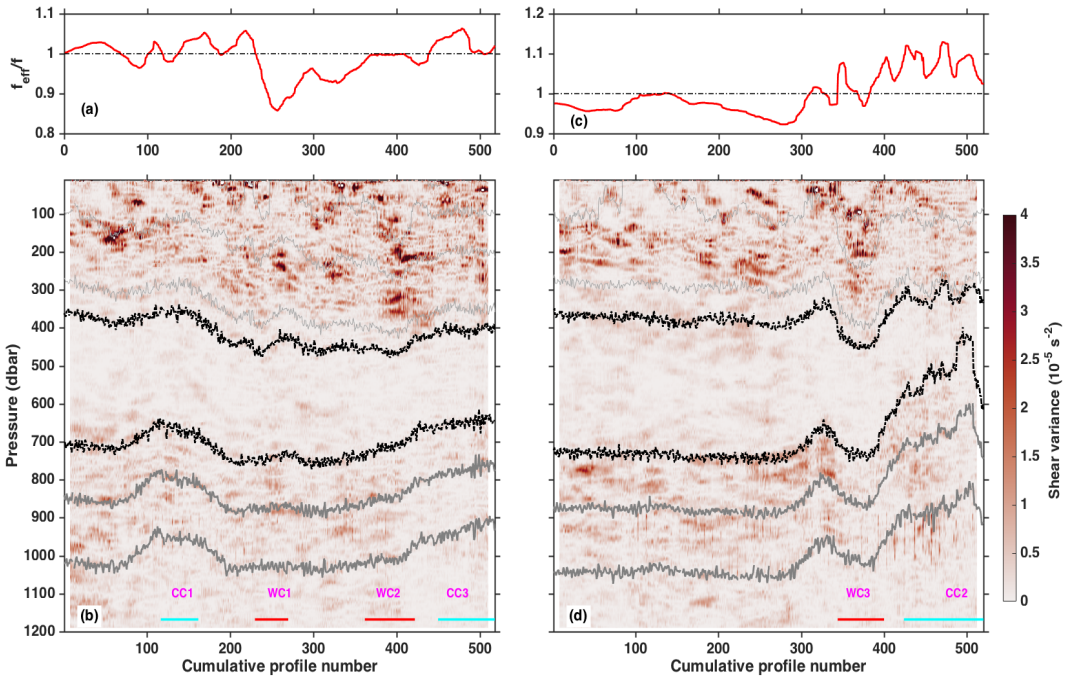

Figure 2.12: The variation of f_{eff}/f (a and c) and NIW shear variance (b and d) along the tracks of EM-6663 (left panels) and EM-6664 (right panels). Light grey contours are isopycnals at every 0.7 kg m^{-3}. The thick black lines are the density contours corresponding to SAMW (26.7 – 26.9 kg m^{-3}) and the thick grey lines are those corresponding to AAIW (27.1 – 27.3 kg m^{-3}).

Away from the surface, we observe patches of higher near-inertial shear variance at depths corresponding to the AAIW (Fig. 2.12). We have identified both upward propagating and downward propagating NIWs at this depth range (Fig. 2.8). Thus, the subsurface patches of elevated near-inertial shear variance could be from a variety of sources including downward propagating, surface-generated NIWs; upward propagating NIWs generated at depth due to interaction of tides with bottom topography; reflected NIW from the ocean bottom (Alford, 2010) and wave-wave interactions or wave-mean interactions. We thus analysed the correlation of inertial shear variance at subsurface between 700 – 1000 m with the topographic roughness to investigate whether there is any relation between the two. Topographic roughness

is derived as the standard deviation of bathymetry, which is 100 km in radius around each float location (Hennon et al., 2014). Since the horizontal wavelength of the first baroclinic mode of internal waves of semidiurnal frequency is of the order of 100 km, we chose 100 km radius following Hennon et al. (2014). We use ETOPO1 (Amante and Eakins, 2009) bathymetry data with a 1-minute arc $(0.01^\circ \times 0.01^\circ)$ resolution. Rough topography is defined as regions where the roughness is larger than the mean (307 m) and the smooth topography as regions where roughness is less than the mean (Meyer et al., 2015).

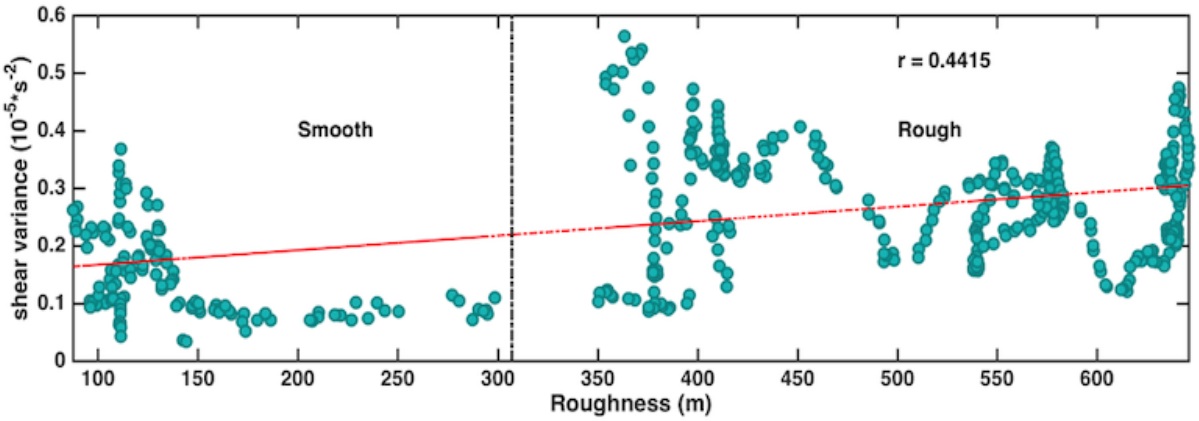

Figure 2.13: Depth averaged shear variance between 700 – 1000 m plotted against topographic roughness estimated along the float track of EM-6664. The dotted black line is the mean of roughness along the trajectories of all deep floats. The red line is the best line of fit with a 95% significant correlation of 0.44.

The high inertial shear variance at the depth of 700 – 1000 m in the record of EM-6664 has a small but statistically significant positive correlation (0.44) with the bottom roughness (Fig.2.13). In addition, we observe two upward propagating NIWs at this depth range in the track of float EM-6664 (Fig. 2.8), suggesting that these waves may contribute to the positive correlation. Even though the correlation for EM-6663 is less, a positive correlation suggests that rough topography can influence the near-inertial shear variance (Fig. A.2). Due to the depth limitation of the floats, it is not possible to identify whether the high shear variance is due to NIWs generated from interaction of deep flow with rough bathymetry. It is possible that the waves observed at depth could have been generated from an earlier wind event or other deep mechanism and propagated vertically and horizontally. Nonetheless, the high near-inertial shear variance at depths within the AAIW (Fig. 2.12) suggests the possible role of NIWs in watermass transformations in this region.

2.7 Interaction of NIWs and mesoscale eddies

The propagation of NIWs into the ocean interior can be affected by oceanic features such as mesoscale eddies. The slow group velocities of the NIWs allow them to interact with mesoscale eddies that can modify the properties of these waves (Alford et al., 2016).

Anticyclonic eddies with a negative relative vorticity can reduce the propagating frequency of the NIWs to an effective frequency below f. The waves are then trapped inside the eddy and as they propagate down from the surface, their vertical wavelength and group velocity reduce. The wave energy accumulates at the bottom of the eddy near a critical depth and eventually a fraction of this energy results in dissipation (Kunze, 1985, 1995). Using a primitive numerical model, Lee and Niiler (1998) found that warm core eddies are efficient in draining near-inertial energy from the surface to below the thermocline whereas in a cold core eddy, the near-inertial waves can freely propagate out leaving energy only in the surface layer.

The effective frequency f_{eff} can be written as

$$f_{eff} = f + \zeta_z/2 \tag{2.10}$$

where ζ_z is the vertical component of relative vorticity. The cyclonic vorticity regions have $(f_{eff}/f) > 1$ whereas the anticyclonic vorticity regions have $(f_{eff}/f) < 1$ in the southern hemisphere (Fig. 2.12a and c).

The near-inertial shear variance is high when there is a warm core eddy present (Fig. 2.13). Also the near-inertial shear variance is lower in cyclonic eddy regions of the float tracks compared to that in anticyclonic eddy regions (e.g. WC3 and CC2, Fig.2.14). This is in agreement with Elipot et al. (2010) where they found that the near-inertial variance is higher in anticyclonic vorticity regions compared to cyclonic vorticity regions, using global drifter and altimetry data. Lee and Niiler (1998) also found high inertial energy shear in the core of an anticyclonic eddy in their primitive equation model, suggesting that the NIWs were trapped inside the anticyclonic eddy (e.g. Kunze, 1985; Lee and Niiler, 1998; Jaimes and Shay, 2010). Here we examine two floats (EM-6663 and EM-6664) that encountered anticyclonic eddies in their tracks.

EM-6663

The warm core eddy (WC1) encountered on the track of EM-6663 has a mean relative vorticity of 1.3×10^{-5} s^{-1}. The eddy vorticity reduces the effective frequency to about 90% of the local inertial frequency (Fig. 2.12a). This suggests that the warm core eddy traps the wind generated NIWs. This is also evident from the increased near-inertial shear variance in the region of warm core eddies WC1 and WC2 in comparison with cyclonic eddies (Fig. 2.12b).

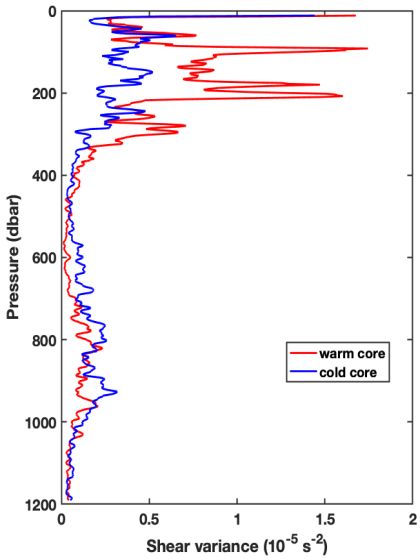

Figure 2.14: Mean shear variance from float EM-6664 in warm core eddy WC3 (red) and cold core eddy (CC2).

EM-6664

The part of the warm core eddy (WC3) sampled by the float is comparatively weak with a mean relative vorticity of 3.1×10^{-6} s^{-1}. Since the float does not have any profiles in the eddy core, we cannot examine the theory of inertial chimney (Lee and Niiler, 1998) where the strong relative vorticity core of the eddy acts as a critical layer where the near-inertial energy reaches its maximum. However, the background vorticity has influenced the inertial frequency (Fig. 2.12c and d). The ratio of f_{eff} to f is less than 1 for the warm core eddy region of the float track suggesting that the vorticity of the eddy reduces the frequency of NIWs resulting in trapping them.

2.8 Discussion and conclusion

The observations of NIWs in the eastern SIO and their interactions with LC eddies are presented for the first time using EM-APEX floats. The floats were deployed in the eastern SIO between 25°S and 32°S along 105°E, in 2013. They profiled up to a depth of 1200 m for 3 – 4 months providing a detailed picture of the watermass properties along their trajectories. The velocity spectra showed higher energy at near-inertial frequencies suggesting that this frequency band is dominant in the data. The presence of NIWs can also be observed from the mirror-imaging of the velocity profiles separated by half an inertial period.

We identified the near-inertial beams using complex demodulation from the float-measured velocity data. Inertial currents with amplitudes larger than 20 cm s^{-1} are generated in the mixed layer which generate

strong NIWs at the base of the mixed layer. Their amplitude reduces as they propagate into the ocean interior. The observed NIWs are a combination of locally generated waves from strong wind events, and remotely generated waves. A blue shift of 10 – 15% towards the equator is observed in the upper 1200 m in agreement with Simmons and Alford (2012) observations in the North Pacific. The vertical energy flux of the downward propagating beams is more than 40% of the wind work done on near-inertial motions in the mixed layer. NIW beams with high KE is observed to penetrate below 700 m, which has the potential to provide energy to mix up to 1200 m deep. This suggests that the wind generated NIWs can play an important role in mixing the ocean interior and watermass transformation. Bottom topography may also result in increased near-inertial shear variance although our data does not extend close enough to the bottom to show this conclusively.

The floats were deployed in a region with a rich eddy field. All floats encountered eddies more than once in their trajectory (Fig. 2.3). The wind generated near-inertial waves can be modified by mesoscale eddies as they propagate down into the ocean interior. We observed stronger near-inertial shear variance in warm core eddies near the surface compared to cold core eddies suggesting that NIWs are trapped inside the warm core eddies. This suggests that the presence of warm core eddies increases the likelihood that wind energy will penetrate into the interior of the ocean. (Fig. 2.10c).

Study	*Region*	*Data*	*NIW amplitude* (cm s^{-1})	*KE*
Kunze and Sanford (1984)	North Pacific Subtropical front	CTDs and XCPs	10 – 20	4 J m^{-3}
Dasaro et al. (1995)	North Pacific	CTDs, Drifters, moorings	35 – 70	8700 J m^{-2}
Alford and Gregg (2001)	Banda Sea	Sonar and VMP	10	25 J m^{-3}
Chaigneau et al. (2008) (Global study)	South Indian Ocean	Drifter climatology	10	200 – 400 J m^{-2}
Saji et al. (2000)	Tropical IO	Drifter	15	-
Alford et al. (2012)	North Pacific	Mooring	-	50 J m^{-3}
Alford et al. (2013)	North Pacific Subtropical front	Shipboard CTD and ADCP	10	7 J m^{-3}
Martini et al. (2014)	Beaufort Sea	Mooring	-	0.58 J m^{-3}
Shengli et al. (2015)	South China Sea	Mooring ADCP	30 (max)	-
This study	eastern SIO	EM-APEX floats	25	30 J m^{-3}

Table 2.3: Comparison of NIW amplitudes and KE published in earlier studies and this study.

The NIW characteristics obtained in this study are in good agreement with previous studies in different regions (Table 2.3). Compared to the northern hemisphere, NIW characteristics are less studied in the southern hemisphere. Using global drifter data from 1999 – 2006, Chaigneau et al. (2008) estimated a mean inertial current amplitude of 10 cm s^{-1} in every ocean basin. They found that the seasonal

cycle of the inertial amplitude is higher during JAS in the southern Indian Ocean, during which the floats were deployed. From our study in the eastern SIO, we observe amplitudes bigger than 20 cm s^{-1} which are stronger than those observed in the north Pacific subtropical front (Kunze and Sanford, 1984; Alford et al., 2013). Dasaro et al. (1995) reported amplitudes and energy 2 – 3 times stronger in the North Pacific where the NIWs were generated in the wake of a strong isolated storm. They observed the inertial energy spreading downward from the mixed layer, and reaching as deep as 1000 m. This is consistent with our study where we observed a NIW beam propagating below 700 m and that of Alford et al. (2012) in the North Pacific where they found that the inertial energy propagated to depths of 800 m. They found that the KE_{in} is higher in winter relative to summer. Chaigneau et al. (2008) also reports larger inertial amplitudes and mixed layer energy during winter for the northern Pacific. Even though the southern Indian Ocean does not have a strong seasonal cycle similar to the northern Indian ocean, it has the strongest near-inertial amplitudes and energy compared to other southern ocean basins (Chaigneau et al., 2008). This is associated with the large energy transfer from wind to near-inertial motions during austral autumn and winter (Alford, 2003).

Strong energy transfer is often associated with strong KE_{in} in the mixed layer. The anticyclonic eddies influence the vertical propagation of near-inertial energy into the ocean interior in agreement with the model results (Zhai et al., 2005). Considering the richness of eddies in this region, it is important to include the effect of mesoscale eddies in mixed layer models. The interaction of eddies and NIWs could be a key factor in the mixing budget of this region which is important for the unique circulation in the southeast Indian Ocean. Diapycnal mixing due to the breaking of internal waves in this region will be explored in Chapter 3.

Chapter 3

Observational estimates of turbulent mixing in the southeast Indian Ocean

Abstract

Turbulent mixing is important in transporting energy, heat, carbon and freshwater throughout the ocean and also plays a major role in the evolution of the large scale circulation. This study investigates the spatio-temporal variability of turbulent mixing in the eastern South Indian Ocean using a collection of data from EM-APEX profiling floats, shipboard CTD and microstructure profiles. The floats collected 1566 profiles of temperature, salinity and horizontal velocity data down to 1200 m over a period of about four months. A fine-scale parameterization is applied to the float and CTD data to estimate turbulent mixing. These estimates are compared with direct measurements of dissipation rate from microstructure profiles. Elevated mixing is observed near the sea surface, over bottom topography and in mesoscale eddies. Elevated mixing is observed in the warm core eddy due to trapped near-inertial waves near the surface. We found that cyclonic eddies contribute to turbulent mixing below 500 m, which is associated with downward propagating internal waves with frequencies other than near-inertial. The mean diffusivity over 250 – 500 m depth is $O(10^{-6})$ m^2 s^{-1} and it increases to $O(10^{-5})$ m^2 s^{-1} in 500 – 1000 m in cyclonic eddies. The turbulent mixing in this region has implications for watermass transformation and large-scale circulation. Higher diffusivity ($O(10^{-5})$ m^2 s^{-1}) is observed in the Antarctic Intermediate Water layer in cyclonic eddies whereas weak diffusivity is observed in the Subantarctic Mode Water layer ($O(10^{-6})$ m^2 s^{-1}). In contrast, the SAMW watermass properties are strongly affected in cyclonic eddies whereas the AAIW layer is less affected. Comparatively high diffusivity is observed within South Indian Countercurrent (SICC) jets associated with mesoscale eddies, suggesting that turbulent mixing may affect the evolution of the SICC structure.

3.1 Introduction

Turbulent mixing plays an important role in large-scale oceanic processes such as watermass transformation, global overturning circulation and stratification. It also distributes heat, salt, chemicals and organisms throughout the world oceans. By distributing the energy input from winds and tides, turbulent mixing due to wave breaking closes the oceanic energy budget (Bryan, 1987; Wunsch and Ferrari, 2004). Turbulence is the final stage of the energy cascade in the ocean where kinetic energy from winds and tides is transformed into molecular heat by viscosity (St. Laurent et al., 2012).

In the interior of the ocean, most of the mixing is attributed to the breaking of internal waves, which act as a bridge between the large scale forcing and the molecular scale dissipation (St. Laurent et al., 2012). Internal waves are generated mainly by fluctuating wind stress (Dasaro, 1985), tidal flow over steep topography (Egbert and Ray, 2000) and geostrophic flow over rough topography (Nikurashin and Ferrari, 2010). Near the ocean surface, the wind energy generates internal waves with near-inertial frequency that dominate the internal wave energy spectrum (Wunsch and Ferrari, 2004). From a global study using Argo floats between 30 – 45°N, Whalen et al. (2018) found that the amplitude of turbulent mixing estimates increases with increasing wind energy at the surface. They also found that the internal wave-driven mixing is strong in regions of anticyclonic vorticity compared to cyclonic vorticity regions. This is in agreement with the modification of wind-generated internal waves by anticyclonic eddies (Kunze, 1985; Lee and Niiler, 1998). The sensitivity of ocean models to the spatial and temporal variability of mixing has implications on ocean heat uptake in climate models (e.g. Harrison and Hallberg, 2008) and ocean circulation in regional models (e.g. Benthuysen et al., 2014).

The intermittent and patchy nature of turbulence makes it difficult to measure from limited ship-based observations. By using a range of inverse models and fine-scale parameterization, Huussen et al. (2012) found that too little internal wave dissipation is available in the deep Indian Ocean to sustain the meridional overturning circulation since most of the internal wave energy is dissipated in the upper 1000 m. Waterhouse et al. (2014) combined a range of measurements from different instruments and calculated a global average diapycnal diffusivity of $O(10^{-5})$ m^2 s^{-1} above 1000 m depth and $O(10^{-4})$ m^2 s^{-1} below 1000 m depth with higher values in the abyssal ocean. They reported relatively low depth-averaged diffusivity ($O(10^{-6})$ m^2 s^{-1}) in the upper 1000 m of the eastern Indian Ocean. Using a strain-only parameterization, Whalen et al. (2012) reported an average diapycnal diffusivity of $O(10^{-5})$ m^2 s^{-1} over 250 – 500 m of the upper eastern south Indian Ocean. They observed elevated dissipation rates in regions of high eddy kinetic energy.

The surface circulation in the subtropical south Indian Ocean is characterized by the eastward flowing

near surface geostrophic South Indian Countercurrent (SICC) (Siedler et al., 2006; Palastanga et al., 2007; Divakaran and Brassington, 2011; Menezes et al., 2014). The SICC splits into different branches (Fig. 3.1) that become stronger and deeper as they approach the west coast of Australia (Divakaran and Brassington, 2011). These branches act as a source of water for the poleward-flowing Leeuwin Current (LC) (Divakaran and Brassington, 2011; Domingues et al., 2007; Menezes et al., 2013, 2014; Furue et al., 2017). The LC is accompanied by the subsurface Leeuwin undercurrent (LUC) which flows equatorward underneath and just offshore of the LC (Thompson, 1987; Furue et al., 2017). Unlike other eastern basins, the eastern south Indian Ocean (SIO) is found to be a region of high seasonal and interannual mesoscale variability (Birol and Morrow, 2001). It possesses one of the highest eddy kinetic energy (EKE) bands in the world ocean between 15 – 30°S (Jia et al., 2011b). The mesoscale eddies generated from instabilities of the LC (Feng et al., 2005) and LUC (Rennie et al., 2007), as well as semi-annual Rossby waves emanating from the eastern boundary (Morrow and Birol, 1998), contribute to the observed variability over this region. These waves and eddies travel westward (Morrow et al., 2004) and interact with the SICC (Siedler et al., 2006). The subtropical south Indian Ocean is also a region of strong surface heat loss. In the seasonal cycle, the mixed layer heat storage in this region is primarily influenced by surface net heat flux and secondarily by turbulent entrainment (Chapter 4).

Due to lack of enough observations, the turbulent mixing and the factors that influence it in the southeast Indian Ocean are not well described. In this study, we use microstructure measurements to validate the estimates of turbulent mixing from Electromagnetic Autonomous Profiling explorer (EM-APEX) floats and shipboard CTD. We then investigate the variability of turbulent mixing in the southeast Indian Ocean, a region dominated by mesoscale eddies. We analyse the spatial and temporal variability of turbulent mixing and investigate its sources and implications for the first time in this climatically important region.

The paper is organised as follows. Section 2 describes the different datasets used in this study. The method of finescale parameterization used to estimate turbulent mixing from floats and shipboard data is explained in Section 3. Section 4 describes the regional ocean characteristics observed from the floats and the shipboard data. The spatial and temporal variability of turbulent mixing in the upper 1000 m is analysed in Section 5. Section 6 investigates the factors influencing the observed mixing distribution. In Section 7, we compare the different datasets and discuss the implications of mixing on watermasses and large-scale circulation. Section 8 provides a summary of the present study.

3.2 Data

3.2.1 Shipboard data

In this study, we use data collected from two voyages of the Marine National Facility (MNF) RV Southern Surveyor. The Voyage IN2012_V04 in 2012 consisted of 30 sampling stations at which CTD and lowered ADCP (LADCP) measurements were made (Fig. 3.1b). The Seabird SBE911 CTD fitted in a rosette with 19 Niskin bottles, measured ocean temperature, salinity, dissolved oxygen and pressure down to a depth of about 2000 m. Due to engine failure, research time was substantially reduced and CTD profiles were limited to the upper 2000 m. The salinity sensor had a standard deviation of 0.002 psu. The data processing report for the shipboard hydrographic and velocity data is available at `https://www.cmar.csiro.au/data/trawler`.

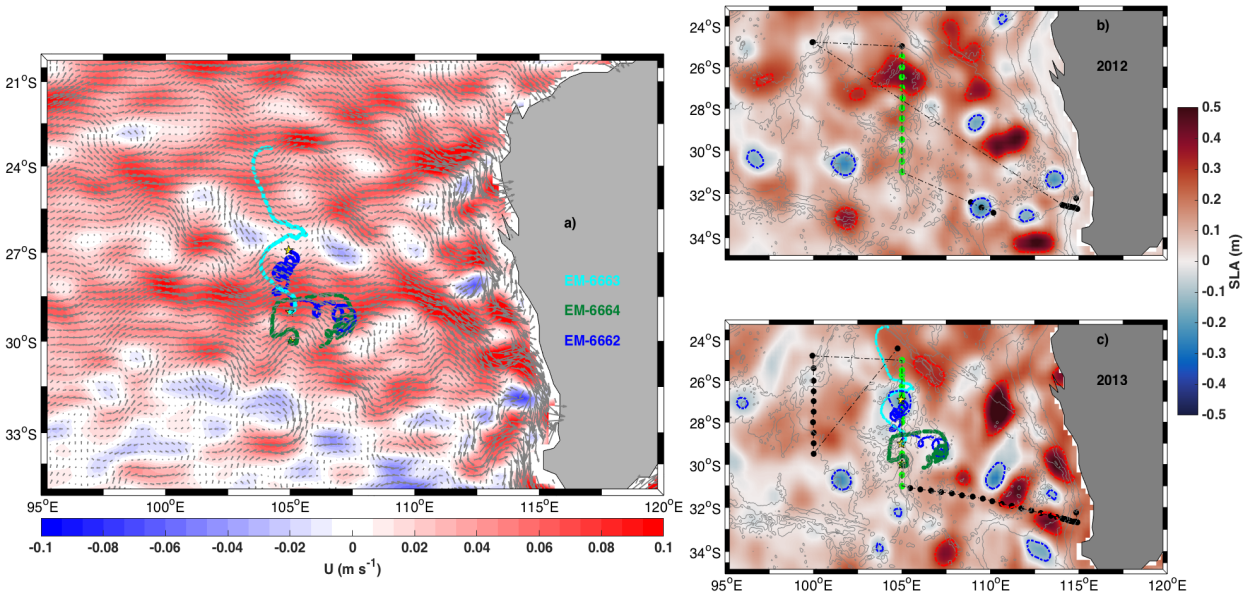

Figure 3.1: a) The tracks of EM-6662 (blue line), EM-6663 (cyan line) and EM-6664 (green line) are plotted over the mean of surface eastward currents (shading) during 2004 – 2015 from AVISO. Arrows show the mean direction of the flow. Yellow stars represent the location of each float deployment. b) Voyage track in 2012 and c) voyage track in 2013. The light green stars in (b) and (c) are the microstructure profiler deployment locations. Background is the mean sea level anomaly during the microstructure measurements with bathymetry contours overlaid (200, 1000, 2000, 4000, 5000 m). Closed sea surface height contours of -0.1 m (blue) and 0.3 m (red) show cyclonic and anticyclonic eddies respectively.

The voyage SS2013_V04 in 2013 consisted of 58 full-depth sampling stations (Fig. 3.1c) extending up to 5000 m. The Seabird SBE911 CTD fitted in a 19 bottle rosette frame, measured full-depth profiles of ocean temperature, salinity, dissolved oxygen and pressure. During the 2013 voyage, five EM-APEX

floats were deployed at various stations along 105°E (Fig. 3.1c). In this study we use measurements from CTD data along the 105°E transect in 2012 and 2013 as well as three EM-APEX floats that profiled down to 1200 m. In both years, CTD processing provided vertical profiles of temperature, salinity and pressure at every 2 dbar. We do not use the LADCP velocity measurements from both years in the finescale parameterization since there was bad data in most of the profiles.

3.2.2 EM-APEX floats

The primary data used for this study are collected from three EM-APEX floats deployed in the south-east Indian Ocean in July 2013 along 105°E. They profiled until October 2013 between 23°S and 32°S. EM-APEX floats are enhanced Argo floats that provide inexpensive high resolution measurements of horizontal velocity in addition to the standard temperature, salinity and pressure measurements. These floats use motional induction to measure the ocean velocity relative to a depth-independent reference velocity by measuring the electric current generated due to the movement of ocean water across the magnetic field of the earth (Sanford et al., 2005). The depth-independent reference velocity is determined from the surface GPS positions, following Phillips and Bindoff (2014). Two independent sets of electrodes measure the electric fields induced by the movement of the float (Sanford et al., 1978), providing two independent measurements of horizontal velocity. Vertical spacing of velocity samples is 3 – 4 dbar. The temperature, salinity and pressure measurements at every 2 – 3 dbar are obtained from a Sea Bird Electronics SBE-41 CTD.

The floats were designed to profile pairs of down-profiles separated by half an inertial period and pairs of up-profiles separated by half inertial period (Inertial period is about 27 hours at 27°S). With this strategy, the floats provided 8 profiles per day down to 1200 m. Towards the end of the deployment voyage, the float profiling was changed to add a drift at 1000 m depths for about 18 hours. The drift was added to extend the life of the float but still allow a rapid burst of profiling over an inertial period between drifts. During the drift, the floats measured temperature, salinity and pressure. The float measures velocity only when it moves vertically. After every up profile, the float spent 0.5 – 1 hour at the surface to transmit the collected data over the Iridium satellite network. More details of the float data processing is provided in Chapter 2 and in Appendix B.

3.2.3 Microstructure

In this study we use upper ocean microstructure measurements of the turbulent dissipation of kinetic energy to provide confidence in the shear-strain parameterization used with the EM-APEX float data.

The instrument used is a Rockland Scientific VMP200, an internally-recording tethered profiler. The VMP measurements were taken during RV Southern Surveyor voyages in 2012 (12 stations) and 2013 (18 stations) (Fig. 3.1b and c). At each CTD station along 105°E, in both 2012 and 2013, we measured turbulent dissipation to 300 m depth with a fall rate of 80 cm s^{-1}. Each time the VMP was deployed, we positioned it at the sea surface and then allowed it to free-fall to the limit of the 400 m neutrally-buoyant line, which was run through a free-running block on the stern A-frame of the ship. We allowed a few minutes for the instrument to complete its descent once the rope was fully extended and then hauled the VMP back into the surface. Three such profiles were completed at each station. During the cast, the ship was moving slowly ahead at half to one knot to keep the VMP away from the propellers. Thus the depth range of the instrument was limited to approximately 300 m. The VMP200 sensors included one temperature and two shear probes. The data were processed using the ODAS Matlab toolbox. Dissipation estimates from the three casts at each station were averaged to provide the final dissipation profile at each station.

3.2.4 Auxiliary data

The hourly wind stress data was obtained from the National Centers for Environmental Prediction (NCEP) Climate Forecast System Version2 (Kanamitsu et al., 2002). It is a fully coupled model in which the interaction between atmosphere, ocean, land and sea ice is incorporated. This hourly data has a spatial resolution of $0.5^\circ \times 0.5^\circ$. We use the ETOPO1 (Amante and Eakins, 2009) bathymetry data with a 1-minute arc ($0.01^\circ \times 0.01^\circ$) spatial resolution. The daily sea level anomaly (SLA) and absolute surface geostrophic velocities are distributed by Archiving, Validation, and Interpretation of Satellite Oceanographic data (AVISO) on a $0.25^\circ \times 0.25^\circ$ spatial grid. The float tracks are analysed using the SLA and relative vorticity calculated from AVISO geostrophic velocities to identify float profiles associated with mesoscale eddies.

3.3 Methods

Shear-strain parameterization

In a stationary and homogeneous internal wave field, the rate of energy transfer from large scales to small scales is assumed to be equal to the turbulent dissipation rate (ε) due to internal wave breaking (Gregg et al., 2003; Polzin et al., 2014). Fine-scale parameterization, which operates on a vertical wavelength range that transfers energy between these scales, connects the turbulent dissipation at smaller scales to non-linearity in the internal wave field (Polzin et al., 2014). This method parameterizes the turbulent

dissipation rate from shear (velocity) and strain (density) variances of the internal waves using internal wave-wave interaction theories (McComas and Muller, 1981; Henyey et al., 1986). It parameterizes the net effects of near-inertial shear in transporting energy associated with high frequency waves to dissipation scales (Polzin et al., 2014). There are two major assumptions for this parameterization: 1) most of the mixing in the ocean interior is due to internal wave breaking, 2) the energy cascade due to non-linear interactions of internal waves results in energy dissipation (Waterman et al., 2013; Whalen et al., 2015). Since it is easier to obtain velocity and density measurements in the finescale than microstructure observations, finescale parameterization is frequently used to estimate the turbulent dissipation rate (Polzin et al., 2014).

With these assumptions, the dissipation rate of turbulent kinetic energy can be written as (Gregg, 1989; Polzin et al., 2002; Garabato et al., 2004; Meyer et al., 2015),

$$\varepsilon = \varepsilon_0 \left(\frac{N^2}{N_0^2}\right) \frac{\langle V_z^2 \rangle^2}{\langle V_{z-GM}^2 \rangle^2} \left(\frac{f}{f_0}\right) \frac{cosh^{-1}(N/f)}{cosh^{-1}(N_0/f_0)} \frac{3(R_\omega + 1)}{2R_\omega \sqrt[2]{2(R_\omega - 1)}}, \tag{3.1}$$

where $\varepsilon_0 = 8 \times 10^{-10}$ W kg^{-1}, $N_0 = 3$ cph, $f_0 = 7.836 \times 10^{-5}$ s^{-1}, N is the local buoyancy frequency and f is the local inertial frequency. Here $\langle V_z^2 \rangle$ is the vertical shear variance normalized by N and $\langle V_{z-GM}^2 \rangle$ is the corresponding shear variance predicted by Garrett and Munk (Cairns and Williams, 1976, GM76) model. The angle brackets denote the wavenumber range over which the shear and strain variances are integrated. The range of integration varies from minimum wavenumber to a cutoff value above which the non-linear effects lead to wave breaking (Polzin et al., 2014). The spectrum is integrated from a vertical wavenumber of 0.0026 cpm^{-1} (383 m) to the high wavenumber limit where integrated shear variance reaches $2\pi N^2/10$ (Polzin et al., 2014). When the estimated cutoff wavenumber exceeds the limit of the spectrum, we set it to 12 m (Kurt Polzin, personal comm.), a reasonable limit up to which the non-linear effects are less important.

The shear-strain ratio R_ω is the ratio of horizontal kinetic energy to potential energy for a single wave frequency averaged over a single internal wave's phase (Polzin et al., 2002, 2014). It can be written as

$$R_\omega = \frac{\langle V_z^2 \rangle}{\langle \xi_z^2 \rangle}, \tag{3.2}$$

where $\langle V_z^2 \rangle$ is the vertical shear variance normalized by N. Here ξ_z is the strain, derived as $\xi_z = \frac{N^2 - \langle N_{ref}^2 \rangle}{\langle N_{ref}^2 \rangle}$ where $\langle N_{ref}^2 \rangle$ is the mean squared buoyancy frequency averaged over a horizontal window of 40 profiles with a vertical pressure window of 24 dbar. The local buoyancy frequency, $N^2 = -\frac{g}{\rho_0} \frac{\partial \rho_\theta}{\partial z}$, is estimated

using the adiabatic levelling method (Bray and Fofonoff, 1981). Here ρ_θ is the potential density relative to the sea surface calculated from the EM-APEX salinity, temperature and pressure profiles. The density gradient is estimated using a vertical pressure window of 9 dbar. Low R_ω values at high vertical wavenumber indicate the presence of high frequency internal waves whereas a decreasing ratio with wavenumber indicates the dominance of near-inertial waves (Polzin et al., 2002). In the ocean interior, R_ω generally varies from 5 to 20 (Polzin et al., 1995; Chinn et al., 2016).

In order to determine the direction of propagation of the internal waves, we have used the ratio of counterclockwise (CCW) to clockwise (CW) shear variance (polarisation ratio) (Leaman and Sanford, 1975). A dominance of the CCW polarised shear indicates downward energy propagation with upward phase propagation whereas a dominance of CW polarised shear indicates upward energy propagation with downward phase propagation in the southern hemisphere.

In this study, we use the Mixing (MX) Oceanographic Toolbox for EM-APEX data (Meyer et al., 2014) which combines finescale parameterization of turbulent dissipation rate from both shear and strain methods using hydrographic and velocity data. The dissipation rate and diffusivity from EM-APEX floats and shipboard data are estimated using the toolbox. In the toolbox, a correction was made to the transfer function in the shear variance calculation and also to the input pressure interval that goes into the calculation of N^2 for the float data (K. Polzin, person.comm.).

Fine-scale strain parameterization

Strain-based parameterization has been used to estimate mixing in regional (e.g. Sloyan, 2005) and global studies (e.g. Whalen et al., 2012, 2015, 2018), where strain-based estimates have been found to agree with microstructure measurements within a factor of 2 – 3 in the open ocean. This method is very effective when only the strain (density) information is available. Here we apply the strain parameterization to CTD data collected from the ship.

The dissipation rate for the strain-only parameterization can be written as

$$\varepsilon = \varepsilon_0 \left(\frac{N^2}{N_0^2}\right) \frac{\langle \xi_z^2 \rangle^2}{\langle \xi_{z-GM}^2 \rangle^2} h(R_\omega) L(f,N), \tag{3.3}$$

where ξ_{z-GM}^2 is the GM76 strain variance, $h(R_\omega)$ describes the dependence on shear-strain ratio and $L(f,N)$ is a latitudinal correction (Polzin et al., 1995; Gregg et al., 2003). R_ω is set to 6 based on the R_ω estimates from the EM-APEX profiles which are close in space and time (within 10 – 30 km and about one day) to the CTD measurements. Following Whalen et al. (2012, 2015), we removed buoyancy

frequency values larger than 5 $\times 10^{-4}$ s^{-2} to avoid large buoyancy jumps at the base of the mixed layer, setting these to missing values. We also removed N^2 less than 10^{-9} s^{-2}.

VMP

The dissipation rate of turbulent kinetic energy ε can be estimated from the VMP measurements of vertical shear, $\frac{\partial u}{\partial z}$, as

$$\varepsilon = \frac{15}{2}\nu\overline{\left(\frac{\partial u}{\partial z}\right)^2} = \frac{15}{2}\nu\int_0^{k_{max}} \psi(k)dk \tag{3.4}$$

where ν is the kinematic viscosity calculated from temperature, salinity and density measurements, the overline indicates a spatial average, u is either one of the two horizontal components of velocity, z is the vertical coordinate, $\psi(k)$ is the spectrum of the vertical shear, and k is the vertical wavenumber (Osborn, 1980). The upper limit of integration, k_{max} is variable. Following Shang et al. (2017), the smallest number among the following is chosen as k_{max} in this study: (i) the lowest frequency that shows corruption of the shear signal by vibrations; (ii) wavenumber of 150 cpm, due to the spatial resolution of the shear probe; (iii) the cut-off frequency of the antialiasing filter; (iv) an estimate of the wavenumber that resolves 90% of the shear variance according to the Nasmyth spectrum as in Lueck (2013); and (v) the location of the spectral minimum determined with a low-order fit to the spectrum in log-log space.

Diffusivity

The turbulent eddy diffusivity K_ρ can be estimated from the turbulent dissipation rate ε using the Osborn (1980) relation

$$K_\rho = \Gamma\frac{\varepsilon}{N^2}, \tag{3.5}$$

where Γ is the mixing efficiency, taken as a constant of 0.2.

Mixed layer depth, relative vorticity, potential vorticity and geostrophic velocity

Here we define the mixed layer depth (MLD), as the depth at which the potential density changes by 0.03 kg m^{-3} from the value at 15 m (de Boyer Montegut et al., 2004). The vertical component of the relative vorticity (ζ) can be written as

$$\zeta = \frac{\partial v}{\partial x} - \frac{\partial u}{\partial y}, \tag{3.6}$$

where u (v) is the daily surface geostrophic eastward (northward) velocity component obtained from satellite altimetry. The ζ values are then subsampled at the time and location of each float profile to construct the along-trajectory variations. Similarly, the relative vorticity along the ship tracks was also

estimated. Relative vorticity helps us to identify the mesoscale eddies in the float tracks where southern hemisphere warm (cold) core eddies have positive (negative) ζ values within their perimeter.

The potential vorticity (PV) can be written as $Q = \frac{(f+\zeta)}{\rho}\frac{\partial \rho}{\partial z}$, where f is the planetary vorticity and ζ is the relative vorticity. In regions of weak currents, ζ is negligible and thus the PV can be written as $Q = -(f/\rho)(\partial\rho/\partial z)$. Following Talley (2011) the PV used in this study is $Q = fN^2/g$, where g is the acceleration due to gravity (9.8 m s^{-2}). Since the LADCP velocities had large errors, we have calculated geostrophic velocities from the shipboard CTD data with a level of no motion of 1500 m. This level is an adequate reference level based on watermass properties (Stramma and Lutjeharms, 1997) and climatology of the south Indian Ocean (Menezes et al., 2014).

3.4 Observed watermass structure and circulation

The surface layer in the northern region of the southeast Indian Ocean is dominated by warm (> 22°C), low salinity (< 35.1 psu) tropical water with the temperature-salinity characteristics of LC water (Woo and Pattiaratchi, 2008). Beneath the surface layer is the subtropical underwater (STUW) (Toole and Warren, 1993) and South Indian Central Water (SICW) (Warren, 1981), which are associated with subduction in the subtropics. The STUW can be identified as the shallow salinity maximum layer at around a potential density, σ_θ of 26.0 kg m^{-3} whereas the SICW is the main part of the pycnocline just below STUW. The Subantarctic Mode Water (SAMW), which has a potential vorticity minimum, is found at the bottom of the SICW. The SAMW in the eastern Indian Ocean is stronger and thicker than that in the west and is called the Southeast Indian Subantarctic Mode Water (SEISAMW). The SEISAMW has a characteristic temperature of 8 – 9°C, salinity of 34.55 psu, and σ_θ of 26.8 – 26.9 kg m^{-3} (Thompson and Edwards, 1981; Hanawa and Talley, 2001). The salinity minimum at the base of the Central Water is the Antarctic Intermediate Water (AAIW), typically found at a depth of about 1000 m in the σ_θ range of 27.0 –27.3 kg m^{-3} (Talley, 2011).

3.4.1 Shipboard observations

The mesoscale eddies along the ship tracks can be identified from daily maps of SLA and relative vorticity. In 2012, the ship sampled two warm core eddies along 105°E with VMP, and CTD measurements (Fig. 3.2a-d). The warm core eddy with centre at station 26 (WC1[1]) is smaller than that at station 21 (WC2). WC1 has weak signature in the SLA (0.2 m) compared to WC2 (0.45 m). However, both have similar relative vorticity signatures (1×10^{-5} s^{-1}). The SLA plots show that WC1 was a small eddy

[1]The eddy names are independent for both floats and shipboard data

detaching from WC2 during the sampling (not shown). Both eddies carried warm and fresh LC water in their centre (Fig. 3.2b and c). Higher geostrophic speed is observed at the edges of the eddies up to a depth of about 600 m (Fig. 3.2d). The isopycnals are affected up to a depth of about 2000 m especially for WC2. WC2 has a deeper mixed layer (160 m) than WC1 (70 m). The different watermasses along the track can be identified from the temperature and salinity data. The warm core eddies carry fresh and warm water above the salinity maximum of STUW. The AAIW is observed between 800 – 1000 m as a salinity minimum between 27.1 – 27.3 kg m^{-3} (Fig. 3.2c). The warm cores push down the AAIW to a slightly deeper depth ($\sim$ 8 m). The SAMW does not have a salinity signature and can be identified as a potential vorticity minimum (less than 1 $\times 10^{-10}$ $(ms)^{-1}$), above the AAIW between 26.7 – 26.9 kg m^{-3}, in a depth range of 300 – 700 m (Fig. 3.2f). The thickness of the AAIW layer does not change much in the warm core eddies whereas the SAMW layer considerably shrinks at the centre of the cyclonic eddy. The buoyancy frequency is high at the base of the mixed layer and also below the lower layer of SAMW (Fig. 3.2e).

In 2013, the transect along 105°E was repeated with VMP and CTD measurements (Fig. 3.2g-l). The EM-APEX floats were deployed in this voyage along the transect (Fig. 3.1c). The ship sampled a cyclonic eddy which had a significant signature in SLA and relative vorticity. The isopycnals are affected below 400 m with less or no impact near the surface. At the centre, the cyclonic eddy carries warm water of about 20°C and slightly less saline water than STUW. From station number 52 – 55, the surface waters are warmer and fresher compared to the centre of the cold core eddy. The sea level anomaly plots shows the presence of a warm core eddy at this location which was not fully developed (Fig. 3.1c) with no signature in relative vorticity (Fig. 3.2g) and no deepening of isopycnals associated with the warm and fresh water at the surface between stations 52 and 55 (Fig. 3.2h and i). The AAIW is observed at the same depth as in 2012 except in the cyclonic eddy. At the centre of the eddy, SAMW is uplifted to a depth of about 400 m and AAIW to a depth of about 600 m. The thickness of the SAMW layer is significantly reduced at the centre of the cyclonic eddy. The cold core eddy upwells cold and fresh water from depth whereas the warm core eddy brings fresh waters from the coast and downwells the salty waters of the eastern south Indian Ocean (SIO). The CTD data in 2013 extends to the sea floor up to a depth of about 5000 m (Fig. A.3) and this data will be used to explore the impact of topography on the turbulent mixing estimates in the deep ocean in Section 3.6.3.

3.4.2 Floats

The floats were strongly influenced by the eddy field at different times in their track (Fig. 3.3). The float profiles are presented as time series with a vertical line separating each float. The horizontal axis

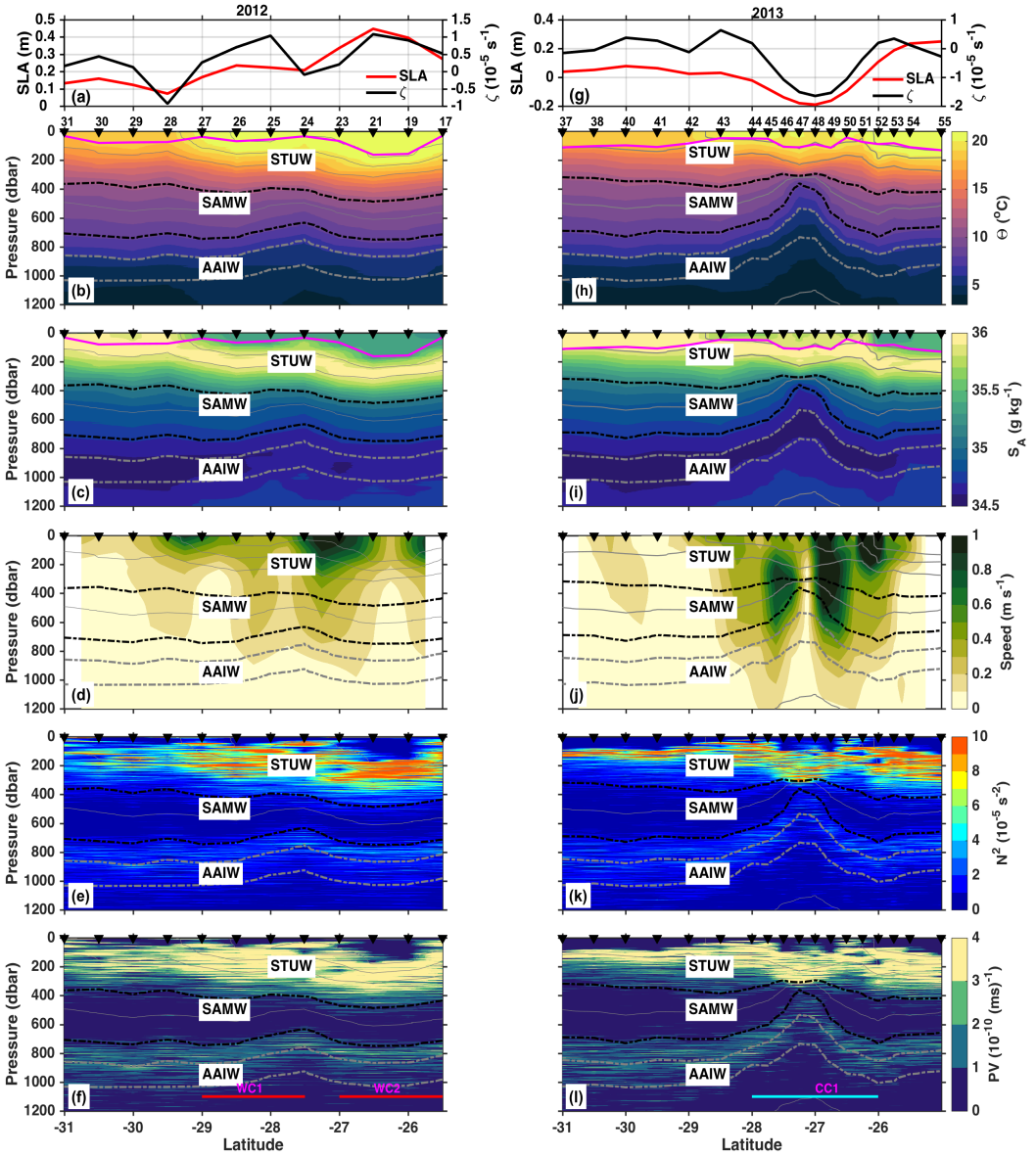

Figure 3.2: The evolution of a) sea level anomaly (red) and relative vorticity (black) b) conservative temperature c) absolute salinity d) geostrophic speed e) buoyancy frequency and f) potential vorticity in 2012. The light grey lines are isopycnals with an interval of 0.7 kg m^{-3}. Panels g), h), i), j), k) and l) are the same for 2013. Station numbers are marked at the top of conservative temperature (b and h). The heavy grey contours in all panels show the density range of AAIW (27.1 – 27.3 kg m^{-3}) and heavy black lines show SAMW (26.7 – 26.9 kg m^{-3}). The STUW is the high salinity near-surface water. In 2012, there were two warm core eddies (WC1 and WC2) and a cold core eddy (CC1) in 2013. The evolution of the mixed layer along the ship tracks are marked over temperature and salinity (magenta line).

is cumulative profile number, which represents both distance along the trajectory and time, but allows a uniform spacing between profiles. The SLA and relative vorticity along the float tracks identify the eddies comparatively well irrespective of their coarse resolution. EM-6662 was deployed in the cold core eddy centered at station 47 (Fig. 3.1c). This float looped around the eddy and moved south with the eddy. After a while, EM-6662 came out of that cyclonic eddy (CC1) and started to profile around another cyclonic eddy (CC2) until its battery died. The isopycnals in CC2 were more strongly uplifted

at depths below 300 m suggesting that it is a subsurface-intensified eddy. The SAMW and AAIW were uplifted to shallow depths as in the shipboard data. CC2 has stronger velocities compared to CC1 which extends to the depth of AAIW (Fig. 3.3d).

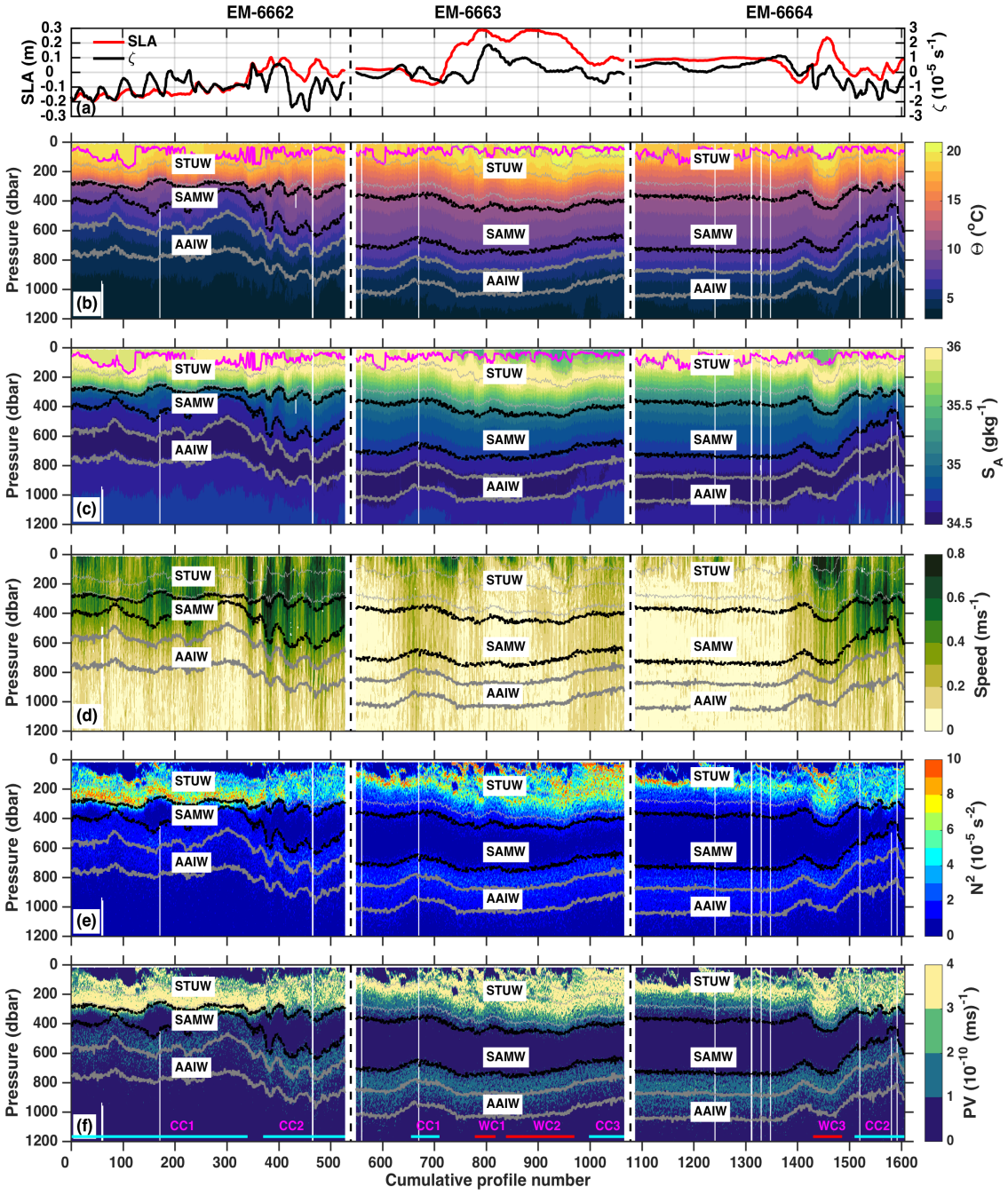

Figure 3.3: Same as in Fig. 3.2 but along the float tracks. EM-6662 profiled two cold core eddies (CC1 and CC2). EM-6663 profiled two warm core eddies (WC1 and WC2). EM-6664 profiled another warm core (WC2) and the same cold core eddy in EM-6662 (CC2). The evolution of the mixed layer along the float tracks are marked over temperature and salinity (magenta line). The numbering of the eddies are different from Fig. 3.2. The X-axis is cumulative profile number which represents the evolution in time. The light grey lines are isopycnals at every 0.7 kg m^{-3}.

The other two deep floats (EM-6663 and EM-6664) were deployed downstream of the eddy CC1 (Fig.

3.1c). EM-6663 continuously profiled towards the north through the western flank of CC1 and the southern edge of two warm core eddies (WC1 and WC2). It then profiled around the western edge of another cyclonic eddy, CC3. The presence of WC1 and WC2 is more evident from SLA and relative vorticity with little impact on the deeper isopycnals. On the contrary, CC1 and CC3 have less surface signature in SLA and relative vorticity with shoaling of isopycnals at depths below 400 m.

EM-6664 profiled north for a while without interacting with any eddy and this is evident from the SLA and relative vorticity along its track. It then profiled the southern edge of a big warm core eddy (WC3) with a big signature in SLA and weak relative vorticity, and was then caught up in the same cyclonic eddy (CC2) that trapped EM-6662. The eddy carries fresh and warm LC water in its centre with a deep mixed layer. Deepening of isopycnals was evident to below 1200 m in the warm core.

The floats provide a finer picture of the different watermasses in this region than the ship based CTD data. Warm, salty subtropical underwater (STUW) lies at the surface in profiles south of around 26°S. North of 25°S the STUW is found beneath the warmer fresher waters of the Indonesian - Australian basin, which is supplied by the Indonesian Throughflow (Fig. 3.3b and c, EM-6663). In warm core eddies, the STUW is capped by a warm fresh layer that is possibly LC water that was trapped during the formation of the eddy close to the Australian coast (Morrow et al., 2003; Mao et al., 2018). The thickness of the SAMW layer varies considerably along the tracks of EM-6662 and EM-6664 when they encountered cyclonic eddies (Fig. 3.3e and f). The AAIW layer also was uplifted to shallower depths by the cyclonic eddies. The impact of eddies on the depths of different watermasses is clearly visible from the track of EM-6664.

3.5 Mixing variability in the upper 1000 m

3.5.1 Microstructure

The microstructure measurements from 2012 and 2013 show that diffusivity is highly variable in the upper 300 m (Fig. 3.4a and c). We observe a similar pattern for the dissipation rate as well (Fig. A.4). In both 2012 and 2013, we observe enhanced diffusivity within the mixed layer as expected. Below the mixed layer, the diffusivity falls to background levels with a change of about 3 – 4 orders of magnitude with depth. The mean values of dissipation rate and diffusivity at different depth ranges and in different eddies is given in table 3.1. The mean dissipation rate in 2012 is higher than that in 2013. However, the mean diffusivity is higher during 2013. The surface diffusivity in WC1 is slightly higher (9.8×10^{-4} m^2s^{-1}) than that in WC2 (3.8×10^{-4} m^2s^{-1}). The elevated diffusivity at the centre of WC1 is more spatially distributed to the base of the mixed layer whereas in WC2, the elevated mixing does not extend

that deep (Fig. 3.4a). The dissipation rate in the mixed layer of the cyclonic eddy in 2013 is weaker than that of the warm core eddies of 2012 (Table 3.1) .

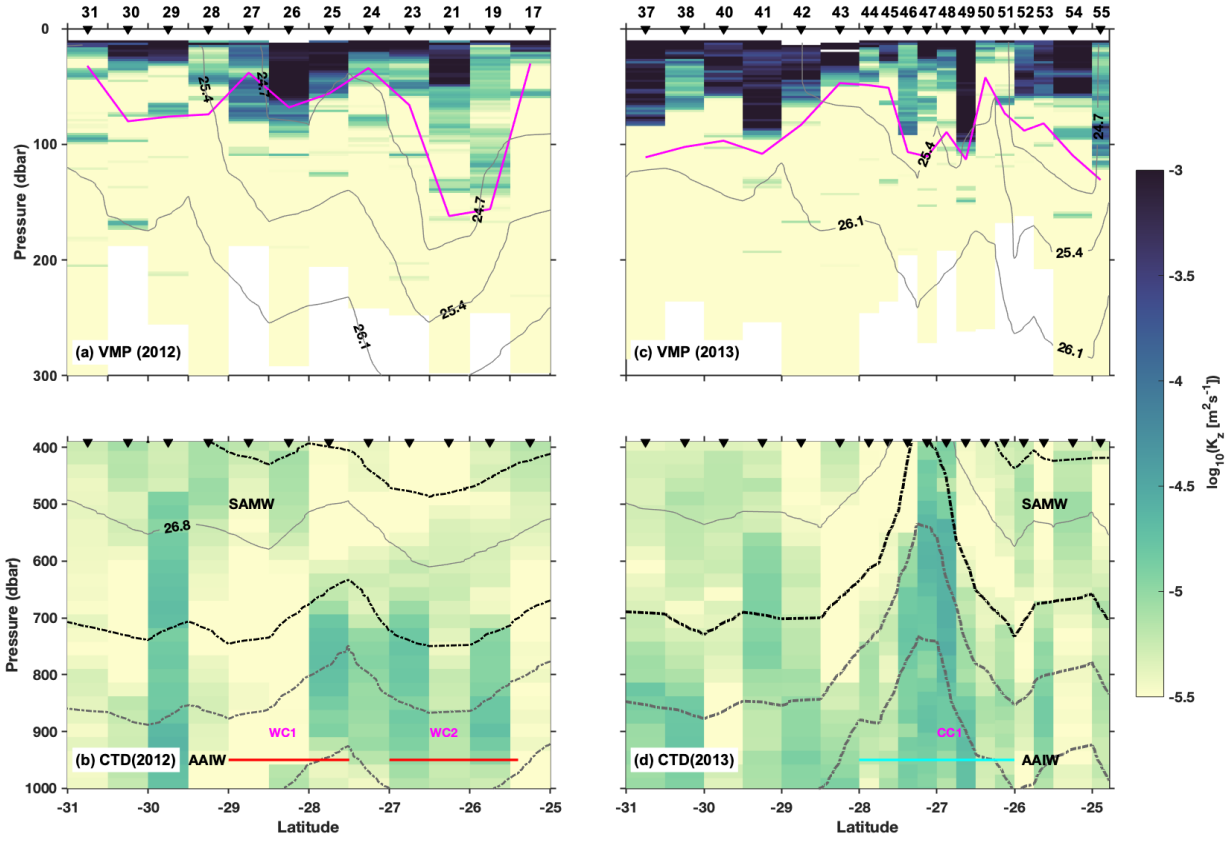

Figure 3.4: Diffusivity along 105°E ship tracks during 2012 (left panels) from a) VMP and b) strain-only parameterization (CTD). The panels on the right side (c and d) are the same during 2013. The grey contours are isopycnals at every 0.7 kg m^{-3}. The magenta line on the upper panels are MLD during both years. The watermasses and eddies are same as in Fig. 3.2.

Depth	Dissipation rate		Diffusivity	
	2012	2013	2012	2013
ML	2.3×10^{-8}	4.3×10^{-8}	8.8×10^{-4}	1.6×10^{-3}
ML warm core	2.8×10^{-8}	–	1.0×10^{-3}	–
ML cold core	–	1.5×10^{-8}	–	2.6×10^{-3}
0 – 300 m warm	5.9×10^{-9}	–	1.8×10^{-4}	–
0 – 300 m cold	–	4.5×10^{-9}	–	5.6×10^{-4}
0 – 300 m total	4.9×10^{-9}	1.1×10^{-8}	1.5×10^{-4}	4.0×10^{-4}

Table 3.1: Mean dissipation rate and diffusivity at different depth ranges from VMP for 2012 and 2013 in both cold core and warm core eddies.

3.5.2 Shipboard CTD

The diffusivity estimates from the shipboard CTD data between 400 – 1000 m also show spatial variability over the transects and with depth (Fig. 3.4b and d). In 2012, the mean diffusivity from the strain-only method is 6.6×10^{-6} m^2s^{-1} with a standard deviation of 1.9×10^{-6} m^2s^{-1}. The diffusivity is slightly elevated below 700 m in the warm core eddies, WC1 and WC2 (9.1×10^{-6} m^2s^{-1}) and is slightly higher than that in 2012. The mean diffusivity in 2013 is 7.4×10^{-6} m^2s^{-1} with a standard deviation of 1.7 $\times 10^{-6}$ m^2s^{-1}. The diffusivity is elevated in the cyclonic eddy in 2013 above 1000m and also near the bottom (Table 3.2). In the cyclonic eddy, the diffusivity is elevated in the AAIW layer whereas the diffusivity is one order magnitude less in the SAMW layer.

Depth	Dissipation rate		Diffusivity	
	2012	2013	2012	2013
400–1000 warm	4.2×10^{-10}	–	6.1×10^{-6}	–
400–1000 cold	–	6.0×10^{-10}	–	1.1×10^{-5}
400–1000 all	4.3×10^{-10}	4.4×10^{-10}	6.6×10^{-6}	7.4×10^{-6}
1000-bottom cold	–	2.1×10^{-10}	–	3.5×10^{-5}
1000-bottom all	–	1.7×10^{-10}	–	1.9×10^{-5}
SAMW warm	3.4×10^{-10}	–	4.8×10^{-6}	–
SAMW cold	–	8.1×10^{-10}	–	5.8×10^{-6}
SAMW all	3.3×10^{-10}	4.3×10^{-10}	5.3×10^{-6}	5.0×10^{-6}
AAIW warm	5.4×10^{-10}	–	8.0×10^{-6}	–
AAIW cold	–	8.5×10^{-10}	–	1.5×10^{-5}
AAIW all	5.8×10^{-10}	6.0×10^{-10}	8.8×10^{-6}	9.7×10^{-6}

Table 3.2: Mean dissipation rate and diffusivity at different depth ranges from strain-only parameterization in both cold core and warm core eddies.

3.5.3 Floats

The dissipation rate and diffusivity estimates from the float data using the shear-strain parameterization also shows strong variability between 200 – 1000 m (Fig. 3.5). Regions of enhanced dissipation rate is associated with Ri< 0.25 (Fig. 3.5a), where Ri is a non-dimensional parameter called Richardson number [$Ri = N^2/(\frac{\partial u}{\partial z})^2$, where $\frac{\partial u}{\partial z}$ is the vertical shear of the horizontal speed]. This suggests that in these regions the shear can overcome stratification and overturning can occur. The mean dissipation rate from the floats is 9.4×10^{-10} W kg^{-1} which is in the background levels observed in mid- and low- latitudes of the global ocean (St. Laurent et al., 2012). The floats have a mean diffusivity of 1.7×10^{-5} m^2s^{-1} with a standard

deviation of 4.6×10^{-5} m^{2}s^{-1}. Mesoscale eddies play an important role in the spatial distribution of diffusivity. Comparatively high diffusivity is observed in cyclonic eddies at subsurface (CC1 and CC2) and in warm core eddies near the surface (WC1, WC2 and WC3) (Fig. 3.5b, Table 3.3). Diffusivity is elevated below 250 m in EM-6662 which was caught up in two cyclonic eddies (e.g. 1.5×10^{-4} m^{2}s^{-1} for profiles from 85 – 120). In EM-6663, diffusivity is mostly on background levels ($O(10^{-6})$ m^{2}s^{-1}). EM-6664 has weak diffusivities at the earlier part of its track (2.8×10^{-6} m^{2}s^{-1}), which become elevated in the warm core eddy in the upper 350 m and in the cyclonic eddy below 250 m (Table 3.3). This is in agreement with the elevated diffusivity observed in both cyclonic and anticyclonic eddies from the VMP and shipboard data. The elevated mixing near the surface ($\sim$ 200 m) and subsurface ($\sim$ 500 m) is often associated with higher values of R_ω suggesting the presence of near-inertial waves (Fig. 3.5c).

Depth	Dissipation rate			Diffusivity		
	$EM-6662$	$EM-6663$	$EM-6664$	$EM-6662$	$EM-6663$	$EM-6664$
250–350m warm	–	1.1×10^{-9}	2.3×10^{-9}	–	5.3×10^{-6}	1.2×10^{-5}
250–350m cold	9×10^{-10}	4.1×10^{-10}	4.9×10^{-10}	5.4×10^{-6}	2.5×10^{-6}	3.7×10^{-6}
250–350m all	9.4×10^{-10}	6.7×10^{-10}	6.6×10^{-10}	5.6×10^{-6}	3.9×10^{-6}	4.9×10^{-6}
250–1000m warm	–	3.8×10^{-10}	6.4×10^{-10}	–	3.6×10^{-6}	5.8×10^{-6}
250–1000m cold	1.9×10^{-9}	2.1×10^{-10}	1.9×10^{-9}	3.8×10^{-5}	2.6×10^{-6}	4.0×10^{-5}
250–1000m all	1.9×10^{-9}	2.6×10^{-10}	6.1×10^{-10}	3.8×10^{-5}	2.9×10^{-6}	1.1×10^{-5}
SAMW warm	–	1.4×10^{-10}	1.5×10^{-10}	–	2.0×10^{-6}	2.4×10^{-6}
SAMW cold	7.4×10^{-10}	1.8×10^{-10}	4.9×10^{-10}	6.1×10^{-6}	2.8×10^{-6}	5.7×10^{-6}
SAMW all	7.7×10^{-10}	1.4×10^{-10}	2.1×10^{-10}	6.2×10^{-6}	2.2×10^{-6}	3.3×10^{-6}
AAIW warm	–	2.3×10^{-10}	4.7×10^{-10}	–	3.2×10^{-6}	6.9×10^{-6}
AAIW cold	3.5×10^{-9}	2.1×10^{-10}	3×10^{-9}	6.4×10^{-5}	3.2×10^{-6}	5.6×10^{-5}
AAIW all	3.4×10^{-9}	2.2×10^{-10}	8.1×10^{-10}	6.2×10^{-5}	3.2×10^{-6}	1.4×10^{-5}

Table 3.3: Mean dissipation rate and diffusivity at different depth ranges from all three floats in both cold core and warm core eddies.

3.6 Mixing distribution and influencing factors

Here we investigate the factors that influence the observed mixing variability from floats, shipboard CTD and VMP. The potential candidates are wind stress at the surface, mesoscale eddies and bottom topography, with internal wave propagation upward or downward depending on the source, and reflections from the boundaries. There are examples of enhanced dissipation throughout the water column, in Fig. 3.5, some near the sea surface, most likely to be generated by wind forcing, and some in the deep.

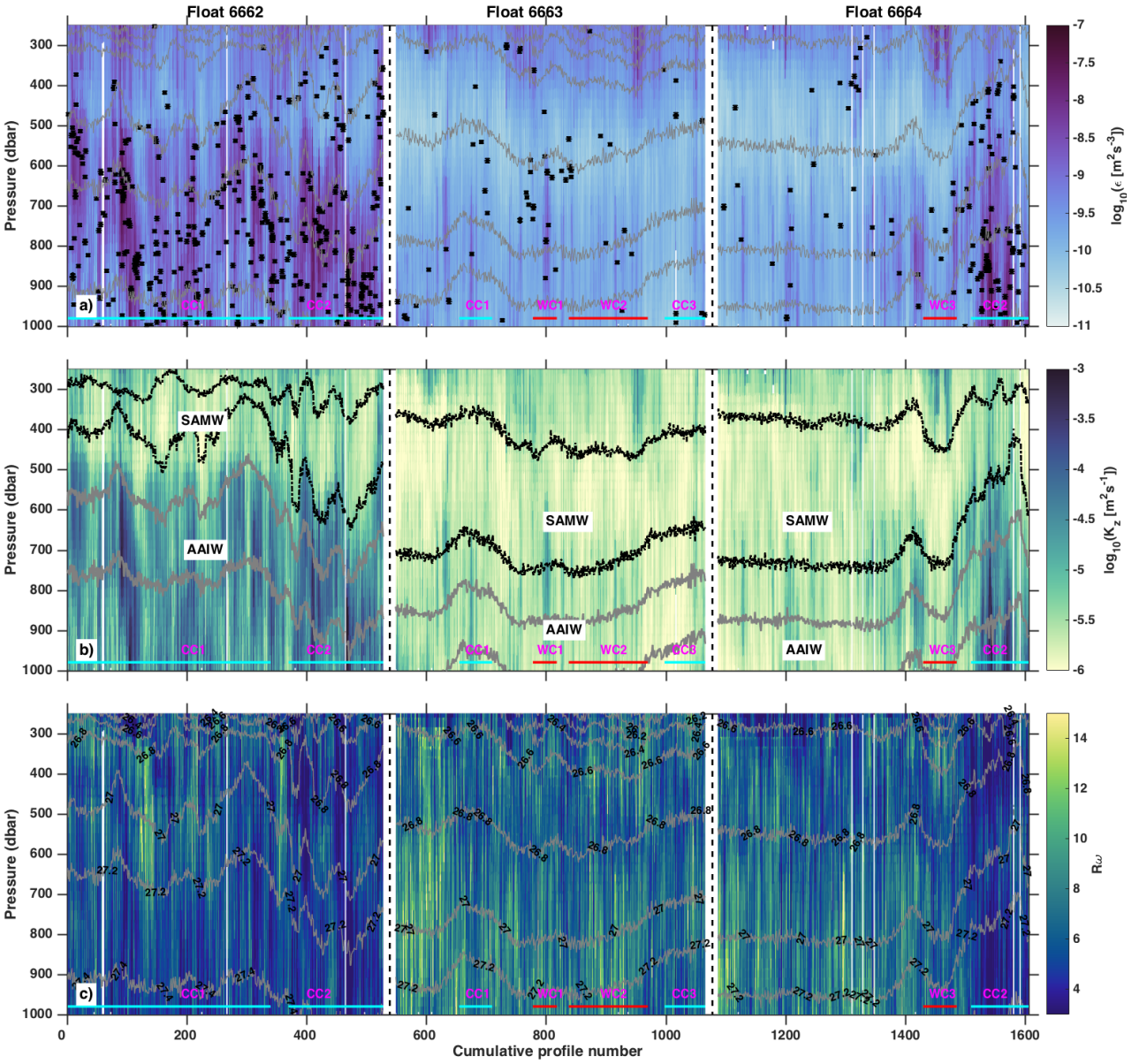

Figure 3.5: The evolution of a) dissipation rate, b) diffusivity and c)shear-strain variance ratio along the float tracks. The watermasses, eddies and isopycnals are same as in Fig. 3.3. The black contours in a) marks the regions with Ri< 0.25.

3.6.1 Wind stress

The wind blowing over the ocean surface generates near-inertial waves that propagate downward into the ocean interior (Alford, 2003). These waves are expected to provide a major portion of the energy needed to support the global overturning circulation (Munk and Wunsch, 1998). From the float data, we have identified many vertically propagating near-inertial waves (Chapter 2). Here we investigate the impact of wind forcing on turbulent mixing estimates.

In the mixed layer, the impact of internal wave breaking may be less important where air-sea interaction

and mesoscale eddies dominate turbulent mixing compared to the ocean interior (Garrett, 2003). However, there are studies showing direct relationship between wind speed and microstructure-measured dissipation rate in the mixed layer (e.g. Oakey and Elliott, 1982; Greenan et al., 2001). We thus looked at the wind stress and diffusivity in the mixed layer in 2012 and 2013. VMP measurements show elevated diffusivity in the mixed layer (Fig. 3.6a and b) as expected. In 2012 and 2013, the wind stress values were quite weak (0.1 – 0.2 N m^2) at the time and location of the VMP measurements. We looked at the surface maps of wind speed during the time of VMP measurements in 2013 and found that there was a strong wind system passing over the region from the south at the beginning of the transect (not shown). This wind system may have contributed to the turbulence measured by the VMP in addition to other mixed layer processes such as night-time convection.

The floats provide mixing estimates only below the mixed layer. Thus we look at the distribution of mixing in the upper 350 m and the wind stress at each float location to find evidence of wind-driven mixing due to breaking of wind-generated near-inertial waves (Fig. 3.6c). The wind in this region has an equatorward component throughout the year (Godfrey and Ridgway, 1985) which is stronger during austral summer (McCreary et al., 1986). For the southeast Indian Ocean, TropFlux is the best reanalysis product (Chapter 4). However, since TropFlux is limited to north of 30°S and some of the float profiles are south of 30°S, we use NCEP wind product to have a full record. Since the floats profiled for about four months, they encountered both weak and a few strong (> 0.5 N m^2) wind events. More than 250 float profiles were collected from locations of strong wind events where the wind stress is larger than two standard deviations. Elevated diffusivity is often observed below the mixed layer following strong wind events in regions of non-eddy activity (e.g. profiles between 590 – 650), as well as in a warm core eddy (e.g. profiles between 1450 – 1460) and a cold core eddy (e.g. profiles between 380 – 400).

To investigate the impact of wind stress on mixing below the mixed layer, we further zoomed in on float profiles between 572 – 660 that spanned over about 15 days and looked at the wind stress, depth averaged diffusivity and polarization ratio in the upper 400 m (Fig. 3.7). We observe three strong wind events in the float track during this time window (Fig. 3.7a). The depth averaged diffusivity is elevated above the mean value approximately 2 – 3 days after each wind event (Fig. 3.7b). Higher polarization ratio is also observed corresponding to the elevated diffusivities (Fig. 3.7c). Strong near-inertial wave beams with amplitudes larger than 20 cm s^{-1} are observed at the same location as this higher diffusivity (Chapter 2). This suggests that the strong wind events generated downward propagating near-inertial internal waves in the mixed layer and they dissipated below the mixed layer after 4 – 5 days. The time lag between wind forcing and the dissipation rate is similar to the 2 – 5 days delay observed in the Southern Ocean from EM-APEX floats (Meyer et al., 2015).

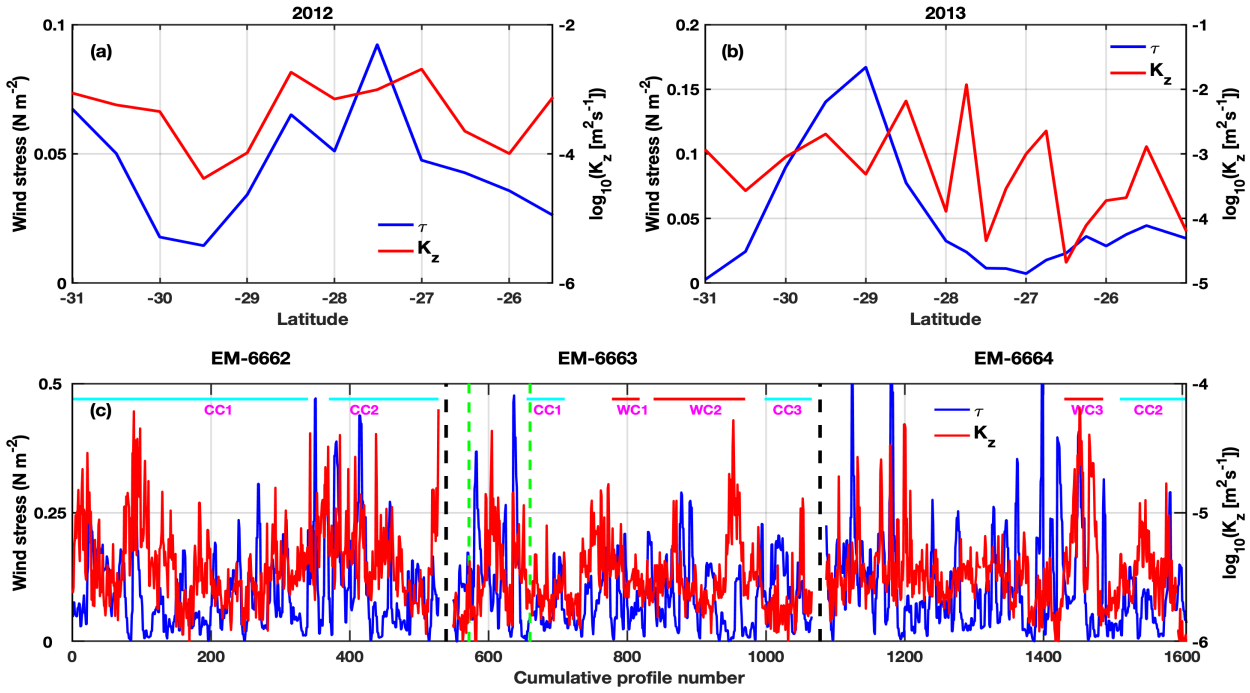

Figure 3.6: Mean diffusivity (red line) in the mixed layer and wind stress measured from the ship (blue line) during a) 2012 and b) 2013 along the transects. Mean diffusivity (red line) in the depth range 250 – 350 m along the float tracks and NCEP wind stresses (blue) at the time and location of the floats. The green dashed vertical lines represent the profiles which are examined in figure 3.7.

We then compared the wind stress with the mean dissipation rate in the mixed layer from VMP measurements and below the mixed layer from float measurements. The linear relationship between the mean dissipation rate in the mixed layer and wind stress is weak with a correlation of 0.13 in 2012 whereas it is quite strong with a correlation of 0.67 in 2013 (Fig. 3.8a). However, in both years the relationship is positive suggesting that the wind stress could be a possible contributor to the observed turbulence. We also looked at the relation between wind stress and dissipation rate estimates below the mixed layer from floats (Fig. 3.8b). Here we colored the float estimates by the magnitude of the polarisation ratio. There is no direct relationship between wind stress and dissipation rate at this depth range. There is a weak tendency for high dissipation rate estimates to be associated with high wind stress. In addition, most of the dissipation rate in this depth range is associated with downward propagating waves reinforcing the idea of surface wave generation.

3.6.2 Mesoscale eddies

The propagation of near-inertial waves generated at the ocean surface can be influenced by mesoscale eddies. Previous studies show elevated dissipation rate associated with anticyclonic eddies in the upper part of the water column (e.g. Sheen et al., 2015; Meyer et al., 2015; Whalen et al., 2018). Here we

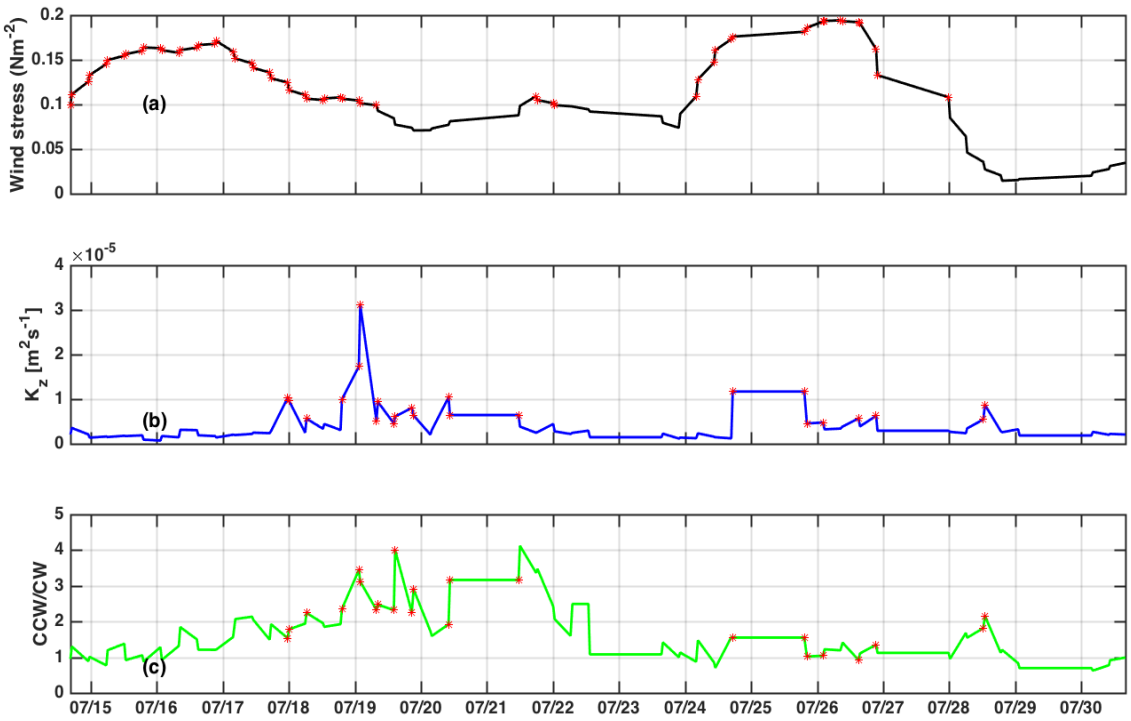

Figure 3.7: a) Smoothed wind stress, depth-averaged b) diffusivity and c) polarisation ratio in the upper 400 m over a period of 15 days along the track of the float EM-6663 between profiles 572 – 660. The red stars on (b) and (c) are values above the mean.

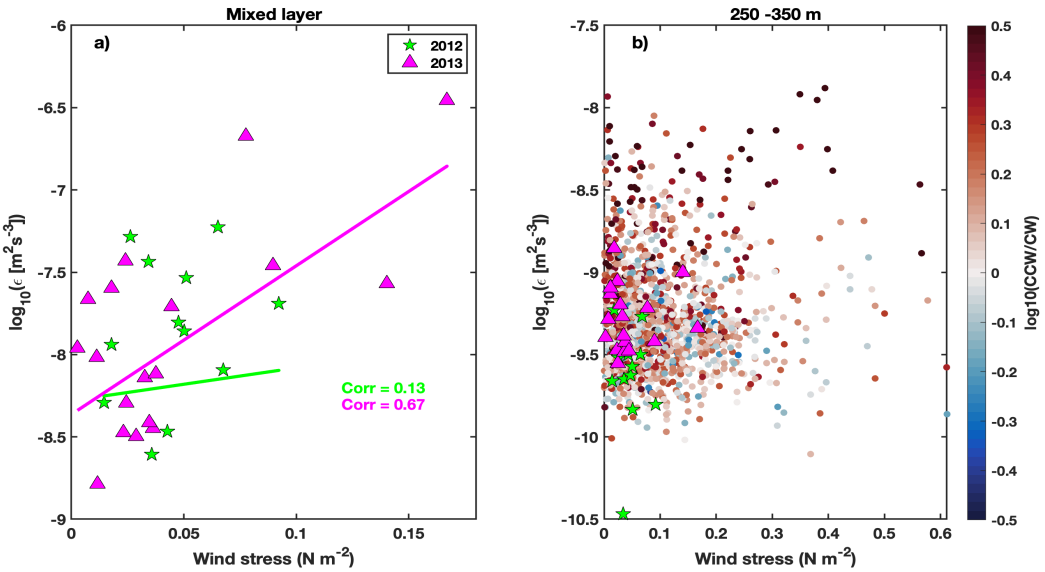

Figure 3.8: Scatter plot of wind stress and mean dissipation rate from VMP in 2012 (red stars) and 2013 (black triangles) a) in the mixed layer and b) below the mixed layer between 250 – 350 m. The open circles in b) are the mean dissipation rate from the floats and are colored by the polarisation ratio.

investigate the diffusivity estimates associated with both cyclonic and anticyclonic eddies in the float data. From the floats we have collected 1566 profiles among which 231 profiles are associated with

warm core eddies and 721 profiles are in cold core eddies.

In the upper 400 m, higher dissipation rate is observed in the region of warm core eddies (Fig.3.9a, Table 3.3). The dissipation rate in cyclonic eddies at this depth range is lower than the warm core eddies and is close to the mean value. For instance, the mean dissipation rate in the upper layer of warm core eddy (WC3) in float EM-6664 is 2×10^{-9} $m^2 s^{-3}$, which is four times larger than that in the cyclonic eddy CC2 (5×10^{-10} $m^2 s^{-3}$) and ~ 3 times larger than the mean dissipation rate in the upper layer of float EM-6664 (7×10^{-10} $m^2 s^{-3}$). It is also two times larger than the overall mean dissipation rate from the floats (9×10^{-10} $m^2 s^{-3}$). We see a similar distribution for the diffusivity in the upper 400 m (Fig. 3.9b). We also looked at the direction of vertical propagation of the waves corresponding to the dissipation rate distribution. The polarisation ratio in the warm core eddies in the upper 400 m (Fig. 3.9c) shows that the downward propagating waves dominate at this depth range. It suggests that the elevated dissipation rate in the upper 400 m of the warm core eddies is associated with downward propagating waves. The shear-to-strain variance ratio is also enhanced in the upper 400 m of the warm core eddy (Fig. 3.9d) suggesting that the elevated mixing in the anticyclonic eddies near the surface is associated with near-inertial waves. The elevated mixing in the anticyclonic eddies is consistent with the near-inertial wave beams identified from the same data set due to wave trapping by the relative vorticity of the anticylonic eddy (Chapter 2). We observe elevated diffusivity in warm core eddies ($O(10^{-4})$ m^2 s^{-1}) in the upper 300 m from VMP measurements as well (Table 3.1). From the strain parameterization, we see weak mixing ($O(10^{-6})$ m^2 s^{-1}) below 400 m where the influence of warm core eddies is less (Table 3.2).

In a cold core eddy, the waves generated at the surface can freely propagate out of the eddy. However, they cannot penetrate into the core of a cold core eddy from outside (Kunze, 1985). In the case of a cold core eddy, waves can be trapped outside the high velocity region where the vorticity changes sign (Sanford, 1984; Kunze, 1985). It is a region where the horizontal strain of the mesoscale field dominates vorticity (Polzin, 2008). From the float data, higher dissipation rate is observed in cyclonic eddies below 500 m compared to the upper water column (Fig. 3.9a). The dissipation rate is higher (2.2×10^{-9} $m^2 s^{-3}$) than that observed in warm core eddies (2.2×10^{-10} $m^2 s^{-3}$) and also higher than the mean value at this depth range, with a similar distribution for diffusivity (Fig. 3.9b). The polarization ratio is higher below 500 m in the cyclonic eddies compared to the upper water column (Fig. 3.9c). Coherent features in velocity profiles with upward phase propagation (downward energy propagation) are also observed corresponding to the elevated dissipation rate in the cyclonic eddies (Chapter 2, Fig. 2.8). This suggests that the higher dissipation rate in the cyclonic eddies below 500 m is associated with downward propagating waves. This result is in contrast to Richardson et al. (1979) where they observed upward propagating internal waves in a cyclonic eddy. The corresponding shear-to-strain variance ratio

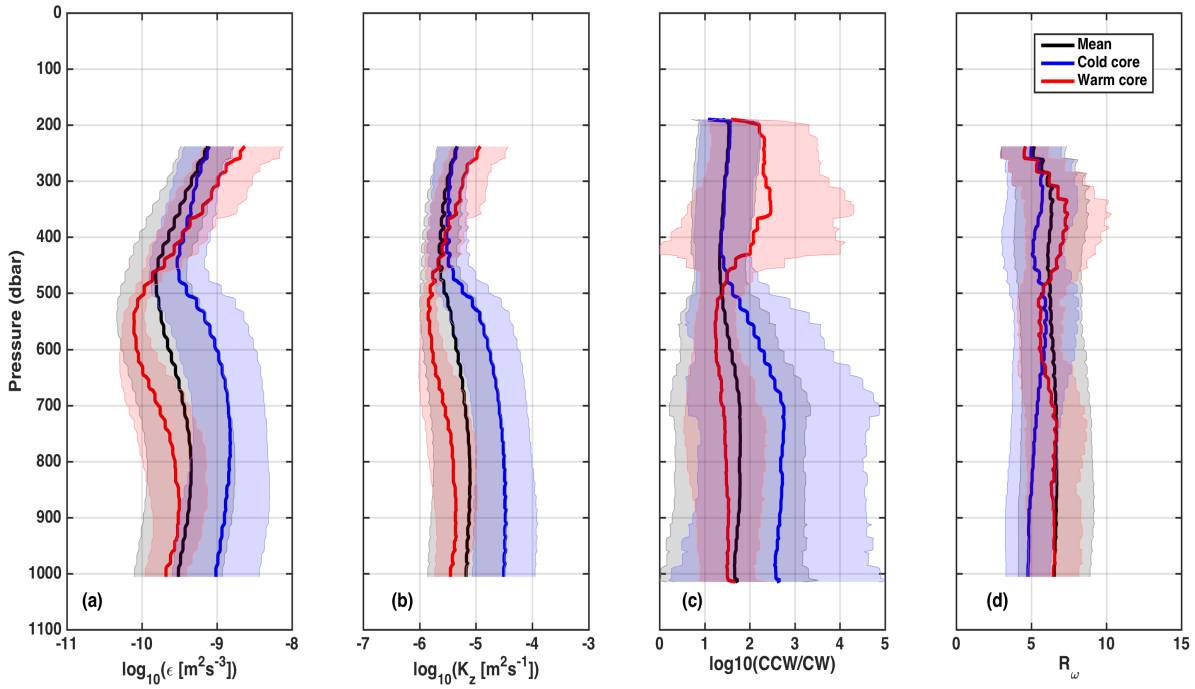

Figure 3.9: Vertical distribution of a) dissipation rate, b) diffusivity, c) polarization ratio, and d) shear-strain variance ratio in regions of cold cores (blue) and warm cores (red) along with the mean (black) value from the float estimates. The shading is one standard error.

is also lower for the coherent features than that near the surface (Fig. 3.9d). Also these coherent features were not identified from the complex demodulation of the near-inertial waves. This suggests that the elevated dissipation rate could be due to waves with frequencies outside the near-inertial band. The downward propagating coherent features may be generated near the surface (e.g. Dasaro, 1985; Leaman and Sanford, 1975).

The features in the cyclonic eddies associated with high dissipation rate could be due to capturing of internal waves by the mesoscale eddy strain field (Buhler and McIntyre, 2005; Polzin, 2008). The capture of internal waves occurs when the strain exceeds relative vorticity. The vertical and horizontal wavenumbers of the internal waves captured by the eddy strain field will grow in magnitude and dissipate eventually (Polzin, 2008). We observe that the higher vertical wavenumber features correspond to higher dissipation rate (not shown). This suggests that the elevated diffusivity could be due to wave capturing by the eddy strain field.

3.6.3 Topography

Elevated mixing is often observed near bottom topography when strong geostrophic flow or tides interact with rough topography (e.g. Waterman et al., 2013). Here we examine the distribution of dissipation rate

and diffusivity near bathymetry from shipboard CTD in 2013 using a strain-only parameterization since the LADCP data were not reliable. On average, the bathymetry in this region is 5000 m deep (Fig. 3.10a) consisting of small seamounts (Fig. A.5). The diffusivity is highly variable throughout the water column due to the patchy and intermittent nature of mixing. Elevated diffusivity is observed near bottom especially in the region of the cyclonic eddy. Although we have only a few full-depth profiles in the cyclonic eddy, the elevated diffusivity is observed almost throughout the water column below 500 m in the eddy in agreement with the shear-strain parameterization estimates from the float data.

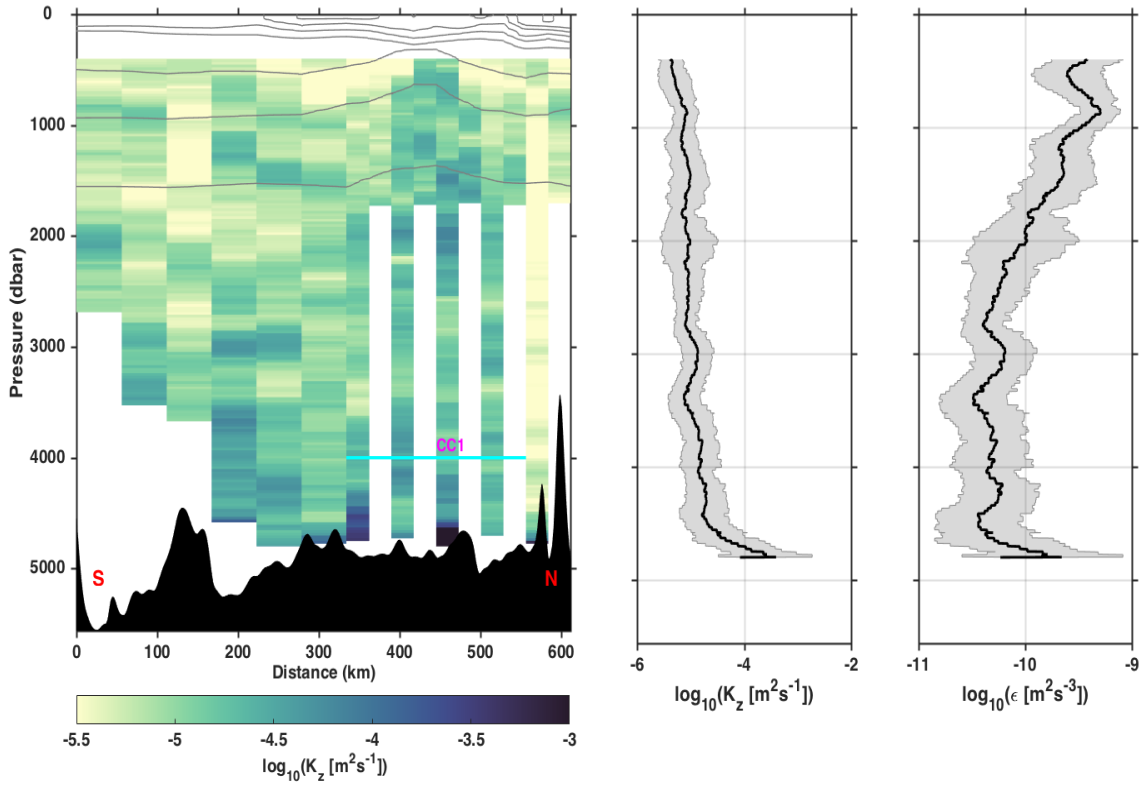

Figure 3.10: a) Estimates of diffusivity along the 105°E transect in 2013 using strain-only method. The X-axis is the distance along the transect from the southernmost station (31°S). The grey lines are the isopycnals in every 0.4 kg m $^{-3}$. The cyclonic eddy is also marked. b) The vertical profile of mean diffusivity for the transect with one standard deviation shading.

The mean diffusivity is fairly low throughout the water column ($O(10^{-5})$ m^2 s^{-1}) except in the bottom-most 1000 – 1500 m where it is elevated ($O(10^{-3})$ m^2 s^{-1}) (Fig. 3.10b). The overall mean diffusivity of the transect is 1.7×10^{-5} m^{2}s^{-1} with a standard deviation of 6.2×10^{-5} m^{2}s^{-1}. The mean diffusivity in the cyclonic eddy is 2.5×10^{-5} m^{2}s^{-1} with 2.3×10^{-4} m^{2}s^{-1} in the bottom 1000 m. The turbulent dissipation rate is also elevated near the bottom and in the upper 1000 m (Fig. 3.10c). The mean dissipation rate for the region, 2.2×10^{-10} m^{2}s^{-3} is quite weak with a standard deviation of 9.9×10^{-11} m^{2}s^{-3}. The cyclonic eddy has a mean dissipation rate of 3.1×10^{-10} m^{2}s^{-3} with a standard deviation of

1.2×10^{-10} m^{2}s^{-3} in the bottom 1000 m. A more detailed breakdown is given in Table 3.4. The average diffusivity at different depths is discussed in the next section.

Interaction of geostrophic flow and tides with topography can result in elevated diffusivity near the bottom. The former will generate internal lee waves and the latter results in the generation of internal tides with tidal frequency. In order to find out which one is dominant, we compared a few good profiles of LADCP velocity with barotropic tidal velocities predicted from a TOPEX/Poseidon 7.2 (TPXO7.2) global tidal model that uses the Laplace tidal equations and along track altimeter data from TOPEX/Poseidon satellites to estimate the depth averaged barotropic currents. Between the eight primary (M_2, S_2, N_2, K_2, K_1, O_1, P_1, Q_1), two long period (Mf, Mm) and three non-linear (M_4, MS_4, MN_4) harmonic tidal constituents, we concentrate on the primary components. We were able to salvage three good velocity profiles from LADCP along the transect. The predicted barotropic tidal velocity is close in magnitude to that of the LADCP velocity except in the strong velocity region of cyclonic eddy in the upper 1500 m (not shown). This suggests that the elevated diffusivity near the bottom could be due to tidal motion interacting with rough bathymetry.

3.7 Discussion

Comparison of dissipation rate and diffusivity estimates from different data sets

In order to validate the finescale parameterization, we compare the float estimates with direct measurements from the VMP taken on the same voyage. The parameterization estimates from the floats are different from what the VMP measures. The parameterization operates at a larger length and time scales with the assumption of internal wave-driven mixing whereas the VMP directly measures the centimeter-scale turbulence. Although we averaged three VMP casts together to derive each dissipation profile, we can consider the VMP measurements as a snapshot of turbulence at an instant, which is not necessarily due to internal wave breaking. The finescale parameterization provides the average dissipation rate over few wave periods (Whalen et al., 2015). Even though we do not have full depth VMP measurements and only one profile at each station, we compare the finescale parameterization estimates with VMP measurements between depths of 240 m and 300 m where they overlap.

We collected 1566 profiles from the EM-APEX floats during July – October 2013 and only 18 VMP profiles between 10 – 14 July 2013 (Fig. 3.1c). The depth averaged float estimates in the upper 300 m show large spatial and temporal variability (Fig. 3.11, upper panel). In four-month time, the floats covered about seven degrees of latitude. During this time, the float estimates vary by about two orders of magnitude in time and space. Comparatively low dissipation rates are observed towards the north from

the float estimates. The VMP measurements only extend to 300 m whereas the parameterization from the floats begins at 240 m. There are only 10 VMP profiles that cover this depth range (Fig. 3.4c). The depth averaged values of float estimates and VMP measurements at this depth range which are close in time are within an order of magnitude (Fig. 3.11, bottom panel). Figure 3.11 gives a comparison between the finescale parameterization and VMP dissipation rate measurements profile by profile. Despite all the spatial and temporal variability as well as the sampling differences and uncertainties from the parameterization due to assumptions in these estimates, overall, the float estimates are in decent agreement with the VMP measurements that are close in time. For instance, we have fairly good agreement at latitudes of 27°S and 29°S whereas an order of magnitude less at 30°S. This gives us some confidence that the float estimates are robust. The mean vertical profile of the parameterization estimates from the floats overestimates the mean vertical profile of VMP measurements in the depth range where they overlap between 200 – 300 m (Fig. 3.12). The large temporal and spatial variability of the float data could be the reason behind the overestimation.

Both shear-strain parameterization and strain-only parameterization have provided mixing estimates which are in good agreement with direct measurements in the open ocean (e.g. Gregg, 1989; Polzin et al., 2014; Whalen et al., 2012). Here we compare the depth averaged diffusivities from all datasets at different depth ranges (Table 3.4). Overall, the estimated diffusivity is weak ($O(10^{-6})$ m^2 s^{-1}) at depths from 250 – 1000 m in agreement with Waterhouse et al. (2014) except in regions of cyclonic eddies. Below 1000m depth, the dissipation rate decreases rapidly with depth and the diffusivity is nearly constant with depth. This suggests that less internal wave dissipation is available below 1000 m, in agreement with Huussen et al. (2012). Near the boundaries, elevated dissipation rate and diffusivity is observed in both direct and parameterized estimates. The finescale parameterization has a mean diffusivity of 5.4×10^{-6} m^{2}s^{-1} in the upper 240 – 300 m whereas the VMP has a mean of 1.7×10^{-6} m^{2}s^{-1}. In 2012 and 2013 voyages, the strain parameterization has consistent diffusivities for the depth ranges of 250 – 500 m and 500 – 1000 m. For depths below 1000 m to the bottom bathymetry, strain parameterization provides mean diffusivity one order higher than that at mid-depths (1.9×10^{-5} m^{2}s^{-1}).

The parameterization estimates are sensitive to the magnitude of R_ω where higher dissipation is observed with smaller values of R_ω (Polzin et al., 1995). However, strain-only parameterization has been widely used since strain (density) measurements are comparatively easy to obtain (Whalen et al., 2012, 2015, 2018; Sloyan, 2005). Shear-strain parameterization estimates the R_ω from the observed shear and strain variances whereas the strain-only parameterization assumes a constant value for R_ω. In this study, the R_ω value for the strain-only parameterization ($R_\omega = 6$) is chosen from the observed R_ω values from float profiles closer in space and time to the shipboard CTD measurements. We found that the shear-strain

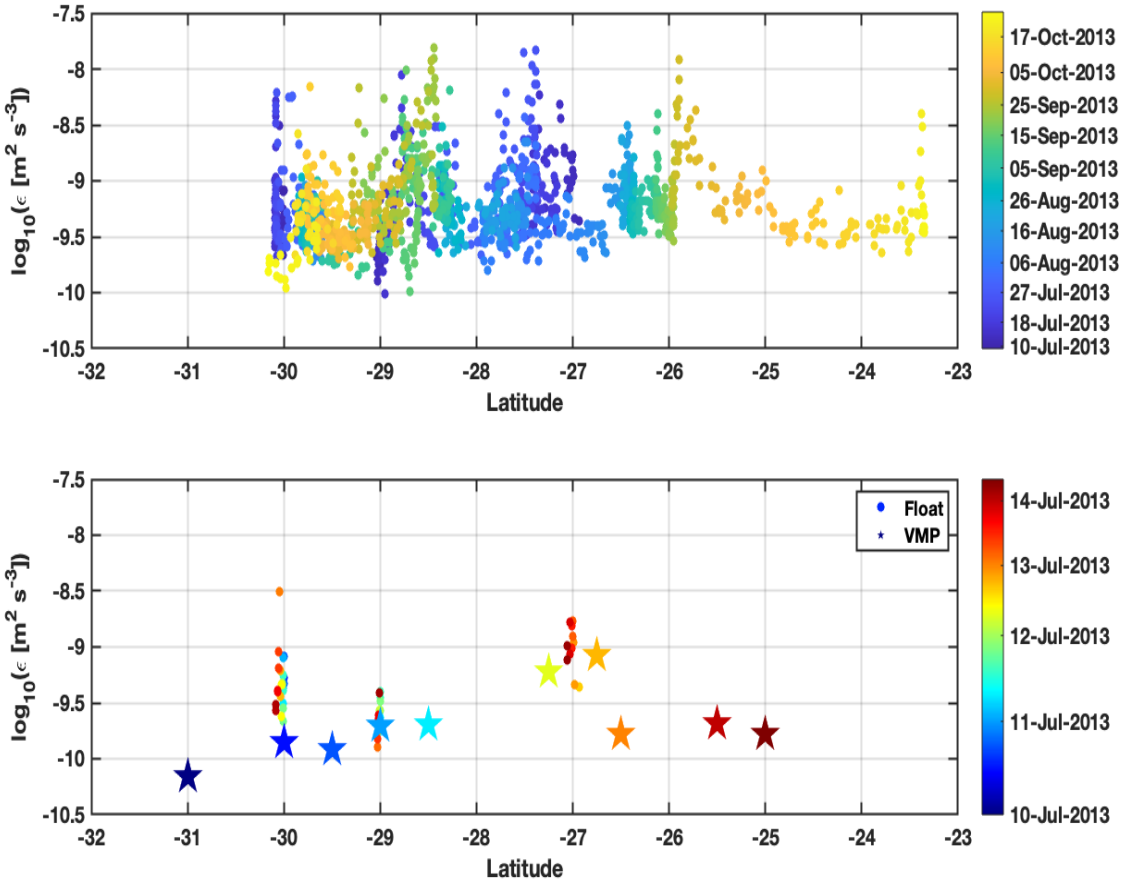

Figure 3.11: Depth averaged dissipation rate estimates between 240 – 300 m from floats as a function of latitude and time (upper panel). Depth averaged dissipation rate from floats and VMP for the same depth range where the floats and VMP overlap in time during 2013 (bottom panel). The color represents time in both panels and circles are float estimates. The filled stars are data from the VMP. Note the difference in the color axis for both panels.

estimates from the floats and the strain-only estimates from the shipboard data match very well (Fig. 3.12) in the southeast Indian Ocean. Whalen et al. (2012) used a constant R_ω of 3 and estimated the distribution of diffusivity globally. They found diffusivity one order higher than our estimates for the southeast Indian Ocean. Our estimates are of the same order of magnitude as that of Waterhouse et al. (2014) where they estimated diffusivity from microstructure profilers and shear-strain parameterization. In addition, the vertical distribution of dissipation rate and diffusivity from our strain parameterization (Fig.3.10) matches with the average Indian Ocean profiles in Kunze et al. (2006). They used a R_ω value of 7 in strain-only parameteriztion and found that it can reproduce the diffusivity estimates using both shear and strain to within a factor of 2. These estimates suggest that the diffusivity estimates are greatly improved by estimates of shear.

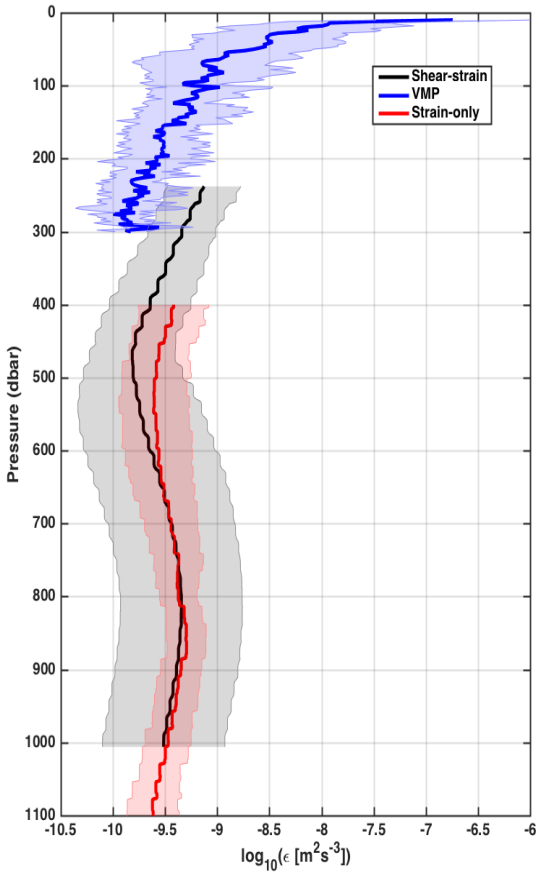

Figure 3.12: Mean depth profile of dissipation rate in the upper 1100 m estimated from all float profiles using shear-strain method (black), shipboard data using strain-only method (red) and VMP measurements (blue).

Depth	*Shear − strain*	*Strain − only*	*VMP*
Surface – 300 m	–	–	$1.5 \times 10^{-4} \pm 0.002$ (2012)
			$4.0 \times 10^{-4} \pm 0.007$ (2013)
240 – 300 m	$(5.4 \pm 2.5) \times 10^{-6}$ (2013)	–	$(2.4 \pm 1.6) \times 10^{-7}$ (2013)
250 – 500 m	$(4.1 \pm 1.8) \times 10^{-6}$ (2013)	$(4.8 \pm 0.7) \times 10^{-6}$ (2012)	–
		$(5.1 \pm 1.1) \times 10^{-6}$ (2013)	–
500 – 1000 m	$(2.4 \pm 4.2) \times 10^{-5}$ (2013)	$(7.0 \pm 2.0) \times 10^{-6}$ (2012)	–
		$(7.9 \pm 1.6) \times 10^{-6}$ (2013)	–
1000 m – bottom	–	$(1.9 \pm 6.6) \times 10^{-5}$ (2013)	–

Table 3.4: Mean diffusivity and one standard deviation at different depth ranges from floats (shear-strain), shipboard data (strain-only) and VMP in the southeast Indian Ocean in 2012 and 2013.

Impact on watermasses and large-scale circulation

The main watermasses in the subtropical Indian Ocean at mid-depth are the Subantactic Mode Water (SAMW) and Antarctic Intermediate Water (AAIW). SAMW in the Indian Ocean, generated between

the subtropical front (STF) and the subantarctic front (SAF), enters the subtropics and ventilates the subtropical gyre (Sallee et al., 2006). They are an integral part of the global overturning circulation as well as global heat, freshwater and carbon budgets (Sloyan et al., 2010).

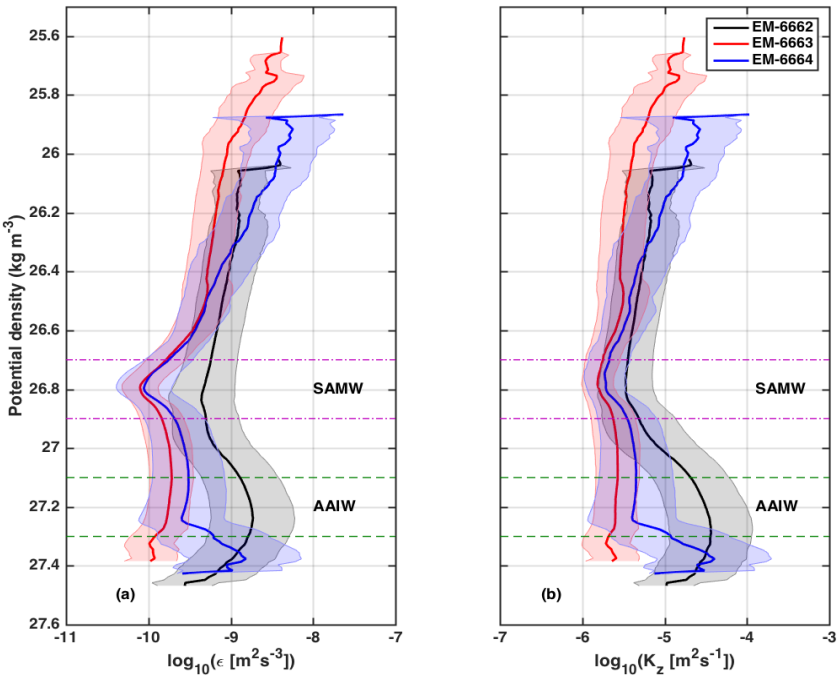

Figure 3.13: a) Mean dissipation rate and b) diffusivity from the floats plotted on a potential density axis. The floats are separated by colors and the SAMW and AAIW are marked. The color shading is one standard error.

The turbulent mixing due to internal waves plays an important role in the deep ocean watermass transformation and is a key factor in the global overturning circulation (Nikurashin and Ferrari, 2013). From the float data in the upper 200 – 1000 m, we observe higher dissipation and mixing at depths corresponding to AAIW (Fig. 3.13). Among the three floats, EM-6662 that looped around two cyclonic eddies has the highest dissipation rate and mixing, peaking at potential density 27.3 kg m^{-3}. Elevated diffusivity is observed in EM-6664 below the AAIW peaking at potential density 27.4 kg m^{-3}. EM-6663 which had a largely meridional track has weak dissipation and mixing in the AAIW with comparatively higher values in the upper water column. All the floats show minimum dissipation rate and diffusivity in the SAMW region at potential density 26.8 kg m^{-3}. EM-6664 has higher diffusivities in the upper part of the water column due to the elevated mixing in the warm core eddy which may affect the STUW. The AAIW region has a mean dissipation rate of 1.5×10^{-9} m^{3}s^{-2} and diffusivity of 2.6×10^{-5} m^{2}s^{-1}. The SAMW region has a weaker dissipation rate of 3.7×10^{-10} m^{3}s^{-2} and diffusivity of 3.7×10^{-6} m^{2}s^{-1}. Overall, most of the mixing of the watermasses takes place in the cyclonic eddies in regions of AAIW and minimum mixing occurs in the SAMW region.

Elevated mixing in the anticyclonic eddies affect the watermasses in the upper part of the water column. This suggests that the turbulent mixing in both cyclonic and anticyclonic eddies plays an important role in the watermass transformation in the southeast Indian Ocean, a region dominated by mesoscale eddies from the LC. Whalen et al. (2018) found regions of anticyclonic vorticity is associated with elevated internal wave-driven mixing in the upper 250 – 500 m, which was not found in cyclonic vorticity regions. In this study, we observe elevated internal-wave mixing in cyclonic eddies below 500 m. The cyclonic eddies generated from the LC system are subsurface-intensified. This study suggests that the interactions between internal waves and cyclonic eddies may impact the watermass transformation below 500 m in this region.

We further looked into the impact of mesoscale eddies on the properties of SAMW and AAIW by plotting the mean properties of each layer observed in each float profile (Fig. 3.14). The temperature and salinity of SAMW is elevated near the centre of the cyclonic eddy (EM-6662, Fig. 3.14a and b) where the SAMW potential density layers come closer (Fig. 3.2 and 3.3). It is less influenced by the warm core eddies where the SAMW layer is well below (EM-6663 and EM-6664). In contrast, the properties of the AAIW layer are less affected by the cold core eddies CC1 and CC2 in EM-6662 and EM-6664 (Fig. 3.14 c and d). This result contradicts the observed mixing distribution where most of the mixing of the watermasses is associated with cyclonic eddies in regions of AAIW and minimum mixing occurs in SAMW layer (Table 3.2 and 3.3). EM-6663, which followed a roughly meridional path northward (Fig. 3.1c), experienced a gradual increase in the temperature and salinity in the AAIW layer consistent with the largescale circulation and property distributions (Talley, 2011). A temperature-salinity plot of this float shows that the AAIW layer was replaced by the more saline Indonesian Intermediate Water (IIW), which occupies the same density range (not shown).

Internal wave breaking can change the strength and spatial pattern of local mixing. This breaking then feeds back on the large-scale circulation and thereby climate (Garrett, 2003). Enhanced mixing in the upper water column is often attributed to the breaking of near-inertial internal waves generated due to wind forcing and also by the trapping of these waves in anticyclonic eddies. The southeast Indian Ocean is one region where the internal waves interact and coexist with mesoscale eddies and the large-scale circulation. From the float EM-6663 which had a meridional transect, we observe elevated diffusivity in the upper 300 m in warm core eddies and in cold core eddies towards north (Fig. 3.15a). From the CSIRO (Commonwealth Scientific and Industrial Research Organisation) Atlas of Regional Seas (CARS09) climatology of geostrophic velocities, the southern branch of the SICC (sSICC) extends between 25 – 29°S at 105°E (Fig. 3.15b, black line). The average surface zonal velocity during the float profiling also shows

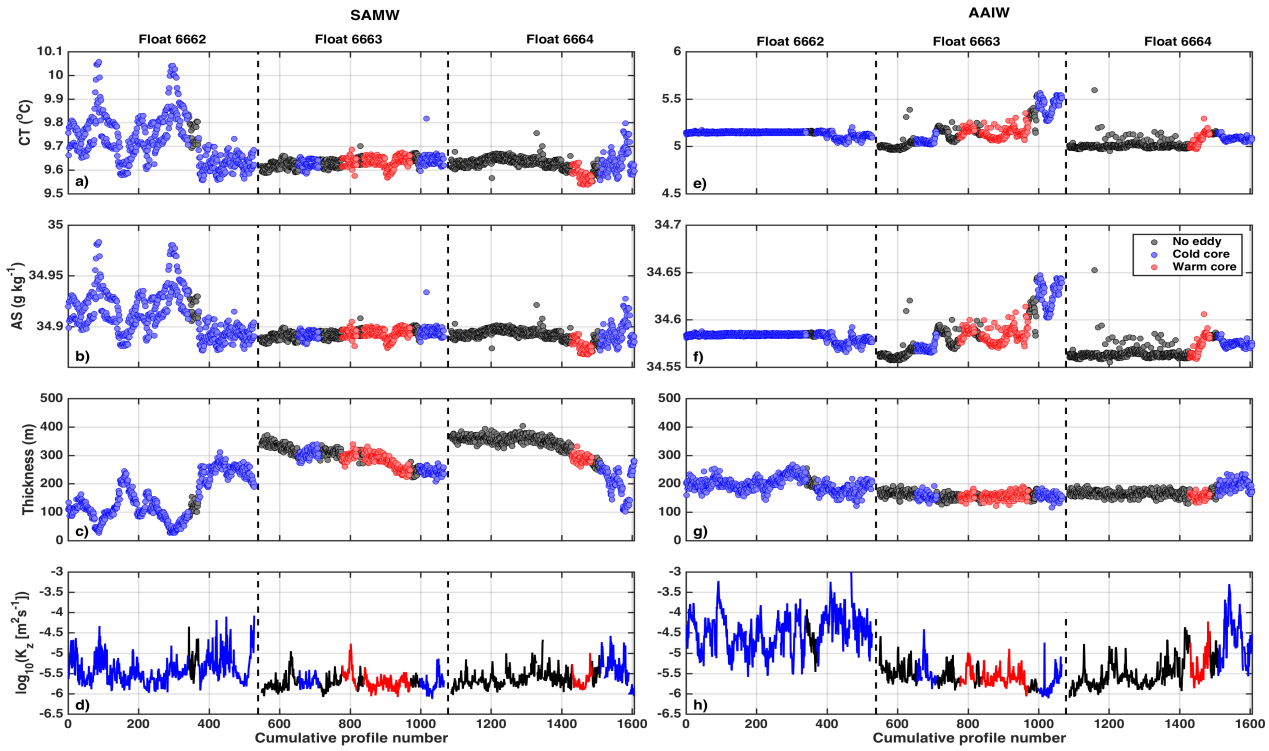

Figure 3.14: Averaged values of a) temperature, b) salinity, c) thickness, and d) diffusivity for the SAMW layer along the float tracks. e), f), g) and h) are the same for AAIW layer. The black circles represent profiles without eddy and red (blue) circles represent profiles associated with warm (cold) core eddies.

a similar pattern except towards north (Fig. 3.15b, red line). We then looked into the relationship between mean surface zonal velocities during the float profiling and depth-averaged diffusivity. There is no direct relation between the two (Fig. 3.15c). However, profiles in warm core eddies show elevated diffusivity in regions of the sSICC. Diffusivity is also elevated in non-eddy regions where the zonal velocity magnitudes correspond to that of the SICC jet (≈ 8 –10 cm s^{-1}). We further looked into the relationship between the climatology of zonal velocity and diffusivity (Fig. 3.15c). A similar pattern with elevated diffusivity in warm core eddies are observed.

3.8 Conclusion

We analysed the spatial and temporal variability of turbulent mixing in the southeast Indian Ocean for the first time using data collected from EM-APEX profiling floats, shipboard CTD and microstructure profilers. Elevated diffusivity is observed near the surface in agreement with the generation and downward propagation of near-inertial internal waves from wind. Most of the observed mixing variability below the mixed layer is associated with mesoscale eddies and/or bottom topography. Both anticyclonic and cyclonic eddies contribute to the distribution of turbulent mixing. We observe elevated mixing in

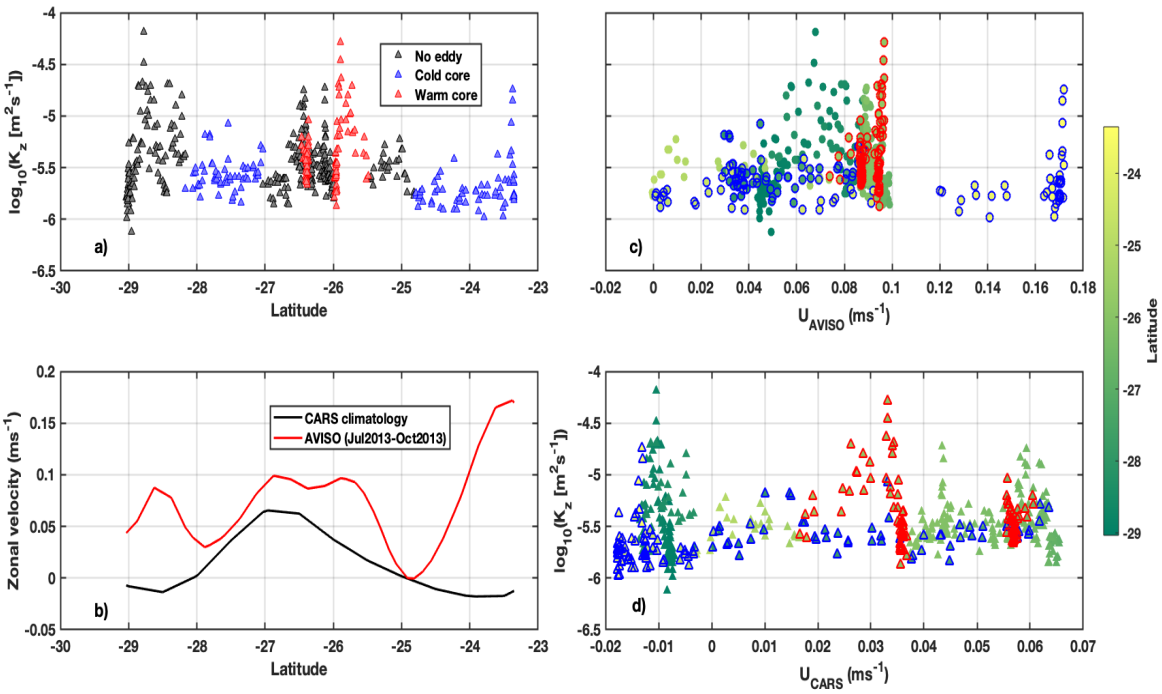

Figure 3.15: a) Depth averaged diffusivity in the upper 300 m along the track of float EM-6662 which covered the widest latitudinal band. The estimates in cold cores (blue) and warm cores (red) are marked. b) The mean zonal geostrophic velocity between 100 –105 °E in the upper 200 m (black line) and the mean surface geostrophic velocity between 100 –105 °E during the float profiling. Scatter plot of depth averaged diffusivity in the upper 300 m between c) surface geostrophic velocity and d) mean CARS climatology in the upper 200 m.

warm core eddies near the surface consistent with near-inertial wave trapping. Enhanced dissipation is observed in cyclonic eddies below 500 m associated with downward propagating high frequency internal waves. The mean diffusivity in the 250 – 500 m is of the $O(10^{-6})$ m^2 s^{-1} and it increases to $O(10^{-5})$ m^2 s^{-1} in the 500 – 1000 m due to elevated diffusivity in cyclonic eddies. Turbulent mixing is weak in the SAMW layer and high in the AAIW layer of cyclonic eddies. However, the properties of SAMW are highly modified in the cyclonic eddies whereas it is less affected in the AAIW layer. The turbulent mixing in the upper layer of mesoscale eddies in this region is likely to influence the strength and distribution of the south Indian Countercurrent jets.

Chapter 4

Seasonal evolution of the surface layer heat balance in the eastern subtropical Indian Ocean

Chapter 4 analyses the surface layer heat budget in the southeast Indian Ocean and investigates the relative roles of atmospheric and oceanic processes on the budget. The content of this chapter is published online and is re-formatted for this thesis but otherwise presented as published in:

Cyriac, A., McPhaden, M., Phillips, H., Bindoff, N., and Feng, M. (2019). Seasonal evolution of the surface layer heat balance in the eastern subtropical Indian Ocean. *Journal of Geophysical Research: Oceans*, https://doi.org/10.1029/2018JC014559.

Abstract

The South Indian Ocean (SIO) is a region of strong air-sea heat loss due to the unique ocean circulation pattern influenced by the Indonesian Throughflow. In this study, the seasonal variation of the surface layer heat budget in the eastern SIO is investigated using 2 years of measurements from a mooring at 25°S, 100°E, the only colocated upper ocean and surface meteorology time series in the subtropical Indian Ocean. The mooring data are combined with other *in situ* and satellite data to examine the role of air-sea fluxes and ocean heat transport on the evolution of mixed layer temperature using heat budget diagnostic models. Results show that on seasonal time scales, mixed layer heat storage in the eastern SIO is mostly balanced by a combination of surface fluxes and turbulent entrainment with a contribution from horizontal advection at times. Solar radiation dominates the seasonal cycle of net surface heat flux, which warms the mixed layer during austral summer (67 Wm^{-2}) and cools it during austral winter (-44 Wm^{-2}). Entrainment is in good agreement with the heat budget residual for most of the year. Horizontal

advection is spatially variable and appears to be dominated by the presence of mesoscale eddies and possibly annual and semiannual Rossby waves propagating from the eastern boundary. Results from the 2-year mooring-based data analysis are in reasonably good agreement with a 12-year regional heat budget analysis around the mooring location using ocean reanalysis products.

4.1 Introduction

The eastern South Indian Ocean (SIO) is a region of strong heat loss to the atmosphere (Josey et al., 1999; Yu et al., 2007). The Indonesian Throughflow (ITF) brings warm surface water into the tropical Indian Ocean from the Pacific. A review of different modeling studies shows that the changes in ocean circulation associated with the ITF can influence the heat loss to the atmosphere in the SIO (Godfrey, 1996). The trade winds drive some of the warm water brought by the ITF to the south through Ekman drift (Godfrey, 1996; Schott and McCreary, 2001). Since the overlying atmosphere is cooler south of 20°S, this heat is lost to the atmosphere (Godfrey, 1996), resulting in deeper winter mixed layers in the SIO compared to other subtropical oceans (Schott and McCreary, 2001). This loss of heat together with strong evaporation leading to high salinity in surface waters generates dense water that subducts into the thermocline (Zhang and Talley, 1998). These subducted waters contribute to the downwelling branches of the southern cell and cross-equatorial cell of the Indian Ocean's shallow meridional overturning circulation south of 20°S (Lee, 2004). The cold, subducted thermocline water will later return to the surface through the upwelling regions in the north Indian Ocean (Schott and McCreary, 2001).

Reanalysis products disagree on the magnitude of the surface heat fluxes in the SIO (Yu et al., 2007). These differences can result in inaccurate heat budget terms especially in regional studies (Schott and McCreary, 2001). A major reason for this difference is the lack of enough observations of air-sea fluxes to validate the reanalysis products (Josey et al., 1999; Fairall et al., 2010; Sun et al., 2003). To address this gap in observations, a Research Moored Array for African-Asian-Australian Monsoon Analysis and Prediction (RAMA) flux mooring (McPhaden et al., 2009) measuring air-sea fluxes was deployed in the eastern SIO to provide high temporal resolution data to constrain the air-sea fluxes there and to examine the ocean-atmosphere coupling in this region.

The surface heat fluxes along with oceanic processes play an important role in the evolution of seasonal and interannual variations in sea surface temperature (SST) (Yu et al., 2007). The ocean circulation in the eastern SIO is dominated by the eastward flowing near-surface geostrophic South Indian countercurrent (SICC) branches (Siedler et al., 2006; Palastanga et al., 2007; Divakaran and Brassington, 2011; Menezes et al., 2014) and the poleward flowing Leeuwin Current (LC). The eastern SIO is rich in eddies from the

LC (Fang and Morrow, 2003) as well as from local shear instability (Jia et al., 2011b, Figure 4.1g-h) and by the occasional passage of sea level anomalies emanating from the eastern boundary with Rossby wave speed (Morrow and Birol, 1998; Morrow et al., 2004). The LC is the only eastern boundary current where the ocean loses heat with comparable magnitudes to a western boundary current (Josey et al., 1999). This heat loss extends westward from the coast in association with the westward movement of LC eddies into the SICC (Morrow and Birol, 1998; Domingues et al., 2007; Feng et al., 2008; Morrow et al., 2003). Using an eddy resolving model, Feng et al. (2008) found that LC advection and air-sea fluxes are important for the mixed layer heat budget in the LC basin (27°S –32°S, 100°E to the coast) on both seasonal and interannual timescales. In recent decades, SST has been increasing in the LC region (Pearce and Feng, 2007; Feng et al., 2008) possibly with some contribution from the increased frequency of Ningaloo Ninos, characterized by anomalous warm SSTs in the LC region (Feng et al., 2015). Such anomalous warming has a great impact on the marine ecosystem off the western coast of Australia (Wernberg et al., 2013; Feng et al., 2013).

Here we analyze the seasonal cycle of mixed layer heat balance, using daily surface heat fluxes from the RAMA mooring deployed at 25°S, 100°E, together with auxiliary data. The highly-resolved time series from this RAMA mooring represents the only time series of air-sea flux observations made in the subtropical SIO. We used data from two consecutive deployments at this location spanning from the end of August 2012 to November 2014 and a combination of *in situ*, satellite and reanalysis products, to estimate the mixed layer heat budget in the eastern SIO. By assuming that the errors in heat budget terms are small, the residual of the budget is attributed primarily to vertical entrainment and heat diffusion at the base of the mixed layer.

The paper is organized as follows. Section 2 describes the datasets used in this study. The mixed layer heat budget equations are discussed in section 3. Section 4 contains the results of the 2 year mixed layer heat balance using mooring data. Results of the 12 year analysis using TropFlux data is presented in section 5. Section 6 compares the results of this study with those of previous studies and also provides a summary.

4.2 Data

The RAMA flux mooring at 25°S, 100°E recorded bulk atmospheric and oceanic variables that are used to compute surface fluxes and upper ocean variability for 27 months. We analyzed the mixed layer heat budget at the mooring location and also over a $2^\circ \times 2^\circ$ box around the mooring using satellite, Argo and

reanalysis products, to supplement the mooring data where necessary. The reanalysis products allowed a calculation of the heat budget over a 12 year period to compare with the 2 year mooring period.

To provide spatial context for the mooring observations, Figure 4.1 presents a comparison of winter and summer conditions around the mooring based on Argo and reanalysis data. During austral winter, the eastern SIO loses more heat to the atmosphere ($\sim$ 200 Wm^{-2}) compared to the heat gain during austral summer ($\sim$ 50 – 100 Wm^{-2}) (Figure 4.1 a-d). The mooring is located in a haline frontal region with cool saltier waters towards the south and comparatively warm fresher waters in the north (Menezes et al., 2014, ; Figure 4.1e-f). The sea surface height (SSH) decreases towards the poles similar to the SST (Figure 4.1 g-h) with larger SSH in the LC region compared to offshore. The sea level anomaly (SLA) is dominated by LC eddies during austral winter when the LC is stronger. The spatial variability of SLA is less in austral summer compared to that in austral winter, consistent with the seasonal cycle of the LC.

4.2.1 Mooring data

The RAMA mooring (Figure 4.1) was deployed in late August 2012, was recovered and redeployed in July 2013, and stopped transmitting in November 2014. The mooring was never recovered due to the unavailability of a ship capable of mooring work at the time.

The mooring recorded hourly measurements of ocean temperature, salinity, current speed and direction, wind speed and direction, air temperature and pressure, relative humidity, short wave and long wave radiation, and rainfall. Ocean temperature sensors were placed at depths of 1 m, 5 m, 10 m, 20 m, 40 m, 60 m, 80 m, 100 m, 120 m, 140 m, 180 m, 300 m, and 500 m. Salinity was measured at 1 m, 10 m, 20 m, 40 m, 60 m, 100 m and 140 m. There were no ocean current data from the first deployment. On the second, there was a point current meter located at 10 m depth. However, it only gave sporadic measurements between July 2013 and November 2014 which were not suitable to use in the calculations (supporting information Figure A.6). These velocities were useful, though, in confirming that the OSCAR velocities were of realistic amplitude.

The shortwave and longwave radiation, and precipitation were measured at 3.5 m above the sea surface. Wind speed and direction were measured at a height of 4 m above the sea surface. Relative humidity, sea level barometric pressure and air temperature were measured at 3 m above the sea surface. Hourly data is only available for the instruments that were recovered from the ocean (August 2012 – July 2013). Daily averages of the data transmitted in near-real time from the mooring are available from the Pacific Marine Environmental Laboratory website (`https://www.pmel.noaa.gov/tao/drupal/disdel/`). We use the daily dataset from August 2012 – November 2014 for our heat budget analysis.

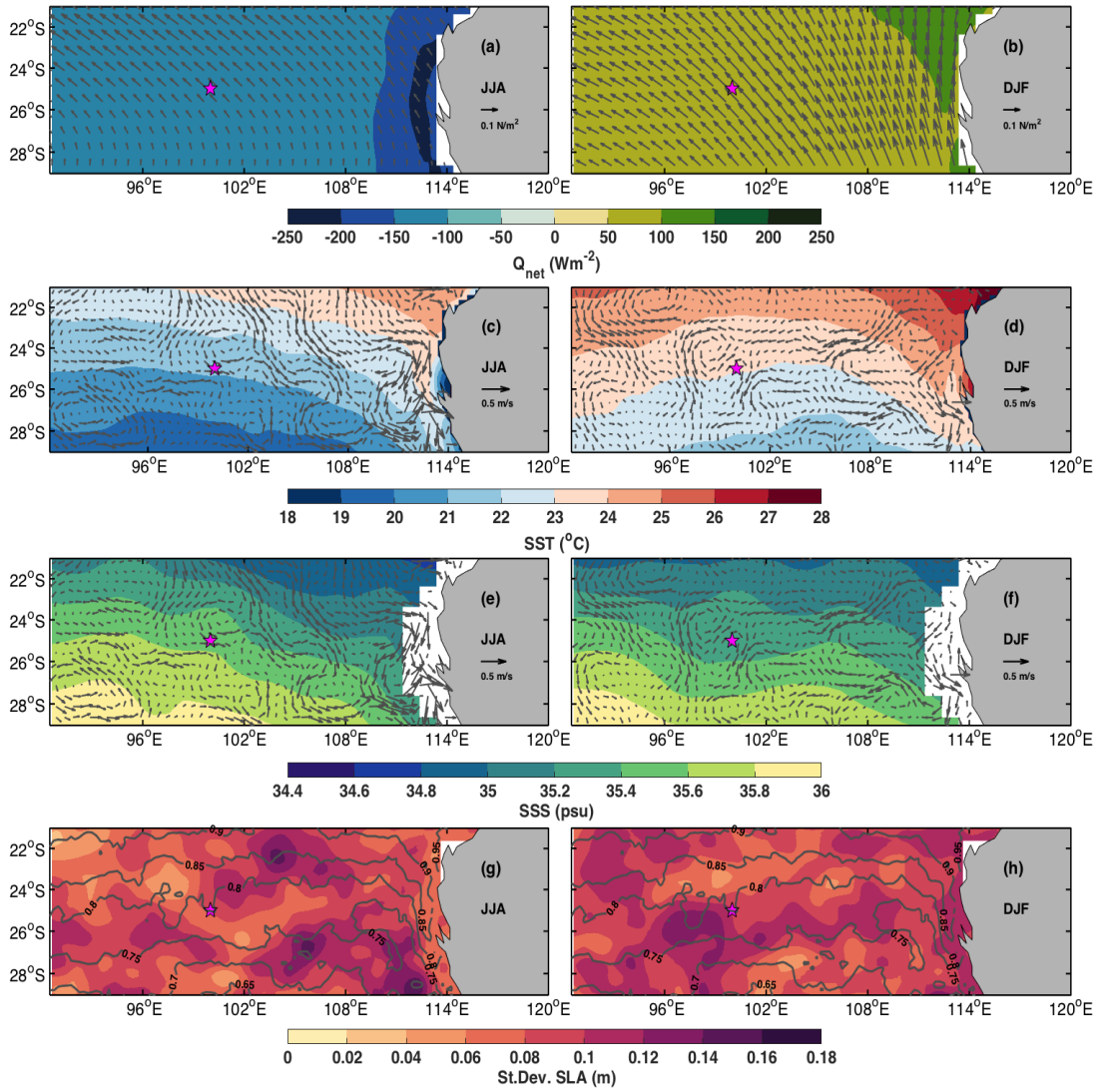

Figure 4.1: a-b) Climatology of net heat flux from TropFlux (overlaid with TropFlux wind stress), c-d) Reynolds SST and e-f) Sea Surface Salinity (SSS) from Argo (overlaid with OSCAR surface currents) during 2004 – 2015. g-h) The standard deviation of SLA from AVISO during 2004 – 2012 overlaid with contours of mean dynamic topography (SSH) climatology for the period 1992 – 2012. The left panels (a, c, e, g) are for austral winter and right panels (b, d, f, h) are for austral summer. The star shows the location of the RAMA mooring. Positive fluxes show heat gain by the ocean.

Figure 4.2 presents time series of a subset of observations from the mooring which will be described further in Section 4.4. There are some gaps in the subsurface temperature and salinity during the mooring operation period (Figure 4.2d-e). The longest gaps are during the second mooring deployment at depths of 80 m and 100 m for temperature and 80 m, 100 m, and 120 m for salinity. These gaps have been filled through vertical interpolation. There is no data at all depths for 14 days towards the end of the second deployment. However, these missing data do not affect conclusions of our analysis since mixed layer depth (MLD) is almost always shallower than the deeper gaps.

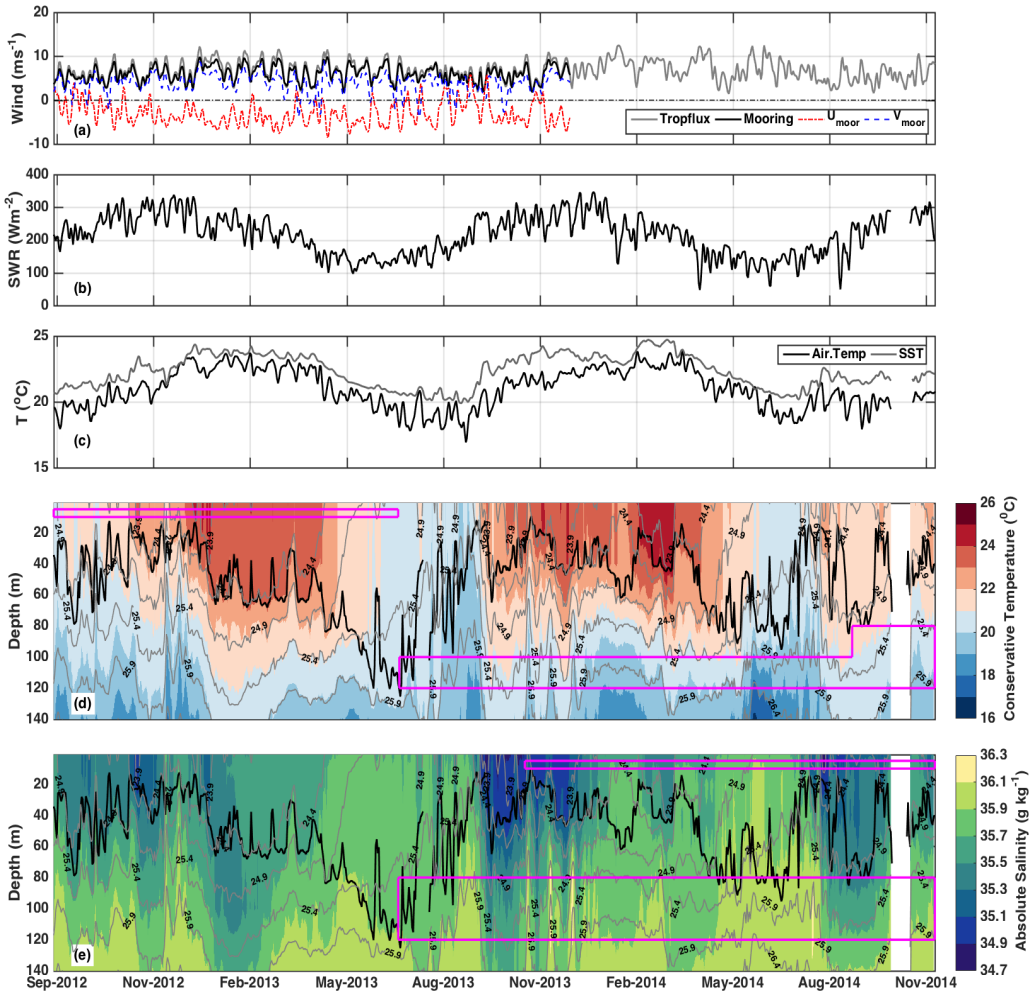

Figure 4.2: Daily time series of a) wind speed with zonal (red dashed line) and meridional (blue dashed line) components from mooring and wind speed from Tropflux b) shortwave radiation from mooring, c) air temperature and SST from mooring d) subsurface temperature and e) subsurface salinity overlaid with potential density contours (grey lines) and MLD (black line). The magenta boxes in (d) and (e) show the gaps that have been filled with linear interpolation in the vertical. All time series are filtered with a 1-2-1 running mean filter.

4.2.2 Atmospheric reanalysis products

Yu et al. (2007) and Kumar et al. (2012) have made a detailed comparison of different reanalysis products with *in situ* measurements for the Indian Ocean (30°N – 30°S) and global ocean (30°N – 30°S) , respectively. They both conclude that OAFLux, ISCCP and ERA-I perform the best and NCEP products are least representative of the net heat flux variability. Kumar et al. (2012) introduces a new data product called TropFlux which is a combination of ERA-I atmospheric variables and OAFLux/ISCCP shortwave radiation fluxes. It is available globally for the latitudinal band 30°N – 30°S on a spatial grid of $1^\circ \times 1^\circ$. TropFlux has been evaluated against mooring data and is a useful reanalysis product to study air-sea interactions and oceanic heat budgets in the tropics (Kumar et al., 2012). Here, for the spatial analysis, we used the monthly averages of TropFlux shortwave radiation and net heat flux during 2004 – 2015.

The wind data from the mooring ends in December 2013. Therefore, we used TropFlux winds instead of mooring winds to extend the time series to the end of the deployment in November 2014. TropFlux wind agrees well with the mooring winds from August 2012 to December 2013, with a correlation of 0.965 (Figure 4.2a). We also compared the mooring surface heat fluxes with those from different reanalysis products such as NCEP2, OA Flux, TropFlux and MERRA data. Among them, TropFlux (NCEP2) has the highest (lowest) correlation and smallest (largest) root mean square deviation (RMSD) with the mooring measurements.

4.2.3 Argo, Satellite and ocean reanalysis products

We used the latest version of Roemmich-Gilson Argo data (Roemmich et al., 2009) for the 12-year analysis. The mapped fields of temperature and salinity on pressure surfaces derived from Argo profiles are available on a spatial grid of $1^\circ \times 1^\circ$. Monthly averages of Argo temperature and salinity profiles are available at the mooring location up to a depth of about 2000 m since 2004. By applying the same method as used for the observations (Section 3), we derived MLD from Argo data and also from Simple Ocean Data Assimilation ocean/sea ice reanalysis (SODA) data (Carton and Giese, 2008). We compared the monthly averages of MLD from Argo and SODA with those from the mooring and found that they match well (Supporting information Figure A.7).

NOAA High Resolution SST data are used to provide information on horizontal gradients of SST. These daily data have a spatial resolution of $0.25^\circ \times 0.25^\circ$ and are provided by the NOAA/OAR/ESRL PSD, Boulder, Colorado, USA (`http://www.esrl.noaa.gov/psd/`). Following Wang and McPhaden (1999) (hereafter WM99), we refer to this dataset as "Reynolds SST" throughout the paper. Reynolds SST matches well with the mooring SST with a correlation (RMSD) of 0.96°C (0.43°C) over the full 2 year record (supporting information Figure A.8).

Since the ocean velocity measurements from the mooring were not reliable, we used Ocean Surface Current Analysis Real-time (OSCAR) current vectors to estimate horizontal advection. OSCAR velocities are provided on a $0.33^\circ \times 0.33^\circ$ grid with a 5 day resolution from `http://dx.doi.org/10.5067/OSCAR-03D01`. The OSCAR climatology is found to capture the surface current variability in the tropical Indian Ocean reasonably well with a difference in magnitude of less than 0.2 ms^{-1} from drifter climatology (Sikhakolli et al., 2013). They also found that the OSCAR currents are in good agreement with currents measured by moorings. Here the OSCAR velocities were interpolated in time to match the daily mooring data, and interpolated spatially to the mooring location. Meridional velocity exhibits more variability than zonal velocity and the correlations between the mooring velocities and OSCAR are correspondingly higher for meridional velocity (0.82) than for zonal velocity (0.26). The RMSD between

5-day averages of available mooring currents and OSCAR is slightly higher for meridional component (0.16 ms^{-1}) than that of the zonal component (0.15 ms^{-1}). This result gives us some confidence that the OSCAR velocities are realistic. We use the daily Reynolds SST and OSCAR velocities for the long term heat budget as well.

4.3 Heat Budget

To identify the processes contributing to the seasonal variability in mixed layer temperature, we analyze the surface layer heat balance at the mooring following WM99. The heat balance equation can be written as,

$$Q_t = Q_{net} + Q_u + Q_v + Q_{res} \tag{4.1}$$

$$Q_{net} = Q_{SW} - Q_{LW} - Q_L - Q_S + Q_{pen} \tag{4.2}$$

$$Q_{pen} = -0.45 \times Q_{SW} \times e^{-\gamma H} \tag{4.3}$$

$$Q_u = -\rho C_p H u \frac{\partial T}{\partial x} \tag{4.4}$$

$$Q_v = -\rho C_p H v \frac{\partial T}{\partial y} \tag{4.5}$$

$$Q_t = \rho C_p H \frac{\partial T}{\partial t}. \tag{4.6}$$

Here H is the mixed layer depth, ρC_p is the volumetric heat capacity of seawater (equal to 4.038×10^6 JK^{-1} s^{-3}), T is the average mixed layer temperature, and u and v are the eastward and northward currents in the mixed layer. Q_t is the mixed layer temperature change rate, and Q_{net} is the net surface heat flux (Equations 4.1 and 4.2) which is the sum of latent (Q_L) and sensible (Q_S) heat fluxes, net surface shortwave (Q_{SW}) radiation obtained from the downward shortwave flux considering an albedo of 6% and net long wave (Q_{LW}) radiation, and the penetrative (Q_{pen}) component of the shortwave radiation through the base of the mixed layer (Equations 4.2 and 4.3). Here positive heat flux terms represent gain to the ocean.

MLD is estimated as the depth at which density is 0.15 kg m^{-3} units denser than that at 5 m depth (Foltz et al., 2010). Since the mixed layer temperature and SST are similar (supporting information Figure A.8) we use mooring SST for the 2 year analysis and Reynolds SST for the 12 year analysis to estimate the heat storage.

Q_{pen} is estimated following Morel and Antoine (1994) solar irradiance parameterization as described

in Sweeney et al. (2005) using a chlorophyll-a concentration of 0.1 mg m^{-3}. The outgoing Q_{LW} is calculated by long wave radiation emission at the sea surface. Q_L and Q_S are estimated using the Coupled Ocean-Atmosphere Response Experiment (COARE) bulk flux algorithm (Fairall et al., 1996),

$$Q_L = \rho_a L_e C_e S(q_s - q) \tag{4.7}$$

$$Q_S = \rho_a C_{pa} C_h S(T_S - \theta), \tag{4.8}$$

where ρ_a is the air density, L_e is the average latent heat of vaporisation and C_{pa} is the specific heat capacity of air. C_e (Dalton number) and C_h (Stanton number) are the transfer coefficients for Q_L and Q_S respectively. q is the water vapour mixing ratio, q_s is the inter-facial value of the water vapour mixing ratio, T_s is the sea surface interface temperature which we consider as the SST and θ is the potential temperature of the air above.

For advection, the temperature gradients were calculated using Reynolds SST (Figure 4.1c-d) around the mooring location. We use upstream differencing following Bond and McPhaden (1995) to estimate the horizontal advection. When the flow is northward (eastward), the gradient south (west) of the mooring is estimated and when the flow is southward (westward), the gradient north (east) of the mooring is considered. We choose 1° spacing to estimate the meridional temperature gradient, and 2° spacing for the zonal temperature gradient, recognising the stronger meridional gradients in this region. We also tried different resolutions (0.5°, 1°, 1.5°, 2°) and found that it does not affect the conclusions of the study.

The vertical turbulent heat flux into the mixed layer is estimated as a residual (Q_{res}) between Q_{net}, advection and heat storage (WM99). It combines the effects of vertical entrainment and vertical heat diffusivity. It also encompasses neglected physical processes and errors in the estimates of the other terms in the heat budget.

We averaged the daily heat budget terms to monthly averages and the seasonal cycles were estimated from the monthly averages. In order to be consistent with the mooring analysis, we estimated the fluxes for the spatial analysis by using each monthly average of MLD for every day of each month to get daily values. Following Foltz and McPhaden (2008), the standard error in the monthly heat budget was estimated using the daily mooring data. The effective degrees of freedom corresponds to a decorrelation timescale of 3 – 4 days. The standard error for the spatial analysis is also calculated in the same way but calculating the standard error from the monthly data. Also, the mean seasonal cycles are smoothed with a 1-2-1 monthly filter to eliminate the intraseasonal noise that tends to obscure the lower frequency component of the seasonal cycle that we are most interested in.

4.4 Mixed layer heat balance from the RAMA mooring

4.4.1 Observed variability

The southeasterly trade winds dominate the wind record with strong daily fluctuations (Figure 4.2a). The Q_{SW} has strong seasonal fluctuations with comparatively weaker interannual variability (Figure 4.2b). SST is always higher than the air temperature for all seasons and synoptic events (Figure 4.2c), with small daily fluctuations. The seasonal cycles of both SST and air temperature follow that of Q_{SW}. The subsurface temperature, salinity and MLD have a strong seasonal cycle (Figure 4.2d and e). Note that the density contours are following temperature contours well suggesting that the salinity is of secondary importance to density variations in this region. The upper ocean is warm and fresh during austral summer with a shallow mixed layer. During austral winter, the upper ocean is colder and more saline with a deeper mixed layer.

4.4.2 Seasonal cycle

The mooring data at 25°S, 100°E show strong seasonal variations (Figure 4.3). The dominant wind direction is from the southeast throughout the year. The wind stress has a weak 2 cycle per year variation with higher values during austral summer and winter (Figure 4.3a). SST is higher during austral summer with a peak value (~ 24°C) in March and decreases to a minimum in July (~ 20.5°C). Sea surface salinity (SSS) follows an opposite variation compared to SST (Figure 4.3b and c) with the highest surface salinity observed in June (35.6 psu) and the lowest in October ($\sim$35 psu). The mixed layer is deepest during June – July ($\sim$80 m), when the mixed layer is colder and saltier, and shallowest in December when the mixed layer is warmer and fresher (Figure 4.3d). Ekman pumping w_E (Figure 4.3e), computed from the curl of the wind stress $\left(w_E = \frac{1}{\rho f}\left[\frac{\partial \tau_y}{\partial x} - \frac{\partial \tau_x}{\partial y}\right]\right)$ is negative on average (downwelling) as would be expected since the mooring is located in a region of net subduction (Zhang and Talley, 1998; Karstensen and Quadfasel, 2002). There is also a strong seasonal cycle in w_E, with largest values in austral winter. These Ekman pumping velocities appear to influence the MLD (Figure 4.3d) which is deepest when downwelling is strongest.

The surface heat fluxes have weak seasonality except the Q_{SW} term (Figure 4.3f) which varies from ~ 150 Wm^{-2} during austral winter up to ~ 290 Wm^{-2} during summer. Winter time Q_{SW} is similar to year round Q_L values. The contribution of Q_{LW} and Q_S to the Q_{net} are small compared to Q_L. The annual mean of Q_{LW} is ~ 60 Wm^{-2} with a weak maximum in austral summer-spring. During austral winter, the ocean experiences a net heat loss at the surface due to reduced incoming Q_{SW}. In austral summer, the increased incoming solar radiation results in a net heat gain at the surface.

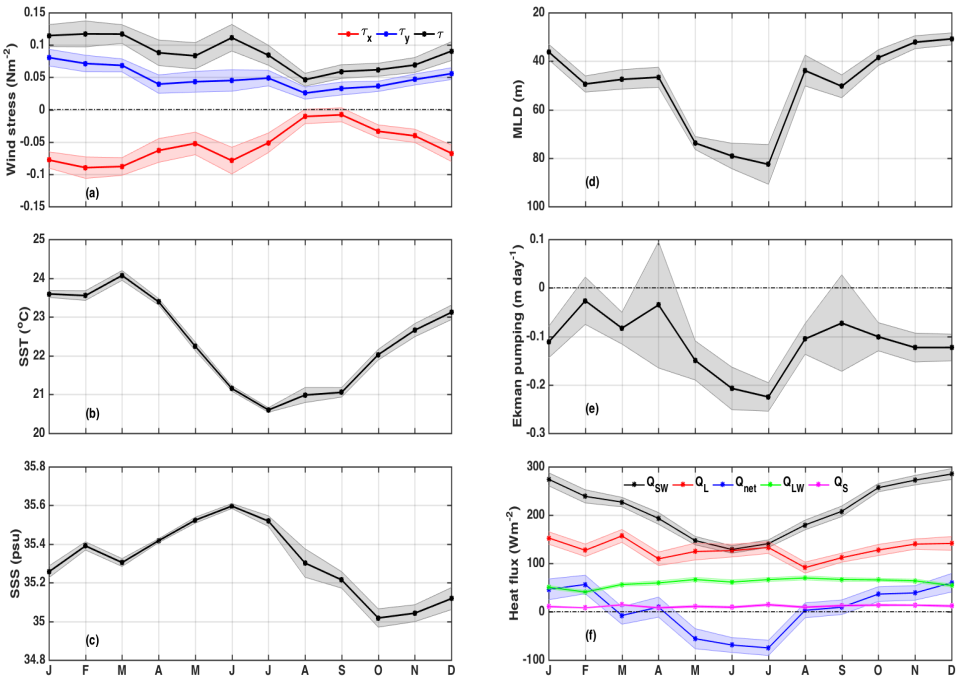

Figure 4.3: Monthly mean seasonal cycles of a) Wind stress and its components, b) SST c) SSS, d) MLD, e) Ekman pumping, and f) surface heat fluxes (Q_{SW}, Q_L, Q_{net}, Q_{LW}, Q_S). Shading shows one standard error.

4.4.3 Heat budget at 25°S, 100°E

The heat budget at the 25°S, 100°E RAMA mooring site is estimated as described in Section 3. Daily heat budget terms overlaid with 30 day smoothed values are presented in Figure 4.4. Q_{pen} is stronger during austral summer when the mixed layer is shallow (Figure 4.4b). The zonal advection is comparatively small during most of the mooring record whereas the meridional advection fluctuates more (Figure 4.4d and e). The daily fluctuations of all terms are substantial except for Q_{pen} (Table 4.1).

The daily heat budget terms are averaged to produce the mean seasonal cycle of the heat budget at the mooring location (Figure 4.5). The ocean gains heat ($\sim$ 50 Wm^{-2}) during austral summer and loses heat ($\sim$ 60 Wm^{-2}) during austral winter through the air-sea interface (Q_{net}, Figure 4.5, blue line). The Q_t heat storage term (Figure 4.5, red line) shows the cooling of the mixed layer during austral winter and warming during austral summer. Q_v (magenta line, Figure 4.5) has a 2 cycle per year variation with warming during austral winter and summer and cooling during austral spring and autumn. Q_u acts to cool the mixed layer in late summer (January – March) and then warms the mixed layer for the rest of the year. The combined effect of Q_u and Q_v is warming during early winter and early summer, significant cooling only in autumn, and little effect on the heat budget at other times. Q_{res} is the main driver of cooling throughout the year, reaching a peak of 80 Wm^{-2} in May and December and reducing to near

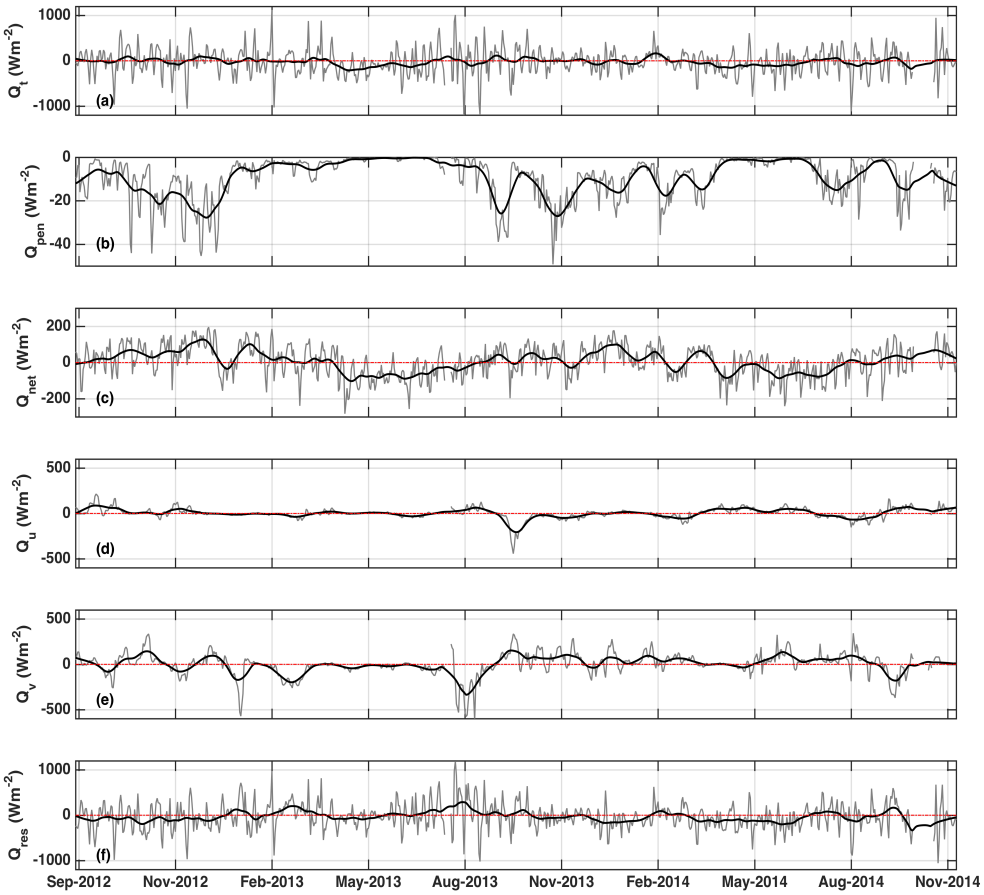

Figure 4.4: Daily estimates (grey line) of a) Q_t, b) Q_{pen} c) Q_{net}, d) Q_u e) Q_v and f) Q_{res} from the RAMA mooring at 25°S, 100°E. The black line is the 30 day smoothed time series. The zero line is highlighted in red.

zero in late summer and late winter. Therefore, Q_{res} is the primary cooling term during austral autumn – winter. Q_{net} is the second largest term. The warming during austral spring – summer is mainly driven by Q_{net} and secondarily by Q_v. The total advection is a non-negligible source of warming during the austral winter, greatly offsetting Q_{net}.

Q_{res} acts to cool the mixed layer throughout the year with the strongest cooling during October – January and April – July. The residual Q_{res} from the mooring analysis has a similar seasonal cycle to the residual in the eddy resolving model of Feng et al. (2008). The model residual is negative most of the year except during austral winter when the mixed layer depth is deeper. The model residual includes vertical mixing and penetrative solar radiation as well as unresolved processes. Possible reasons for the seasonality of Q_{res} are explored in Section 4.5.

Heat flux	Daily		Monthly
	Mean	Std.Dev.	Std.Dev.
Q_t	-20.25	313.68	68.92
Q_{pen}	-7.39	8.34	5.7
Q_{net}	6.19	85.2	49.55
Q_u	0.62	60.74	46.67
Q_v	3.53	128.61	82.71
Q_{res}	-30.86	314.35	99.41

Table 4.1: The mean and standard deviation (Wm^{-2}) of heat fluxes from the mooring for daily and monthly time series. The monthly standard deviation contains both seasonal and interannual variability. This includes influences from the La Nina conditions in early 2012 and the positive Indian Ocean Dipole event in 2012.

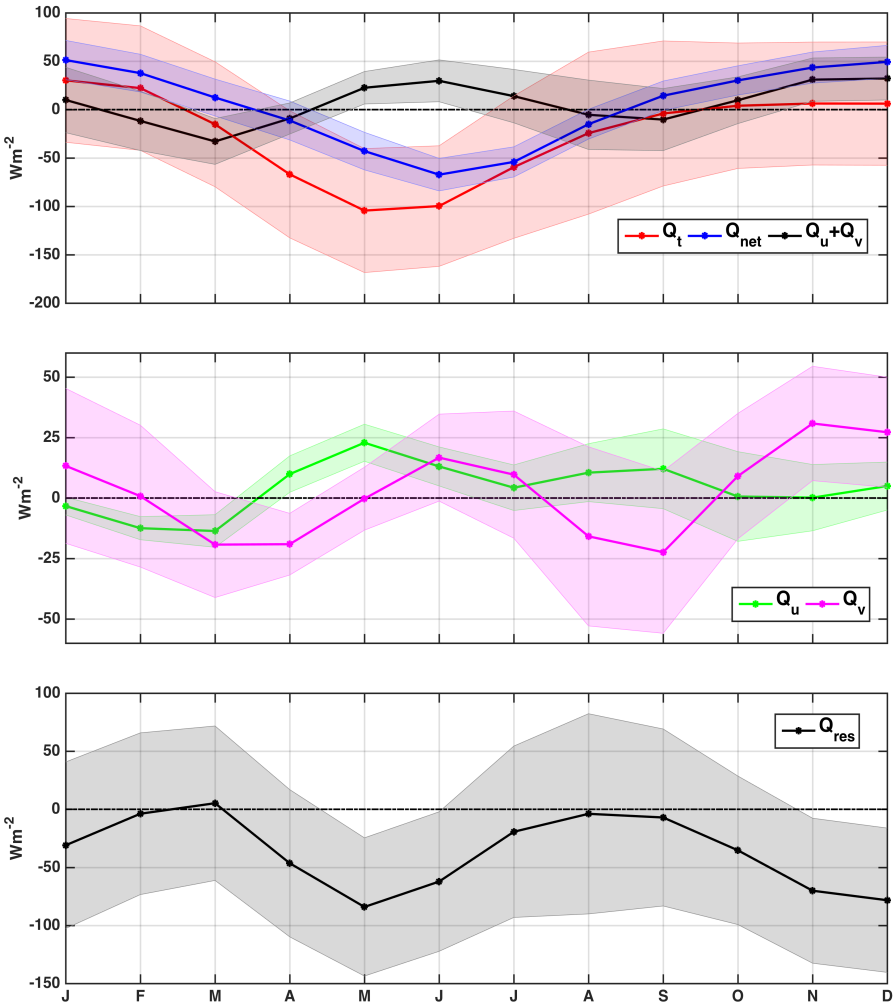

Figure 4.5: Seasonal cycle of Q_t, Q_{net}, Q_u, Q_v and Q_{res} from the RAMA mooring at 25°S, 100°E. The standard error for each term is shown in shading. All seasonal cycles are filtered by a 1-2-1 running mean filter.

4.4.4 Horizontal advection

We consider the two cycle per year of warming due to horizontal advection in light of the strong eddy field in this region (Morrow and Birol, 1998; Fang and Morrow, 2003; Feng et al., 2007; Jia et al., 2011b) We separated the advection terms into low-frequency (mean) and high-frequency (eddy) components to investigate the impact of eddies on the advection terms. For example, the advection term can be written as $\overline{Q_u} = -\rho \times C_p \times \left(\overline{u}\overline{H}\frac{\partial \overline{T}}{\partial x} + \overline{u'H'\frac{\partial T'}{\partial x}} + \overline{H}\overline{u'\frac{\partial T'}{\partial x}} + \overline{u}\overline{H'\frac{\partial T'}{\partial x}} + \frac{\partial \overline{T}}{\partial x}\overline{u'H'}\right)$, where overbar denotes monthly means and primes denote deviations from the monthly means (Zhang and McPhaden, 2010). Note that the velocities used are from OSCAR 5-day data and so do not resolve daily fluctuations. The decomposition shows that the eddy component dominates the mean component for both zonal and meridional advection (Figure 4.6), suggests that the high-frequency components play an important role in the advection terms.

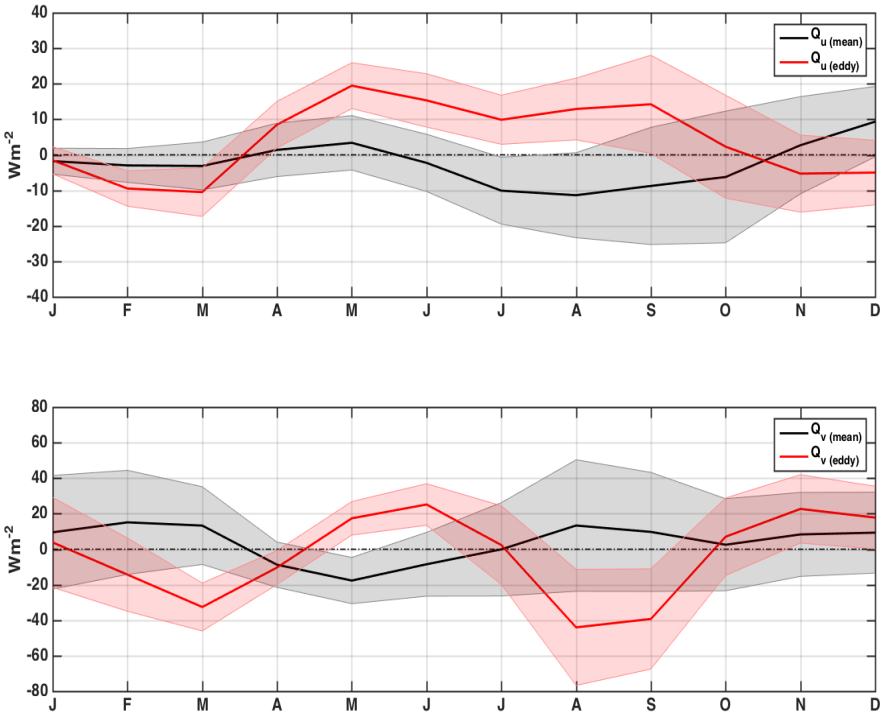

Figure 4.6: Time-longitude diagram of sea level anomaly (left panel) from AVISO, OSCAR zonal velocity (middle panel) and meridional velocity (right panel) during the mooring period at 25°S. The sea level anomalies propagate westward with a speed of ~ 6.3 cm s^{-1}.

The unusually strong EKE in this region with a maximum close to the eastern boundary, has been investigated in many studies to identify the source of the variability. Several possibilities have been suggested: Rossby waves with annual and semi-annual frequencies (Morrow and Birol, 1998); baroclinic instability of the LC leading to generation of the mesoscale eddies that propagate westward far into the Indian

Ocean (Fang and Morrow, 2003; Morrow et al., 2003; Feng et al., 2003, 2007); baroclinic instability of the eastward flowing SICC (Jia et al., 2011b) that generates eddies away from the coast. The Rossby waves propagating from the LC region are associated with propagating anomalies in both SST and SSH (Morrow and Birol, 1998) with peak anomalies in May and November. Morrow and Birol (1998) found SST anomalies of $\pm 1^{\circ}$C propagating through the basin with a lifetime of more than six months (their Figure 6). The LC transport, and the associated EKE close to the Australian coast, is strongest during austral winter and weaker during austral summer (Godfrey and Ridgway, 1985; Feng et al., 2003, 2007; Fang and Morrow, 2003). This is opposite in phase to peaks in EKE reported by Jia et al. (2011b) for the central Indian Ocean (15 – 30°S, 60 – 110°E) where they found highest EKE in austral summer and lowest in austral winter. This suggests a role for propagation of anomalies from the coast. Indeed, Jia et al. (2011a) found that the strongest EKE signals occur east of 90°E with decaying amplitudes towards the west.

We estimate the time taken for eddies generated in the LC to propagate westward to the mooring location using SSH variability. The slope of the time-longitude diagram of SSH (Figure 4.7, left panel) indicates a speed of propagation of 6.3 ms^{-1}. This is slightly larger than the propagation speed of nondispersive baroclinic Rossby waves at 25°S (Chelton et al., 2007). Eddies travelling due westward therefore take about 6 months to reach the mooring location from the coast of western Australia, arriving in November/December at the time of the summer peak in the heat advection (Figure 4.5). The peak SSH variability at the mooring location during the deployment period occurs from September – February (Figure 4.7), which could include inter-annual as well as seasonal variability. The summer peak in heat advection may also have a contribution from the local generation of eddies (Jia et al., 2011b). The zonal transport of the central and southern branches of the SICC (north and south of the mooring, respectively) reaches a maximum in September – October (Menezes et al., 2014). This coincides with the peak in vertical shear between the SICC and subsurface westward flow, and precedes the summer peak in EKE by 2 – 4 months (Jia et al., 2011b). Thus, the relationship between the timing of the winter peak in meridional advection and variability in the SICC is tantalizing and warrants further investigation.

Mechanisms driving the winter peak in heat advection at the mooring could include propagation of signals from the coast such as the annual and semi-annual Rossby waves identified by Morrow and Birol (1998), LC eddies, and local instabilities of the SICC near the mooring location (Jia et al., 2011b). We also note that some of the anomalies in Figure 4.7 do not seem to originate at the coast. Eddies in this region are known to propagate meridionally as well as zonally: warm core eddies tend to move equatorward and cold core eddies poleward (Morrow et al., 2004). Therefore, eddies may cut across our 25°S line, and appear to originate away from the coast when their origin at the coast is clear in SSH

animations.

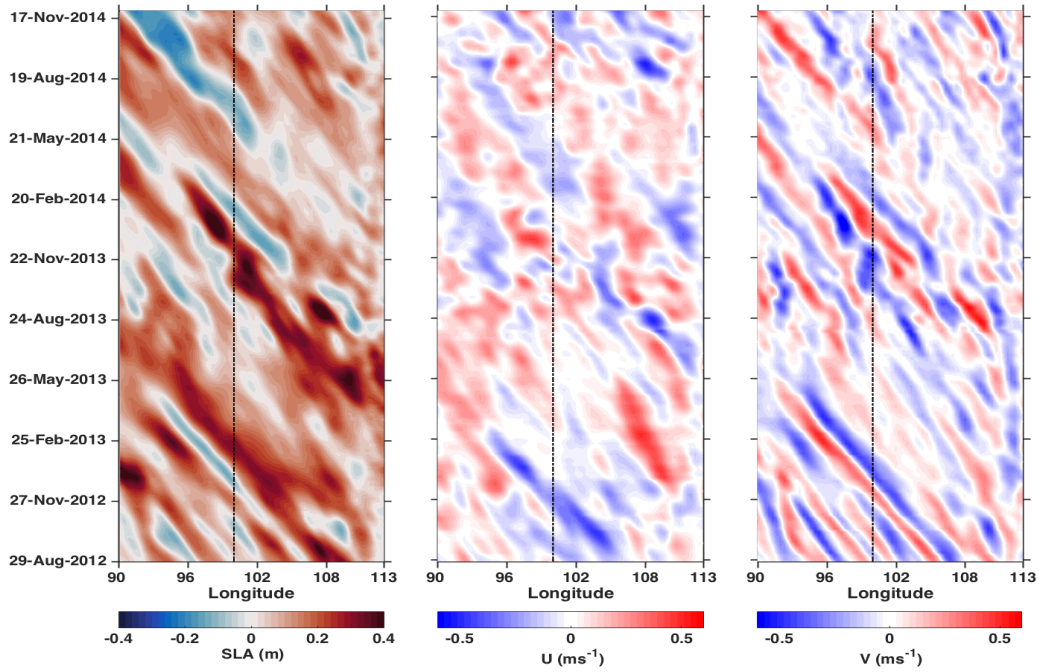

Figure 4.7: Time-longitude diagram of sea level anomaly (left panel) from AVISO, OSCAR zonal velocity (middle panel) and meridional velocity (right panel) during the mooring period at 25°S. The sea level anomalies propagate westward with a speed of ~ 6.3 cm s^{-1}.

4.4.5 Residual

The residual (Q_{res}) represents the effect of vertical processes such as turbulent heat diffusion, vertical advection, entrainment that cools the mixed layer, detrainment that warms the mixed layer when it shoals (Niiler, 1977; Cronin et al., 2015), neglected physical processes, and the errors in estimating other terms in the heat budget. The neglected physical processes include lateral induction and the effects of vertical movements of the thermocline due to adiabatic motions (Stevenson and Niiler, 1983). In principle, the detrainment is identically zero if the mixed layer is perfectly isothermal (Cronin et al., 2015) and it usually does not warm the mixed layer except if slightly colder water sheds off during mixed layer shoaling (Kim et al., 2007). The effect of large-scale entrainment mixing in cooling and deepening the mixed layer (Cronin et al., 2015) is usually larger than the detrainment warming. Therefore negative residuals are more likely to represent a physically meaningful process that cools the mixed layer. Positive residuals could be due to sampling and computational errors or due to some processes that we have neglected.

According to the turbulent energy balance of the surface mixed layer, turbulent entrainment can be driven by wind and buoyancy flux. The resulting entrainment velocity w_e can be written as (Niiler, 1977),

$$w_e = \frac{2mu_*^3 + \frac{H}{2}[(1+n)B - (1-n)|B|] + \left(H - \frac{2}{\gamma}\right)J}{c_i^2 - s|\Delta v|^2}. \tag{4.9}$$

Here we follow the notations of Foltz et al. (2010) where m, n, and s are proportionality constants, H is the mixed layer depth, $1/\gamma$ is the shortwave extinction depth, J is proportional to the surface shortwave radiation, c_i^2 is proportional to the buoyancy difference across the mixed layer base, and Δv is the difference of averaged mixed layer horizontal velocity from that at the mixed layer base. Also u_* is the friction velocity (Niiler, 1977; Foltz et al., 2010) where

$$u_* = \sqrt{\tau/\rho}. \tag{4.10}$$

Here τ is the wind stress and ρ is the ocean density. The buoyancy flux B can be written as (Foltz et al., 2010)

$$B = \alpha c_p^{-1} Q_{net} + \beta \rho S(P - E), \tag{4.11}$$

where α is the coefficient of thermal expansion and β is the saline contraction coefficient. Here, S is the sea surface salinity, P is the rate of precipitation and E is evaporation.

Q_{res} is weak during the beginning of austral spring and autumn compared to austral summer and winter (Figure 4.8a). The seasonal cycle of Q_{res} can be partially explained by that of u_*^3 and buoyancy flux (Figure 4.8b and c). During austral summer, the wind stirring drives entrainment when the mixed layer is shallow and there is gain of buoyancy. During austral winter, the wind stirring, augmented by buoyancy loss from the surface, drives the entrainment. The two sources of turbulence during austral winter can result in deeper mixed layers than in austral summer. Since the behaviour of friction velocity and buoyancy flux seems to partially explain the seasonal cycle of Q_{res} only during austral summer and winter, the residual flux may not be entirely driven by buoyancy flux and wind stirring.

Assuming m = 0.4 and n = 0.6 as in Foltz et al. (2010), we estimated the entrainment velocity using equation 4.9. We neglected the Δv term since we do not have velocity measurements from the mooring.

We also estimated entrainment velocity from the mixed layer depth variation as

$$w_e = H\left(\frac{dh}{dt} + w(-h)\right), \tag{4.12}$$

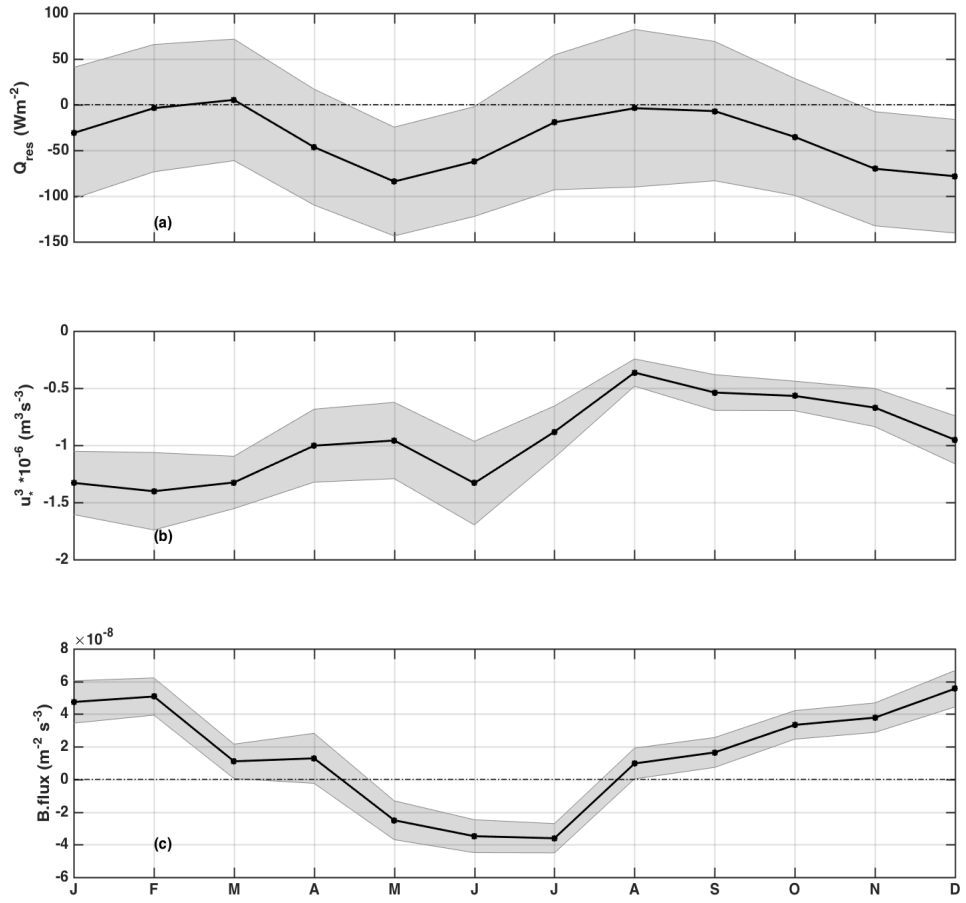

Figure 4.8: Seasonal cycle of a) Q_{res}, b) cube of friction velocity and c) buoyancy flux. Shading in all plots are the corresponding standard errors.

where $H = 0$ for $\frac{\partial h}{\partial t} \leq 0$ and $H = 1$ for $\frac{\partial h}{\partial t} > 0$. Here $w(-h)$ is the vertical velocity at the base of the mixed layer which is the time rate of change of the depth of an isotherm not far below the mixed layer. The w_e from this method is sensitive to the choice of the MLD and isotherm.

The entrainment heat flux due to w_e from both methods can then be written as $Q_e = \rho c_p \Delta T w_e$ where ΔT is the difference between average mixed layer temperature and the temperature at the base of the mixed layer.

The magnitude of the entrainment fluxes from equation (4.9) ($Q_{ent(N)}$) and equation (4.12) ($Q_{ent(-h)}$) is shown in figure 4.9a. The entrainment cooling from $Q_{ent(N)}$ and $Q_{ent(-h)}$ is comparatively higher during austral summer than austral winter in agreement with the residual from the heat budget. During austral winter, the cooling from $Q_{ent(N)}$ reaches a minimum whereas the heat budget residual is much higher. During austral spring and autumn, the cooling due to entrainment flux from both methods is

stronger than the residual which is assumed to be due to vertical processes. In an attempt to better resolve the residual, we also estimated a new residual ($Q_{res(N)}$ and $Q_{res(-h)}$) by explicitly including the entrainment fluxes in the heat budget. The new residuals are reduced during austral summer especially during November – December, when the entrainment cooling from both methods is high. During austral winter, explicitly accounting for $Q_{ent(N)}$ does not reduce the residual much whereas explicitly accounting for $Q_{ent(-h)}$ does (Figure 4.9b). However, $Q_{ent(-h)}$ is positive throughout the year except during the key cooling phase of the cycle, April – June. This could be due to a number of reasons such as 1) the noise in the heat budget calculation is underestimated, 2) the entrainment flux estimates do not fully capture the vertical processes, 3) the horizontal eddy processes are not fully captured with OSCAR velocities, 4) neglecting the detrainment, which is important when buoyancy fluxes re-stratify the mixed layer or 5) some combination of the above.

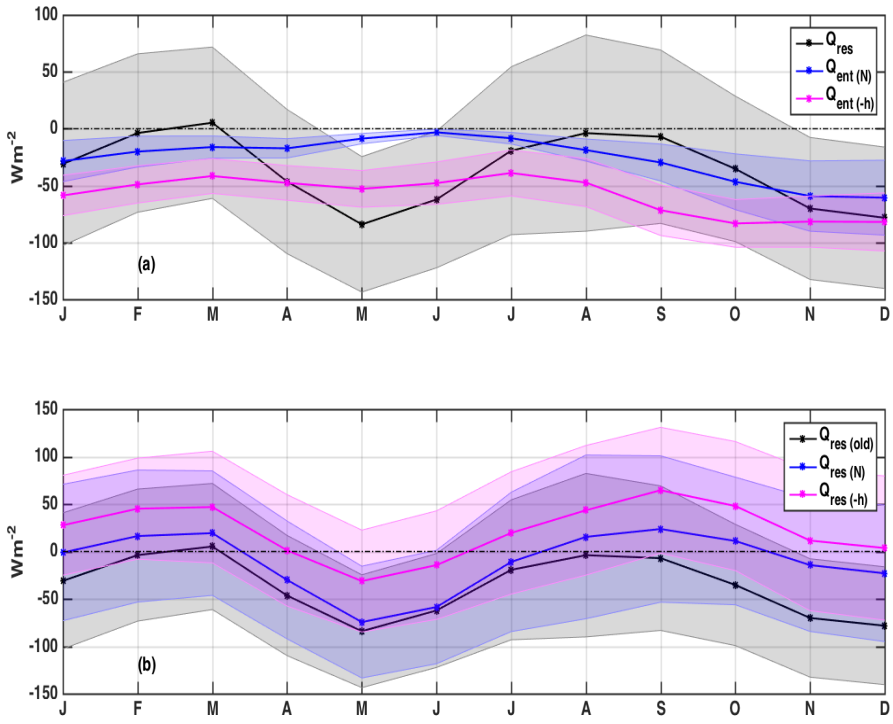

Figure 4.9: Seasonal cycle of a) Q_{res} (black), entrainment using equation 4.9 (blue) and equation 4.12 (magenta) and b) Q_{res} (black) as originally calculated and the residual with entrainment removed, where entrainment is calculated using equation 4.9 (blue) and equation 4.12 (magenta).

4.5 Mixed layer heat balance from TropFlux, Argo and OSCAR

The two year mooring record is relatively short to accurately quantify a seasonal heat balance. In order to support the mooring heat budget, we analyzed the upper ocean heat balance using daily reanalysis products and monthly Argo mixed layer depth data for the period 2004 – 2015 over a larger region around the mooring. The mooring is located at the northern edge of the subduction zone with deeper mixed layers toward the south (Figure 4.10).

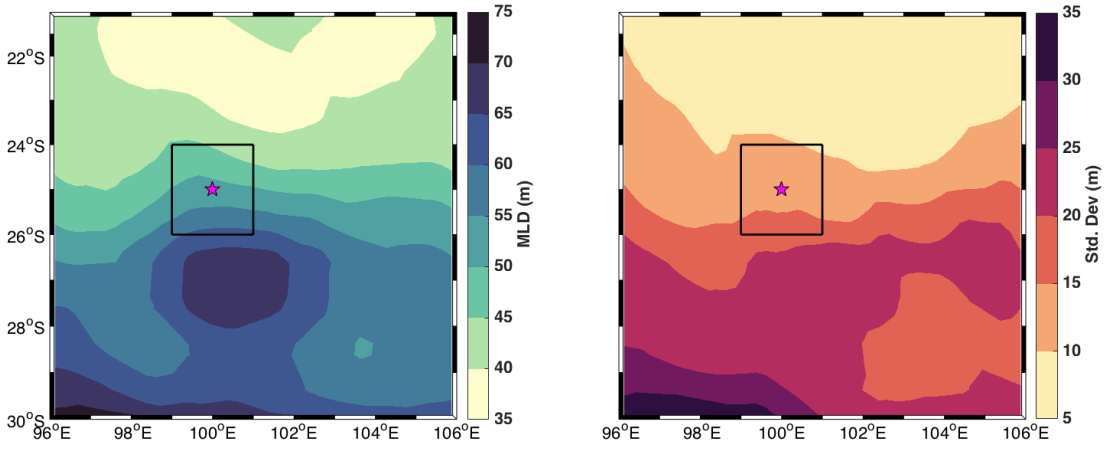

Figure 4.10: a) 12 year average and b) monthly standard deviation of mixed layer depth (m) from Argo data. The box encloses the region over which the seasonality of the heat budget terms are analyzed. The star represents the location of the mooring.

4.5.1 TropFlux adjustment

For the spatial analysis, we used the monthly averages of TropFlux shortwave radiation and net heat flux during 2004 – 2015 (Figure 4.11). When we compared the monthly averages of mooring fluxes with those from TropFlux, we found that the TropFlux shortwave radiation and net heat flux are underestimated during austral summer and winter with a difference in magnitude of ~ 50 Wm^{-2} during austral winter (Figure 4.11). This difference could be due to the fact that TropFlux was corrected using mooring data until only 2009 (Kumar et al., 2012) when the subtropical Indian Ocean mooring was not yet deployed.

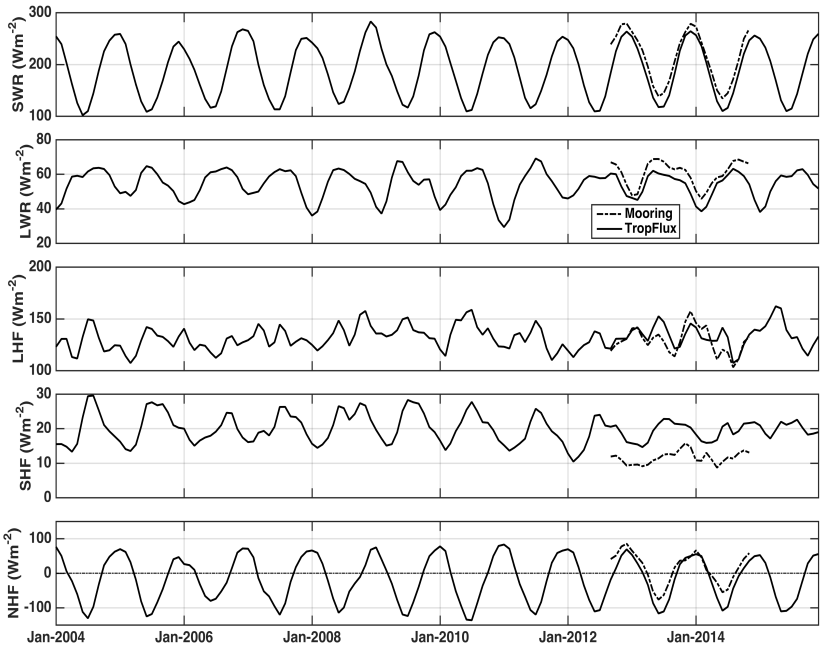

Figure 4.11: Monthly averages of surface fluxes from TropFlux (bold) and mooring (dashed) at the mooring location.

Therefore we used a linear regression to correct the TropFlux shortwave radiation and net heat flux against the mooring measurements (Figure 4.12). The mooring shortwave radiation and net heat flux are highly correlated with that of TropFlux (0.93 and 0.77 respectively) suggesting that the two data sets are coherent with one another. Using the empirical relations from the regression, we adjusted the TropFlux shortwave radiation and net heat flux for the full 12 year period and used the adjusted TropFlux data for the spatial analysis around the mooring site.

4.5.2 Spatial and temporal variability

The mean of mixed layer heat storage during 2004 – 2015 shows a stronger cooling trend to the northwest of the mooring (Figure 4.13a). This suggests that the loss of heat from the mixed layer during austral winter is not balanced by the heat gain during austral summer. The spatial distribution of Q_{pen} is in accordance with that of the MLD with less loss towards the south where the mixed layer is deep (Figure 4.13c-d). The mean of Q_{net} is weakly positive with less spatial variability throughout the region (Figure 4.13e-f) suggesting that the ocean gains heat through the air-sea interface in this region.

The spatial variability of advection terms is larger than that of the surface heat fluxes (Figure 4.14e-h)

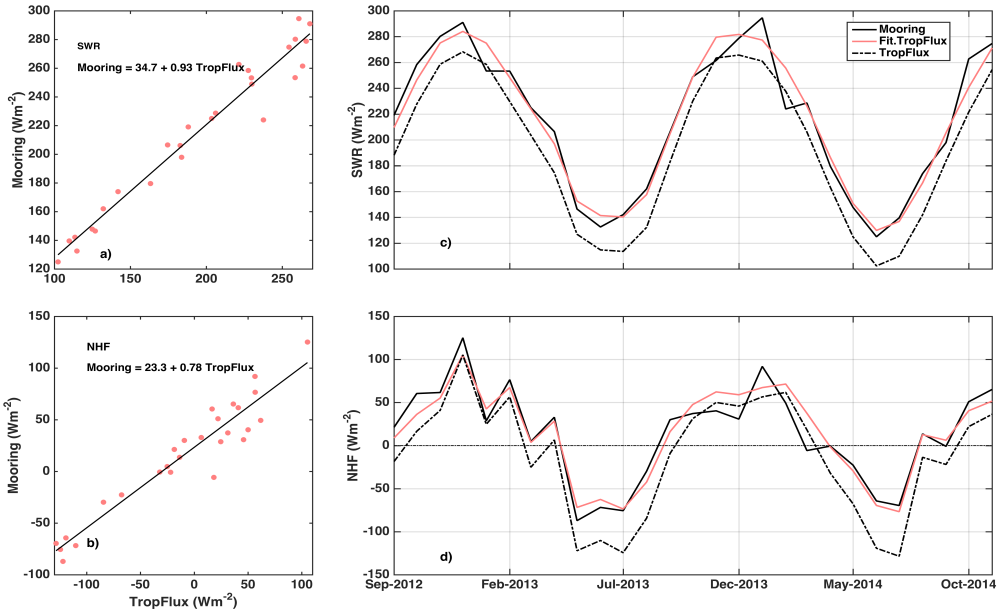

Figure 4.12: Linear regression (left panels) between mooring and TropFlux shortwave radiation and net heat flux and the fitted TropFlux fluxes with mooring and the actual TropFlux fluxes (right panels).

which could be related to the large eddy variability in this region (Section 4.4). The semiannual Rossby waves and eddies could be contributing to the advection terms. We separated the mean and eddy terms for the long term analysis at the mooring location as described in Section 4.4 and found that the eddy fluxes are large and dominate the zonal component of the total flux (not shown). The meridional eddy fluxes are of similar magnitude to the mean fluxes and have a 2 cycle per year variability as seen in the mooring analysis. On average, Q_u cools the mixed layer around the mooring whereas Q_v warms it. The warming from Q_v is stronger towards the south of the mooring. The spatial variability of Q_{res} is broadly similar to that of the advection which is highly variable compared to the surface heat fluxes. There are areas with evident positive residuals where possible sampling and computational errors may be prominent enough to overwhelm any signature of vertical mixing.

4.5.3 Heat balance around the mooring

Here we compare the seasonal cycle of 2 year mooring heat fluxes with the seasonal cycles of a) area averaged fluxes during 2004 – 2015 and b) fluxes at the mooring location for the mooring period from the spatial analysis (Figure 4.15). The seasonal cycle of Q_t in all cases shows net cooling in the mixed layer during austral winter and net warming in austral summer (Figure 4.15 a). The areal average of Q_t shows more warming than that at the mooring location during April – June and November – December.

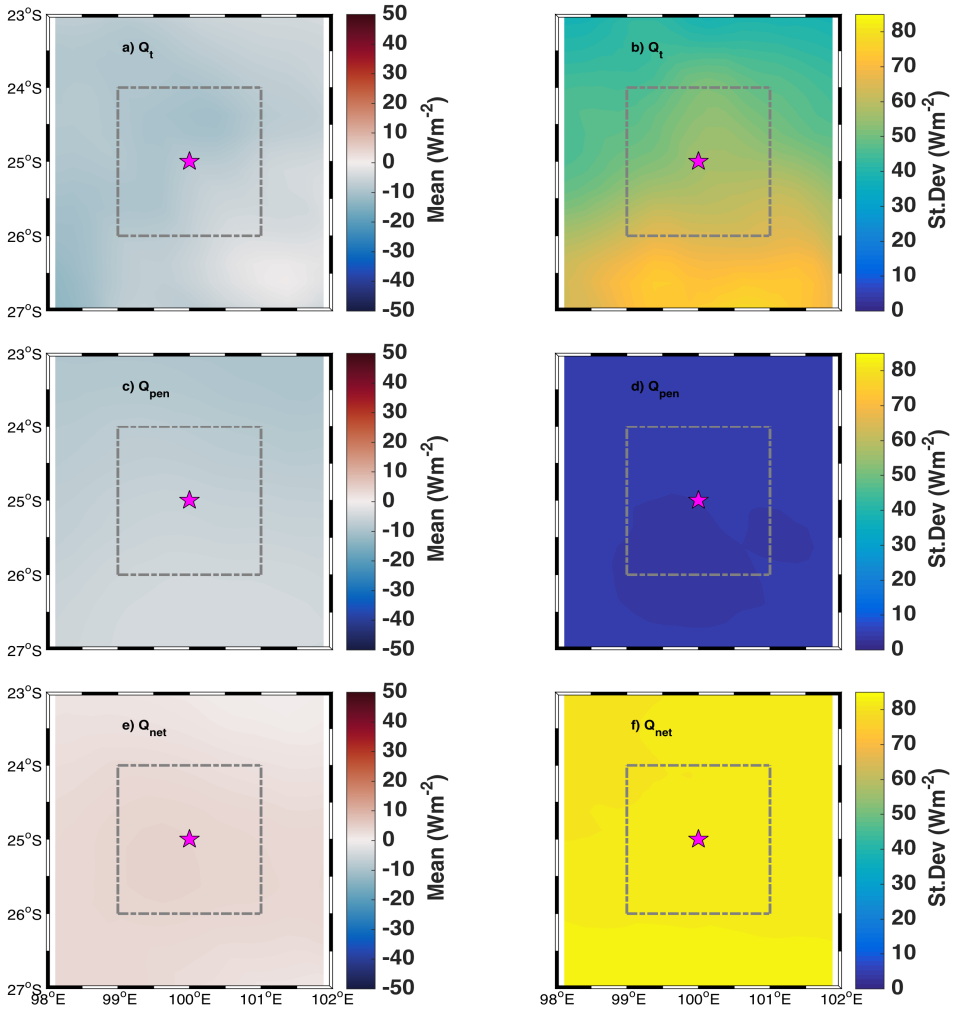

Figure 4.13: Annual mean (left panels) and standard deviation (right panels) of Q_t, Q_{pen}, and Q_{net} for the period 2004 – 2015. The box encloses the region over which the seasonality of the heat budget terms are analyzed. The star represents the location of the mooring.

The Q_{net} cycles are very similar from the three analyses with only a small residual since we did the adjustment to the TropFlux surface fluxes. The Q_t term is in phase with the Q_{net} suggesting that the surface fluxes play an important role in driving the mixed layer heat storage.

The areal average of Q_u shows a net cooling throughout most of the year except a slight warming in August and September. At the mooring location, the Q_u warms the mixed layer except during January – March. The Q_v term maintains the 2 cycle per year variability in all cases with peak warming during austral summer and winter. The areal average of Q_v shows net warming throughout the year whereas it cools the mixed layer during austral spring and autumn at the mooring location.

The Q_{res} flux at the mooring location shows similar seasonal cycle with variations in magnitude. The areal average has comparatively weak seasonal cycle. The spatial budget from the regional analysis for

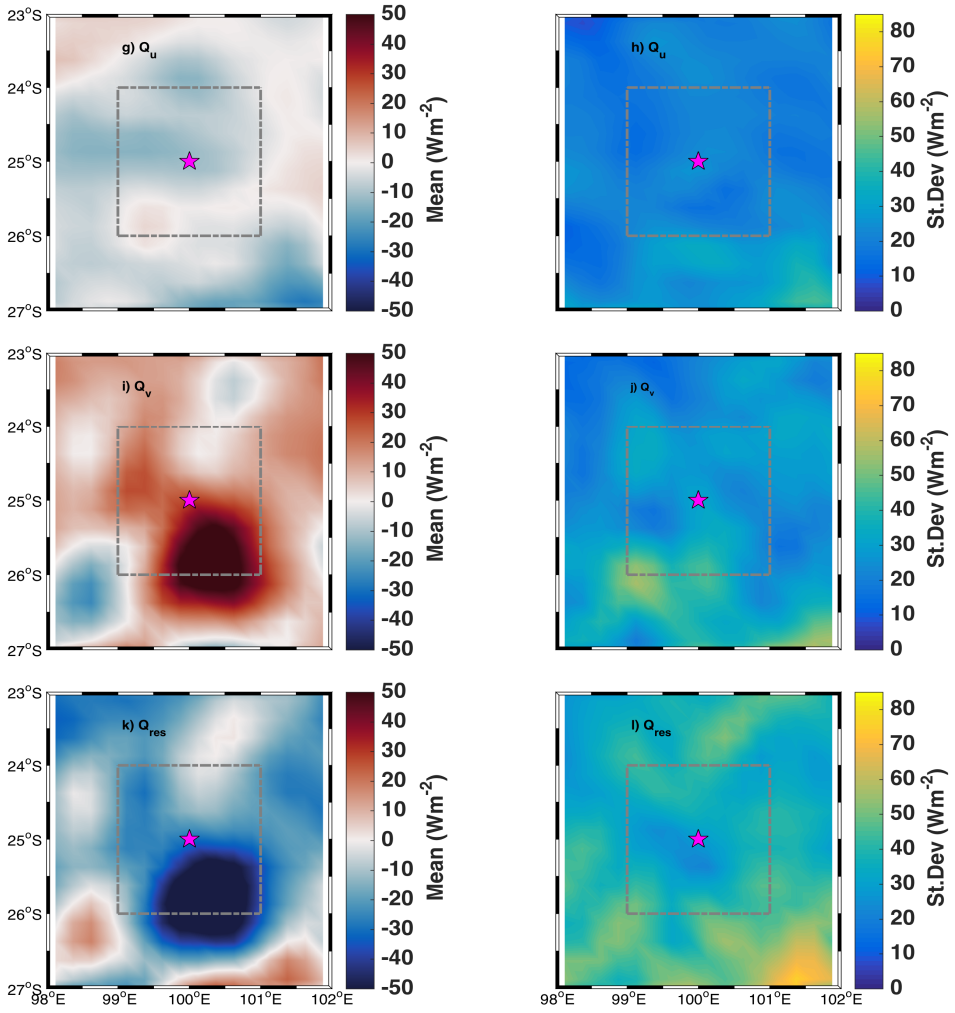

Figure 4.14: Same as in Fig.4.13 but for Q_u, Q_v, and Q_{res}.

12 years and for the mooring period suggest strong vertical processes at work during austral summer and winter in agreement with the conclusion that we obtained from the mooring analysis. The cooling from residual is stronger from the mooring analysis than that from the regional analysis during May – December. We also calculated the seasonal cycle of the spatial average of entrainment flux using equation 4.12 and found it to be very small (not shown). It is possible that entrainment calculated from the gridded data is consistently underestimated due to any or all of the reasons mentioned in Section 4.5.

4.6 Discussion and conclusions

In this study, we have quantified the seasonal heat budget of the mixed layer in the southeast Indian Ocean at 25°S, 100°E for the first time using *in situ* observations. This region is characterized by year-long

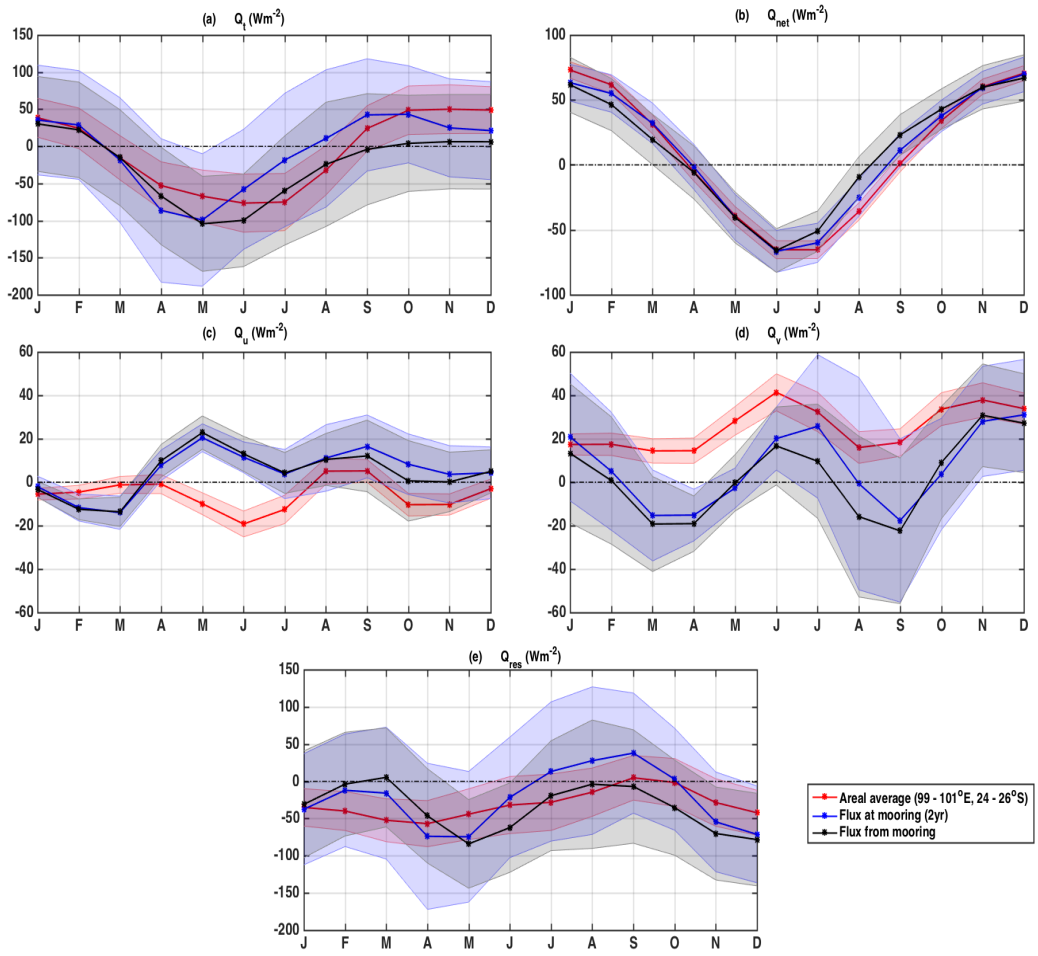

Figure 4.15: Seasonality of a) Q_t, b) Q_{net}, c) Q_u, d) Q_v and e) Q_{res} overlaid with standard error shading which in great part represents interannual variability. Note that the vertical axes are different. The red line in all plots is the areal average of heat fluxes in a $2^\circ \times 2^\circ$ box around the mooring location during 2004 – 2015. The seasonality of heat fluxes interpolated at the mooring location for the mooring period is shown in blue. The black line is the seasonality of heat fluxes from the mooring observations. All seasonal cycles are filtered with a 1-2-1 running mean filter.

Ekman downwelling and strong air-sea fluxes. For this study, the rate of change of heat storage and air-sea fluxes were obtained primarily from the RAMA mooring at 25°S, 100°E and the horizontal advection terms were estimated using Reynolds SST and OSCAR velocities. The vertical heat fluxes through the base of the mixed layer are estimated as a residual. Assuming that the errors in estimating the heat budget terms are correctly characterised in Figure 4.5, the residual can be interpreted as comprising of turbulent heat diffusion, vertical advection, lateral induction, entrainment and neglected physical processes. The heat budget from the 2-year *in situ* data is complemented by a heat budget calculated using a 12-year time series from the TropFlux reanalysis and Argo, both at the mooring location and in a $2^\circ \times 2^\circ$ box around the mooring. After first correcting the reanalysis surface fluxes using the observed fluxes at the mooring, this heat budget analysis provides a longer term context for understanding the processes that

drive the surface layer heat budget in this region.

We have shown that the mixed layer heat balance in this region is dominated by surface net heat flux. Despite the uncertainties in the entrainment calculation, it has a good agreement with the residual especially during austral summer, autumn and early austral winter. For most of the year, the vertical subsurface fluxes contribute more to the mixed layer heat balance than the horizontal advection, which is influenced by eddies and possibly annual and semi-annual Rossby waves. Of the surface heat fluxes, Q_{SW} and Q_L are the two dominant terms. The contribution of Q_{LW} and Q_S to Q_{net} is comparatively small. The Q_{net} tends to warm the mixed layer during austral summer and cool during austral winter. The penetrative component of short wave radiation is a large term in the balance during austral summer when the mixed layer is shallow. Among the heat budget terms in Figure 4.5, zonal advection makes the smallest contribution to the mixed layer heat balance. It warms the mixed layer throughout the year except during January – March. Meridional advection has more influence on the mixed layer temperature by warming the mixed layer during austral winter and summer and cooling it during austral spring and autumn. During austral summer, all heat flux terms tend to warm the mixed layer, with Q_{net} and Q_v contributing more compared to Q_u. The cooling by vertical processes keeps the mixed layer temperature from becoming even warmer. During winter, horizontal advection of heat tends to warm the mixed layer whereas the Q_{net} and vertical processes cool the mixed layer.

As discussed in WM99, horizontal advection seems to be sensitive to the location and the time period for which it is calculated (Figure 4.14g-j). At the mooring location, the meridional advection has a 2 cycle per year variability. The warming by meridional advection during winter may be associated with generation of eddies due to local baroclinic instability near the mooring (Jia et al., 2011a). The warming by meridional advection in austral summer could be due to the arrival of Leeuwin Current eddies 6 months after they form at the coast during winter when the Leeuwin Current is strongest and most baroclinically unstable (Feng et al., 2003, 2007). Wesward propagating annual and semi-annual Rossby waves (Morrow and Birol, 1998) may also contribute to both summer and winter peaks in heat advection. The variability of the geostrophic current is larger than that of the Ekman current suggesting that the geostrophic component of velocity dominates meridional advection in the mixed layer. The seasonality of meridional advection at the mooring location is quite different from that in the LC region in an eddy resolving model (Feng et al., 2008). However, the model agrees with the mooring analysis that meridional advection is one of the dominant terms in driving the mixed layer temperature in spite of the large uncertainties. The residual from the mooring analysis has a 2 cycle per year variability which mainly reflects the fact that the total advection has two large warming phases and two much weaker and time-compressed cooling phases.

The strong seasonal cycle of Q_{net} in this subtropical region with warming in austral summer and strong cooling in austral winter is quite different to that found in the tropics where Q_{net} is warming throughout the year (Wang and McPhaden, 1999; Yu et al., 2007; Foltz et al., 2010; Vialard et al., 2008). The meridional advection term is found to be a significant contributor to the heat balance in both equatorial and subtropical zone heat budget studies; these include the equatorial Pacific, where meridional heat advection is mainly due to tropical instability waves (Wang and McPhaden, 1999), and the southwestern tropical Indian Ocean due to strong seasonally varying surface currents and SST gradients (Foltz et al., 2010), and the subtropical convergence zone of the North Atlantic due to northward advection of fronts (Rudnick and Weller, 1993). In our study of the eastern subtropical Indian Ocean, we suggest that the meridional heat advection is dominated by eddy fluxes and annual and semi-annual Rossby waves at the mooring location.

There are a number of limitations to this study. The unavailability of direct velocity measurements from the mooring made it difficult to estimate the advection terms accurately. In place of mooring velocities, we used 5-day OSCAR currents interpolated to a daily time step to match the mooring time series. This may result in an overestimation of the uncertainty of the OSCAR product. Also due to the lack of subsurface velocity observations at the mooring, we neglected the shear across the base of the mixed layer when estimating entrainment velocity, which is a key source of turbulence. This resulted in underestimating the corresponding entrainment flux.

As discussed above, the ocean dynamics in this region are quite different from other regions where the heat budget has been analyzed. The interaction between the eastward flowing SICC and westward propagating mesoscale eddies/Rossby waves in this region makes the ocean dynamics very complex. Vertical processes were not well resolved in our study, hence potentially important subsurface fluxes originating from meso-to-submesoscale eddy activity (Griffies et al., 2015; Cummins et al., 2016; Morrison et al., 2013) and subduction (Spall et al., 2000) of Subtropical Water are unaccounted for. Future analysis of a high-resolution, well-validated dynamical model that captures these interactions is required to fully resolve the processes responsible for modifying the mixed layer temperature in this region.

Chapter 5

Summary and conclusion

5.1 Research Overview

A remarkable feature of the upper ocean circulation in the south Indian Ocean is the eastward flowing near-surface geostrophic currents. They are remarkable because they flow against the Sverdrup gyre circulation and the wind-driven surface Ekman flow. Eastward flows exist in the subtropics of other ocean basins, but they are much weaker than those in the south Indian Ocean, and they don't extend all the way to the eastern boundary. These zonal flows act as a source of water for the Leeuwin Current, which is the only poleward flowing mid-latitude eastern boundary current in the world. The eddies generated from the instabilities of the Leeuwin Current and annual and semi-annual Rossby waves propagate offshore from the eastern boundary into the region of the eastward flows. These features result in an intense mesoscale eddy field in this region, which is identified as a high eddy kinetic energy band that extends all the way across the basin. They also contribute to the heat and fresh water exchange in this region, which makes this ocean basin lose more heat to the atmosphere than any other subtropical basins. The co-existence of these phenomena indicates interactions between the atmosphere and ocean, and across scales of motion in the ocean which contributes to the uniqueness of this region.

Many aspects of the South Indian Ocean dynamics are still not well known, primarily due to a lack of observations. The near-inertial internal waves possess most of the energy in the internal wave spectra. They interact with mesoscale eddies and play an important role in transferring wind energy into the ocean interior. However, up until now, there have been no observations capable of investigating the near-inertial wave field in this region. In this study, our new observations revealed that more than 40% of the wind work done on near-inertial motions is associated with downward propagating near-inertial waves below mixed layer. Strong near-inertial internal waves are seen to propagate into the ocean interior below 700 m, with the potential to contribute to deep ocean mixing. This suggests that the near-inertial internal waves could play an important role in providing energy to maintain deep ocean stratification in the southeast Indian Ocean.

Ocean modelling studies show that the large-scale circulation in this region is sensitive to vertical mixing. However, the existing estimates of turbulent mixing differ in their magnitudes and many are drawn from studies that have no information about velocity shear. We found that our estimates of dissipation rate and diffusivity from fine-scale shear and strain observations match in magnitude with direct microstructure measurements of previous studies such as the global study Waterhouse et al. (2014) and parameterization estimates of Kunze et al. (2006). In contrast to previous studies, we found that cyclonic eddies contribute substantially to turbulent mixing in the ocean interior associated with downward propagating internal waves, especially below 500 m. This has implications on the internal wave energy distribution in high

EKE regions such as the Antarctic Circumpolar Current where anticyclonic eddies are thought to be the primary contributor to the turbulent mixing in the upper 500 m (e.g. Whalen et al., 2018).

The reanalysis products disagree on their magnitude of heat fluxes in the southeast Indian Ocean, which makes it difficult to understand the role of air-sea fluxes in mixed layer properties of this region. By comparing the fluxes in reanalysis products with that measured by a flux mooring, we found that TropFlux products can best describe the air-sea interactions in this region. We also analysed the seasonal cycle of the surface layer heat balance in this region and found that on seasonal timescales, mixed layer heat storage in this region is mostly balanced by a combination of surface fluxes and turbulent entrainment with a contribution from horizontal advection at times.

The work of this thesis has improved our understanding in these areas by examining the different scales of motion and the interactions between them in the southeast Indian Ocean using a collection of observational data sets, reanalysis products and satellite altimetry. Our results strongly show that mesoscale eddies and annual and semiannual Rossby waves generated from the eastern boundary play an important role in driving the ocean dynamics in this region. With the availability of high resolution data from EM-APEX floats, it has been made possible to analyse the near-inertial internal wave field and turbulent mixing variability in this climatically important region for Australia. The only flux mooring in the entire subtropical Indian Ocean provided 2-years of surface fluxes data which allowed us to do a mixed layer heat budget.

Specifically, this study was designed to:

- characterize the spatial and temporal variability of the near-inertial internal waves in the southeast Indian Ocean
- estimate the strength and distribution of turbulent mixing due to internal wave breaking and their sources
- investigate the role of mesoscale eddies in modifying internal waves, turbulent mixing and water-mass characteristics in this region
- investigate the relative roles of air-sea interaction and ocean circulation in setting the mixed layer properties and stratification

5.2 Contributions

Each of the above objectives has been addressed in the thesis chapters, summarized as follows:

Characterize the spatial and temporal variability of the near-inertial internal waves in the southeast Indian Ocean (Chapter 2)

- Velocity measurements collected from three deep (up to 1200 m) and one shallow (up to 300 m) floats, profiling for four months in the southeast Indian Ocean, were analysed to identify near-inertial internal waves. The near-inertial peak in the velocity rotary spectra and the mirror-imaging of velocity profiles which are half an inertial period apart confirms the presence of near-inertial waves.

- A total of 15 near-inertial internal waves with a mean amplitude of 10 cm s^{-1} were identified in the data with a mean vertical wavelength of 89 m, a mean horizontal wavelength of 69 km, a mean horizontal group velocity of 3 cm s^{-1} and a mean vertical group velocity of 9 m day^{-1}.

- Wind is found to be the main source of near-inertial internal waves in the upper 1000 m where most of the beams propagate down into the ocean interior. More than 40% of the wind work is transferred into the ocean interior by downward propagating near-inertial waves.

- Strong near-inertial beams are found to propagate below 700 m suggesting that the breaking of these waves can contribute to deep ocean mixing.

- A blue-shift of 10 – 15% is observed in the frequency of the near-inertial wave field indicating propagation toward the equator from the wave generation region, in agreement with theory.

Estimate the size and distribution of turbulent mixing due to internal wave breaking and their sources (Chapter 3)

- The spatio-temporal variability of turbulent mixing caused by the breaking of internal waves is estimated from the three deep EM-APEX floats and shipboard CTD data using fine-scale parameterization, and compared with direct measurements of mixing from microstructure profilers.

- Diffusivity is estimated from the floats using both shear (velocity) and strain (density) data. The float estimates using fine-scale parameterization have a mean difffusivity of $O(10^{-6}$ $m^2s^{-1})$ in the upper 250 – 500 m and diffusivity of $O(10^{-5}$ $m^2s^{-1})$ at 500 – 1000 m. Using only strain information, the diffusivity estimates from the shipboard CTD are of $O(10^{-6}$ $m^2s^{-1})$ in the upper 1000 m.

- Elevated diffusivity of $O(10^{-3}$ $m^2s^{-1})$ is associated with near-inertial internal waves near the sea surface in warm core eddies, internal waves in cold core eddies and flow near topography.

- The fine-scale parameterization from both floats and shipboard CTD overestimates the direct measurements of turbulent mixing from microstructure profilers in the depths where they overlap (240 – 300 m). However, shear-strain parameterization from the floats and strain-only parameterization from shipboard CTD match well below 300 m since the shear-strain ratio used in the strain-only method is estimated from measurements of shear and strain from the floats.

Investigate the role of mesoscale eddies in modifying internal waves, turbulent mixing and watermass characteristics in this region

- Elevated near-inertial shear variance is observed in near-surface anticyclonic eddies and not in cyclonic eddies, suggesting that the waves are being trapped by the vorticity field of the anticyclonic eddy (Chapter 2).

- The trapping of near-inertial waves by the anticyclonic eddies results in elevated mixing near the ocean surface (Chapter 3).

- Elevated mixing in cold core eddies below 500 m, that could be associated with capturing of internal waves by the strain field of the eddy (Chapter 3).

- Higher diffusivity is associated with AAIW whereas comparatively low diffusivity is observed in the SAMW density layer especially in cyclonic eddies. In contrast, the SAMW properties are strongly modified in cyclonic eddies whereas the AAIW properties remain unchanged (Chapter 3).

- Elevated diffusivity is observed in regions of SICC jets associated with mesoscale eddies suggesting that the turbulent mixing may be important in the evolution of the jet-like structure of the SICC (Chapter 3).

Investigate the relative roles of air-sea interaction and ocean circulation in setting the mixed layer properties and stratification (Chapter 4)

- The seasonal cycle of the mixed layer heat budget in the southeast Indian Ocean is analysed using the first moored time series of air-sea fluxes from a RAMA flux mooring.

- The seasonal cycle of the surface mixed layer heat budget is primarily dominated by surface net heat flux and secondarily by turbulent entrainment with a contribution from horizontal advection at times.

- The horizontal advection is dominated by mesoscale eddies and annual and semi-annual Rossby waves propagating from the eastern boundary.

- The 2-year mooring analysis was compared with a 12-year heat budget analysis over a small region around the mooring location and found that they are in reasonably good agreement implying that the mooring time series is a good representative of the region.

5.3 Future directions and implications

- Coherent feature analysis

  The turbulent mixing estimates show that there are mixing patches at regions where near-inertial beams were not observed (Fig. 5.1). This suggests that internal waves with other frequencies also contributed to the observed mixing. A coherent feature analysis combined with the observed mixing patches would help to bring out the internal waves of all frequencies in the data. It will be interesting to compare the demodulation with the spectral analysis. This problem will be analysed in a future study.

  There are strong near-inertial beams propagating deep into the ocean and a brief analysis suggests that they may be generated remotely at the surface and propagated into the region where the floats were profiling. A ray tracing analysis to trace back the beams to their origin and look at the evolution of the beam over space and time would be an interesting future study. This would also help us to understand the interaction of the beams with mesoscale eddies during their generation and propagation.

- Shear measurements

  The turbulent mixing estimates we have combined from different instruments at different depths demonstrate the importance of having shear information to improve estimates of mixing. We used the shear-to-strain ratio estimated from the float data to calculate mixing from the shipboard CTD with a strain-only parameterization. The float (shear-strain) and shipboard CTD (strain-only) parameterization estimates agree well with each other, and with colocated VMP estimates. Global estimates of turbulent mixing would be more robust if a varying shear-to-strain ratio was used. This would require characterisation of the spatial distribution of shear variance from historical velocity observations.

- Long time series of velocity

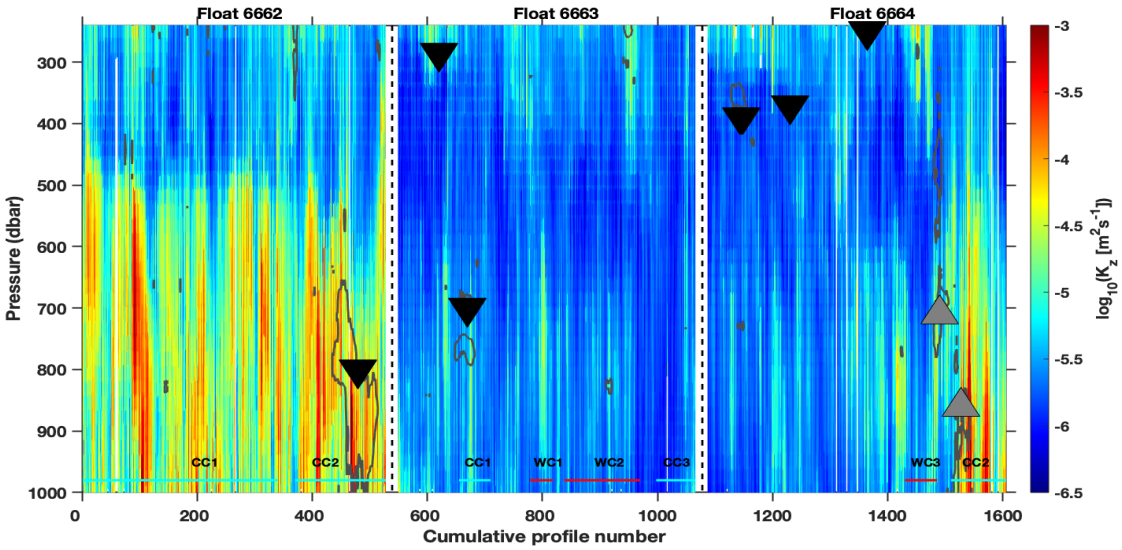

Figure 5.1: The turbulent diffusivity along the float tracks (color shading). The downward (black inverted arrows) and upward (grey arrows) propagating near-inertial waves identified from demodulation below 250 m is also marked. The grey contours are the near-inertial amplitudes larger than 0.1 ms^{-1}.

The mixed layer heat budget analysis revealed that horizontal advection and mesoscale eddies play an important role in determining the mixed layer temperature. Longer time series and direct velocity measurements from more flux moorings would improve the understanding of the evolution of mixed layer temperature in this climatically important region and would provide a better understanding of the physical processes in play. Also long time series of velocity measurements from moorings would aid in increasing the estimates of turbulent mixing and would also provide long time series of mixing estimates which are currently rare (Ivey et al., 2018).

5.4 Final remarks

The southeast Indian Ocean is a region of strong air-sea exchanges where small-scale features such as internal waves interact and coexist with the large-scale circulation and mesoscale eddies. Mesoscale eddies contribute to the turbulent mixing distribution and mixed layer properties and stratification in this region, which can impact the large-scale circulation and marine ecosystems. Thus mixed layer slab models should include the effect of eddies in distributing wind energy into the ocean interior.

Turbulent mixing helps to distribute heat, salt and nutrients throughout the ocean interior, which also plays an important role in nurturing the marine ecosystems. The marine environment of the south Indian Ocean has significant economic value for Australia through fisheries, and oil and gas extraction. The

high-resolution observations from the EM-APEX floats have provided more accurate estimates of turbulent mixing in this region. These estimates of mixing can be included in ocean circulation models to simulate the large-scale circulation and air-sea interactions more accurately.

Appendix A

Supporting Materials

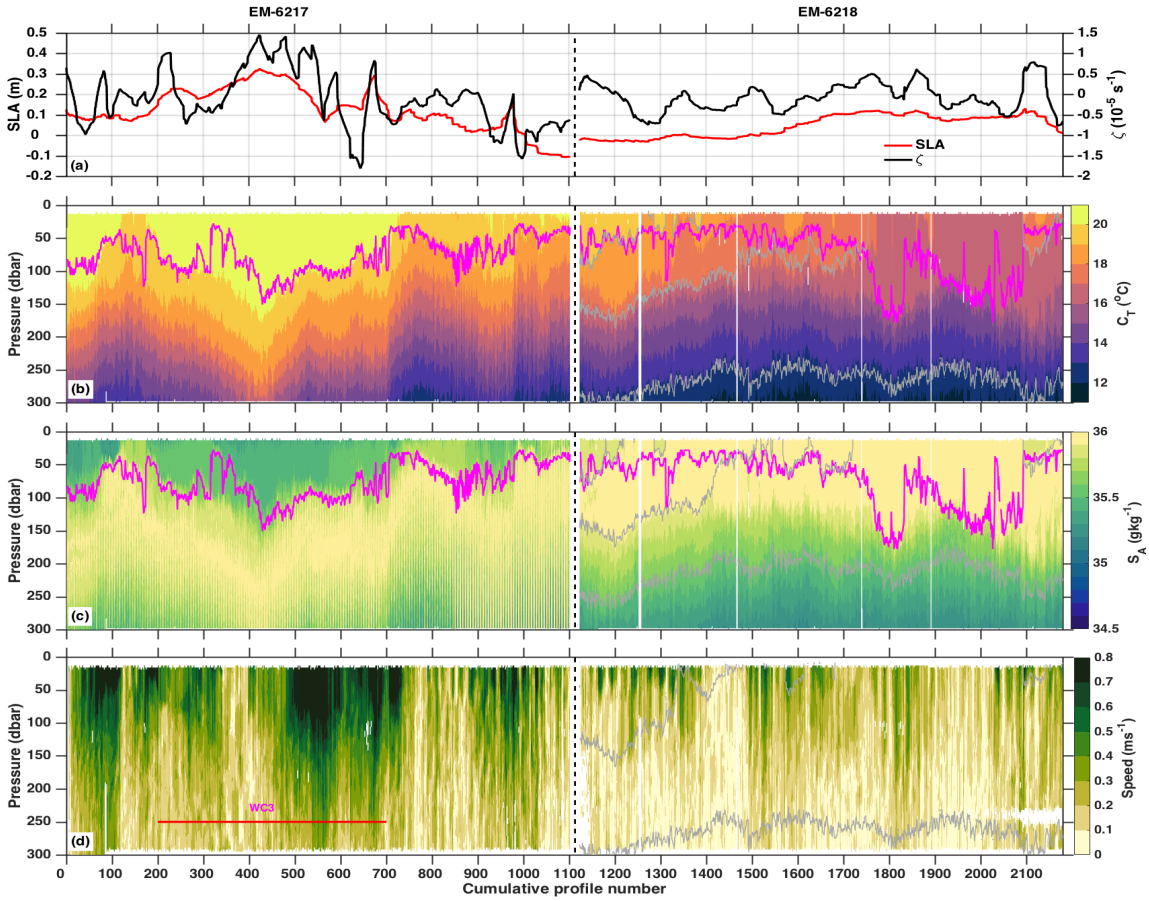

Figure A.1: Same as in Fig. 2.4 but for the shallow floats, EM-6217 and EM-6218.

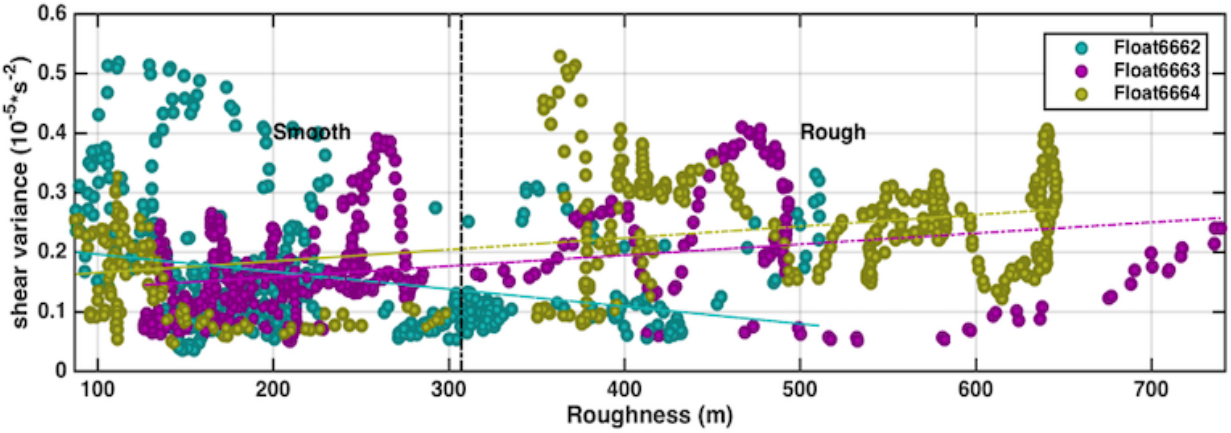

Figure A.2: Same as in Fig. 2.12 but for all deep floats EM-6662, EM-6663 and EM-6664.

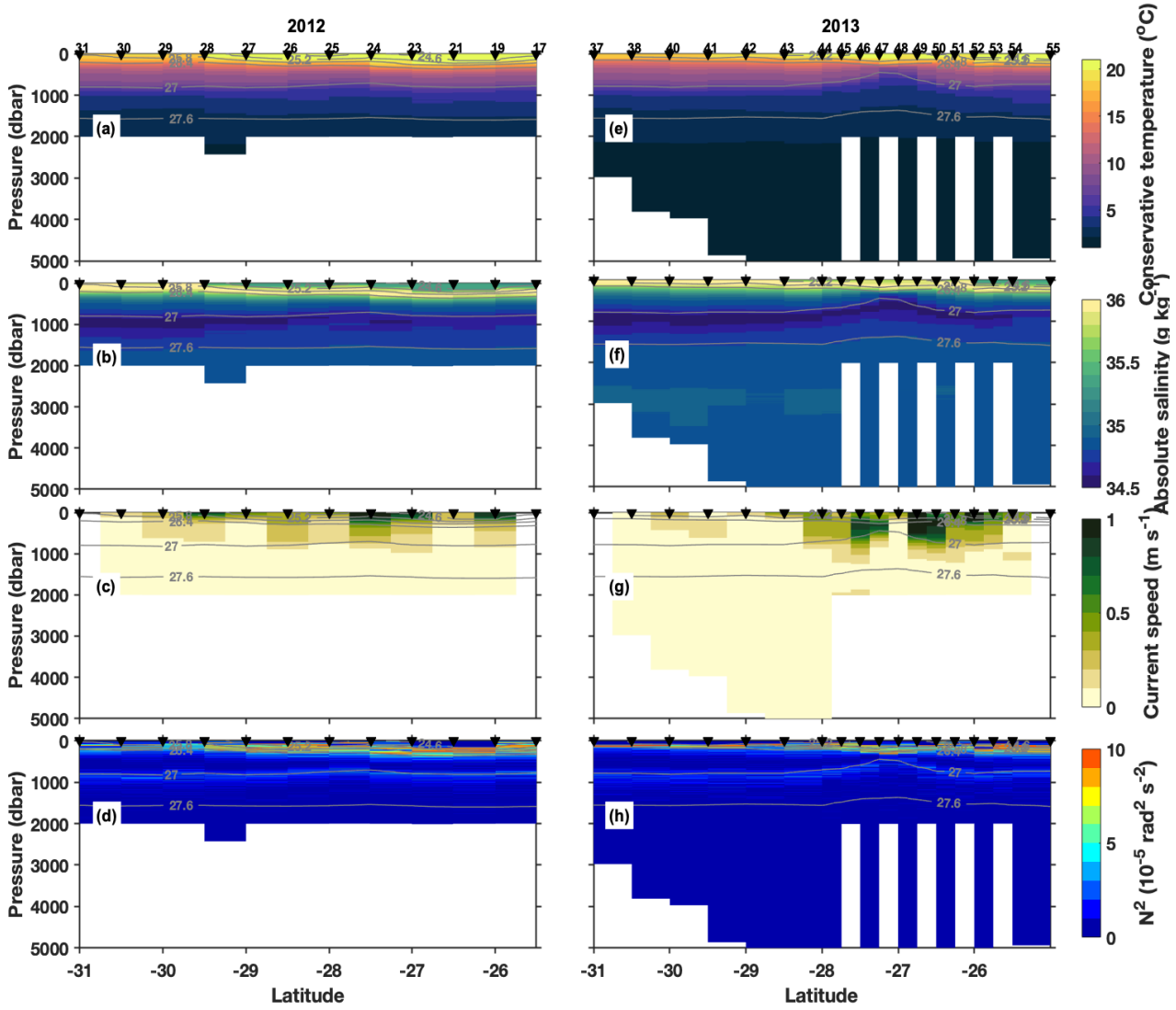

Figure A.3: Full depth plots of a) conservative temperature, b) absolute salinity c) geostrophic speed and d) buoyancy frequency in 2012. Panels e), f), g), and h) are the same for 2013. Station numbers are marked at the top of conservative temperature (a and e). The light grey lines are isopycnals with an interval of 0.7 kg m^3.

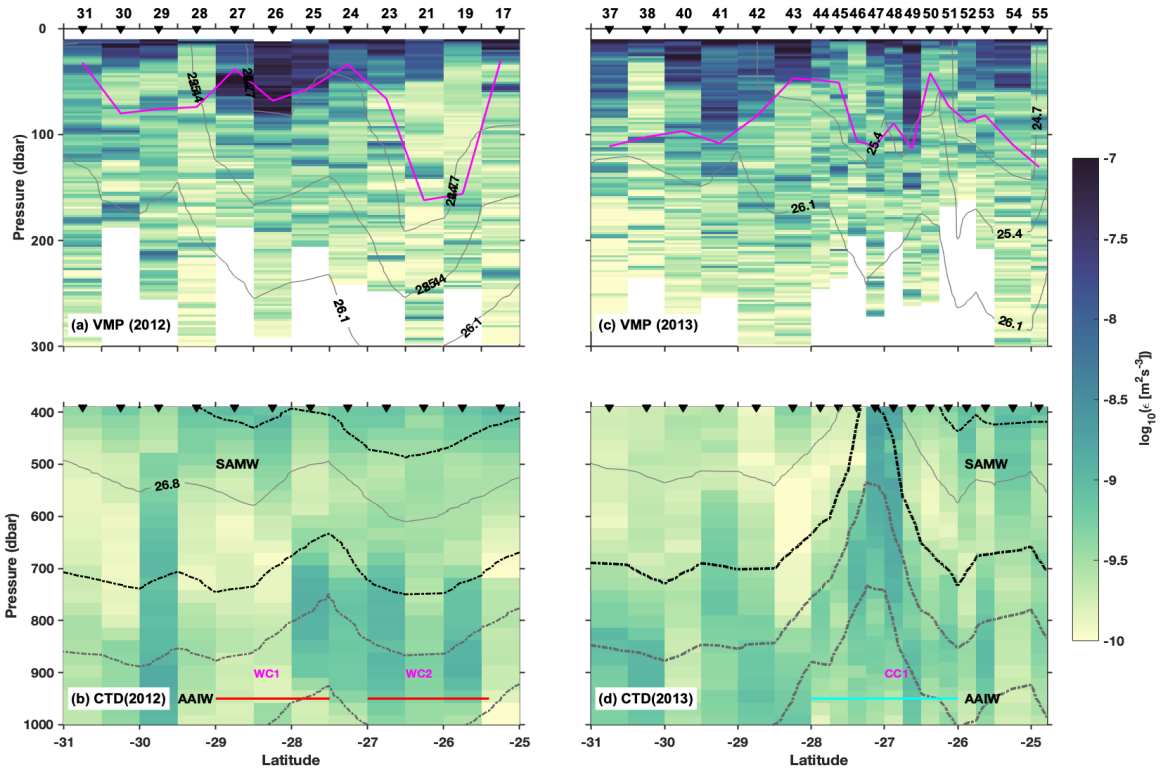

Figure A.4: Same as in Fig. 3.4 but for dissipation rate.

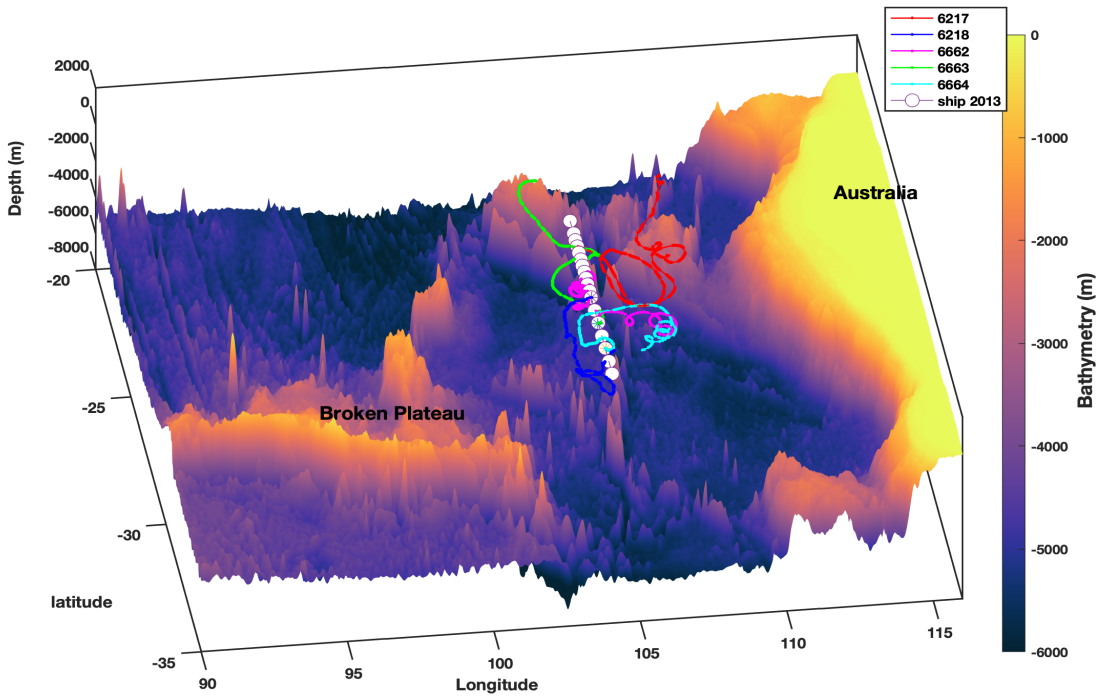

Figure A.5: Three dimensional structure of the bathymetry along the ship track in 2013. The tracks of all EM-APEX floats are also plotted with colors as in 2.1.

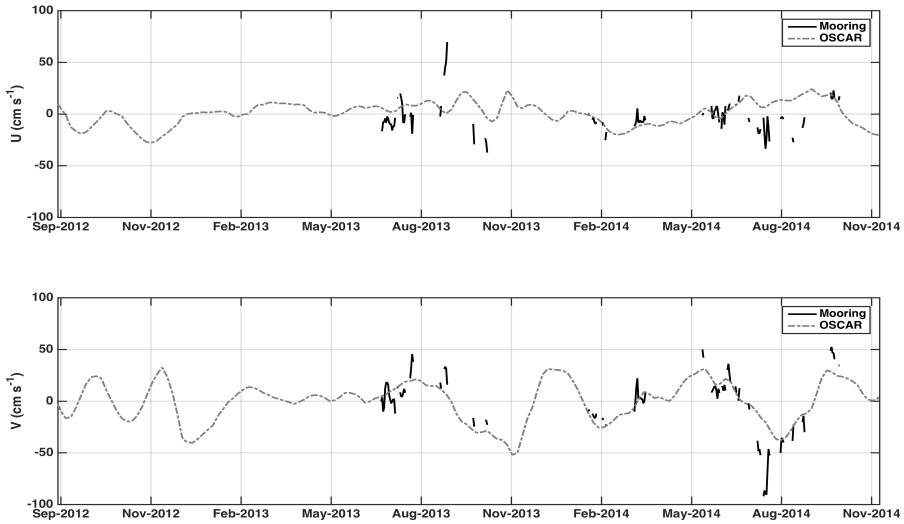

Figure A.6: Observations of zonal velocity (upper panel) from mooring (black line) and from OSCAR (dashed line). The lower panel is the same as upper panel but for meridional velocity.

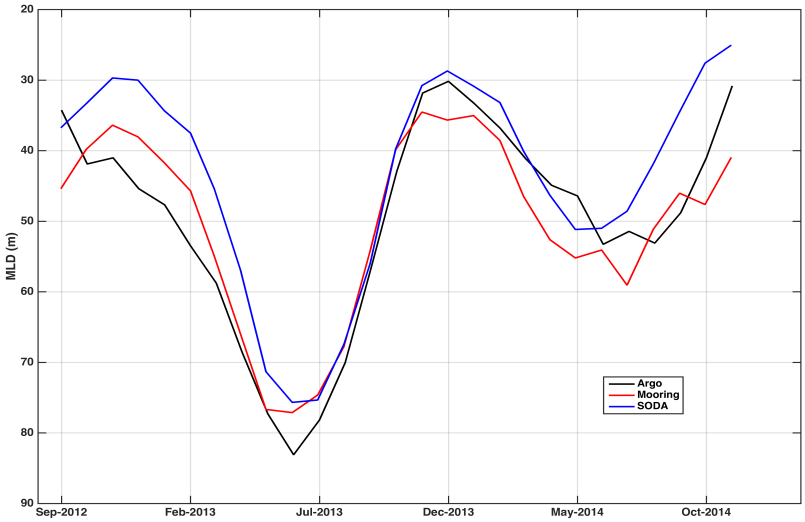

Figure A.7: Monthly averages of mixed layer depth (MLD) from mooring (red), Argo (black) and SODA (blue).

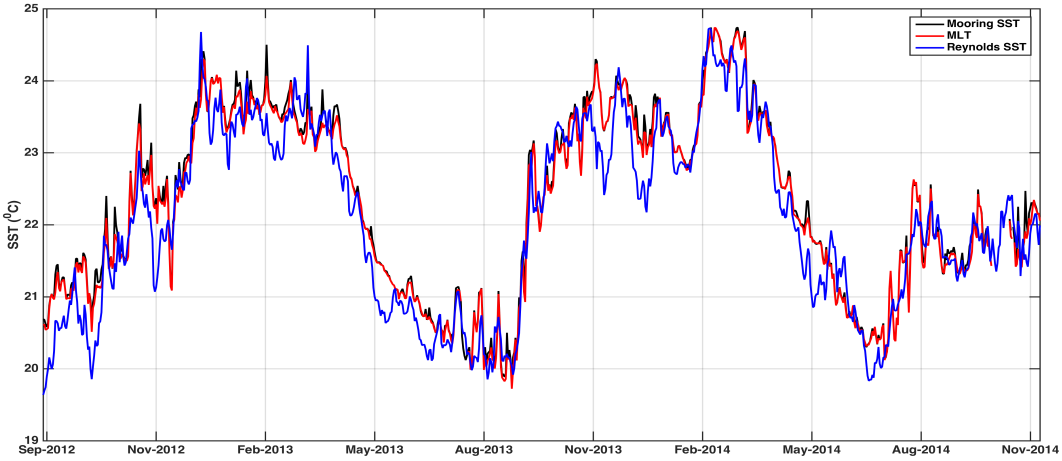

Figure A.8: Observations of SST from mooring (black), mixed layer temperature (MLT, red) and Reynolds SST (blue).

Appendix B

Quality control of EM-APEX data

B.1 Quality control procedures

The procedures are in good agreement with the results of standard Argo delayed-mode quality control at CSIRO for the EM-APEX data from north of Kerguelen Plateau collected from the SOFINE experiment in 2008 (Meyer et al., 2015). The steps followed for quality control are:

B.1.1 Location correction

Occasionally the GPS position of the profile was wrong considering the float's position at earlier and later profiles. These wrong positions were removed and the missing locations were linearly interpolated from the profile positions before and after the one in question.

B.1.2 Pressure drift correction

The pressure sensor on the floats may develop a pressure drift with time. So we removed the pressure offset due to drift from both CTD and velocity pressure measurements. The surface pressure value was subtracted from all pressure values in each profile which effectively resets the surface pressure to zero. The calculated pressure offset value for the first profile in all floats were higher. These values were replaced by the offset value of adjacent profile. Similarly, the last two missing offset values for each float were replaced by the offset of nearest profiles. The pressure drift correction was applied and the original values were saved separately.

B.1.3 Temperature and Salinity correction

The temperature and salinity profiles were compared with the CARS2009 (CSIRO Atlas of Regional Seas 2009) climatology to identify erroneous data and spikes. The upper 200 m of the profiles were not compared since the diurnal and seasonal variability in temperature and salinity is strong there, and not captured in the climatology. The CARS climatology for temperature and salinity was extracted for the study region and was interpolated to the position of each profile along each float trajectory. The climatology was plotted along with the float measurements and each profile was inspected visually. Occasional spikes were detected and removed. Much of the salinity data from float EM-6217 is ruined. So we removed the EM-6217 salinity data from further analysis for this study. For all other floats, temperature and salinity measurements are in good agreement with the climatology below 200 m (Fig. B.1).

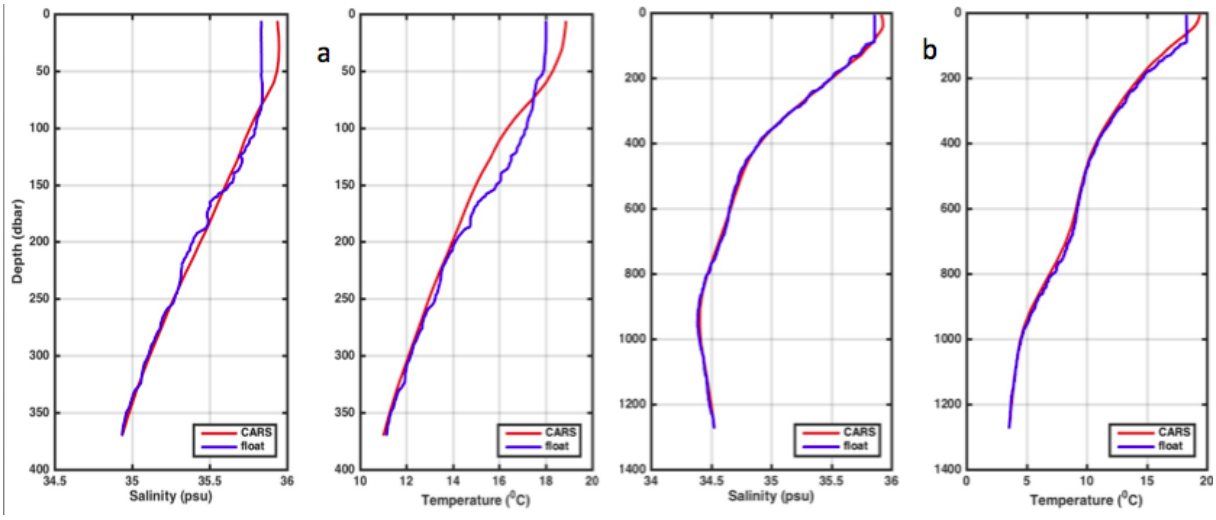

Figure B.1: An example of comparison of temperature and salinity measurements from float (blue line) and CARS climatology (red line) for a) shallow float and b) deeper float.

B.1.4 Salinity drift correction

There is a chance for salinity drift in the data due to a drift in the conductivity sensor. First we calculated the dynamic height along each float track and looked for spikes. Then we interpolated the salinity values to different potential temperature (θ) surfaces and checked for drift or trend in the salinity values.

B.1.5 Velocity correction

For the calibration of relative velocity measured by the floats, we followed the procedure in Phillips and Bindoff (2014) for the EM-APEX data from the Southern Ocean. The first step is to calibrate the angle between the electrode axes and the compass orientation. An error in the angle measurement can cause error in the velocity observed by the float. However, the method followed in Phillips and Bindoff (2014) gave velocity profiles which are 180° out of phase for both electrodes. We then adjusted the compass orientation to calibrate the angle between electrode axes and the compass to get the velocity profiles in phase.

Velocity spikes At each depth below 100 m, we defined a depth dependent cut-off based on a statistical analysis of the RMS error of velocity (Table B.1). We removed all velocity values based on this cut-off. For velocities above 100 m where the surface waves dominate, we did not apply the cut-off based on RMS error. However, we excluded velocities greater than 2 m s^{-1} above 100 m.

We visually checked the velocity values again and removed obvious spikes that were not detected by the RMS error cut-off values. If more than 50 values were removed from a profile, the entire profile is

Pressure range $(dbar)$	$Cut-off\ RMS\ error\ (cms^{-1})$
Less than 100	None
100 – 220	1.5
220 – 900	0.8
Greater than 900	0.5

Table B.1: The RMS error cut-off values for velocity at different depths (adapted from Phillips and Bindoff (2014)).

deleted. This procedure was ignored for the shallow floats EM-6217 and EM-6218.

Absolute velocity calculation The relative velocity (u_{rel}, v_{rel}) measured by the EM-APEX and the absolute velocity (u_{abs},v_{abs}) differ by a depth-independent offset (u_{off},v_{off}), which can be calculated by integrating the depth-averaged absolute velocity from the sea surface to the sea floor (Fig. B.2). The additional information about the offset can be obtained from the GPS positions of the float (Phillips and Bindoff, 2014).

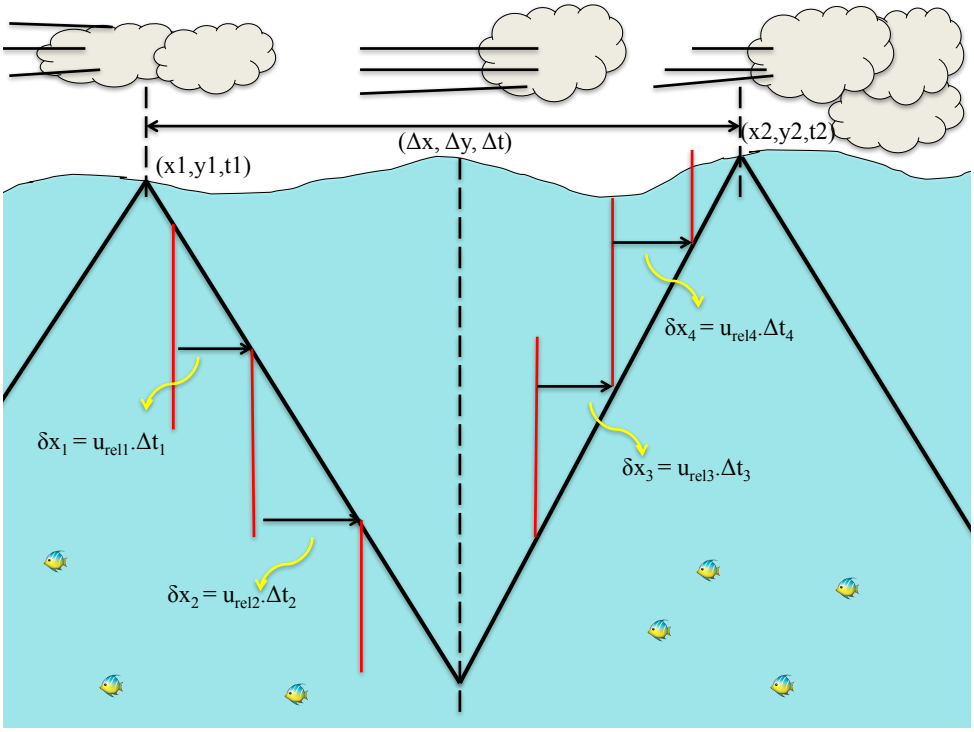

Figure B.2: Schematic representation of the estimation of absolute velocity from the floats. All the variables are explained in the main text.

Let (x_1, y_1) be the surface position of the float at the beginning of a descending profile at time t_1 and (x_2, y_2) be the surface location of the float at the end of subsequent ascending profile at time t_2. The horizontal displacement between the surface positions of a down profile and up profile is given as

$$\Delta x = x_2 - x_1; \Delta y = y_2 - y_1 \tag{B.1}$$

and the time taken for this displacement is given by

$$\Delta t = t_2 - t_1 \tag{B.2}$$

The relative horizontal displacement of the float (δx,δy) during t_1 and t_2 is given by the integral of relative velocity measured by the float during its subsurface path.

$$\delta x = \int_{t_1}^{t_2} u_{rel} dt; \delta y = \int_{t_1}^{t_2} v_{rel} dt \tag{B.3}$$

The absolute displacement of the float is given by

$$\Delta x = \delta x + x_{off}; \Delta y = \delta y + y_{off} \tag{B.4}$$

where (x_{off}, y_{off}) is the depth independent displacement offset.

$$x_{off} = (x_2 - x_1) - \int_{t_1}^{t_2} u_{rel} dt; y_{off} = (y_2 - y_1) - \int_{t_1}^{t_2} v_{rel} dt \tag{B.5}$$

$$u_{off} = \frac{x_{off}}{\Delta t} = \frac{(x_2 - x_1) - \int_{t_1}^{t_2} u_{rel} dt}{\Delta t} \tag{B.6}$$

Similarly,

$$v_{off} = \frac{y_{off}}{\Delta t} = \frac{(y_2 - y_1) - \int_{t_1}^{t_2} v_{rel} dt}{\Delta t} \tag{B.7}$$

From equations B.3, B.5 and B.6, we can calculate the velocity offset. Then the absolute velocity is given by

$$u_{abs} = u_{rel} + u_{off}; v_{abs} = v_{rel} + v_{off}. \tag{B.8}$$

After estimating the absolute velocities from both electrodes, the velocity profiles were averaged to get a single profile from the float at each location.

Bibliography

Alford, M. H. (2003). Improved global maps and 54-year history of wind-work on ocean inertial motions. *Geophys. Res. Lett.*, 30(8).

Alford, M. H. (2010). Sustained, full-water-column observations of internal waves and mixing near mendocino escarpment. *J. Phys. Oceanogr.*, 40(12):2643–2660.

Alford, M. H., Cronin, M. F., and Klymak, J. M. (2012). Annual cycle and depth penetration of wind-generated near-inertial internal waves at ocean station papa in the northeast pacific. *J. Phys. Oceanogr.*, 42(6):889–909.

Alford, M. H. and Gregg, M. C. (2001). Near-inertial mixing: Modulation of shear, strain and microstructure at low latitude. *J. Geophys. Res.-Oceans*, 106(C8):16947–16968.

Alford, M. H., MacKinnon, J. A., Pinkel, R., and Klymak, J. M. (2017). Space–time scales of shear in the north pacific. *Journal of Physical Oceanography*, 47(10):2455–2478.

Alford, M. H., MacKinnon, J. A., Simmons, H. L., Nash, J. D., Carlson, C. A., and Giovannoni, S. J. (2016). Near-inertial internal gravity waves in the ocean. *Annu. Rev. Mar. Sci.*, 8:95–123.

Alford, M. H., Shcherbina, A. Y., and Gregg, M. C. (2013). Observations of near-inertial internal gravity waves radiating from a frontal jet. *J. Phys. Oceanogr.*, 43(6):1225–1239.

Amante, C. and Eakins, B. (2009). ETOPO1 Global Relief Model converted to PanMap layer format. *NOAA-National Geophysical Data Center, doi*, 10.

Benthuysen, J., Furue, R., McCreary, J. P., Bindoff, N. L., and Phillips, H. E. (2014). Dynamics of the leeuwin current: Part 2. impacts of mixing, friction, and advection on a buoyancy-driven eastern boundary current over a shelf. *Dyn. Atmos. Oceans*, 65:39–63.

Birol, F. and Morrow, R. (2001). Source of the baroclinic waves in the southeast indian ocean. *J. Geophys. Res.-Oceans*, 106(C5):9145–9160.

Bond, N. A. and McPhaden, M. J. (1995). An indirect estimate of the diurnal cycle in upper ocean turbulent heat fluxes at the equator, 140-degrees-w. *J. Geophys. Res.-Oceans*, 100(C9):18369–18378.

Bray, N. A. and Fofonoff, N. P. (1981). Available potential-energy for mode eddies. *J. Phys. Oceanogr.*, 11(1):30–47.

Bryan, F. (1987). Parameter sensitivity of primitive equation ocean general-circulation models. *J. Phys. Oceanogr.*, 17(7):970–985.

Buhler, O. and McIntyre, E. (2005). Wave capture and wave-vortex duality. *J. Fluid Mech.*, 534:67–95.

Cairns, J. L. and Williams, G. O. (1976). Internal wave observations from a midwater float .2. *J GEOPHYS RES-OC ATM*, 81(12):1943–1950.

Carton, J. A. and Giese, B. S. (2008). A reanalysis of ocean climate using simple ocean data assimilation (soda). *Mon. Weather Rev.*, 136(8):2999–3017.

Chaigneau, A., Pizarro, O., and Rojas, W. (2008). Global climatology of near-inertial current characteristics from lagrangian observations. *Geophys. Res. Lett.*, 35(13).

Chelton, D. B., Schlax, M. G., Samelson, R. M., and de Szoeke, R. A. (2007). Global observations of large oceanic eddies. *Geophys. Res. Lett.*, 34(15).

Chinn, B. S., Girton, J. B., and Alford, M. H. (2016). The impact of observed variations in the shear-to-strain ratio of internal waves on inferred turbulent diffusivities. *Journal of Physical Oceanography*, 46(11):3299–3320.

Clemens, S., Prell, W., Murray, D., Shimmield, G., and Weedon, G. (1991). Forcing mechanisms of the indian-ocean monsoon. *Nature*, 353(6346):720–725.

Clement, L., Frajka-Williams, E., Sheen, K. L., Brearley, J. A., and Garabato, A. C. N. (2016). Generation of internal waves by eddies impinging on the western boundary of the north atlantic. *J. Phys. Oceanogr.*, 46(4):1067–1079.

Cronin, M. F., Pelland, N. A., Emerson, S. R., and Crawford, W. R. (2015). Estimating diffusivity from the mixed layer heat and salt balances in the north pacific. *J. Geophys. Res.-Oceans*, 120(11):7346–7362.

Cummins, P. F., Masson, D., and Saenko, O. A. (2016). Vertical heat flux in the ocean: Estimates from observations and from a coupled general circulation model. *J. Geophys. Res.-Oceans*, 121(6):3790–3802.

Dasaro, E. A. (1985). The energy flux from the wind to near-inertial motions in the surface mixed layer. *J. Phys. Oceanogr.*, 15(8):1043–1059.

Dasaro, E. A., Eriksen, C. C., Levine, M. D., Niiler, P., Paulson, C. A., and Vanmeurs, P. (1995). Upper-ocean inertial currents forced by a strong storm .1. data and comparisons with linear-theory. *J. Phys. Oceanog.*, 25(11):2909–2936.

de Boyer Montegut, C., Madec, G., Fischer, A. S., Lazar, A., and Iudicone, D. (2004). Mixed layer depth over the global ocean: An examination of profile data and a profile-based climatology. *J. Geophys. Res.-Oceans*, 109(C12).

Divakaran, P. and Brassington, G. B. (2011). Arterial ocean circulation of the southeast indian ocean. *Geophys. Res. Lett.*, 38(L01802).

Domingues, C. M., Maltrud, M. E., Wijffels, S. E., Church, J. A., and Tomczak, M. (2007). Simulated lagrangian pathways between the leeuwin current system and the upper-ocean circulation of the southeast indian ocean. *Deep-Sea Res. Part II-Top. Stud. Oceanogr.*, 54(8-10):797–817.

Domingues, C. M., Wijffels, S. E., Maltrud, M. E., Church, J. A., and Tomczak, M. (2006). Role of eddies in cooling the leeuwin current. *Geophys. Res. Lett.*, 33(5).

Early, J. J., Samelson, R. M., and Chelton, D. B. (2011). The evolution and propagation of quasi-geostrophic ocean eddies. *J. Phys. Oceanogr.*, 41(8):1535–1555.

Egbert, G. D. and Ray, R. D. (2000). Significant dissipation of tidal energy in the deep ocean inferred from satellite altimeter data. *Nature*, 405(6788):775–778.

Elipot, S. and Lumpkin, R. (2008). Spectral description of oceanic near-surface variability. *Geophys. Res. Lett.*, 35(5).

Elipot, S., Lumpkin, R., and Prieto, G. (2010). Modification of inertial oscillations by the mesoscale eddy field. *J. Geophys. Res.-Oceans*, 115(C09010).

Fairall, C., Barnier, B., Berry, D., Bourassa, M., Bradley, F., Clayson, C., de Leeuw, G., Drennan, W., Gille, S., Gulev, S., et al. (2010). Observations to quantify air-sea fluxes and their role in climate variability and predictability. *Proceedings of OceanObs*, 9:299–313.

Fairall, C. W., Bradley, E. F., Rogers, D. P., Edson, J. B., and Young, G. S. (1996). Bulk parameterization of air-sea fluxes for tropical ocean global atmosphere coupled ocean atmosphere response experiment. *J. Geophys. Res.-Oceans*, 101(C2):3747–3764.

Fang, F. and Morrow, R. (2003). Evolution, movement and decay of warm-core leeuwin current eddies. *Deep Sea Research Part II: Topical Studies in Oceanography*, 50(12-13):2245–2261.

Federiuk, J. and Allen, J. S. (1996). Model studies of near-inertial waves in flow over the oregon continental shelf. *J. Phys. Oceanogr.*, 26(10):2053–2075.

Feng, M., Biastoch, A., Boening, C., Caputi, N., and Meyers, G. (2008). Seasonal and interannual variations of upper ocean heat balance off the west coast of australia. *J. Geophys. Res.-Oceans*, 113(C12).

Feng, M., Hendon, H. H., Xie, S.-P., Marshall, A. G., Schiller, A., Kosaka, Y., Caputi, N., and Pearce, A. (2015). Decadal increase in ningaloo nino since the late 1990s. *Geophys. Res. Lett.*, 42(1):104–112.

Feng, M., Majewski, L. J., Fandry, C. B., and Waite, A. M. (2007). Characteristics of two counter-rotating eddies in the leeuwin current system off the western australian coast. *Deep-Sea Res. Part II-Top. Stud. Oceanogr.*, 54(8-10):961–980.

Feng, M., McPhaden, M. J., Xie, S.-P., and Hafner, J. (2013). La nina forces unprecedented leeuwin current warming in 2011. *Sci Rep*, 3(1277).

Feng, M., Meyers, G., Pearce, A., and Wijffels, S. (2003). Annual and interannual variations of the leeuwin current at 32 degrees s. *J. Geophys. Res.-Oceans*, 108(C11).

Feng, M., Waite, A., and Thompson, P. (2009). Climate variability and ocean production in the leeuwin current system off the west coast of western australia. *Journal of the Royal Society of Western Australia*, 92:67.

Feng, M., Wijffels, S., Godfrey, S., and Meyers, G. (2005). Do eddies play a role in the momentum balance of the leeuwin current? *J. Phys. Oceanogr.*, 35(6):964–975.

Ferrari, R. and Wunsch, C. (2009). Ocean circulation kinetic energy: Reservoirs, sources, and sinks. *Annu. Rev. Fluid Mech.*, 41:253–282.

Foltz, G. R. and McPhaden, M. J. (2008). Seasonal mixed layer salinity balance of the tropical north atlantic ocean. *J. Geophys. Res.-Oceans*, 113(C2).

Foltz, G. R., Vialard, J., Kumar, B. P., and McPhaden, M. J. (2010). Seasonal mixed layer heat balance of the southwestern tropical indian ocean. *J. Clim.*, 23(4):947–965.

Frankignoul, C. and Müller, P. (1979). Quasi-geostrophic response of an infinite β-plane ocean to stochastic forcing by the atmosphere. *Journal of Physical Oceanography*, 9(1):104–127.

Fu, L. L. (1981). Observations and models of inertial waves in the deep ocean. *Rev. Geophys.*, 19(1):141–170.

Furue, R., Guerreiro, K., Phillips, H. E., McCreary, Julian P., J., and Bindoff, N. L. (2017). On the leeuwin current system and its linkage to zonal flows in the south indian ocean as inferred from a gridded hydrography. *J. Phys. Oceanogr.*, 47(3):583–602.

Furue, R., McCreary, J. P., Benthuysen, J., Phillips, H. E., and Bindoff, N. L. (2013). Dynamics of the leeuwin current: Part 1. coastal flows in an inviscid, variable-density, layer model. *Dyn. Atmos. Oceans*, 63:24–59.

Garabato, A. C. N., Polzin, K. L., King, B. A., Heywood, K. J., and Visbeck, M. (2004). Widespread intense turbulent mixing in the southern ocean. *Science*, 303(5655):210–213.

Garrett, C. (2001). What is the "near-inertial" band and why is it different from the rest of the internal wave spectrum? *J. Phys. Oceanogr.*, 31(4):962–971.

Garrett, C. (2003). Mixing with latitude. *Nature*, 422(6931):477–478.

Gill, A. E. (1984). On the behavior of internal waves in the wakes of storms. *J. Phys. Oceanogr.*, 14(7):1129–1151.

Godfrey, J. S. (1996). The effect of the indonesian throughflow on ocean circulation and heat exchange with the atmosphere: A review. *J. Geophys. Res.-Oceans*, 101(C5):12217–12237.

Godfrey, J. S. and Ridgway, K. R. (1985). The large-scale environment of the poleward-flowing leeuwin current, western-australia - longshore steric height gradients, wind stresses and geostrophic flow. *J. Phys. Oceanogr.*, 15(5):481–495.

Gonella, J. (1972). Rotary-component method for analyzing meteorological and oceanographic vector time series. *DEEP-SEA RES*, 19(12):833–846.

Greenan, B. J., Oakey, N. S., and Dobson, F. W. (2001). Estimates of dissipation in the ocean mixed layer using a quasi-horizontal microstructure profiler. *Journal of Physical Oceanography*, 31(4):992–1004.

Gregg, M. C. (1989). Scaling turbulent dissipation in the thermocline. *J. Geophys. Res.-Oceans*, 94(C7):9686–9698.

Gregg, M. C., Sanford, T. B., and Winkel, D. P. (2003). Reduced mixing from the breaking of internal waves in equatorial waters. *Nature*, 422(6931):513–515.

Griffies, S. M., Winton, M., Anderson, W. G., Benson, R., Delworth, T. L., Dufour, C. O., Dunne, J. P., Goddard, P., Morrison, A. K., Rosati, A., Wittenberg, A. T., Yin, J., and Zhang, R. (2015). Impacts on ocean heat from transient mesoscale eddies in a hierarchy of climate models. *J. Clim.*, 28(3):952–977.

Halkides, D. and Lee, T. (2011). Mechanisms controlling seasonal mixed layer temperature and salinity in the southwestern tropical indian ocean. *Dynamics of atmospheres and oceans*, 51(3):77–93.

Hanawa, K. and Talley, L. D. (2001). .4 mode waters. In *International Geophysics*, volume 77, pages 373–386. Elsevier.

Harrison, M. J. and Hallberg, R. W. (2008). Pacific subtropical cell response to reduced equatorial dissipation. *J. Phys. Oceanogr.*, 38(9):1894–1912.

Hennon, T. D., Riser, S. C., and Alford, M. H. (2014). Observations of internal gravity waves by argo floats. *J. Phys. Oceanogr.*, 44(9):2370–2386.

Henyey, F. S., Wright, J., and Flatte, S. M. (1986). Energy and action flow through the internal wave field - an eikonal approach. *J. Geophys. Res.-Oceans*, 91(C7):8487–8495.

Hughes, T. P., Kerry, J. T., Álvarez-Noriega, M., Álvarez-Romero, J. G., Anderson, K. D., Baird, A. H., Babcock, R. C., Beger, M., Bellwood, D. R., Berkelmans, R., et al. (2017). Global warming and recurrent mass bleaching of corals. *Nature*, 543(7645):373.

Huussen, T. N., Naveira-Garabato, A. C., Bryden, H. L., and McDonagh, E. L. (2012). Is the deep indian ocean moc sustained by breaking internal waves? *J. Geophys. Res.-Oceans*, 117(C08024).

Ivey, G. N., Bluteau, C. E., and Jones, N. L. (2018). Quantifying diapycnal mixing in an energetic ocean. *Journal of Geophysical Research: Oceans*, 123(1):346–357.

Jaimes, B. and Shay, L. K. (2009). Mixed layer cooling in mesoscale oceanic eddies during hurricanes katrina and rita. *Mon. Weather Rev.*, 137(12):4188–4207.

Jaimes, B. and Shay, L. K. (2010). Near-inertial wave wake of hurricanes katrina and rita over mesoscale oceanic eddies. *J. Phys. Oceanogr.*, 40(6):1320–1337.

Jensen, T. G. (2003). Cross-equatorial pathways of salt and tracers from the northern indian ocean: Modelling results. *Deep-Sea Res. Part II-Top. Stud. Oceanogr.*, 50(12-13):2111–2127.

Jia, F., Wu, L., Lan, J., and Qiu, B. (2011a). Interannual modulation of eddy kinetic energy in the southeast indian ocean by southern annular mode. *J. Geophys. Res.-Oceans*, 116(C02029).

Jia, F., Wu, L., and Qiu, B. (2011b). Seasonal modulation off eddy kinetic energy and its formation mechanism in the southeast indian ocean. *J. Phys. Oceanogr.*, 41(4):657–665.

Jiang, J., Lu, Y., and Perrie, W. (2005). Estimating the energy flux from the wind to ocean inertial motions: The sensitivity to surface wind fields. *Geophysical research letters*, 32(15).

Josey, S. A., Gulev, S., and Yu, L. (2013). Exchanges through the ocean surface. In *International Geophysics*, volume 103, pages 115–140. Elsevier.

Josey, S. A., Kent, E. C., and Taylor, P. K. (1999). New insights into the ocean heat budget closure problem from analysis of the soc air-sea flux climatology. *J. Clim.*, 12(9):2856–2880.

Kanamitsu, M., Ebisuzaki, W., Woollen, J., Yang, S. K., Hnilo, J. J., Fiorino, M., and Potter, G. L. (2002). Ncep-doe amip-ii reanalysis (r-2). *Bull. Amer. Meteorol. Soc.*, 83(11):1631–1643.

Karstensen, J. and Quadfasel, D. (2002). Water subducted into the indian ocean subtropical gyre. *Deep-Sea Res. Part II-Top. Stud. Oceanogr.*, 49(7-8):1441–1457.

Kim, S.-B., Lee, T., and Fukumori, I. (2007). Mechanisms controlling the interannual variation of mixed layer temperature averaged over the nino-3 region. *J. Clim.*, 20(15):3822–3843.

Klymak, J. M. and Moum, J. N. (2007). Oceanic isopycnal slope spectra. part ii: Turbulence. *J. Phys. Oceanogr.*, 37(5):1232–1245.

Kobashi, F. and Kubokawa, A. (2012). Review on north pacific subtropical countercurrents and subtropical fronts: role of mode waters in ocean circulation and climate. *J. Oceanogr.*, 68(1):21–43.

Kobashi, F., Mitsudera, H., and Xie, S.-P. (2006). Three subtropical fronts in the north pacific: Observational evidence for mode water-induced subsurface frontogenesis. *J. Geophys. Res.-Oceans*, 111(C9).

Kozlov, I., Romanenkov, D., Zimin, A., and Chapron, B. (2014). Sar observing large-scale nonlinear internal waves in the white sea. *Remote sensing of environment*, 147:99–107.

Kumar, B. P., Vialard, J., Lengaigne, M., Murty, V. S. N., and McPhaden, M. J. (2012). Tropflux: air-sea fluxes for the global tropical oceans-description and evaluation. *Clim. Dyn.*, 38(7-8):1521–1543.

Kunze, E. (1985). Near-inertial wave-propagation in geostrophic shear. *J. Phys. Oceanogr.*, 15(5):544–565.

Kunze, E. (1995). The energy-balance in a warm-core rings near-inertial critical layer. *J. Phys. Oceanog.*, 25(5):942–957.

Kunze, E., Firing, E., Hummon, J. M., Chereskin, T. K., and Thurnherr, A. M. (2006). Global abyssal mixing inferred from lowered adcp shear and ctd strain profiles. *Journal of Physical Oceanography*, 36(8):1553–1576.

Kunze, E. and Sanford, T. B. (1984). Observations of near-inertial waves in a front. *J. Phys. Oceanogr.*, 14(3):566–581.

Last, P. R., White, W. T., Gledhill, D. C., Hobday, A. J., Brown, R., Edgar, G. J., and Pecl, G. (2011). Long-term shifts in abundance and distribution of a temperate fish fauna: a response to climate change and fishing practices. *Global Ecology and Biogeography*, 20(1):58–72.

Leaman, K. D. and Sanford, T. B. (1975). Vertical energy propagation of inertial waves - vector spectral analysis of velocity profiles. *J GEOPHYS RES*, 80(15):1975–1978.

Ledwell, J. R., St Laurent, L. C., Girton, J. B., and Toole, J. M. (2011). Diapycnal mixing in the antarctic circumpolar current. *J. Phys. Oceanogr.*, 41(1):241–246.

Lee, D. K. and Niiler, P. P. (1998). The inertial chimney: The near-inertial energy drainage from the ocean surface to the deep layer. *J. Geophys. Res.-Oceans*, 103(C4):7579–7591.

Lee, T. (2004). Decadal weakening of the shallow overturning circulation in the south indian ocean. *Geophys. Res. Lett.*, 31(18).

Levitus, S., Antonov, J. I., Boyer, T. P., and Stephens, C. (2000). Warming of the world ocean. *Science*, 287(5461):2225–2229.

Levy, M., Ferrari, R., Franks, P. J. S., Martin, A. P., and Riviere, P. (2012). Bringing physics to life at the submesoscale. *Geophys. Res. Lett.*, 39(L14602).

Liang, X. and Yu, L. (2016). Variations of the global net air–sea heat flux during the "hiatus" period (2001–10). *Journal of Climate*, 29(10):3647–3660.

Lilly, J. (2017). jLab: a data analysis package for Matlab, v. 1.6. 5. *See http://www. jmlilly. net/jmlsoft. html*.

Lueck, R. (2013). Calculating the rate of dissipation of turbulent kinetic energy. *Rockland Scientific International Tech. Note TN-028*.

Mao, H., Feng, M., Phillips, H. E., and Lian, S. (2018). Mesoscale eddy characteristics in the interior subtropical southeast Indian ocean, tracked from the Leeuwin Current system. *Deep Sea Research Part II: Topical Studies in Oceanography*.

Martini, K. I., Simmons, H. L., Stoudt, C. A., and Hutchings, J. K. (2014). Near-inertial internal waves and sea ice in the beaufort sea. *J. Phys. Oceanogr.*, 44(8):2212–2234.

McComas, C. H. and Muller, P. (1981). The dynamic balance of internal waves. *J. Phys. Oceanogr.*, 11(7):970–986.

McCreary, J. P., Shetye, S. R., and Kundu, P. K. (1986). Thermohaline forcing of eastern boundary currents - with application to the circulation off the west-coast of australia. *J. Mar. Res.*, 44(1):71–92.

McPhaden, M. J., Meyers, G., Ando, K., Masumoto, Y., Murty, V. S. N., Ravichandran, M., Syamsudin, F., Vialard, J., Yu, L., and Yu, W. (2009). Rama the research moored array for african-asian-australian monsoon analysis and prediction. *Bull. Amer. Meteorol. Soc.*, 90(4):459–+.

Menezes, V. V., Phillips, H. E., Schiller, A., Bindoff, N. L., Domingues, C. M., and Vianna, M. L. (2014). South indian countercurrent and associated fronts. *J. Geophys. Res.-Oceans*, 119(10):6763–6791.

Menezes, V. V., Phillips, H. E., Schiller, A., Domingues, C. M., and Bindoff, N. L. (2013). Salinity dominance on the indian ocean eastern gyral current. *Geophys. Res. Lett.*, 40(21):5716–5721.

Meyer, A., Phillips, H., Sloyan, B., and Polzin, K. (2014). Mixing (MX) Oceanographic Toolbox for EM-APEX* float data applying shear-strain finescale parameterization.

Meyer, A., Polzin, K. L., Sloyan, B. M., and Phillips, H. E. (2016). Internal waves and mixing near the kerguelen plateau. *J. Phys. Oceanogr.*, 46(2):417–437.

Meyer, A., Sloyan, B. M., Polzin, K. L., Phillips, H. E., and Bindoff, N. L. (2015). Mixing variability in the southern ocean. *J. Phys. Oceanogr.*, 45(4):966–987.

Morel, A. and Antoine, D. (1994). Heating rate within the upper ocean in relation to its biooptical state. *J. Phys. Oceanogr.*, 24(7):1652–1665.

Morrison, A. K., Saenko, O. A., Hogg, A. M., and Spence, P. (2013). The role of vertical eddy flux in southern ocean heat uptake. *Geophys. Res. Lett.*, 40(20):5445–5450.

Morrow, R. and Birol, F. (1998). Variability in the southeast indian ocean from altimetry: Forcing mechanisms for the leeuwin current. *J. Geophys. Res.-Oceans*, 103(C9):18529–18544.

Morrow, R., Birol, F., Griffin, D., and Sudre, J. (2004). Divergent pathways of cyclonic and anti-cyclonic ocean eddies. *Geophys. Res. Lett.*, 31(24).

Morrow, R., Fang, F. X., Fieux, M., and Molcard, R. (2003). Anatomy of three warm-core leeuwin current eddies. *Deep-Sea Res. Part II-Top. Stud. Oceanogr.*, 50(12-13):2229–2243.

Müller, P. and Frankignoul, C. (1981). Direct atmospheric forcing of geostrophic eddies. *Journal of Physical Oceanography*, 11(3):287–308.

Munk, W. and Wunsch, C. (1998). Abyssal recipes ii: energetics of tidal and wind mixing. *Deep-Sea Res. Part I-Oceanogr. Res. Pap.*, 45(12):1977–2010.

Nagai, T. and Hibiya, T. (2015). Internal tides and associated vertical mixing in the i ndonesian a rchipelago. *Journal of Geophysical Research: Oceans*, 120(5):3373–3390.

Niiler, P. P. (1977). One-dimensional models of the upper ocean. *Modelling and Prediction of the Upper Layers of the Ocean*, pages 143–172.

Nikurashin, M. and Ferrari, R. (2010). Radiation and dissipation of internal waves generated by geostrophic motions impinging on small-scale topography: Application to the southern ocean. *J. Phys. Oceanogr.*, 40(9):2025–2042.

Nikurashin, M. and Ferrari, R. (2011). Global energy conversion rate from geostrophic flows into internal lee waves in the deep ocean. *Geophys. Res. Lett.*, 38(L08610).

Nikurashin, M. and Ferrari, R. (2013). Overturning circulation driven by breaking internal waves in the deep ocean. *Geophys. Res. Lett.*, 40(12):3133–3137.

Oakey, N. and Elliott, J. (1982). Dissipation within the surface mixed layer. *Journal of Physical Oceanography*, 12(2):171–185.

Oliver, E. C., Benthuysen, J. A., Bindoff, N. L., Hobday, A. J., Holbrook, N. J., Mundy, C. N., and Perkins-Kirkpatrick, S. E. (2017). The unprecedented 2015/16 tasman sea marine heatwave. *Nature communications*, 8:16101.

Osborn, T. (1980). Estimates of the local rate of vertical diffusion from dissipation measurements. *Journal of physical oceanography*, 10(1):83–89.

Palastanga, V., van Leeuwen, P. J., Schouten, M. W., and P. M. de Ruijter, W. (2007). Flow structure and variability in the subtropical indian ocean: Instability of the south indian ocean countercurrent. *J. Geophys. Res.-Oceans*, 112(C1).

Pearce, A. and Feng, M. (2007). Observations of warming on the western australian continental shelf. *Mar. Freshw. Res.*, 58(10):914–920.

Phillips, H. E. and Bindoff, N. L. (2014). On the nonequivalent barotropic structure of the antarctic circumpolar current: An observational perspective. *J. Geophys. Res.-Oceans*, 119(8):5221–5243.

Plueddemann, A. and Farrar, J. (2006). Observations and models of the energy flux from the wind to mixed-layer inertial currents. *Deep Sea Research Part II: Topical Studies in Oceanography*, 53(1-2):5–30.

Polzin, K., Kunze, E., Hummon, J., and Firing, E. (2002). The finescale response of lowered adcp velocity profiles. *J. Atmos. Ocean. Technol.*, 19(2):205–224.

Polzin, K. L. (2008). Mesoscale eddy-internal wave coupling. part i: Symmetry, wave capture, and results from the mid-ocean dynamics experiment. *J. Phys. Oceanogr.*, 38(11):2556–2574.

Polzin, K. L., Garabato, A. C. N., Huussen, T. N., Sloyan, B. M., and Waterman, S. (2014). Finescale parameterizations of turbulent dissipation. *J. Geophys. Res.-Oceans*, 119(2):1383–1419.

Polzin, K. L., Toole, J. M., and Schmitt, R. W. (1995). Finescale parameterizations of turbulent dissipation. *J. Phys. Oceanog.*, 25(3):306–328.

Poulain, P.-M. and Centurioni, L. (2015). Direct measurements of world ocean tidal currents with surface drifters. *J. Geophys. Res.-Oceans*, 120(10):6986–7003.

Qiu, B., Scott, R. B., and Chen, S. (2008). Length scales of eddy generation and nonlinear evolution of the seasonally modulated south pacific subtropical countercurrent. *J. Phys. Oceanogr.*, 38(7):1515–1528.

Rennie, S. J., Pattiaratchi, C. P., and McCauley, R. D. (2007). Eddy formation through the interaction between the leeuwin current, leeuwin undercurrent and topography. *Deep-Sea Res. Part II-Top. Stud. Oceanogr.*, 54(8-10):818–836.

Richardson, P. L., Maillard, C., and Stanford, T. (1979). The physical structure and life history of cyclonic Gulf Stream ring Allen. *Journal of Geophysical Research: Oceans*, 84(C12):7727–7741.

Ridgway, K. R. and Godfrey, J. S. (2015). The source of the leeuwin current seasonality. *J. Geophys. Res.-Oceans*, 120(10):6843–6864.

Roemmich, D., Johnson, G. C., Riser, S., Davis, R., Gilson, J., Owens, W. B., Garzoli, S. L., Schmid, C., and Ignaszewski, M. (2009). The argo program observing the global ocean with profiling floats. *Oceanography*, 22(2):34–43.

Roemmich, D., Riser, S., Davis, R., and Desaubies, Y. (2004). Autonomous profiling floats: Workhorse for broad-scale ocean observations. *Mar. Technol. Soc. J.*, 38(2):21–29.

Rudnick, D. L., Boyd, T. J., Brainard, R. E., Carter, G. S., Egbert, G. D., Gregg, M. C., Holloway, P. E., Klymak, J. M., Kunze, E., Lee, C. M., Levine, M. D., Luther, D. S., Martin, J. P., Merrifield, M. A., Moum, J. N., Nash, J. D., Pinkel, R., Rainville, L., and Sanford, T. B. (2003). From tides to mixing along the hawaiian ridge. *Science*, 301(5631):355–357.

Rudnick, D. L. and Weller, R. A. (1993). The heat-budget in the north-atlantic subtropical frontal zone. *J. Geophys. Res.-Oceans*, 98(C4):6883–6893.

Saji, P. K., Shenoi, S. C., Almeida, A., and Rao, G. (2000). Inertial currents in the indian ocean derived from satellite tracked surface drifters. *Oceanol. Acta*, 23(5):635–640.

Sallee, J.-B., Wienders, N., Speer, K., and Morrow, R. (2006). Formation of subantarctic mode water in the southeastern indian ocean. *Ocean Dyn.*, 56(5-6):525–542.

Sanford, T. (1984). Circulation and Internal Waves in a Cold Gulf Stream Waves. Technical report, Washington Univ Seattle Applied Physics Lab.

Sanford, T. B. (1971). Motionally induced electric and magnetic fields in the sea. *Journal of Geophysical Research*, 76(15):3476–3492.

Sanford, T. B., Drever, R. G., and Dunlap, J. H. (1978). Velocity profiler based on principles of geomagnetic induction. *DEEP-SEA RES*, 25(2):183–&.

Sanford, T. B., Dunlap, J. H., Carlson, J. A., Webb, D. C., and Girton, J. B. (2005). Autonomous velocity and density profiler: Em-apex. In *Proceedings of the IEEE/OES Eighth Working Conference on Current Measurement Technology, 2005.*, pages 152–156. IEEE.

Schiller, A. and Oke, P. R. (2015). Dynamics of ocean surface mixed layer variability in the indian ocean. *J. Geophys. Res.-Oceans*, 120(6):4162–4186.

Schott, F. A. and McCreary, J. P. (2001). The monsoon circulation of the indian ocean. *Prog. Oceanogr.*, 51(1):1–123.

Schott, F. A., Xie, S.-P., and McCreary, Julian P., J. (2009). Indian ocean circulation and climate variability. *Rev. Geophys.*, 47(RG1002).

Shang, X., Qi, Y., Chen, G., Liang, C., Lueck, R. G., Prairie, B., and Li, H. (2017). An expendable microstructure profiler for deep ocean measurements. *Journal of Atmospheric and Oceanic technology*, 34(1):153–165.

Sheen, K. L., Brearley, J. A., Garabato, A. C. N., Smeed, D. A., St Laurent, L., Meredith, M. P., Thurnherr, A. M., and Waterman, S. N. (2015). Modification of turbulent dissipation rates by a deep southern ocean eddy. *Geophys. Res. Lett.*, 42(9):3450–3457.

Shengli, C., Jianyu, H., and Polton, J. A. (2015). Features of near-inertial motions observed on the northern south china sea shelf during the passage of two typhoons. *Acta Oceanol. Sin.*, 34(1):38–43.

Siedler, G., Rouault, M., and Lutjeharms, J. R. E. (2006). Structure and origin of the subtropical south indian ocean countercurrent. *Geophys. Res. Lett.*, 33(24).

Sikhakolli, R., Sharma, R., Basu, S., Gohil, B. S., Sarkar, A., and Prasad, K. V. S. R. (2013). Evaluation of oscar ocean surface current product in the tropical indian ocean using in situ data. *J. Earth Syst. Sci.*, 122(1):187–199.

Silverthorne, K. E. and Toole, J. M. (2009). Seasonal kinetic energy variability of near-inertial motions. *J. Phys. Oceanogr.*, 39(4):1035–1049.

Simmons, H. L. and Alford, M. H. (2012). Simulating the long-range swell of internal waves generated by ocean storms. *Oceanography*, 25(2):30–41.

Sloyan, B. M. (2005). Spatial variability of mixing in the southern ocean. *Geophysical research letters*, 32(18).

Sloyan, B. M., Talley, L. D., Chereskin, T. K., Fine, R., and Holte, J. (2010). Antarctic intermediate water and subantarctic mode water formation in the southeast pacific: The role of turbulent mixing. *J. Phys. Oceanogr.*, 40(7):1558–1574.

Smith, R. L., Huyer, A., Godfrey, J. S., and Church, J. A. (1991). The leeuwin current off western australia, 1986-1987. *J. Phys. Oceanogr.*, 21(2):323–345.

Spall, M. A., Weller, R. A., and Furey, P. W. (2000). Modeling the three-dimensional upper ocean heat budget and subduction rate during the subduction experiment. *J. Geophys. Res.-Oceans*, 105(C11):26151–26166.

St. Laurent, L., Naveira Garabato, A. C., Ledwell, J. R., Thurnherr, A. M., Toole, J. M., and Watson, A. J. (2012). Turbulence and diapycnal mixing in drake passage. *Journal of Physical Oceanography*, 42(12):2143–2152.

Stevenson, J. W. and Niiler, P. P. (1983). Upper ocean heat-budget during the hawaii-to-tahiti shuttle experiment. *J. Phys. Oceanogr.*, 13(10):1894–1907.

Stramma, L. and Lutjeharms, J. R. (1997). The flow field of the subtropical gyre of the south indian ocean. *Journal of Geophysical Research: Oceans*, 102(C3):5513–5530.

Sun, B. M., Yu, L. S., and Weller, R. A. (2003). Comparisons of surface meteorology and turbulent heat fluxes over the atlantic: Nwp model analyses versus moored buoy observations. *J. Clim.*, 16(4):679–695.

Sweeney, C., Gnanadesikan, A., Griffies, S. M., Harrison, M. J., Rosati, A. J., and Samuels, B. L. (2005). Impacts of shortwave penetration depth on large-scale ocean circulation and heat transport. *J. Phys. Oceanogr.*, 35(6):1103–1119.

Talley, L. D. (2011). *Descriptive physical oceanography: an introduction*. Academic press.

Thompson, R. O. and Edwards, R. (1981). Mixing and water-mass formation in the australian subantarctic. *Journal of Physical Oceanography*, 11(10):1399–1406.

Thompson, R. O. R. Y. (1987). Continental-shelf-scale model of the leeuwin current. *J. Mar. Res.*, 45(4):813–827.

Thomson, R. E. and Emery, W. J. (2014). *Data Analysis Methods in Physical Oceanography*. Newnes.

Toole, J. M. and Warren, B. A. (1993). A hydrographic section across the subtropical south indian ocean. *Deep Sea Research Part I: Oceanographic Research Papers*, 40(10):1973–2019.

Vialard, J., Foltz, G. R., McPhaden, M. J., Duvel, J. P., and Montegut, C. d. B. (2008). Strong indian ocean sea surface temperature signals associated with the madden-julian oscillation in late 2007 and early 2008. *Geophys. Res. Lett.*, 35(19).

Wang, P., Clemens, S., Beaufort, L., Braconnot, P., Ganssen, G., Jian, Z., Kershaw, P., and Sarnthein, M. (2005). Evolution and variability of the asian monsoon system: state of the art and outstanding issues. *Quaternary Science Reviews*, 24(5-6):595–629.

Wang, W. M. and McPhaden, M. J. (1999). The surface-layer heat balance in the equatorial pacific ocean. part i: Mean seasonal cycle. *J. Phys. Oceanogr.*, 29(8):1812–1831.

Warren, B. A. (1981). Transindian hydrographic section at lat. 18 s: Property distributions and circulation in the south indian ocean. *Deep Sea Research Part A. Oceanographic Research Papers*, 28(8):759–788.

Watanabe, M. and Hibiya, T. (2002). Global estimates of the wind-induced energy flux to inertial motions in the surface mixed layer. *Geophys. Res. Lett.*, 29(8).

Waterhouse, A. F., MacKinnon, J. A., Nash, J. D., Alford, M. H., Kunze, E., Simmons, H. L., Polzin, K. L., St Laurent, L. C., Sun, O. M., Pinkel, R., Talley, L. D., Whalen, C. B., Huussen, T. N., Carter, G. S., Fer, I., Waterman, S., Garabato, A. C. N., Sanford, T. B., and Lee, C. M. (2014). Global patterns of diapycnal mixing from measurements of the turbulent dissipation rate. *J. Phys. Oceanogr.*, 44(7):1854–1872.

Waterman, S., Garabato, A. C. N., and Polzin, K. L. (2013). Internal waves and turbulence in the antarctic circumpolar current. *J. Phys. Oceanogr.*, 43(2):259–282.

Wernberg, T., Smale, D. A., Tuya, F., Thomsen, M. S., Langlois, T. J., de Bettignies, T., Bennett, S., and Rousseaux, C. S. (2013). An extreme climatic event alters marine ecosystem structure in a global biodiversity hotspot. *Nat. Clim. Chang.*, 3(1):78–82.

Whalen, C. B., MacKinnon, J. A., and Talley, L. D. (2018). Large-scale impacts of the mesoscale environment on mixing from wind-driven internal waves. *Nat. Geosci.*, 11(11):842–+.

Whalen, C. B., MacKinnon, J. A., Talley, L. D., and Waterhouse, A. F. (2015). Estimating the mean diapycnal mixing using a finescale strain parameterization. *J. Phys. Oceanogr.*, 45(4):1174–1188.

Whalen, C. B., Talley, L. D., and MacKinnon, J. A. (2012). Spatial and temporal variability of global ocean mixing inferred from argo profiles. *Geophys. Res. Lett.*, 39(L18612).

Wilkin, J. L. and Morrow, R. A. (1994). Eddy kinetic energy and momentum flux in the southern ocean: Comparison of a global eddy-resolving model with altimeter, drifter, and current-meter data. *Journal of Geophysical Research: Oceans*, 99(C4):7903–7916.

Woo, M. and Pattiaratchi, C. (2008). Hydrography and water masses off the western australian coast. *Deep Sea Research Part I: Oceanographic Research Papers*, 55(9):1090–1104.

Wunsch, C. and Ferrari, R. (2004). Vertical mixing, energy and thegeneral circulation of the oceans. *Annu. Rev. Fluid Mech.*, 36:281–314.

Yu, L., Jin, X., and Weller, R. A. (2007). Annual, seasonal, and interannual variability of air-sea heat fluxes in the indian ocean. *J. Clim.*, 20(13):3190–3209.

Zervakis, V. and Levine, M. D. (1995). Near-inertial energy propagation from the mixed-layer - theoretical considerations. *J. Phys. Oceanog.*, 25(11):2872–2889.

Zhai, X., Johnson, H. L., and Marshall, D. P. (2010). Significant sink of ocean-eddy energy near western boundaries. *Nat. Geosci.*, 3(9):608–612.

Zhai, X. M., Greatbatch, R. J., and Zhao, J. (2005). Enhanced vertical propagation of storm-induced near-inertial energy in an eddying ocean channel model. *Geophys. Res. Lett.*, 32(18).

Zhang, H. M. and Talley, L. D. (1998). Heat and buoyancy budgets and mixing rates in the upper thermocline of the indian and global oceans. *J. Phys. Oceanogr.*, 28(10):1961–1978.

Zhang, S., Alford, M. H., and Mickett, J. B. (2015). Characteristics, generation and mass transport of nonlinear internal waves on the w ashington continental shelf. *Journal of Geophysical Research: Oceans*, 120(2):741–758.

Zhang, X. and McPhaden, M. J. (2010). Surface layer heat balance in the eastern equatorial pacific ocean on interannual time scales: Influence of local versus remote wind forcing. *J. Clim.*, 23(16):4375–4394.

Zheng, S., Du, Y., Li, J., and Cheng, X. (2015). Eddy characteristics in the south indian ocean as inferred from surface drifters. *Ocean Sci.*, 11(3):361–371.